**2012 E-MRS**       **FALL MEETING**

# PROCEEDINGS OF SYMPOSIUM A

# ADVANCED COMPOSITE MATERIALS

# TECHNOLOGIES, PROPERTIES, APPLICATIONS

## Edited by Prof. V. Skorokhod

## September 17-21, 2012
## Warsaw, Poland

This book of proceedings is the presentations of the participants of one of symposia (Advanced Composite Materials: technologies, properties, applications) to be held within the framework of E-MRS Fall Meetings on September 17-21, 2012 in Warsaw, Poland

*Наукове видання*

**"Перспективні композиційні матеріали:технології, властивості, застосування"**

Матеріали Симпозіуму А Варшавської осінньої конференції Європейського матеріалознавчого товариства 2012 року

Англійською мовою

Dear reader!

This edition is devoted to scientific results presented in Warsaw at E-MRS Fall Meeting 2012 symposium A " Advanced composite materials: technologies, properties, applications". This symposium had been organized for the fourth time by  Ukrainian leading academician institute - Frantsevich Institute for Problem of Materials Sciences of National Academy of Sciences of Ukraine from Kiev and leading Polish University - Warsaw University of Technology. For the fourth time Ukrainian Materials Research Society with about 20 regional departments all over Ukraine is an co organizer of  these symposia. Preliminary efforts of all organizers had been successful and more than 100 participants from various European countries had a possibility to present their scientific results and discussed the most actual problems concerning production, characterization, investigation of various properties and areas of applications with special attention to the new kinds of composite materials and new ways of their using in aeronautic  and transport, in biomedicine and electronics, in automobile industry and energetics.

Unfortunately under the technical reasons which didn't depend upon us this issue of proceedings is published with considerable delay but we hope that the presented results hadn't lost their actuality.

We thanks all authors of presented edition for preparation of their materials for publication.

We highly appreciate  the efforts of one of the largest public European organization E-MRS on widening all materials concerning this symposium and its practical organization. We would like to emphasize the large personal contribution of prof. P.Siffert, prof. K.Kurzydlowski, prof. M.Lewandowska and prof. A.Mycielski in organization of our symposium and other ones during f EMRS Fall Meetings 2012.

Our organizing activity wouldn't be successful without organization and  scientific support of Prof. M.Szafran and his collaborators.


On behalf of Kiev regional organizing Committee
Prof. Valerii Skorokhod
Dr. Iryna Bilan
Dr.L.Chernyshev

# TABLE OF CONTENTS

# KNITTED SOLDERED COPPER MESHES AND NANO-STRUCTURE CARBON PARTICLES FOR LIGHTNING PROTECTION OF COMPOSITE MATERIALS FOR WIND TURBINE BLADES

**Vishnyakov L.R.**, Pereselentseva L.N., Vishnyakova K.L.

*Frantsevich Institute for Problems of Materials Science of NASU, Kyiv, Ukraine*
*e-mail: leon.vishnyakov@gmail.com*

## Abstract

The experience in constructing of aircraft components was used to develop knitted soldered copper meshes that shall allow reduction of panel damages and delamination of the composite material due to improved dissipative properties. Electric conductive carbon nano-structure modifiers were suggested for the polymer matrix to increase electric conductivity in carbon plastic fiber laminates and to enhance adhesion strength between the carbon fibers and binder. Knitted soldered copper meshes were suggested for use as being able to improve the wind turbine blade lightning protection system, i.e. lightning capturer and lightning current conductive bus. The results of the work shall be useful for an efficient overall protection of wind turbine blades from lightning.

**Keywords:** *Polymer Composites, Binder, Knitted Soldered Meshes, Nano-structured Particles, Lightning Protection*

## 1.Introduction

Polymer composite materials (PCMs) are in more increased use in aircraft components and wind power production units applications. An efficient lightning protection for modern aircrafts where carbon fiber plastics use yet reaches 50% of the whole mass of their structures and as well as for high power wind units with blades measuring 80 to 100 m in length, and for off-shore (or near-shore) operation conditions specifically, is a challenge. A lightning when strokes a structure made of composite material causes warming that leads to destruction of the composite while the pressure of resulting gases leads to delaminating and fracture of PCM structures. The blade may inflame at the lightning attachment site thus jeopardizing complete destruction of the expensive wind power unit (Fig. 1).

It is to note that lightning protection for PCMs represents any new task, for instance, aircraft structural bodies use means of surface metallization (meshes, foils, metal powder sprayed layers), while wind power production industry uses bar- or rod- and tape-like metal buses that are electrically connected to the wind power unit grounding.

Fig. 1. Eventual pattern of destruction of wind power rotor blades

Methods of lightning protection for aircraft structures mainly depend on the aircraft design philosophy, technical and economical factors, practice and preferences of aircraft designers.

*Objective*

The work has as objective the using of previous expertise in designing lightning protection systems for aircraft structures and their expansion to the wind power units.

**2.Conception and elaboration of technical solutions**

In the power production field, there are international and national standards of lightning blade protection in use [1], which regulate application of specific materials (usually metal) in lightning current conductors.

As can be seen from the previous practice in making and using components from composite materials, their lightning protection systems require improvement, firstly for positioning and minimization of PCM damages. The lightning protection means should have high heating conductivity, high electric conductivity, good feasibility as well as to be able to energy dissipate. Our knowledge in the field of designing and using knitted or knitted soldered meshes in aircraft components lightning protection showed that destructing effect of lightning strike could be considerably reduced when permanent soldered contacts between the loops of the mesh loose and break. The efficient energy dissipation is also contributed by evaporation of the solder from the contact sites of the wire loops and from the wire surfaces [2].

It should be noted that in the wind power production, knitted soldered meshes have not yet found sufficient application. However, the energy dissipation effect, in case of using knitted soldered meshes as lightning current conductors, is of particular attention, to our opinion, and also their use in components of wind power units from composites that are produced by worldwide companies. We should emphasize on the difference of principle between the lightning protection systems for wind turbine blade and existing technical solutions for aircraft protection from lightning. In contrast to aircraft structures that require severe limitations in weight (including the weight of lightning current conductive meshed coatings) the wind power production industry shows relatively mild limitations. In wind turbine blades, the current conductive meshed fabric should have increased cross-section to pass considerable quantity of electricity, especially to safely conduct the current from the lightning attachment site to the ground of wind unit, hence, also its weight increases. Increased cross-section of the meshed fabric can be achievable by the following two ways: i/ creating a fine-meshed fabric with a great number of loops per unit area of the fabric, or ii/ by an increased number of wires in a bundle that form mesh interweaving. In principle, combinations of the first and the second techniques are admitted to create increased cross-section of the mesh that shall conduct current.

A reliable soldering of adjacent loops of meshed fabrics shall have a noticeable importance for increasing conductivity of lightning protection meshes. Soldering is performed using a special technology involving the step-by-step soldering of the meshed fabric across its whole area. A melted solder is used for this, additionally introduced into the zone to be soldered. Here, we should make note the quantity of introduced solder should be restricted because its extra quantity shall lead to non-desirable increasing of surface resistance (e.g. electric resistance of solder ПОС-61 exceeds that for copper about one order).

As we have found when we conducted our works, aircraft structures needed knitted soldered meshes made of copper wires 0.08 and 0.12 mm in diameter (Table 1).Now we produce in volumes and deliver to customers fabrics made of copper wire 0.08 mm covered with tin-lead solder ПОС-61 GOST 1499-54, and of copper wire 0.12 mm covered with the same solder.
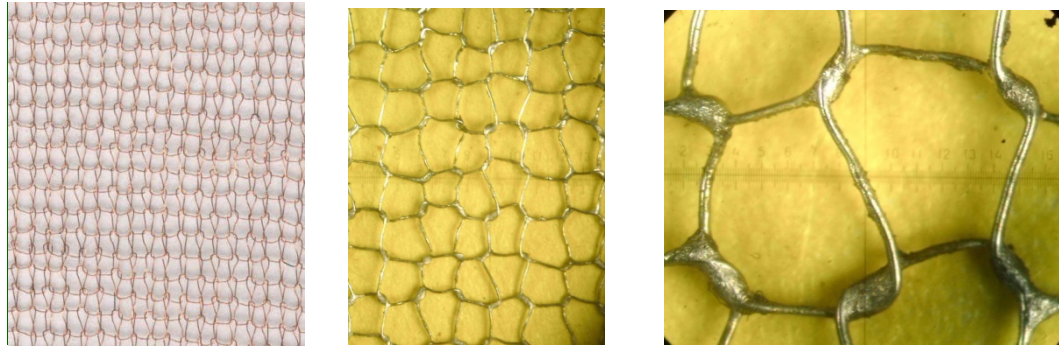
| *a* knitted mesh | *b* knitted soldered mesh | *c* cells formed from loops |

Fig.2. Knitted and knitted soldered meshes from copper wire for aircraft structure lightning protection

Fig. 2 shows photos of knitted soldered meshes. In case of aircraft structures, we suggested one-wire meshes basing on their range of characteristics (weight of 1 sq. m, specific surface conductivity), while for wind turbine blades, meshes with 2 and 3 threads in a bundle at the same pattern of metal wire knitting "Lasting 1×1» proved to be useful (Fig.3). Lightning protection meshes feature anisotropy of mechanical properties and electric conductance (Table 1) and this feature should be taken into consideration while designing lightning protection systems for PCM structures.
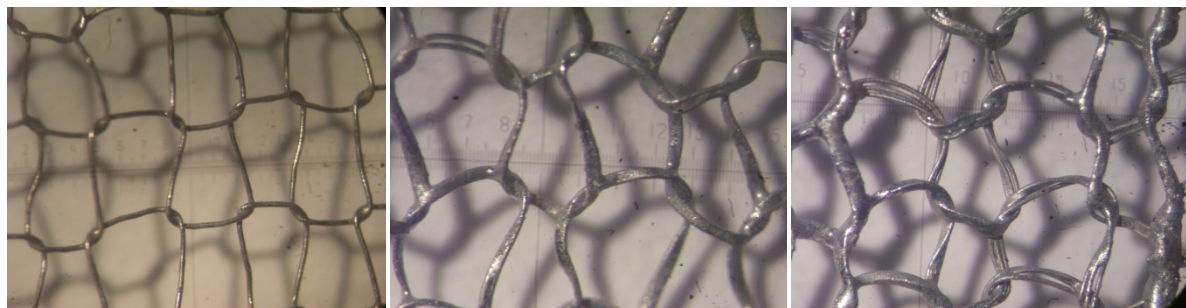


| *a* single wire | *b* double wire | *c* triple wire |

Fig. 3. Knitted soldered meshes from copper wire Ø 0.12 mm differing in number of wires in a bundle

The dependence of specific electric conductance of lightning protection meshed fabrics on their areal densities (Fig.4) shows the specific surface electric conductance can be reduced to the desired value through optimization of the procedure of soldering and by varying the number of copper wires in a bundle that form loops.

11

| | |
|---|---|
| *a* relates to copper wire 0.08 mm*;* | *b* relates to copper wire 0.12 mm |
| 1, 4 longitudinally to wales; 2, 3 transversally to wales | |
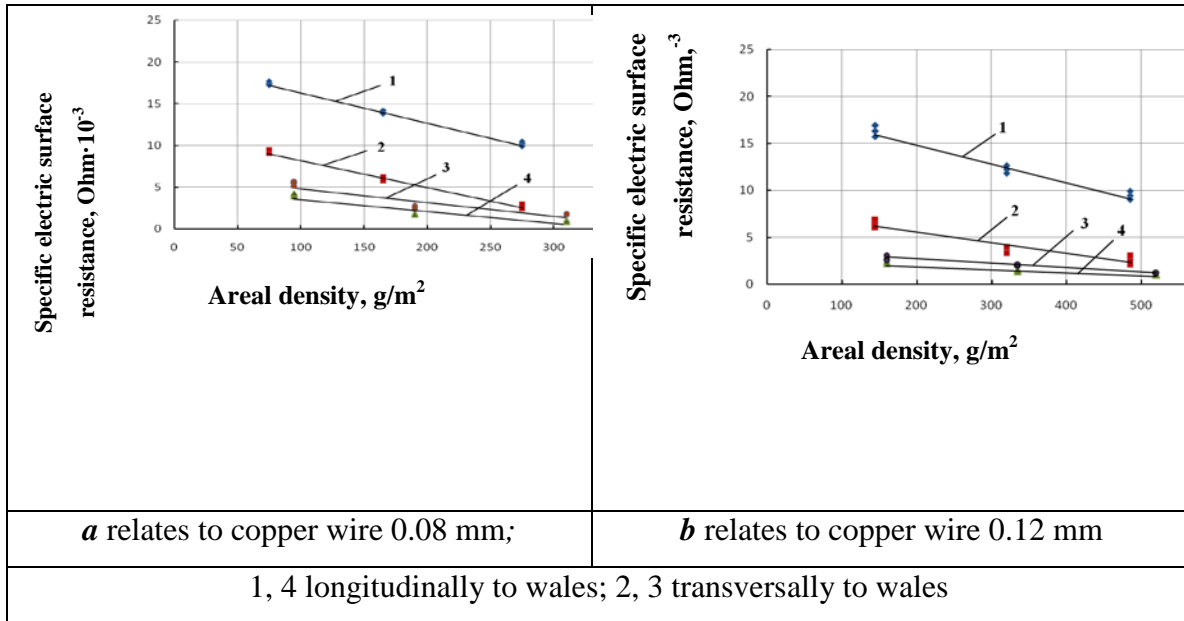
Fig 4. Dependence of specific surface resistance of knitted (1,2)and knitted soldered (3,4) meshes on areal density

Basing on the obtained experimental data (Table 1) for wind turbine blades, we recommend for use knitted soldered meshes made of double wire or triple wire of 0.12 mm in diameter. Such meshes being used for making panels from composite materials passed lightning simulation test on a certified bench at Research Institute "Molniya" of Polytechnic Institute of Kharkiv-city. The panel specimens as tested (Fig. 5) testify a positive influence of the surface reinforcement with a mesh demonstrating considerable reduction of the area and depth of damages in contrast to non-protected panels [3, 4].

Table 1 Properties of lightning protection meshes of knitted pattern made of copper wires

| Diameter of wire, mm | Class of equipment | Type of mesh | Number of wires in a bundle, pcs | Areal density, g/m² | Thickness of mesh, mm | Breaking strength of wire in bundle, N | Relative deformation of wires in bundle when breaking, % | Breaking strength of a strip cut from mesh of 50 mm in width, N Longitudinally to wales | Transversely to wales | Coefficient of anisotropy of mesh strength, $K_c$ | Relative deformation of strip cut from mesh of 50 mm in width at breaking, % Longitudinally to wales | Transversely to wales | Coefficient of anisotropy of mesh strength, $K_L$ | Specific electric surface resistance of meshes, mOhm Longitudinally to wales | Transversely to wales |
|---|---|---|---|---|---|---|---|---|---|---|---|---|---|---|---|
| 0.08 | 10 | knitted | 1* | 70 | 0.15 | 1.25 | 22.4 | 17.8 | 14.6 | 1.22 | 70.4 | 170.5 | 0.41 | 17.4 | 12.3 |
| | | | 2 | 165 | 0.16 | 2.55 | 26.7 | 32.6 | 33.5 | 0.97 | 105.7 | 208.8 | 0.50 | 13.9 | 6.0 |
| | | | 3 | 275 | 0.20 | 3.30 | 28.5 | 59.5 | 62.4 | 0.95 | 130.4 | 255.6 | 0.51 | 10.2 | 2.6 |
| | | Knitted soldered | 1* | 85 | 0.3 | - | - | 35.4 | 27.3 | 1.30 | 15.2 | 36.3 | 0.38 | 4.9 | 6.7 |
| | | | 2 | 190 | 0.32 | - | - | 68.2 | 53.6 | 1.27 | 19.5 | 40.2 | 0.48 | 1.8 | 2.3 |
| | | | 3 | 310 | 0.36 | - | - | 94.7 | 80.7 | 1.17 | 22.3 | 46.4 | 0.48 | 1.2 | 1.7 |
| 0.12 | 8 | Knitted | 1 | 145 | 0.21 | 3.25 | 12.2 | 34.3 | 25.3 | 1.36 | 117.6 | 180.5 | 0.65 | 16.3 | 6.4 |
| | | | 2 | 320 | 0.25 | 6.20 | 16.7 | 68.7 | 57.6 | 1.19 | 170.8 | 250.7 | 0.68 | 12.2 | 3.5 |
| | | | 3 | 485 | 0.35 | 9.20 | 19.5 | 102.6 | 89.7 | 1.14 | 230.5 | 290.4 | 0.79 | 9.4 | 2.5 |
| | | Knitted soldered | 1* | 155 | 0.32 | - | - | 45.5 | 38.5 | 1.18 | 18.3 | 16.8 | 1.08 | 2.7 | 3.5 |
| | | | 2 | 335 | 0.38 | - | - | 90.3 | 80.6 | 1.12 | 32.4 | 33.5 | 0.97 | 1.5 | 2.0 |
| | | | 3** | 520 | 0.45 | - | - | 120.7 | 108.4 | 1.11 | 40.6 | 45.7 | 0.89 | 1.0 | 1,2 |

Note: * produced as per technical documentation

      ** technical documentation in stage of development

$K_c$ is determined as ratio of strength efforts of mesh longitudinally to wales versus breaking effort transversally to wales

$K_L$ is determined as ratio of relative deformation of mesh longitudinally to wales versus relative deformation transversally to wales

*a -* non-protected panel: through-punching

*b* - panel covered with lightning protection mesh: the outer layer damaged in depth 0.5 mm and area 90 cm²

*c* combined lightning protection scheme (mesh + carbon nano-structure particles): any through-punching observed

Fig. 5. Photos of panels after simulating lightning tests

Provision of a reliable conducting to earth high lightning currents under direct strike of a lightning is a feature among others of the lightning protection system in the wind power production field. The current conducting bus connected to earth should be built in into the bulk of a polymer composite (material of blade). Technical requirements of international standard [1] regulate conditions for performing such buses (metal rods, meshes, strips) and dimensions of their cross-sections for various metals, such as copper, aluminum or steel. Our suggestion implies manufacturing of the current conductive bus from several plies of knitted mesh. When doing such a way, we can meet the requirements of the standard relative to electric resistance of current conductive buses while at the same time provide a porous structure of current conductive bus having a high level of feasibility, i.e. being flexible it is able to be inserted into a blade of any curvature whereas the bus porosity and relief contribute its good fit to the material of polymer composite. So, the standard requirements in term of electric resistance is fulfilled for the current conductive buses and at the same time a current conductive bus with porous structure is suggested that has a high level of manufacturability, i.e. the bus being flexible can fit any curvature of the blade, while its porosity and relief contribute good adherence to the material of polymer composite.

Therefore, to catch the lightning charge on the turbine blade, a mesh which covers the surface of the blade with a single ply is provided, while to conduct charges to earth,

we recommend multi-layered bus of, for instance, 300-400 mm in width. The grounding bus shall be then imbedded into the carbon fiber plastics surface along the whole length of the blade and electrically connected to the single-ply mesh of the lightning capturer. Thus, with using knitted or knitted soldered meshes, one shall be able to improve the lightning protection system for turbine blade made of composite materials.

Another efficient means for polymer composite lightning strike protection we recommend for aircraft components protection along with meshes, shall be electrically conductive nano-structure carbon particles (Fig.6).
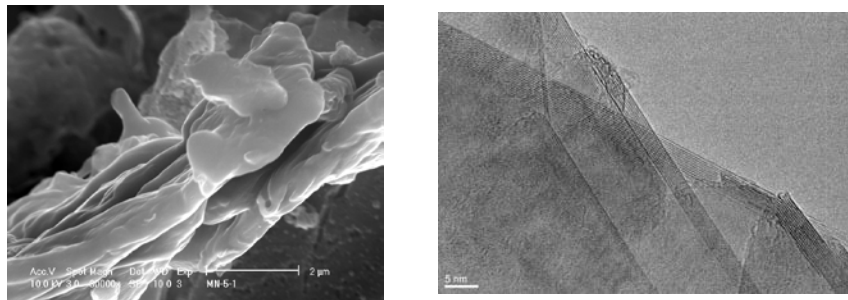


Nano-graphites
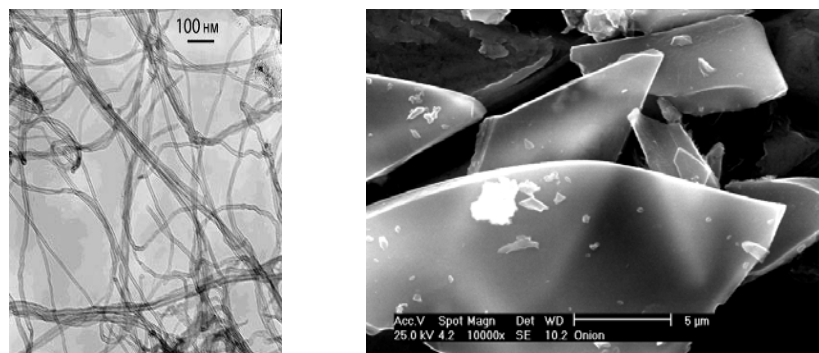


Nano-tubes                    Graphite nano-plates

Fig. 6.  Nanostructure particles for composite modification

Several types of them are produced from vegetables, e.g. pin chips [5]. These particles when used in wind turbine blades contribute both increasing of electric conductance of polymer binder, at the carbon fiber-binder boundary in particular, and enhancing the bonding strength of the fiber to the polymer matrix due to creation of additional cross –linking centers of polymer, and nano-profiling of the carbon fiber surface. We obtained positive results from simulating lightning tests of panels where we

used our combined lightning protection scheme that included knitted soldered meshes and carbon nano-structure particles as fillers for polymer matrix within the surface plies of composite (Fig.5 c).

In some cases, wind turbine blades use glass fiber plastics along with plies from carbon fiber plastics. Glass fiber laminates as blade material being dielectric ones and being located more closely to the outer surface of the blade (within both its leeward side and opposite side) as issuing from some design considerations, are prone to be affected by the punch-through by a lightning discharge (like capacitor) in the direction from the surface of the lightning capturer and through the dielectric layer to electric conductive laminates made of carbon fiber plastics that are located nearing the inner surfaces of half-blades. To avoid the above effect, conditions have to be created that shall guaranty propagation of the current charge across the blade surface (due to its increased electric conductivity) via introduction of electroconductive additives into the surface laminates that are below the lightning protection mesh.

It should be noted that enhanced adhesion bonding at the carbon fiber-polymer matrix boundary shall cause an additional loading upon the carbon fiber, so, more cost effective mean-strength carbon fibers (T300) shall be profitable for use in wind turbine blades instead of costly Japan high-strength fibers T700(800). Thus, the adopted technical solutions can be considered as valid ones that shall allow issuing practical recommendations relative to the composition and design of wind turbine blades that shall use knitted or knitted soldered meshes and carbon nanostructure particles.

## 3.Conclusions

1. Previous achievements in the field of using knitted and knitted soldered copper meshes in the aircraft construction industry were used to develop advanced products, improved dissipative properties of which shall provide reduction of the panel damage area and delamination of composite material.

2. Electric conductive carbon nano-structure modifiers for polymer matrix are proposed that shall increase electric conductivity of the carbon fiber plastics laminates, and enhance adhesion strength between the carbon fibers and binder.

3. Knitted soldered copper meshes are suggested for improvement of the lightning protection system of wind turbine blade, i.e. lightning capturer and lightning current conductor (bus).

4. The results of the work are recommended for making an efficient combined protection system for lightning protection of wind turbine blades.

## References

1. National Standard of Ukraine.  Wind turbine power system units. Lightning protection of wind power turbines.  DSTU IEC 61400-24-2001.

2. L.R.Vishnyakov, I.I.Chernyaskiy, O.V.Zubkov// Study of potential of lightning protection for polymer composite materials reinforced with knitted copper mesh. Visnik of Ingenernoi Academiy Ukrainy, No.2 – K.,2012 – P.143-148.

3. L.R.Vishnyakov, A.M.Barannikov, Yu.F.Hrin, Z..N.Demidenko et al. // Manufacturing products from polymer composites reinforced with surface-reinforced knitted meshes// Visnik of Ingenernoi Academiy Ukrainy, No. 3-4 – K., 2009 – P.182-186.

4. L.R.Vishnyakov, O.K.Nedzelskiy, Yu. F. Hrin, I.I. Chernyavskiy, Yu.M.Vasilenkov // Simulating lightning tests of composite materials having lightning protection based on knitted copper meshes // Visnik of Ingenernoi Academiy Ukrainy, No. 3-4 – K., 2009 – P.187-191.

5. L.R.Vishnyakov //Development and use of knitted soldered copper meshes for lightning protection of carbon fiber plastics in aircraft structures // Technologicheskie systemi, No.1 (%*).- K., 2012 – P.29-33

# ELABORATION OF C/C COMPOSITES BASED ON THE INFILTRATION INTO THE PREFORM ON AN HYDROCARBIDE IN ITS SUPERCRITICAL STATE

**Maillé L., Guette A., Pailler R., Le Petitcorps Y., Weisbecker P.**

*Univ. de Bordeaux, LCTS, UMR 5801, F-33600, Pessac, France*
*e-mail:maille@lcts.u-bordeaux1.fr*

## Abstract

A work based on the development of a new process for the fabrication of a C/C composite for aeronautic and aerospace industries, in order to reduce the infiltration duration of the carbon preform, is reported in this paper. The infiltration of a carbon fibrous preform by the mean of a hydrocarbon in the supercritical fluid state is done at high temperature in order to get a carbon matrix. The microstructure of the pyrocarbon coating is characterized by SEM and TEM. The experimental parameters (temperature, hydrocarbon pressure, residence time) are tuned in order to elaborate the carbon matrix. The best conditions lead to a rapid densification in-depth from the top of the preform. After several experiments, the densification has been improved.

**Keywords**: *supercritical fluid, Chemical Vapor Infiltration, C/C composites*

## 1.Introduction

Ceramic Matrix Composites are developed for aeronautic and spatial applications [1-2] for their refractoriness and their low density. These composites are usually get by a long infiltrating step of a weaved preform by Chemical Vapor Infiltration (CVI) using a hydrocarbon precursor as the propane for example [1]. However, the CVI-step is a rather long process which is a huge drawback. As a result, the manufacturing cost of these composites is very expensive. In order to reduce the cost, other processes can also be employed to get the matrix, as liquid phase routes with mineral charges [3-9].

In this paper, we explore an original and new densification process in order to elaborate a Carbon/Carbon (C/C) composite: the Chemical Supercritical Fluid Infiltration. A supercritical fluid is a substance at a temperature and pressure above its thermodynamic critical point. Its properties are simultaneously those of gases and liquids [10]. Indeed, it has the unique ability to diffuse through porous solids like a gas, and to dissolve materials like a solvent. This combination of the solvent ability and the high diffusivity should enable a rapid infiltration and a good densification of the porous preform.

## 2. Materials and experimental procedures

Two types of materials are used: (i) graphite pipes (length 6 cm, diameter 0.6 cm) are used as a substrate for kinetic studies of the deposition rate, and (ii) 3D porous carbon fibrous preforms (length 2 cm, diameter 1.5 cm) for infiltration study. The initial open porosity of the preforms is around 77%.

A cold wall reactor schematic represented in Fig. 1, is used at high pressure, in batch flow. It is made of inconel alloys. The graphite pipe is heated, using the Joule effect. The temperature is measured by a thermocouple located inside the graphite pipe protected by an alumina tube. The carbon films or matrix are elaborated using the methane as the hydrocarbon precursor. The kinetic of the carbon deposit can be studied by modifying the values of the residence time of the methane. The other parameters (initial pressure, initial temperature) are kept constant. The temperature selected for each samples is 950°C, with an initial pressure of 50 bars, in these conditions the methane is a supercritical fluid ($T_{critical}$ = -82.6°C and $P_{critical}$ = 46 bar). For kinetic studies of the deposition rate, thin films are performed on the graphite pipes from 2.5 to 20 minutes of deposition. The duration selected (cf. Table 1) for one step infiltration of the carbon matrix texture 3 D, is fixed to 60 minutes.

Another experiment with several steps of infiltration, described table 1, is used to improve the matrix densification, with an initial pressure of 50 bar. The polished cross sections of thin carbon films or matrix are observed with an optical microscope, (Reichert-Jung MEF3).
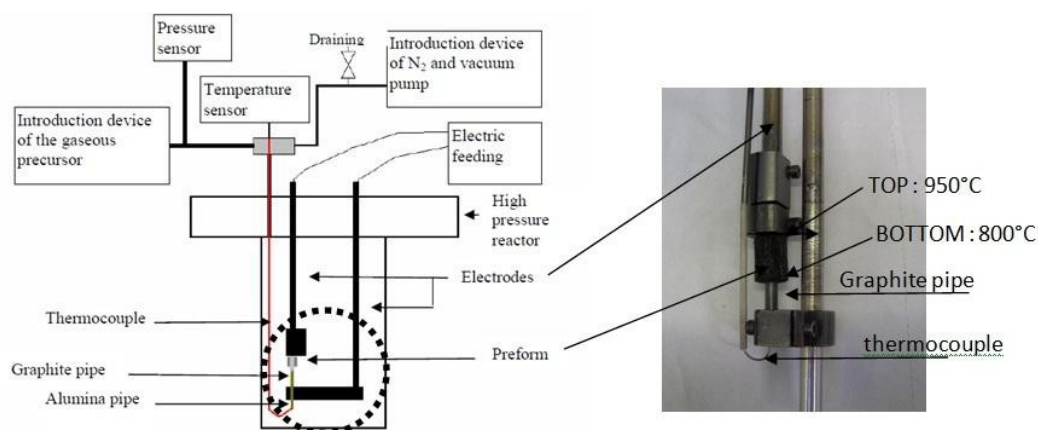


Fig. 1. Schematic representation of the cold wall reactor.

## 3. Results and discussion

### 3.1 Pyrocarbon coating on a graphite pipe

With the variation of the residence times, it is possible to reach an important thickness of pyrocarbon: from 3µm to 30 µm for 2.5-5 minutes and 10-20 minutes respectively. It confirms the interest to work using a supercritical fluid, by comparison, several hours are necessary to reach the same thickness with the CVI-process [11].

The thickness of the pyrocarbon coating varies significantly along the pipe due to a presence of a temperature gradient (Fig. 2). The temperature is a particularly significant and sensitive parameter. The texture of the pyrocarbon coating is similar to the one elaborated with CVI-process (Fig. 3). Pyrocarbon thin film is characterized by a cone-like growth structure [12].
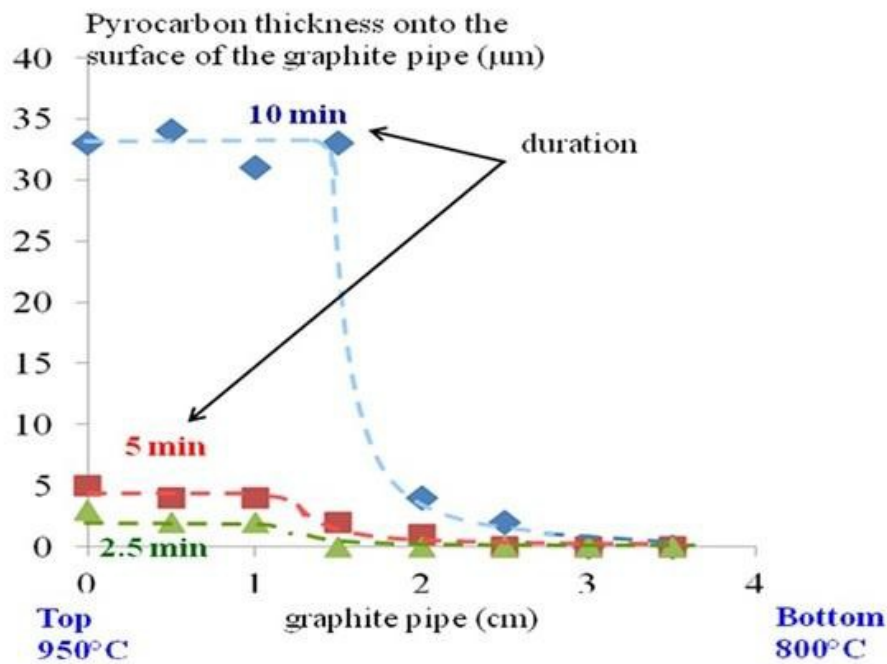


Fig. 2. Influence of the gradient temperature of the graphite pipe on the pyrocarbon thickness.

In order to demonstrate the feasibility to perform a pyrocarbon thin film with a hydrocarbon precursor in supercritical state, carbon preforms have been densified with the same protocol.
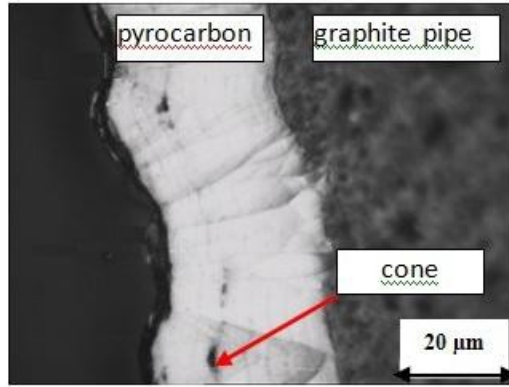
Fig. 3. Cross section of a pyrocarbon layer deposited on the carbon pipe (pyrocarbon elaborated with 20 minutes of residential time).

*3.2 Infiltration of the pyrocarbon matrix into a fibrous preform*

The influence of the hydrocarbon precursor residence time during the matrix infiltration is studied. The temperature and the initial pressures are fixed at 950°C and 50 bars respectively. These first experiments show a good densification (infiltrated of 0.5 minute depth of the preform) for a short residence time (10 minutes). However, as it could be observed on the sample performed with residence time of 60 min, the densification is not complete (Fig. 4). Various pores are present between some fibers even on the surface of the preform.
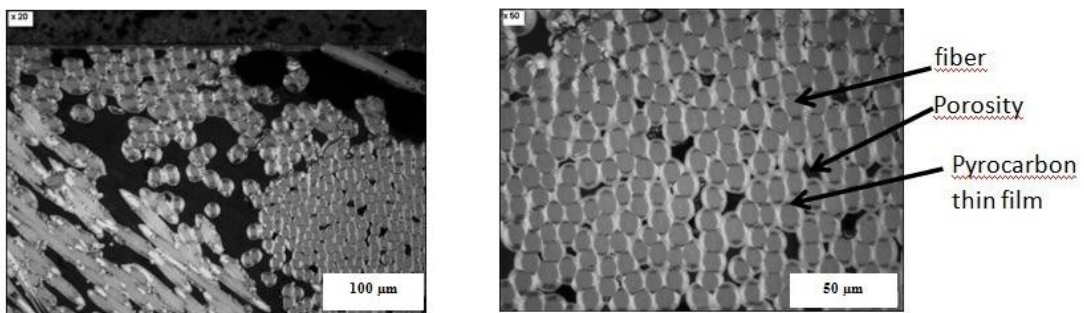


Fig. 4. Cross sections of the infiltrated of C/C composite with a residence time of 60 min, at different scale.

The cross sections observations show a densification thickness of 1.5 mm in the depth of the preform with a residence time of 60 minutes (against 0.5 mm with 10 minutes). Consequently, with this experiment, the densification is significantly improved

to the first one, but a lot of porosities are presents in the matrix. However, the pyrocarbon thin film is homogeneous in thickness and adherent to the fiber.

Table 1. Infiltration conditions of the 3 D carbon preforms.

| samples | temperatures (°C) | durations (min) | conditions | Mass gain |
|---------|-------------------|-----------------|------------|-----------|
| A | 950 | 60 | One step infiltration | 43 % |
| B | | | Semi-continuous feeding | 41 % |
| | 950 | 10 | Step 1(*) | |
| | 950 | 10 | Step 2 | |
| | 950 | 10 | Step 3 | |
| | 1050 | 10 | Step 4 | |
| | 1050 | 2 | Step 5 | 90 |

*(\*) For each step, the vessel is evacuated and then feed with the $CH_4$ precursor at a constant pressure of 50 bar.*

In order to improve the densification, other experiments are performed, using the semi continuous feeding reactor (table 1). Five steps of infiltration have been done, equivalent to 42 min for the residence time. The change in the temperature between the step 3 and 4 was done in order to introduce the pyrocarbon at low temperature inside the preform, and to finish the densification at high temperature, to fill the porosities.

The matrix densification using the semi continuous feeding of the reactor has been improved. After these five steps, the gain mass of the sample is increased to 90% by this way. Whereas it varies from 41% and 43% for one batch of 10 minutes and 60 minutes respectively (table 1). It is possible to compare the cross sections of the figure 3 and 4, and to observe an improvement of the infiltration with the semi continuous feeding reactor. A good densification thickness of 1.5 mm in the depth of the preform is observed. A pyrocarbon coating is observed around each fiber until 2.5 mm in-depth of the preform (figure 5 a-b). Homogeneous nucleation of carbon grains is present in an area without fibers (figure 5 c). This is confirmed by the TEM characterizations with present 3 zones: i) a polynucleated heart, with graphene plans oriented (002) around the center (2 – 2.5 µm); ii) new growth cones (100 nm) the material is highly textured typical of the pyrocarbon, and iii) a carbon nanograins without organization (Fig. 6).
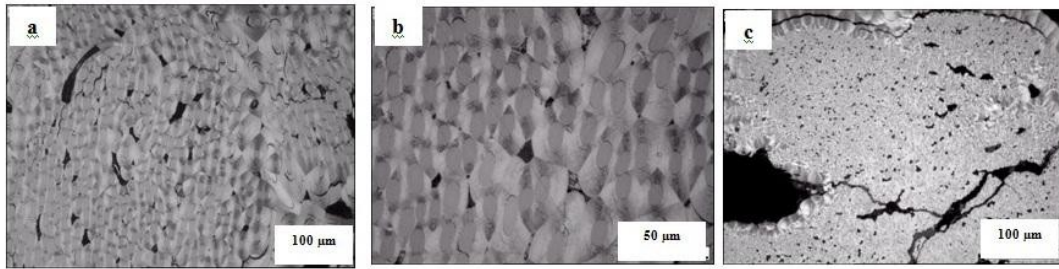
Fig. 5. Cross section of sample realised with the five steps described in table 1
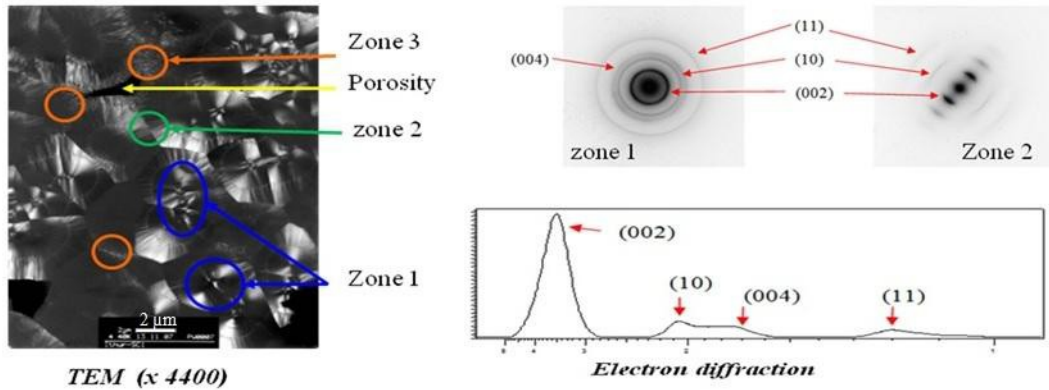


Fig. 6. Homogeneous nucleation characterized by TEM.

## 4. Conclusion

The objective of this study was to demonstrate that a pyrocarbon coating could be deposited around each carbon fibres within a 3D carbon preform with a methane precursor in its supercritical state. A device has been set up for this purpose alloying to work under a pressure of 50-100 bar at 950-1050°C for less than one hour of infiltration. According to the experimental parameters chosen the infiltration depth of the preform could reach 1.5 mm and a pyrocarbon coating is observed around each fiber until 2.5 mm in-depth. The results were interesting, however other experiments have to be conducted in order to get a full infiltrated preforms if necessary.

**References**

1.      Naslain R. SiC-Matrix Composites: Non brittle Ceramics for Thermo-Structural Application. International Journal of Applied Ceramic Technology 2005; 2: p.75-84.

2.      Naslain R., Introduction aux matériaux composites. Tome 2 : Matrices métalliques et céramiques, Edition du CNRS, France 1979.

3.      Rietveld H.M. A profile refinement method for nuclear and magnetic structures. Journal of Applied Crystallography 1969; 2: p.65-&.

4.      Rodriguez-Carvajal J. Recent advances in magnetic structure determination by neutron powder diffraction. Physica B: Condensed Matter 1993; 192:p.55-69.

5.      Sambasivan S., Petuskey W.T. Phase chemistry in the system – thermochemical review with phase – stability diagrams. Journal of Materials Research 1994; 9: p.2362-2369.

6.      Paulasto M., Kivilahti J.K., Van Loo F.J.J. Interfacial reactions in $Ti/Si_3N_4$ and TiN/Si diffusion couples. Journal of Applied Physics 1195; 77: p. 4412 – 4416.

7.      Hillig W.B. Making ceramic composites by melt infiltration. American Ceramic Society Bulletin 1994; 73: 56-62.8.   Le Ber S., Dourges M.A., Maillé L., Pailler R., Guette A. Ceramic matrix composites densification by active filler impregnation followed by PIP process. Ceramic Transactions 2010; 215: p.113-123.

9.      Magnant J., Maillé L., Pailler R., Ichard J.C., Guette A., Rebillat F., Philippe E., Carbon fiber/reaction-bonded carbide matrix for composite materials – Manufacture and characterization, Journal of the European Ceramic Society 2012; 32:p. 4497-4505.

10.     Le Trequesser Q., Mesguich D., You E., Aymonier C., Watkins J. Supercritical fluid deposition of compositionally uniform yttria stabilized zirconia films. The Journal of Supercritical Fluids 2012; 66:p. 328-332.

11. Christin F., Design - fabrication and application of thermostructural composites (TSC) like C/C - C/SiC and SiC/SiC composites. Advanced engineering materials 2002; 4: p.903-912.

12.     Bourrat X., Fillion A., Naslain R., Chollon G., Brendlé M. Regenerative laminar pyrocarbon. Carbon 2002 ; 40 :p. 2931-2945.

# STUDY OF THE DEGREE OF POLYMERIZATION OF CARBON-EPOXY COMPOSITE PARTS USING THERMAL ANALYSIS AND RAMAN SPECTROSCOPY

**Garcia J.A., <u>Mari B.</u>, Rosado M., Moliner C., Badia J., Ribes A., Sans J.A., Manjon F.J.**

*Universitat Politecnica de Valencia (UPV), Cami de Vera s/n, 46022 Valencia. Spain.*
*e-mail: bernabe.mari@gmail.com*

## Abstract

Mechanical characterization of thermosetting such us epoxy resins are conditioned by the polymerization degree or cure. A high degree of curing is important to maximize the mechanical properties. Several Carbon-Fiber reinforcement polymer matrix specimens were manufactured in an aluminium mold with vacuum bagging and autoclave curing and with a low temperature cure epoxy Prepreg System, SE 84LV. The samples were analysed by TGA for the determination of the percentage of each carbon, resin, and residue fraction. Three different curing conditions were used in this study. In the present work, the degree of cure of different samples was monitored/assessed/checked by SEM imaging, thermal haracterization, and Raman spectroscopy. Results obtained by Raman spectroscopy are complementary with that obtained from classical thermal characterization techniques such as Thermogravimetry and Differential Scanning Calorimetry.

## 1.Introduction

Nowadays, Carbon-Fiber Reinforcement Polymer Matrix (CFRP) parts are intensively used in various industrial applications. The high strength-to-weight ratio of CFRP composites make them ideal for the aerospace, yacht racing, wind blades, automobile, and civil engineering industries. Due to the nature of these materials, the characterization of their mechanical, rheological and kinetics properties is complex and therefore the optimization of the manufacturing process becomes complicated. The difficulty arises from the complex chemistry associated with the resin cure step. Then, the study of cure kinetics is of great interest in polymer processing [1].

One of the most popular methods of preparing a composite is the Prepreg technology. Prepregs are prepared from a woven sheet of reinforcement fiber pre-impregnated with polymer matrix, thermoset or thermoplastic. Prepreg sheets must be shaped and cured in a pressure mold, mostly in autoclave. Prepreg sheets are cut and layered on a mold with a release agent. There are many types of release agents, depending on the cure temperature, pressure, etc. Prepreg sheet is wrapped in a breather cloth to absorb excess resin. Finally, it is enclosed in a vacuum bag and sealed. The mold is then placed into the autoclave and cured under some temperatures stages (two ramps, two holds, and one cool down). The ability to control and monitor the cure reaction of CFRP, particularly epoxy resins, could help the designer to develop high quality composite parts

[1]. The curing phase is a critical parameter in order to obtain high quality parts, the most important parameters are composition, amount of hardener and diluents, curing temperature, and holding time [2].

The work presented here shows preliminary results of measurements performed with a commercial Prepreg sheet used to manufacture high-performance racing yacht masts. America's Cup syndicates chosen this resin to be used in the Volvo Ocean Race boats. Thermal analysis was carried out to investigate the cure reaction of a low-temperature cure epoxy Prepreg system.

Thermal characterization was performed using Differential Scanning Calorimetry (DSC) and Thermogravimetry (TGA) as the most common techniques for cure analysis of thermosetting systems [3-4]. Both DSC and TGA are destructive methods while Raman spectroscopy is a complementary non-destructive method. The feasibility of this technique has been studied for several authors and demonstrates its industrial interest [2-5]. Further, the PBO/epoxy composite material has been studied for yacht applications and compared the behaviour with the predictions of available cure models [6]. Raman spectroscopy is also an efficient analytical method for the prediction of numerical models for a storage temperature of epoxy resin prepregs [7].

In this paper Raman Spectroscopy has been used to check the composition of three samples with different degree of cure (DOC) through the vibrational properties of the samples at different DOC. Three samples of carbon-fiber reinforced plastic (CFRP) composite material have been analysed using the techniques mentioned above. Results obtained from Raman spectroscopy have been compared with those from Thermal Gravimetric Analysis (TGA) and Differential Scanning Calorimetry (DSC) and have shown to agree with the two classical thermal characterization techniques thus paving the way for non-destructive characterization of manufactured CFRP composites.

## 2.Experimental

The process by which the specimens were manufactured is vacuum bagging and curecompaction in autoclave. This material is laminated in positive or negative tool shapes with very precise fibre alignment. This manufacturing process also includes an autoclave curing and post curing at controlled pressure and temperature. Pressure and vacuum conditions yield the maximum quality of the part. A Prepreg product's life is

reduced anytime it is taken out of the cooling environment. Material may have a total life of 64 hours outside of the cooler.

The minimum infrastructures required by the process are:

- CNC machines for the manufacture of molds and inserts, and also for the fiber cutting.
- Autoclave for compression and curing.
- Cold store for Prepregs.
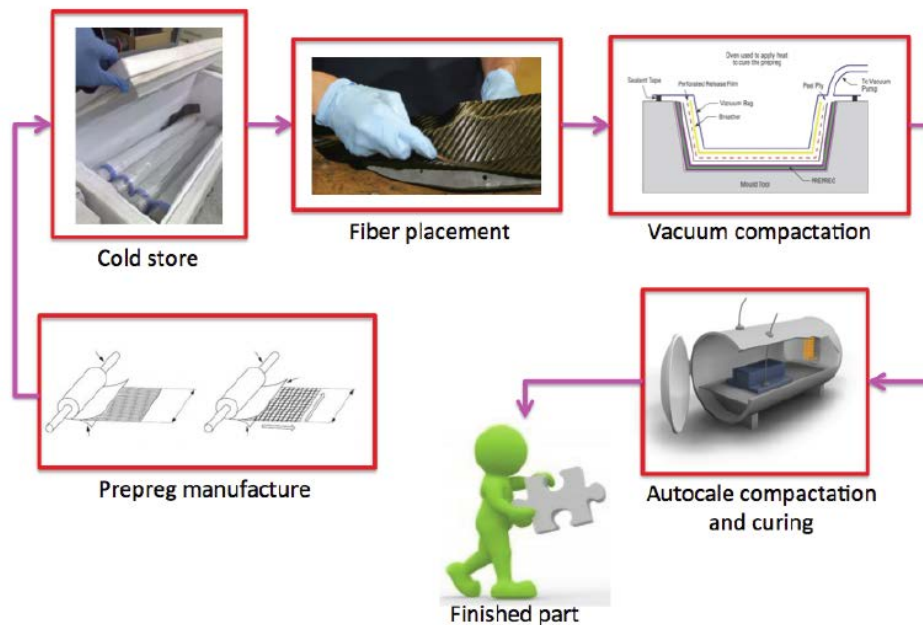


Fig. 1. Schematic steps of Prepreg technology

The SE 84LV system can be cured at low temperature (85.C), or for faster moulding of components at 120.C. The samples were prepared according the followings steps (Figure 1).

1. Place the lay-up on a tool previously treated with a release agent or film.

2. Apply a peel ply to the surface of the lay-up. Cover the peel ply entirely with a perforated release film.

3. Install a vacuum bag and position part in the oven or autoclave.

4. The heat-up cycle, typically 1°C/min to the final cure temperature. At 85°C, the temperature should be held for 10 hours.

5. Turn off heat and cool, when fully cooled, the part may be debagged.

Thermogravimetric (TGA) experiments were performed to simulate and optimize the experimental conditions for the determination of the percentage of each carbon, resin, and residue fractions in all samples represented in Figure 1. Once these conditions are set, the samples were introduced in a muffle furnace.

Multi-rate non-isothermal thermogravimetric experiments were carried out in a Mettler-Toledo TGA/SDTA 851 (Columbus, OH). Samples weighing 10-11 mg were heated in an alumina holder with capacity for 70 µL. Experiments were performed from $30^0C$ to $1000^0C$ at a heating rate of $10^0C$ /min under constant flow of oxygen (50 mL/min) to simulate the experimental conditions inside a muffle furnace. Experiments were repeated three times, and the averages were considered as representative values. Characterization was assessed with the aid of the software STAR® 9.10 from Mettler-Toledo.

Each sample composition was obtained according to **ASTM D3171-11 [4]**, *"Standard methods for constituent content of composite materials"*, applying the following expressions:

$$P1\ (\%) = \frac{P_1}{P_0} \cdot 100 \tag{1}$$

$$P2\ (\%) = \frac{P_2}{P_0} \cdot 100 \tag{2}$$

$$P3\ (\%) = \frac{P_3}{P_0} \cdot 100 \tag{3}$$

$$\text{Residue}\ (\%) = P1 - P2 - P3 \tag{4}$$

where $p_0$, $p_1$, $p_2$ and $p_3$ represent the initial, final, carbon, and resin masses, respectively. Differential Scanning Calorimetry (DSC) was used to obtain the degree of cure of Sample 1 (Figure 2). Thermograms were obtained using a Mettler Toledo DSC 822 analyser. About 4-6 mg of each composite was sealed in aluminum pans with capacity for 40 µL and heated from - up to $300^0C$ at a rate of $10^0C$ /min for dynamic DSC scanning. The total heat of reaction, $H_T$, was estimated by the total area and the heat of curing.

Isothermal analyses were performed at temperatures ranging from 125 to 145 $^0C$ in 5 $^0C$ increments at a rate of 10 $^0C$/min. The total area under these exothermic curves was used to calculate the isothermal heat of cure, $H_i$, at a given temperature.

After each isothermal scan, the sample was cooled and re-heated again from -25 to $300^0$C at $10^0$C /min to evaluate the residual heat of reaction, $H_R$, which could be calculated from the area under the exothermic peak in the resulting curve.

Raman spectra were collected in backscattering geometry by a confocal HORIBA Jobin-Yvon LabRam high-resolution ultraviolet microRaman spectrometer with a 1200 grooves/mm grating, a 100-μm slit, and a 50× objective, in combination with a thermoelectrically-cooled multichannel CCD detector (spectral resolution below 3 cm$_{-1}$). A 532.12 nm DPSS laser line with a power of 50 mW was used.

## 3.Results and discussion

Three different samples have been analyzed in order to check the degree of cure. Sample 1 is a carbon sheet with nearly cero degree of cure (non-cured sample); i.e., it corresponds to the sample at the beginning of the manufacturing process. On the other hand, samples 2 and 3  ave been semi-cured and cured in autoclave, respectively. Figure 2 shows three photographs of the three studied samples with different degrees of cure: non-cured, semi-cured, and cured.
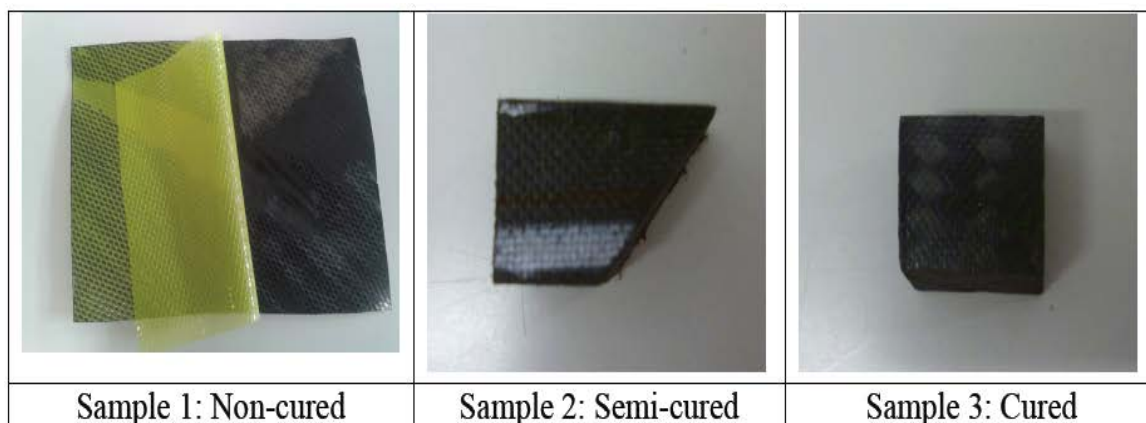


Fig. 2. Pictures of CFRP samples with different degree of cure.

Figure 3 shows the SEM micrographs for the three studied samples. The effect of the cure time is evident in these micrographs, as the cure time becomes longer the carbon fibers are best resolved because the resins covering the carbon fibers disappear with the cure treatment. Diameter of carbon fibers was found to be about 6 μm.
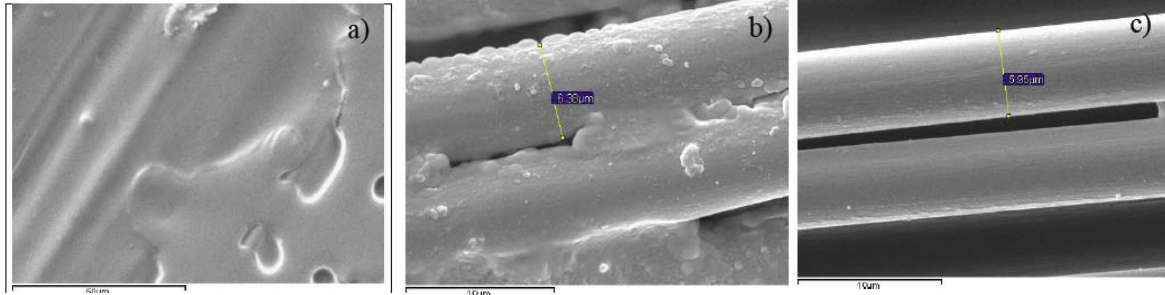
Fig. 3. SEM micrographs of composite samples: a) Non-cured, b) Semi-cured, c) Cured.

Thermogravimetric (DTG) results are shown in Figure 4.
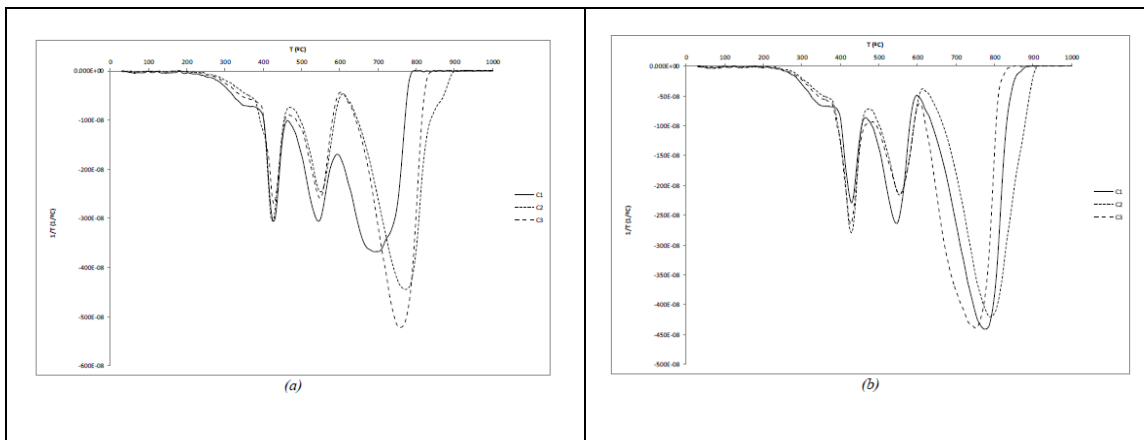


Fig.4. DTG thermographs for composite samples with different degree of cure:
a)Semicured (Sample 2), b)Cured (Sample 3).

Three stages were observed for the dynamic thermogravimetric studies in oxidative conditions (Table 1).

Table 1. Temperature of degradation for samples 2 and 3

|  | $T_{peak1}$ | $T_{peak2}$ | $T_{peak3}$ |
|---|---|---|---|
| **Sample 2** | 427ºC | 551ºC | 773ºC |
| **Sample 3** | 430ºC | 553ºC | 790ºC |

The first step begins at about 425°C while the second step shows a maximum rate near 550°C. The third step corresponds to the degradation of the residue with a rapid rate at 790$^0$C. For both samples 2 and 3, the initial (lost) masses are gathered in Table 2 (Table 3).

Table 2. Initial Mass for samples 2 and 3

| Scan | $P_0$ (mg) Sample 2 | $P_0$ (mg) Sample 3 |
|---|---|---|
| C1 | 1,1655 | 1,1276 |
| C2 | 1,1630 | 1,1634 |
| C3 | 1,0930 | 1,1214 |

Table 3. Mass loss for samples 2 and 3

| Sample 2 | | | Sample 3 | | |
|---|---|---|---|---|---|
| Tc = 427°C | Tc = 551°C | Tc = 773°C | Tc = 430°C | Tc = 553°C | Tc = 790°C |
| Mass loss $P_1$ (mg) | Mass loss $P_2$ (mg) | Mass loss $P_3$ (mg) | Mass loss $P_1$ (mg) | Mass loss $P_2$ (mg) | Mass loss $P_3$ (mg) |
| 0,4103 | 0,0681 | 0,6859 | 0,4098 | 0,2497 | 0,4648 |
| 0,4192 | 0,2413 | 0,5009 | 0,4174 | 0,5555 | 0,1862 |
| 0,3805 | 0,0359 | 0,6755 | 0,3855 | 0,0276 | 0,7073 |

Table 4 represents the fraction percentages for samples 2 and 3, after applying (1) to (4) cure steps.

Table 4. Fraction percentages for samples 2 and 3

| Fraction | Sample 2 | | | Sample 3 | | |
|---|---|---|---|---|---|---|
| | Replica 1 (%) | Replica 2 (%) | Replica 3 (%) | Replica 1 (%) | Replica 2 (%) | Replica 3 (%) |
| P1 | 35 | 36 | 34 | 36 | 35 | 34 |
| P2 | 5 | 20 | 3 | 22 | 47 | 2 |
| P3 | 58 | 43 | 61 | 41 | 16 | 63 |
| Residue | 2 | 1 | 2 | 1 | 2 | 1 |

The analysis of the decomposition process suggests that the initial degradation step corresponds to the elimination of volatiles and low molecular mass species, with a rate of approximately 35% for the three replies of both samples. The second stage of the thermal decomposition would be the one related to the polymer network scission and the later decomposition stage would correspond to the thermal degradation of the carbon fibre [3].

As shown in Table 5, high standard deviation values were found for fraction P2 and P3. This fact could be attributed to a non-uniform curing process.

Table 5. Average and standard deviation for samples 2 and 3

| | Sample 2 | | Sample 3 | |
|---|---|---|---|---|
| Fraction | Average | Standard deviation | Average | Standard deviation |
| P1 | 35,0 | 1,0 | 35,0 | 1,0 |
| P2 | 9,3 | 9,3 | 23,7 | 22,5 |
| P3 | 54,0 | 9,6 | 40,0 | 23,5 |
| Residue | 1,7 | 0,6 | 1,3 | 0,6 |

The degree of cure of the epoxy carbon composites was obtained by means of **Differential Scanning Calorimetry** (DSC). Figure 5a shows the exothermic heat curves of the epoxy system (Sample 1) at a heating rate of 10.C/min. The total area under the curve, based on the extrapolated baseline at the end of the reaction was used to calculate the total heat of cure obtaining a value of $H_T = 135$ J/g.
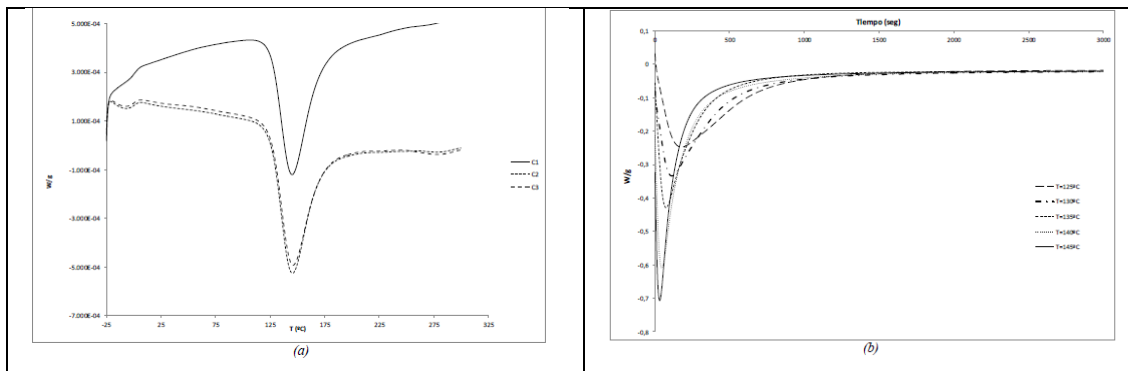


Fig.5. DTG thermographs for composite samples:
a) Exothermic heat cures of the epoxy system (Sample 1) at a heathing rare of $10^0$C/min,b) Isothermal DSC curves.

In general, the curing reaction of a thermosetting resin can proceed over a wide temperature range. However, considering the sensitivity and response limitation to heat changes, the isothermal DSC analysis is usually operated in a moderate curing temperature range. [3] The optimum curing temperature range ($T_i=125^0$C - $T_{peak}=145^0$C) was determined based on the dynamic curing DSC curves (Figure 5a).

The isothermal degree of cure was obtained from isothermal DSC curves (Figure 5b). As expected, with the increase of curing temperature, the time to the maximum value

became shorter. The total area under the curve was used to calculate the isothermal heat of cure, $\Delta H_i$. In order to calculate and evaluate the residual heat of reaction, $\Delta H_R$, a cooling and heating process was performed for each value of $T_{iso}$. Both $\Delta H_i$ and $\Delta H_R$ values at a given temperature $T_{iso}$ are gathered in Table 6.

Table 6. $\Delta H_i$ and $\Delta H_R$ for each isothermal experiment

| $T_{iso}$ (°C) | $\Delta H_i$ (J/g) | $\Delta H_R$ (J/g) |
|---|---|---|
| 125 | 132.70 | 2.87 |
| 130 | 134.50 | 3.12 |
| 135 | 118.26 | 3.50 |
| 140 | 135.99 | 3.62 |
| 145 | 123.60 | 6.12 |

$$\alpha_{HR} = \frac{\Delta H_T - \Delta H_R}{\Delta H_T} \qquad (5) \qquad \alpha_{Hi} = \frac{\Delta H_i}{\Delta H_T} \qquad (6)$$

The values of $\alpha$ for each $T_{iso}$ are presented in Table 7. The results suggest that a non-uniform process is occurring, as no clear tendency is shown. This fact is in accordance to the results obtained from the previous TGA analysis.

Table 7. Degree of cure for sample 2

| $T_{iso}$ (°C) | $\alpha_{HR}$ | $\alpha_{Hi}$ |
|---|---|---|
| 125 | 0.98 | 0.98 |
| 130 | 0.98 | 0.99 |
| 135 | 0.97 | 0.88 |
| 140 | 0.97 | 1.00 |
| 145 | 0.95 | 0.92 |

**Raman spectroscopy**

We have performed Raman scattering measurements of the three samples (1, 2, and 3) under the same conditions: 120 s of exposure time, 2 accumulations, and 0.6 neutral density filter. The use of an attenuator became necessary to avoid the radiation damage on the sample. Analysis of several combinations of exposure time and attenuators

was carried out to obtain optimal conditions. No changes were observed in the surface of the non-cured carbon sheets under the above conditions after the Raman measurements. The Raman spectra shown for each sample is the result of the average along three points of one fiber after checking that several fibers gave similar results.

Figure 6 displays the Raman spectra of the three studied fibers. Two main Raman peaks located at 1352 and 1585 cm-1 were observed. The Raman spectra were shifted vertically for clarity. The peak at 1585 cm-1 is attributed to ordered or graphitic carbon (G band), while peaks located at 1352 cm-1 (D band) and 1620 cm-1 (D' band) are assigned to disordered carbon [8-10]. The ratio between both intensities could give us an idea of the crystalline order of the sample and using the Knight formula, $L_a = C(I_D/I_G)^{-1}$, the crystalline size C [11, 12].
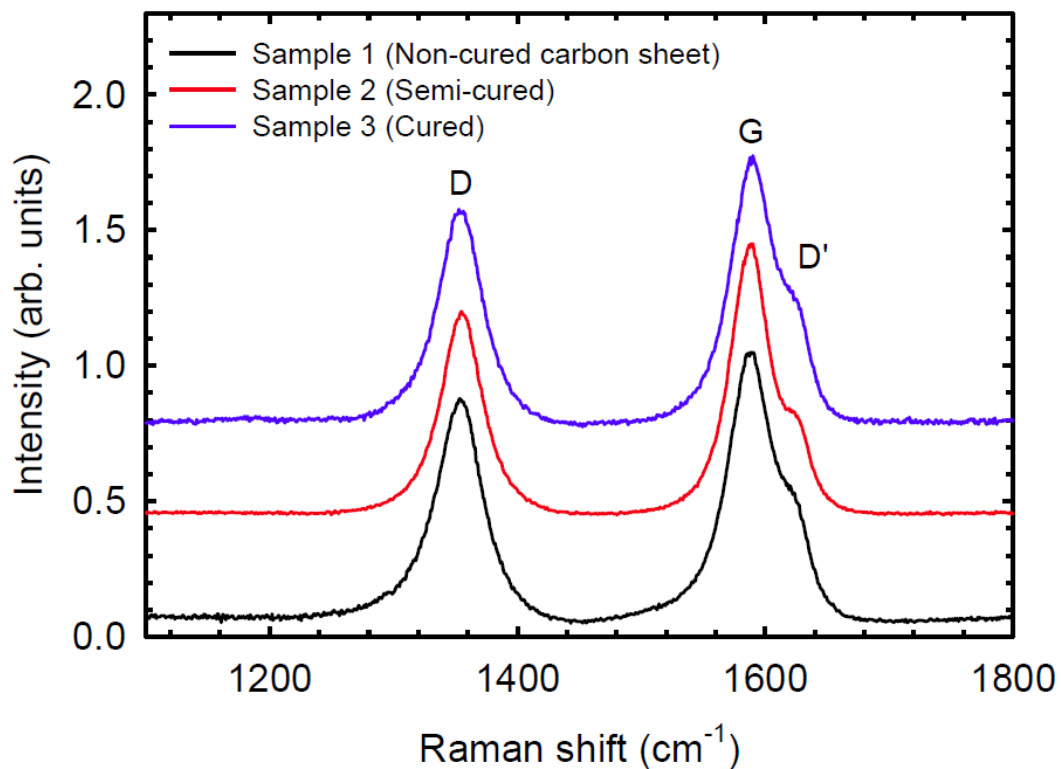


Fig.6. Raman spectra of three composite samples.

The results about the crystalline order and the crystalline size are shown in Table 8.

The degree of cure is related to an increase of the temperature peaks observed in DTG studies, which according to Raman results, is a consequence of the enhancement of crystalline order in cured samples.

34

Table 8

| Sample | $I_D/I_G$ | $L_a$ (Å) |
| --- | --- | --- |
| 1 | 0.77 | 38 |
| 2 | 0.87 | 43 |
| 3 (Carbon sheet) | 0.90 | 45 |

## 4. Conclusions

SEM, TGA, DSC, and Raman spectroscopy were used to investigate the degree of polymerization of carbon-epoxy composites. Carbon fibers are better resolved in SEM micrographs when the cure time becomes longer due to the homogeneous redistribution of covering resins. TGA and DSC results show that thermal characteristics of cured samples depend on the cure process. Further, Raman spectroscopy provides an assessment of the crystalline order through the ratio between intensities of D and G bands corresponding to disordered and ordered phases of graphitic Carbon, respectively. The results show that both Thermal analysis and Raman spectroscopy are complementary techniques for evaluating the degree of cure in composite materials.

## Acknowledgments

## References

1.     S. Farquharson, W.W. Smith, E.J. Rigas, D Granville. Characterization of polymer composites during autoclave manufacturing by Fourier transform Raman spectroscopy. Optical Methods for Industrial Processes, Stuart Farquharson, Editors, pp.103-270, 2001.

2.      L. Merad, M. Cochez, S. Margueron, F. Jauchem, M. Ferriol, B. Benyoucef, P. Bourson. Insitu monitoring of the curing of epoxy resins by Raman spectroscopy. Polymer Testing, 2008. doi:10.1016/j.polymertesting.2008.10.006

3.      N. Regnier, S. Fontaine, "Determination of the thermal degradation kinetic parameters of carbon reinforced epoxy using TG", Journal of Thermal Analysis and Calorimetry, Vol 64, (2001) 789-799.

4.      W. Cheng, P. Li, Y. Yu, X. Yang, "Curing kinetics study of an epoxy resin system for T800 carbon fibre filament wound composites by Dynamic and Isothermal DSC", Journal of Applied Polymer Science, Vol 107, 1493-1499, (2008)]

5.      D. Puglia, L. Valentini, J. M. Kenny. Analysis of the Cure Reaction of Carbon Nanotubes/Epoxy Resin Composites Through Thermal Analysis and Raman Spectroscopy. Journal of Applied Polymer Science, Vol. 88, 452–458 (2003).

6.      S.Y. Lei, R.J. Young. Deformation of PBO/epoxy plain weave fabric laminae followed using Raman spectroscopy. Composites: Part A 32 (2001) 499–509.

7.      H. Vaskova, V. Kresalek, Raman spectroscopy of epoxy resin crosslinking, WSEAS International Conference on AUTOMATIC CONTROL, MODELLING & SIMULATION (ACMOS 11), May 27-29, 2011, Lanzarote, Canary Islands, Spain, ISBN: 978-1-61804- 004-6, ISSN: 2223-2907, pp. 357-361.

8.      G. Katagiri, H. Ishida, and A. Ishitani, Raman spectra of graphite edge planes, Carbon 26, 565 (1988).

9.      M. J. Matthews, M. A. Pimenta, G. Dresselhaus, M. S. Dresselhaus, and M. Endo, Origin of dispersive effects of the Raman D band in carbon materials, Physical Review B 59, R6585- R6588 (1999).

10.     R. C. Mani, Mahendra K. Sunkara, Richard P. Baldwin, Jayadeep Gullapalli, John A. Chaney, Gopinath Bhimarasetti, John M. Cowley, Apparao M. Rao, and Rahul Rao, Nanocrystalline Graphite for Electrochemical Sensing, Journal of The Electrochemical Society 152, E154-E159 (2005).

11.     D.S. Knight and W. White, Characterization of diamond films by Raman spectroscopy, Journal of Materials Research 4, 385-393 (1989).

12.     L. G. Cancado, K. Takai, and T. Enoki, M. Endo, Y. A. Kim, H. Mizusaki, A. Jorio, L. N. Coelho, R. Magalhaes-Paniago, and M. A. Pimenta, General equation for the determination of the crystallite size $L_a$ of nanographite by Raman spectroscopy, Applied Physics Letters 88, 153106 1-3 (2006).

# IN SITU COMPACT TENSILE TEST DEVICE FOR POLYMER NANOCOMPOSITE: SPECIMENS TO BE ANALYZED IN AN X-RAY MICRODIFFRACTOMETER

**Copeta A.**[a], **Brisotto M.**[a] , **Dassa L.**[a]., **Depero L.**[a] , **Giannini L.**[b] , **Villa V.** [a]

[a]*Dipartimento di Ingegneria Meccanica ed Industriale,Università di Brescia,via Branze 38,25123 Brescia - Italy*
[b]*Pirelli Tyre SpA,V.le Sarca, 22220126 - Milano - Italy*
*e-mail: alessandro.copeta@ing.unibs.it*

## Abstract

X-ray diffraction is a non-destructive technique for structural analysis of materials. Applications include the evaluation of the residual stresses in real components, wherein the crystalline planes are used as strain gauges. In case of polymer nanocomposites, this technique allows to study the filler structural changes, in particular its orientation as a function of polymer deformation.

A tensile test device to apply uniaxial stretching on polymer nanocomposite specimens has been designed and built to equip a commercial X-ray microdiffractometer.

The main feature of this compact device is allowing setting the specimen strain up to 400% inside the microdiffractometer. X-ray diffraction measurements are carried out at different strains at the same point without removing the sample from the stage. The maximum load applied to the specimen is 100 N. We report the design phases and the results of preliminary tests on commercial rubber samples.

**Keywords:** *X-ray diffraction, stress/strain measurement, polymer nanocomposite*

## 1.Introduction

Adding inorganic fillers to rubber it is possible to obtain a reinforcement and in general an improvement of the physical properties, such as resistance to temperature, aging and better impermeability [1].

The best results are obtained when the dispersed fillers are nano-sized. As a matter of fact in a chain of natural rubber 6 or 7 units are needed to make a nanometer, therefore the interaction between fillers and elastomers must be at the nanometer level.

In this case we refer to them as nanocomposites, which possess properties not achievable with conventional composites, thanks also to the fact that the use of nano-particles allows to reach a high degree of dispersion within the rubber matrix and hence a considerably high volume/surface ratio.

Among the nanocomposites currently used as reinforcement in rubbers a growing role is played by lamellar phyllosilicates based on clays, which are organically modified to improve the dispersion within the elastomer. If filler is oriented the behavior cannot be isotropic

In the present work different specimens, provided by Pirelli, were analyzed. The composition of the specimens is summarized in Table 1

Table 1 **-** Specimens Composition

| Natural Rubber |
| --- |
| Carbon Black |
| Bentonite |
| Ammonium Salt |

The purpose of the tests performed in the laboratory is to detect, through microXRD analyses, the micro structural variations of nanofilled elastomers when they are subjected to uniaxial tension.

In particular, the aim is to verify the tendency of the elastomer to convert the strain energy supplied by the traction device into rubber crystallization; moreover the tendency of the nanofillers to be oriented by the traction force itself.

**2.Instrumentation**

For XRD measurements it has been used a micro diffractometer Rigaku D Max equipped with a two-dimensional curved detector (Image Plate). In a single exposure it covers an interval of 204° in 2θ and β from 88° (2θ = 90°) up to 360° (2θ <45°). The detector allows to collect data with high resolution with spatial distortion error lesser than 2%. The dynamic range of the signal collected covers six orders of magnitude, making it possible to measure very weak signals. Unlike linear and punctual detectors, that must move to cover all the angular positions of the circle of diffraction, the detector collects the entire two-dimensional diffraction spectrum with a single exposure, with acquisition times reduced. 2D images allow highlighting the entire Debye rings. The comparison of two-dimensional images before and after samples elongation allows visualizing the appearance of reflexes or preferential orientations by the presence of discontinuities in the Debye ring.

### 3.Design of new equipment

The micro diffractometer has been equipped with a custom tensile test device designed by our group. It starts from previous equipment designed for similar purposes [2] [3].

To ensure the repeatability of the results, during the design it was considered to perform a symmetrical traction with respect to the axis of the diffractometer collimator in order to analyze the micro structural variations of the same material portion.

The basic idea is to design a device that can be installed directly within the microdiffractometer, upon the dedicated interface, so as to perform the elongation of the specimens in situ, greatly increasing the convenience and simplicity of the test procedures.

Furthermore the device makes possible to carry out multiple diffraction analyses on the same sample on different level of strain, without having to remove the tensile device from the active area. This results in a remarkable reduction of working time.

Each specimen is mounted on the tensile test device at the relaxed state (strain 0%), the whole system is then inserted inside the microdiffractometer and there housed. The specimen is then ready to be analyzed. After the first analysis, once the X-ray source is turned off it is possible to vary the elongation of the specimen directly inside the diffractometer active area, with no need to remove the tensile device. The portion of the specimen subjected to analysis remains always in the same position regardless of the level of strain reached.

To realize such an apparatus is required an important condition of work as shown in figure 1. The elongation must be symmetrical with respect to a central point that corresponds to the point the collimator will irradiate during the test. This precaution allows us to monitor changes in the microstructure that the material undergoes in the various phases and to compare the results obtained.

In addition, the specimen must be perfectly aligned with the collimator, so as to be properly irradiated during the analysis.

To meet this requirement it is necessary that the two grips moves in a symmetrical way with respect of the collimator axis.
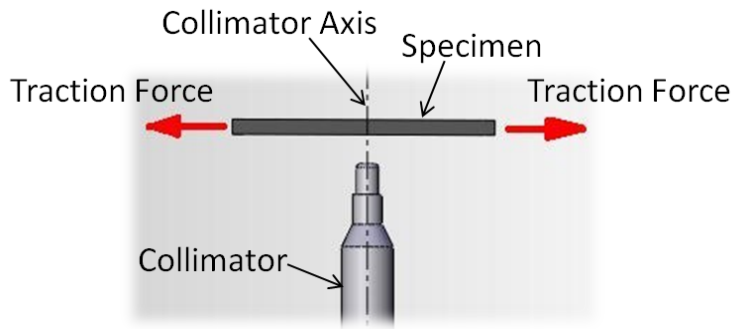
Fig.1. Tensile test condition
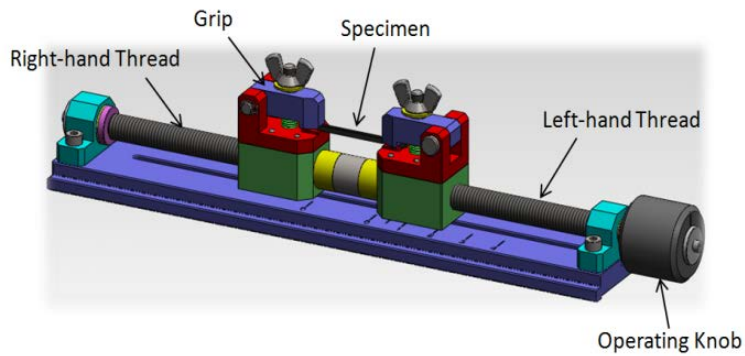


Fig.2.  Tensile test device



Fig.3. Device in situ - Fully operational

## 4.Laboratory Tests

The tests were performed in transmission with the parameters shown in Table 2 for different levels of strain.

Table 2 - Diffractometer parameters

| Voltage | 40 kV |
|---|---|
| Current Intensity | 30 mA |
| Duration | 30 min |
| Angle ω | 0 ° |
| Collimator diameter | 0.8 mm |
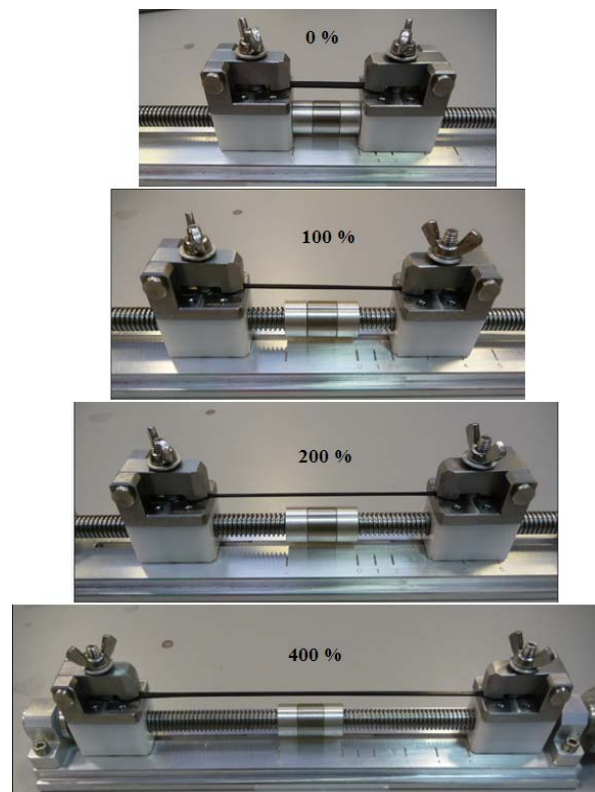


Fig.4. Different levels of strain

The qualitative comparison between two-dimensional images obtained at different levels of strain shows the occurrence of reflections at angles around 2θ 18° and 20°.

The reflection intensity is proportional to the amount of strain and it indicates a significant crystallization of the elastomeric matrix [4], [5], [6].

The preferred orientation of the nanofillers is particularly visible at strain of 400%.
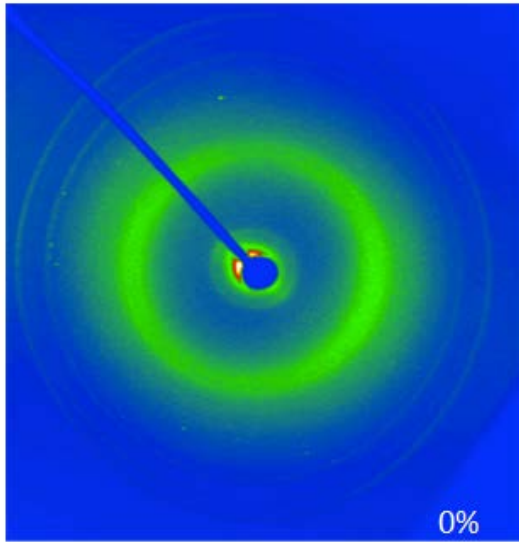
Fig.5. XRD pattern at 0% strain
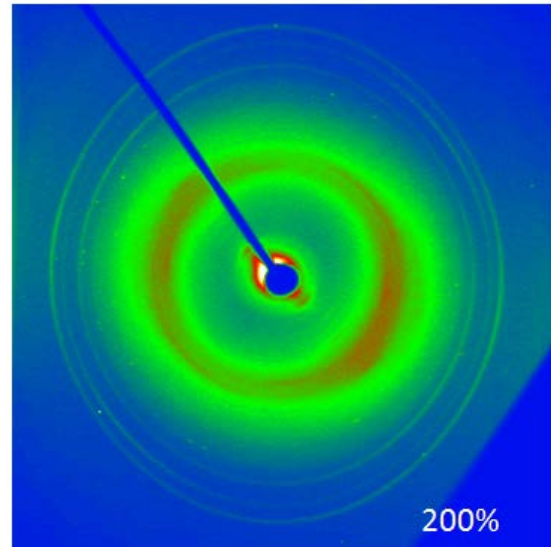


Fig.6. XRD pattern at 200% strain

The two-dimensional images have been integrated subtracting a value of background equal to 10.

The comparison of the resulting spectra, for different values of elongation, confirm the micro structural changes that occur as a result of elongation.

In Figure 8 we can observe the appearance of peaks, more evident for samples at 400% of strain, as shown in detail in figure 7.
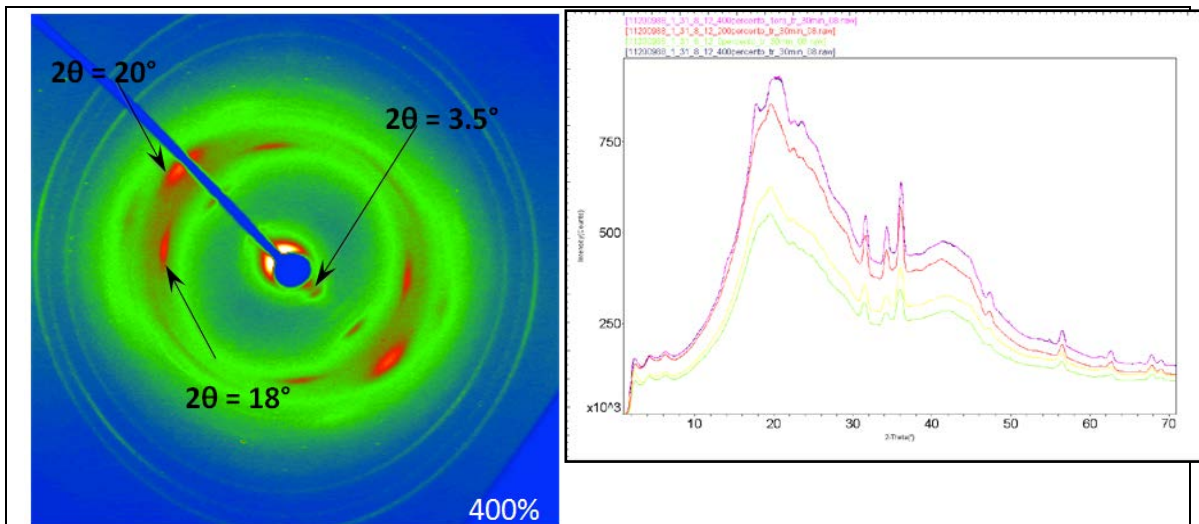


| Fig.7. XRD pattern at 400% strain | Fig.8. Spectra comparison |
| --- | --- |

From the qualitative comparison of the two-dimensional images obtained for values of strain of 0% in two different phases of the test (before the test and after the unload of the specimen) no substantial difference is observed.

This indicates that the micro structural changes induced by the stress state (uniaxial tension) to which the specimens were subjected are reversible.
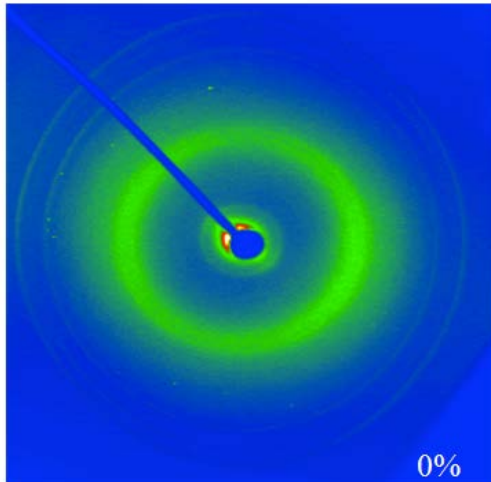


Figure 9. - XRD pattern at 0% strain
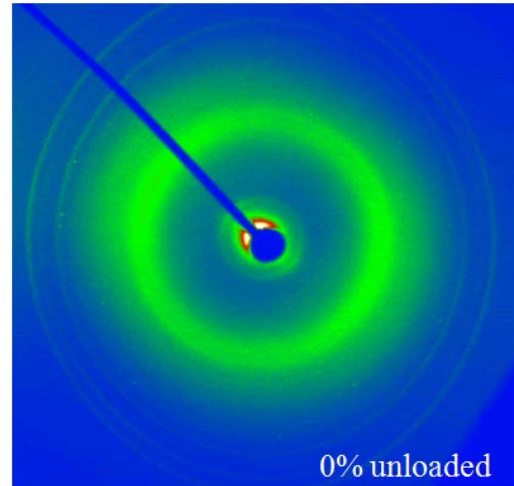


Figure 10. - XRD pattern at 0% strain (Unloaded)

To verify possible permanent variations of the nanocomposite microstructure subjected to a constant elongation over time the specimens has been kept at a constant strain of 400% for 17 hours.

Figures 11 and 12 show the 2D images obtained from a specimen at the strain of 400% at t = 0h and at t = 17h and the related images before and after elongation.
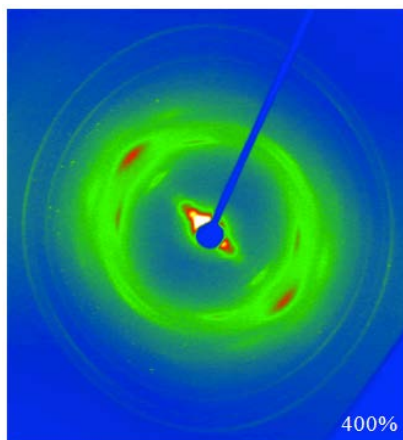


Fig.11. XRD pattern at 400% strain
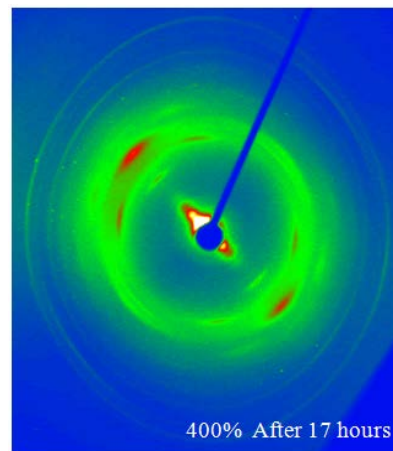


Fig.12. XRD pattern at400% strain (After 17 hours)

The comparison of the images does not show qualitative differences, index that the micro structural changes that occur as a result of strain are reversible, even when the specimen is maintained under stress for a prolonged period of time.
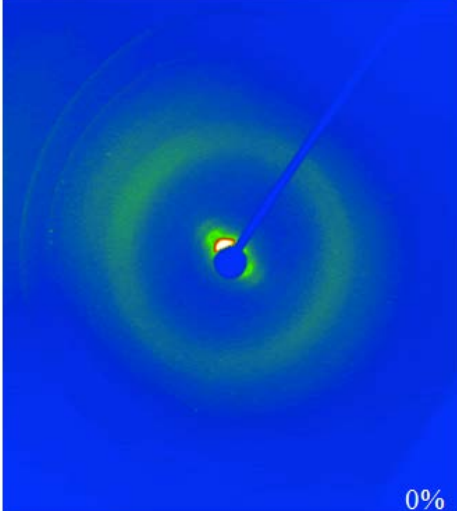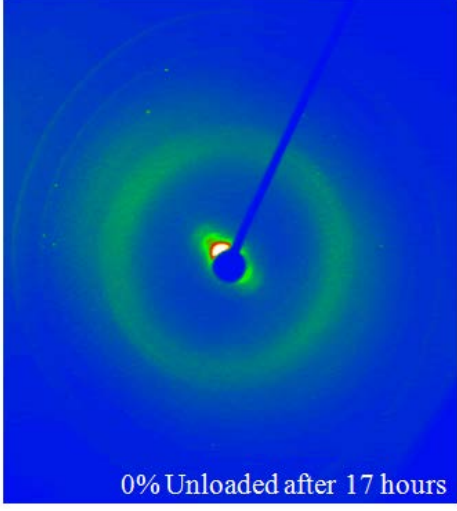


| Fig.13. XRD pattern at 0% strain | Fig.14. XRD pattern at 0% strain (Unloaded after 17 hours) |

## 5.Conclusions

The possibility, given by this new equipment, to achieve strain of 400% for the rubber specimens has brought the desired and expected results from the microXRD analysis. As a matter of fact it was possible to successfully study micro structural changes occurring at strain values not attainable with former equipment.

The two-dimensional images of specimens elongated up to 400% show the occurrence of a number of reflections the more pronounced the greater the strain level.

This leads to the conclusion that the stress (uniaxial tension) induced on the specimens generates an orientation of the nanofillers and a marked preferential crystallization of the elastomeric matrix.

The orientation of the fillers and the crystallization of the polymer are, however, recovered once the outer stimulus ceases to act. This allows us to conclude that the micro structural changes are qualitatively reversible.

# References

1.      Nguyen Quang Duy, Nguyen Ngoc Bich - Nanocomposite from natural rubber latex and organoclay by dispersion destabilization -Rubber Research Institute of Vietnam – pg 1-6

2.      L. Dassa, V. Villa - Design and testing of a mechanical device able to make possible XRD stress analysis – Proc. of Congreso Internacional Conjunto XXI Ingegraf - XVII ADM, Lugo, Spain, 2009.

3.      A. Copeta, L. Dassa - Preliminary calibration and future developments of a miniaturized tensile test device based on flexure hinges - International Conference on Innovative Technologies, IN-TECH 2012,Rijeka.

4.      Masatoshi Tosaka a,*, Kazunobu Senoo b, Kenta Sato b, Miki Noda b, Noboru Ohta- Detection of fast and slow crystallization processes in instantaneously-strained samples of cis-1,4-polyisoprene Polymer 53 (2012) 864-872.

5.      Yijing Nie, Guangsu Huang*, Liangliang Qu, Xiaoan Wang, Gengsheng Weng, Jinrong Wu - New insights into thermodynamic description of strain-induced crystallization of peroxide cross-linked natural rubber filled with clay by tube model Polymer 52 (2011) 3234-3242

6.      S. Murakami, K. Senoo, S. Toki, S. Kohjiya-Structural development of natural rubber during uniaxial stretching by in situ wide angle X- ray diffraction using a synchrotron radiation. – Polymer 43 (2002) 2117-2120

# THE KERMEL-PTFE MACRO-COMPOSITE AS A MATERIAL FOR MOBILE ROBOTS ANTI-CONTAMINATION SHIELD

**Romelczyk Barbara**, **Kaminski Marek, Jastrzębska Anna, Brynk Tomasz, Pakiela Zbigniew**

*Warsaw University of Technology, Faculty of Materials Science and Engineering, Warsaw, Poland*
*e-mail: barbara.romelczyk@inmat.pw.edu.pl*

## Abstract

The paper shows results of macro-composite contained Kermel and PTFE layers prepared by stitching. The material was designed to be an anti-contamination shield for mobile robot body which was made of aluminum alloy. The samples were investigated as a individual materials and as a macro-composite. The tensile and thermal tests were carried out. The test of resistance to percolation by liquids were also performed. Due to final product expectation the samples were immersed in different liquids. Obtained results were compared with the results for samples in the initial sate.

It was proved that macro-composite containing Kermel and PTFE layers gives an opportunity to protect robots body from chemical liquids with keeping high mechanical properties and usage temperatures above 200ºC.

**Keywords**: *PTFE, Teflon, composite, Kermel, meta-aramid, percolation, chemical resistance*

## 1.Introduction

The investigations presented in this paper are the part of a project dedicated to rescue operations. Three mobile robots are important parts of the project. In some type of rescue operations there is a need for anti-contamination shield to protect the robot body in case of aggressive liquid leakage. The work is directed to design and tests anti-contamination shield which covers robot body, which is made of aluminium alloys. The shield secures robots body from malfunctioning and prevents them from being destroyed in case of exposition in aggressive liquids. Mobile robot anti-contamination shield requirements are defined as follows: low relative density, thermal resistance up to 200° C, high relative strength, chemical resistance in aggressive liquids, low production costs.

High-strength polymer fabrics are rapidly developing materials used for protective systems due to their good mechanical properties and elevated temperature resistance [1, 2, 3]. Light-weight shields for personnel or vehicles are often designed as armours prepared of aramid and polyethylene fabric composite. To meet the project challenges the macro-composite based on Polythetrafluoroethylene (PTFE) and Kermel fabrics was designed. Macro-composite was prepared by means of sewing materials by non-combustible thread.

The properties combination of Kermel and PTFE allowed us to expect that macro-composite made of this two materials would have better chemical resistance, thermal and mechanical properties than each of the components separately.

Kermel is meta-aramid material. Kermel fabric has good heat resistance, high strength and relatively cheap cost. Out of many advantages, the best known attribute of Kermel is flame resistance which is caused by its aromatic structure [2, 4, 5].

PTFE is fluorocarbon material. It offers very good chemical resistance and no absorbtion of water [2, 6]. Mechanical properties of PTFE material are well known. Doban investigated mechanical properties in temperature range from -40 to 350°C [7]. He also performed tests after 24h exposition in some solvents, but he didn't observe any mechanical changes. The temperature effect was also investigated by Rae [8], Fisher and Brown [9, 10]. Thermal and mechanical properties of Kermel are also reported in the literature [3, 11, 12].

According to the authors' knowledge there is no published data in the literature about properties of composite made of PTFE and Kermel, especially there is no information about percolation resistance to liquids. This paper presents the results of percolation for liquids tests, mechanical, thermal and chemical resistance of macro-composite made of Kermel and PTFE fabrics.

**2.Material and methodology**

Commercially available Kermel and PTFE fabrics were used for the investigation. PTFE fabrics of 0.07 mm and 0.13 mm thickness were used. Kermel fabric thickness was 0.37 mm. The investigated samples were cut along the fabric rolls. The macro-composite was prepared by means of sewing. To stitch macro-composite samples, non-combustible thread was used. The macro-composite consisted of two layers. Kermel fabric was an external part while PTFE secured robot as an internal layer. The continuous contact between materials layers were achieved by using PTFE fabric with gluing layer. Due to the final product expectations the investigation was carried out after exposition in different liquids. The following liquids were used for experiments: acetone, methanol, toluene, triethylamine, n-acetate, hydrofluoric acid, nitric acid 65%, dipping acid 50%, dipping acid 95%. The liquids and the time of exposure were the same as in the specifications used in the case of the firemen suits. The results were compared with the

results of initial state samples. The individual samples were investigated as well as a macro-composite made of them.

The tensile tests of individual material and in the samples with stitches were performed. Before the tensile tests samples were immersed for 1-hour in the selected liquids. After 1 hour immersion, the samples were washed in distilled water and dried in air. The samples were weighed before and after the exposition into the liquids. The tensile tests were carried out using Zwick Z005 stand with a long distance extensometer and pneumatically driven grips. The crosshead velocity was 5 mm/min. The extensometer was mounted at the pre-load of 1N. The samples gage length was 100 mm. Fig. 1 presents samples used for the tensile test. The ultimate strength and elongation to failure for all samples were determined.

The surfaces of samples after tensile tests were observed by means of scanning Hitachi S-3500 microscope in low vacuum mode. This mode allows to observe of nonconductive materials without the conductive layer coating. Kermel and PTFE thermal properties were examined using thermogravimetric analyzer TGA Q 500 (TA). The samples were heated in temperature range of 25 to 800°C temperature with a constant heating rate of 10°C min$^{-1}$. The tested samples of about 10 mg weight were heated in the air atmosphere.

The resistance to penetration by liquids tests were performed in accordance to EN ISO 6530 standard. The Kermel samples and stitches manufactured across the samples were tested. The samples size was 360 x 235 mm, the test duration was 60 s. The samples were weighted before and after the test. Three indexes were determined as the results of tests: percolation index (I$_P$), non-wettability index (I$_R$) and absorbtion index (I$_A$). The indexes were calculated due to the following formulas.

$$I_P = \frac{M_p}{M_t} \times 100$$

$$I_R = \frac{M_r}{M_t} \times 100 \qquad\qquad \text{Formula (1)}$$

$$I_A = \frac{M_a}{M_t} \times 100$$

where:

I$_P$ – percolation index; I$_R$ – non–wettability index; I$_A$ – absorbtion index; M$_p$ – liquid volume absorbed by the absorbent paper [g]; M$_t$ – liquid volume used for experiment [g];

$M_r$ – liquid volume accumulated in the beaker [g]; $M_a$ - liquid volume absorbed by investigated material [g].
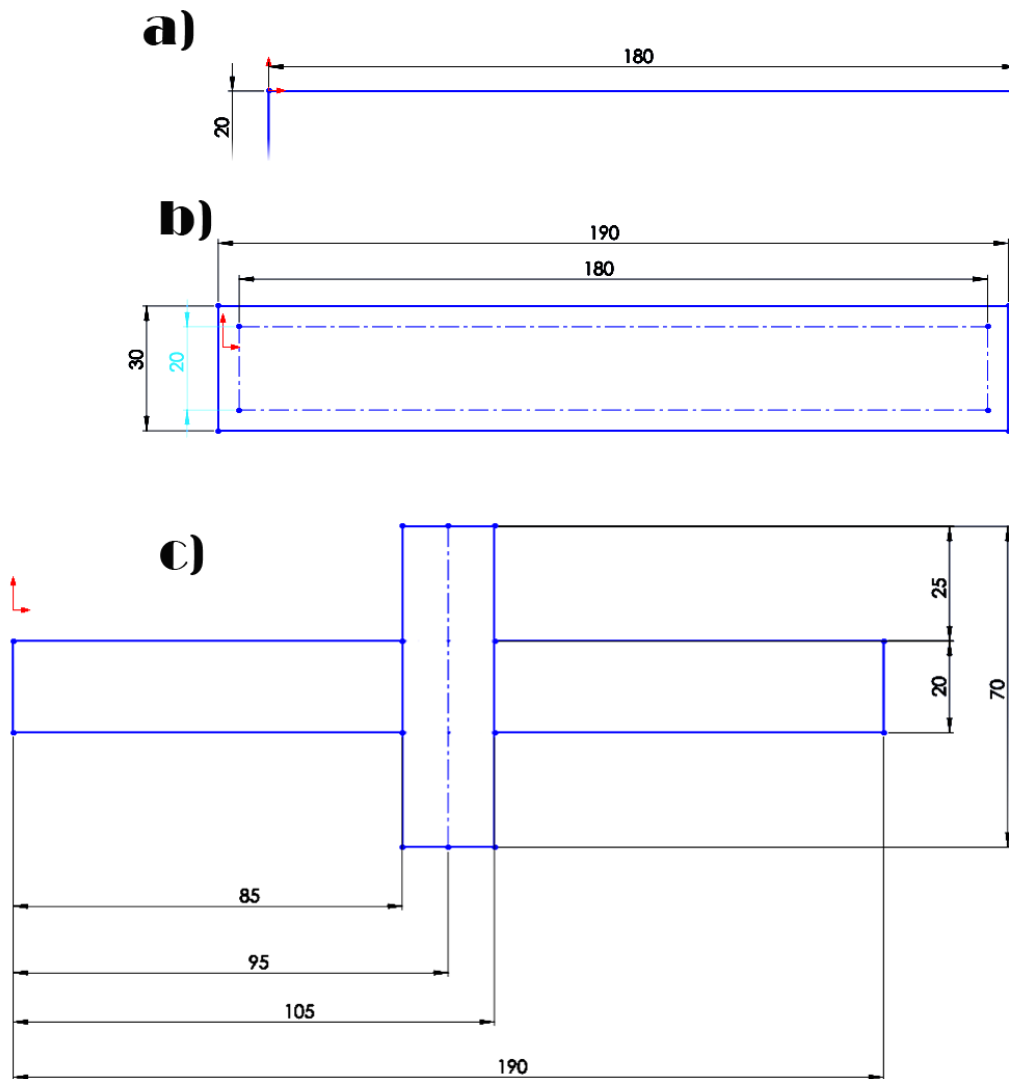


Fig. 1. Samples used for ultimate tensile tests

## 3.Results and discussions

### 3.1Mechanical properties and surface observations

Figures 2-3 present tensile tests results of Kermel and PTFE samples in the initial states and immersed in different liquids before tests. Figure 4 presents ultimate strength of stitches performed on Kermel/Kermel, PTFE/PTFE, PTFE/Kermel materials in the initial

state. Figure 5 shows examples of the stress-strain curves for the initial state of the investigated materials. PTFE fabrics of two thicknesses (0.07 mm and 0.13 mm) were used for tensile tests. The UTS values for PTFE fabrics were lower for 0.07 mm than 0.13 mm thick. Moreover, the standard deviations achieved higher value in the case of thinner samples. This is the evidence of larger susceptibility of thinner samples for even small surface damage. Therefore for the further investigation only the 0.13 mm thick PTFE fabrics were chosen.
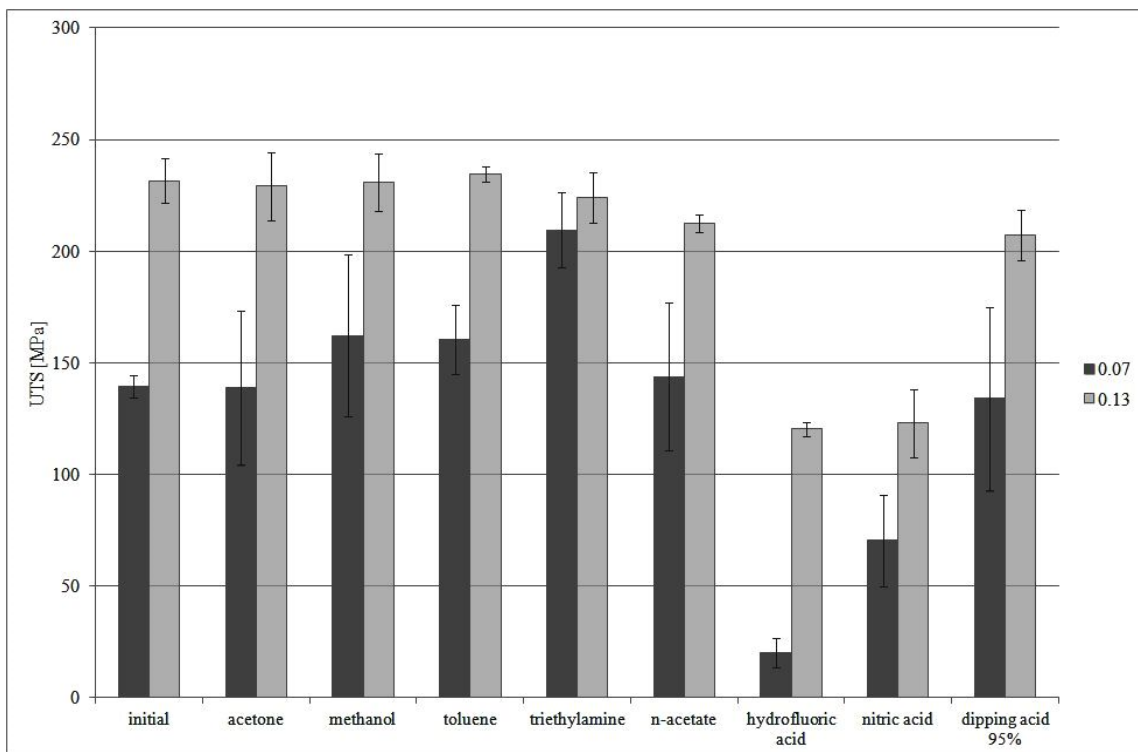


Fig. 2. Ultimate tensile stress for PTFE fabrics exposed in various liquids

PTFE of 0.13 mm thickness in comparison to Kermel counterparts revealed higher strength in all cases. Nitric Acid 65% exposition caused approximately 50% decrease in strength in both materials. Kermel fabrics were resistant to weak dipping acid, but 95% concentration of this substance caused total destruction even after 10 minute exposition. The samples immersed in other liquids didn't reduce strength more than 10% in the case of both materials. The total elongation to failure was higher for Kermel than PTFE fabrics. The samples exposed in the strong acids (nitric and dipping) revealed decrease in elongation to failure. The tensile tests of macro-composite in the initial state were

performed. The UTS value for the macro-composite was determined mainly by Kermel component. The macro-composite stress - strain curves show two local maximum points: first when the PTFE fabric underwent damage, then the second when Kermel fabric damages. Average stress of PTFE achieved approximately the same value as in the case of Kermel fabric, but the macro-composite achieved smaller elongation to failure value.
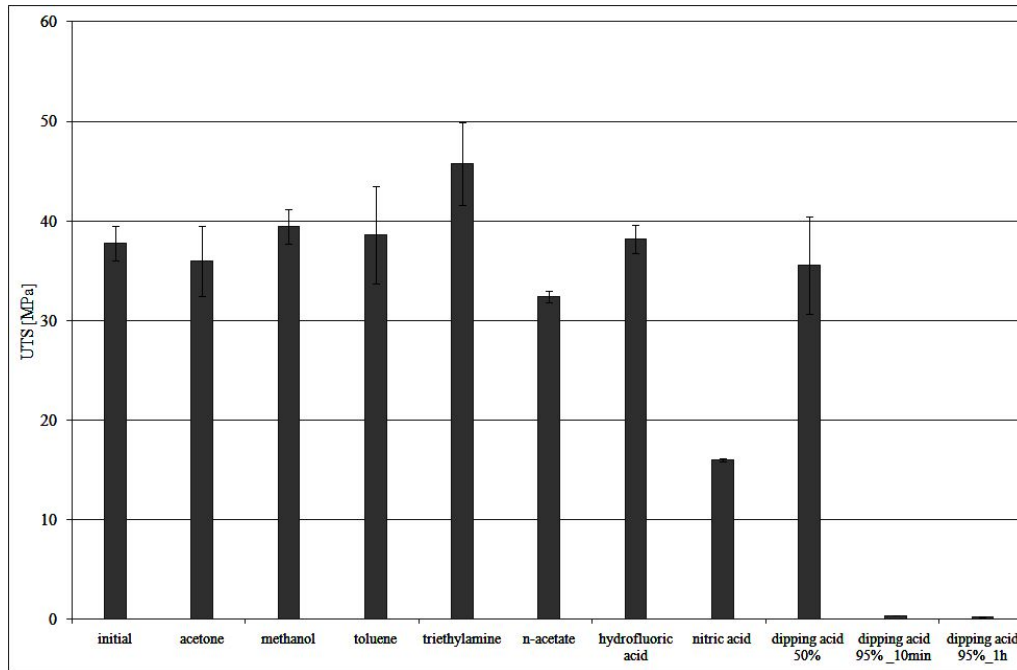


Fig. 3. Ultimate tensile stress for Kermel fabrics exposed in various liquids
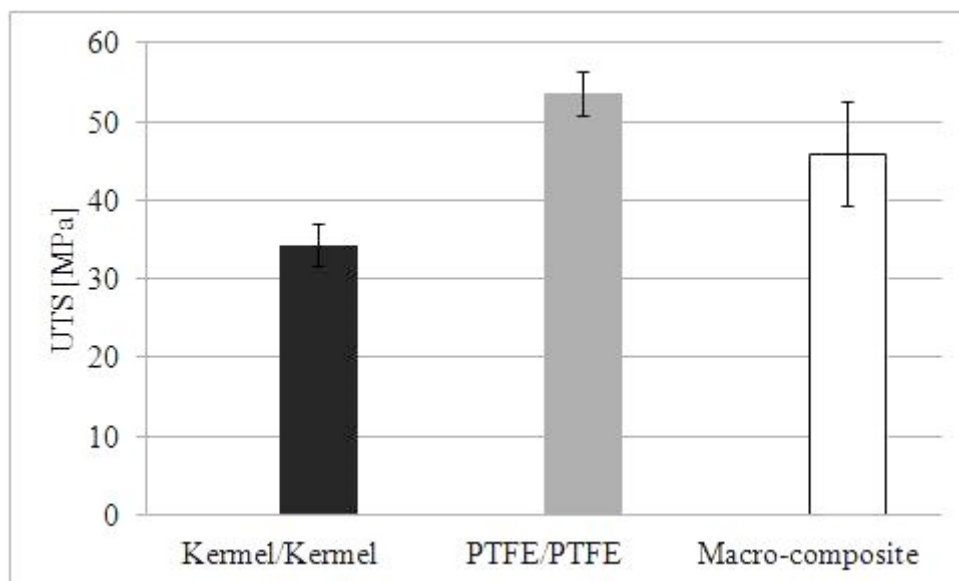


Fig. 4. Ultimate tensile stress for materials stitches in the initial state
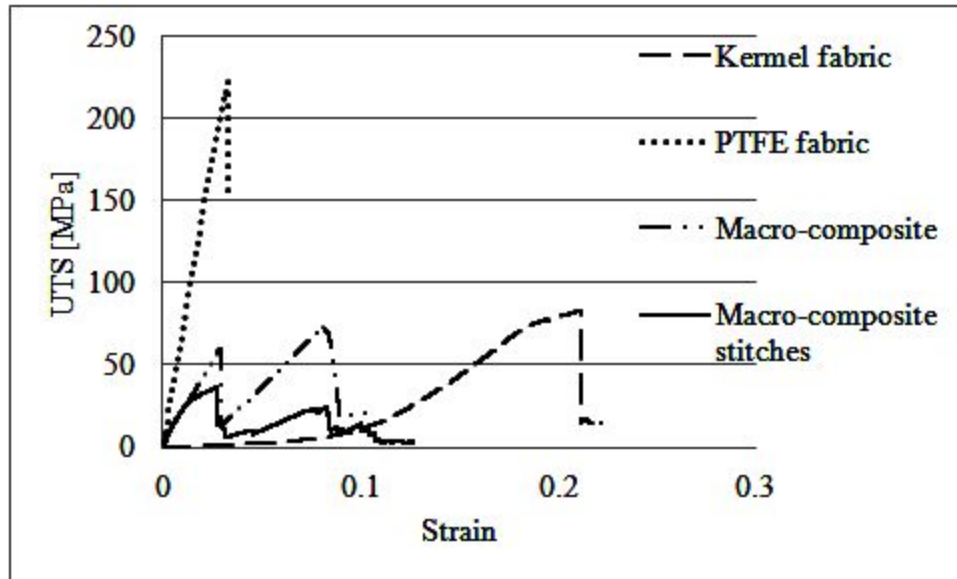
Fig. 5. Stress-strain curves obtained for materials in the initial state

The stitches caused a decrease in strength. Approximate 15% decrease in strength was observed for Kermel, 25% for PTFE and 75% for the macro-composite in comparison to non-stitched materials. During the tensile test damages of Kermel/Kermel stitches were observed on non-combustible thread but PTFE/PTFE and macro-composite PTFE/Kermel damages were placed on the materials along the stitch line. The holes made by needle, which were made in PTFE fabric acted as stress concentrators. During the macro-composite tensile test firstly the PTFE fabric underwent damage, then it was pulled out from the thread, and in the last stage the thread and Kermel fabric were destroyed.

Textiles during contact with different liquids may undergo degradation, which can be caused by chemical structure modifications. It leads to mechanical properties changes. The samples after tensile tests were observed by means of SEM. The changes of fibres morphology after expositions were investigated. The chemical compositions of materials were examined by EDS technique. There were no chemical composition changes revealed. It means that the samples, which had been exposed were dried well and didn't contain any liquids near the samples surface. Surface changes were observed in the case of the Kermel and PTFE samples immersed in Nitric Acid 65%. Fig. 6-7 present examples of samples fractures. Kermel and PTFE surfaces on the initial state were smooth but materials exposed in nitric acid underwent degradation. As the effect of degradation some damages and depositions on fibres and matrix surface were noticed. PTFE surfaces in the initial state were continuous and rather smooth, but after nitric acid

exposition some pits were showed. The same effect of surface degradation was revealed on the Kermel samples exposed in dipping acid. In both cases near surface chemical composition didn't change, but the surface damage and changes in mechanical properties were observed. The mechanical properties modifications with surface condition maintaining might be caused by chemical bonding splitting. The fibres and matrix surface didn't undergo degradation in other liquids.
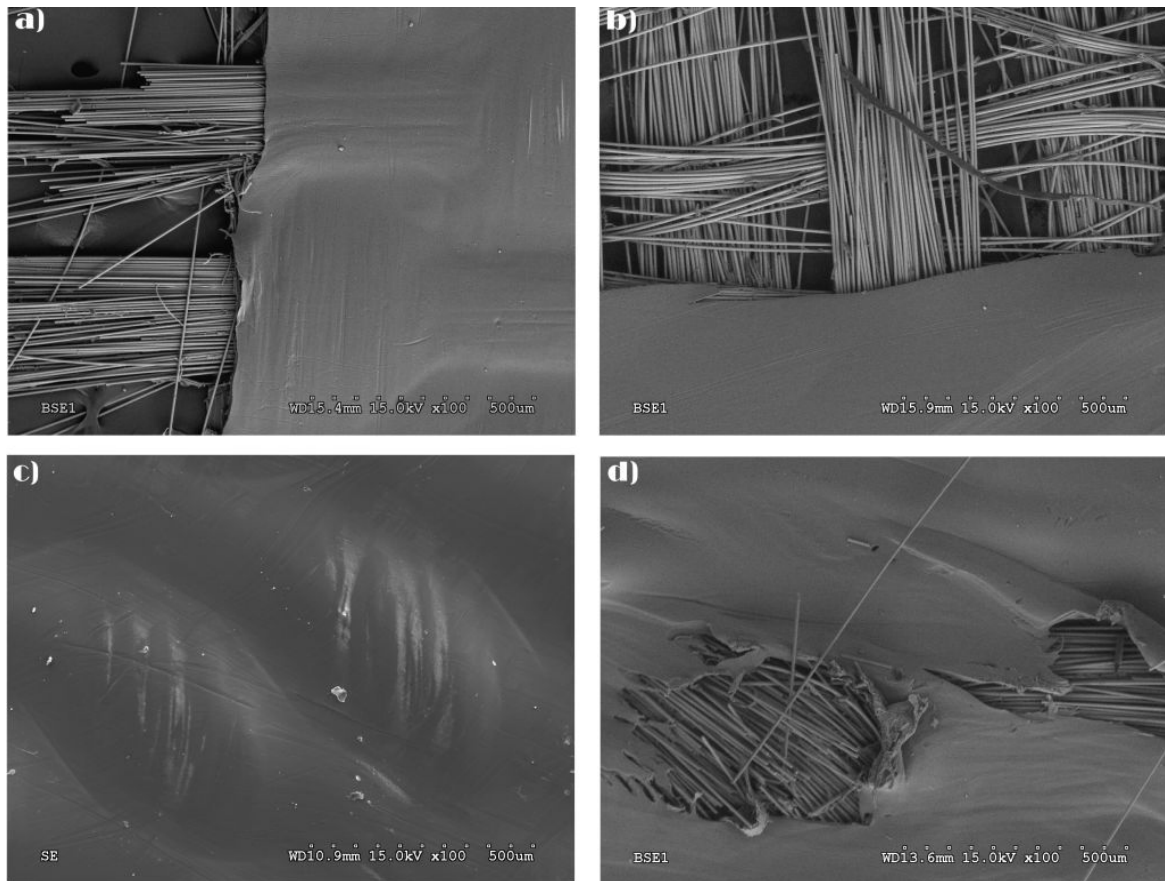


Fig. 6. Surfaces of PTFE fabrics after ultimate tensile tests exposed in various liquids: a)initial, b)triethylamine, c) dipping acid, d) nitric acid
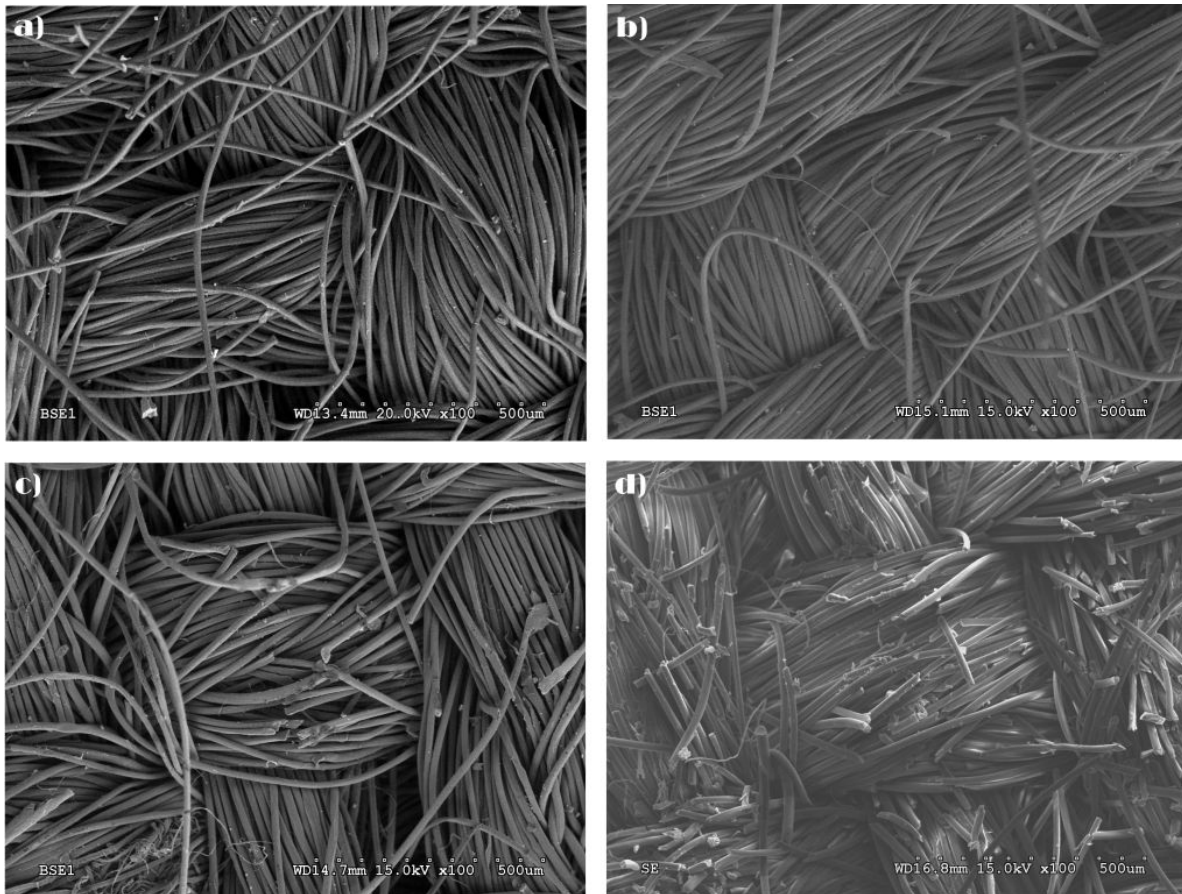
Fig. 7. Surfaces of Kermel fabrics after ultimate tensile tests exposed in various liquids: a)initial, b)triethylamine, c) dipping acid, d) nitric acid

## 3.2.Thermal properties

Thermogravimetric curves obtained from Kermel and PTFE fabrics are shown in Fig. 8. based on thermogravimetric analyzes three temperatures were determined: 5%, 10% and 50% of weight loss. The temperature of 5% of mass loss was chosen to define initial decomposition temperature [13]. The value of the calculated temperatures are presented in the Table 1-2. Thermogravimetric analysis showed feasibility of application of the investigated materials in the temperatures above 250ºC. The lowest initial decomposition temperature was revealed for Kermel fabric exposed in nitric acid. For Kermel fabric initial decomposition temperature decreased from 417ºC observed in the initial state to 341ºC for nitric acid and to 274ºC for dipping acid exposition. In the other exposed samples the thermal changes in comparison to the initial material state weren't significant. The initial decomposition temperatures for PTFE fabrics were approximately

54

at the level of 520ºC and there weren't observed changes caused by exposition in the investigated liquids.

From the rescue application point of view it is important to know that after Kermel degradation PTFE fabric is going to prolong the shielding effect provided by the macro-composite.

Table 1. Thermal gravimetric analyze results performed on Kermel fabrics

| Deposition | $T_{5\%}$[1] [°C] | $T_{10\%}$[2] [°C] | $T_{50\%}$[3] [°C] | $T_{max}$[4] [°C] | $W_{1000}$[5] [%] |
|---|---|---|---|---|---|
| initial state | 417.0 | 471.8 | 544.4 | 545.1 | 0.97 |
| toluene | 419.1 | 472.2 | 543.0 | 544.3 | 0.86 |
| triethylamine | 417.4 | 471.2 | 543.9 | 545.4 | 0.90 |
| n-acetate | 415.5 | 470.4 | 544.7 | 545.6 | 0.92 |
| nitric acid 65% | 274.6 | 428.2 | 544.7 | 547.7 | 0.90 |
| dipping acid 95% | 341.4 | 458.3 | 545.8 | 548.7 | 0.96 |

Table 2 Thermal gravimetric analysis results performed on PTFE fabrics

| Deposition | $T_{5\%}$[1] [°C] | $T_{10\%}$[2] [°C] | $T_{50\%}$[3] [°C] | $T_{max}$[4] [°C] | $W_{1000}$[5] [%] |
|---|---|---|---|---|---|
| initial state | 522.4 | 532.2 | 556.6 | 557.6 | 28.9 |
| triethylamine | 521.2 | 532.2 | 557.0 | 557.8 | 30.0 |
| n-acetate | 522.1 | 531.1 | 553.3 | 552.8 | 32.9 |
| nitric acid 65% | 521.8 | 531.8 | 556.4 | 557.0 | 29.9 |
| dipping acid 95% | 521.6 | 531.5 | 556.6 | 557.3 | 50.0 |

1 - initial decomposition temperature; 2 – temperature by 10% weight loss; 3 – temperature by 50% weight loss; 4 – tem-
perature at the maximum of weight loss rate read from the peak values of the DTG; 5 – residue by temperature 1000°C.
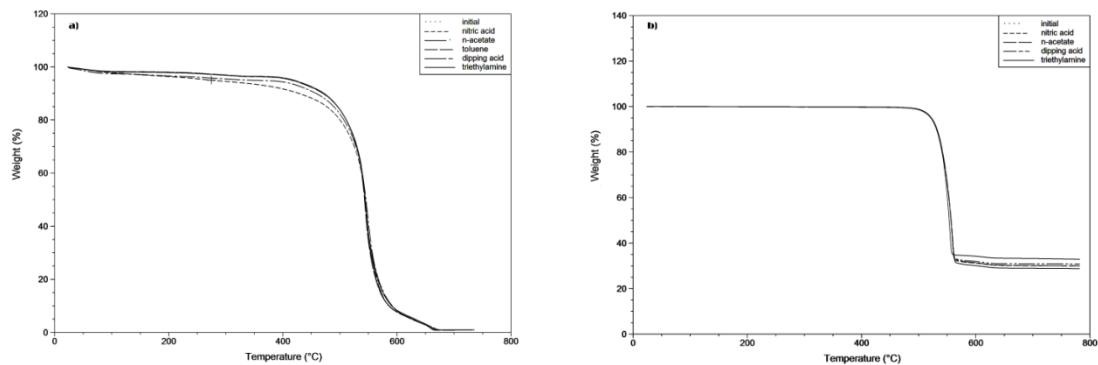
Fig.8. Thermal gravimetric analyze results: a) Kermel, b) PTFE

### 3.3.Chemical resistance

The tables 3 and 4 present the results obtained from the test of resistance to penetration by liquids. The indexes were calculated as presented in formula 1. The tests were performed of Kermel fabric and macro-composite samples in the initial state and after exposition to different liquids. Non-wettability index ($I_R$) was defined as a proportion of liquid volume accumulated in the baker to liquid volume used for the experiment. The results show the same $I_R$ value for Kermel as for macro-composite. It means that only Kermel determined $I_R$ index because liquids doesn't influence on PTFE fabric. PTFE is non-absorb material so liquids flow on the surface of fabric. The highest $I_R$ index was calculated for acids. What is more the values were higher than 50% for all samples. Opposite to $I_R$ index is the percolation ($I_P$) and absorbtion ($I_A$) indexes. $I_P$ and $I_A$ for Kermel fabrics and for macro-composite achieved similar values. The indexes didn't exceed the 6%. It means that materials didn't absorb or percolate the liquids. High non-wettability indexes and low value of percolation and absorbtion indexes proved that the materials are resistant to the investigated liquids.

Table 3 Resistance to percolation by liquids tests results of Kermel fabrics

| liquid | $I_P$ | $I_R$ | $I_A$ |
|---|---|---|---|
| methanol | $4.7 \pm 0.9$ | $57.6 \pm 3.1$ | $5.8 \pm 0.7$ |
| toluene | $4.4 \pm 0.1$ | $59.1 \pm 5.4$ | $4.2 \pm 0.7$ |
| triethylamine | 4.2 | 63.7 | 4.7 |
| n-acetate | $6.2 \pm 0.0$ | $61.5 \pm 5.4$ | $3.9 \pm 0.6$ |
| nitric acid 65% | $3.9 \pm 0.1$ | $87.8 \pm 3.6$ | $4.7 \pm 2.4$ |
| dipping acid 95% | $1.9 \pm 0.1$ | $98.8 \pm 1.0$ | $1.4 \pm 0.5$ |

Table 4 Resistance to percolation by liquids tests results of macro-composite

| Na liquid | $I_P$ | $I_R$ | $I_A$ |
|---|---|---|---|
| methanol | $4.6 \pm 0.8$ | $57.6 \pm 3.1$ | $5.9 \pm 0.8$ |
| toluene | $4.3 \pm 0.1$ | $59.1 \pm 5.4$ | $4.3 \pm 0.7$ |
| triethylamine | 4.1 | 63.7 | 4.8 |
| n-acetate | $6.0 \pm 0.0$ | $61.5 \pm 5.4$ | $4.1 \pm 0.6$ |
| nitric acid 65% | $3.9 \pm 0,1$ | $87.8 \pm 3.6$ | $4.7 \pm 2.4$ |
| dipping acid 95% | $1.9 \pm 0.1$ | $98.8 \pm 1.0$ | $1.4 \pm 0.6$ |

## 4.Summary

The findings in this study are important from a design viewpoint of light-weight anti-contamination shield. The designed macro-composite gives an opportunity to create a shield with good mechanical and thermal properties, which would cover an aluminum alloy body robot. It gives chance to separate mobile robot from various liquids such as acetone, methanol, toluene, triethylamine, n-acetate, hydrofluoric acid, nitric acid 65%, dipping acid 50%. This macro-composite lets the piece production maintain acceptable cost, which is important while manufacturing the final system dedicated to rescue operations. Moreover the designed anti-contamination shield will effectively secure robot body up in the above 250°C temperature for a short time period. The author thinks that thermal isolation properties require additional investigation in the future.

## Acknowledgments

**References**

1.      Kermel develops aramid fibre for high-temperature air filtration media, Technical Textiles International 2004: 4.

2.      Smith W. C. High-performance fibers protect, improve lives. Textile World 1998; 148: 53-56.

3.      Tabiei A., Nilakantan G. Ballistic impact of dry woven fabric composites: a review. Appl. Mech. Rev. 2008; 61: 10801-10813.

4.      Fink J. High Performance Polymers. William Andrew Inc. 2008; ISBN: 9780815515807: 423-448.

5.      Bourbigot S., Flambard X. Heat resistance and flammability of high performance fibres: A review. Fire and Mater. 2002; 26: 155 -168.

6.      Ylianttila L., SchrederJ. Temperatue effects of PTFE diffusers. Optical Materials 2005; 2: 1811-1814.

7.      Doban R.C., Sparelli C.A. Sandt B.W. The physical properties of 'teflon' polytetrafluoroethylene, The Society of Plastics Engineers J. 1955, 11.

8.      Rae P.J, Brown E.N. The properties of poly(tetrafluoroethylene) (PTFE) in tension. Polymer 2005;46: 8128–8140.

9.      Fisher S, Brown N. Deformation of polytetrafluoroethylene from 78 to 298 k and the effect of environmental crazing. J Appl Phys. 1973; 44: 4322-4327.

10.     Brown N, Parrish M. Effect of liquid nitrogen on the tensile strength of polyethylene and polytetrafluoroethylne. J Polym Sci, Polym Lett Ed 1972; 10: 777-779.

11.     Kermel guide "Making a commitment to protecting those at the centre of the action ([www.kermel.com](www.kermel.com) 15.10.2012).

12.     Kim E., Jang J. Surface Modification of meta-aramid films by UV/ozone irradiation, Fibers and Polymers 2010; 11: 677-682.

13.     Ciecierska E., Boczkowska A., Kurzydlowski K.J. and et.al. The effect of carbon nanotubes on epoxy matrix nanocomposites, J Therm Anal Calorim. 2012; 16.

# EFFECT OF 3D-BRAIDED STRUCTURE ON THERMAL EXPANSION OF PIP-C$_F$/SIC COMPOSITES

**Deke Zhang[1], Yingbin Cao [1], Rongjun Liu[1], Changrui Zhang[1], Yanan Jiao[2], Chunlei Yan[1]**

[1]*National Key Laboratory of Science and Technology on Advanced Ceramic Fibers and Composites, College of Aerospace and Materials Engineering, National University of Defense Technology, Changsha, 410073, PR China*
[2]*Composites Research Institute, Tianjin Polytechnic University, Tianjin, 300160, China*
*e-mail: rongjunliu@163.com*

## Abstract

3D3d、3D4d、3D5d braided structure C$_f$/SiC composites were fabricated by precursor infiltration and pyrolysis (PIP) with polycarbosilane as the matrix precursor. Coefficient of thermal expansion (CTE) of C$_f$/SiC composites was measured in longitudinal and transversal direction in the temperature range from -150℃ to 25℃. The longitudinal CTE varies in range 0.09~1.14×10$^{-6}$/℃, and the transversal CTE varies in range 0.25~1.95×10$^{-6}$/℃. Varies CTE of 3D braided C$_f$/SiC composites was mainly determined by different braided structure of carbon fiber. The longitudinal CTE lower than transversal CTE for the negative axial expansion of carbon fiber in cryogenic temperature. Micro-crack was researched to understand the effect to thermal expansion of composites.

**Keywords:** *C$_f$/SiC composites; coefficient of thermal expansion; braided structure; carbon fiber; SiC*

## 1. Introduction

The development of light-weight and near-zero thermal expansion material is a key issue for space opto-mechanical structure, in which the materials were usually used in cryogenic environment for keep sensitivity sharp[1].Carbon fiber reinforced silicon carbide(C$_f$/SiC) composites have been considered as one of the promising materials for characteristic of lightweight, high mechanical strength, low thermal expansion, and high thermal shock resistance[2-4.] As an important value, Coefficient of thermal expansion (CTE) of C$_f$/SiC composites has been investigated in many researches, However, CTE of C$_f$/SiC composites reported is generally high[5-7], and can't meet the application of the space opto-mechanical structure.

CTE of C$_f$/SiC composites are mainly determined by micro-structure, matrix compositions and the orientation of carbon fiber. Micro-structure and matrix compositions are mainly related to fabrication process. Liquid silicon infiltration (LSI) process was widely used to fabricate C$_f$/SiC composites for relatively economic and fast as compared to Precursor infiltration and pyrolysis (PIP) process, but residual silicon of LSI-C$_f$/SiC composites may improve CTE of the composites, and LSI-C$_f$/SiC had low mechanical properties generally. PIP process has gained increasing attention in recent

years for its advantages such as precursor designable and controllable ceramic compositions, which can obtain pure SiC matrix and hardly any other materials. 3D braided $C_f$/SiC composites have excellent CTE and mechanical properties for its good monolithic structure. Thus, it is well suited as large precise structure and mirror in space materials.

Due to the points above to obtain low CTE $C_f$/SiC composites, it was decided to fabricate 3D3d, 3D4d and 3D5d braided $C_f$/SiC composites by precursor infiltration and pyrolysis (PIP) with polycarbosilane as the matrix precursor. The paper here provides experimental results of CTE on longitudinal and transversal of 3D braided $C_f$/SiC composites in cryogenic temperature, to see the effect of different braided structure on CTE of $C_f$/SiC composites. The reason would effect thermal expansion was discussed.

## 2. Experimental procedure

### 2.1 Raw materials

3D3d、3D4d、3D5d braided structure preforms were made by T300 carbon fiber with 12K per bundle through four-steps method, volume fraction were 50%. Faint yellow solid polycarbosilane (PCS), with the softening point is 217℃~227℃, was selected as precursor for SiC ceramics. Xylene was selected as cross-linking reagent for PCS.

### 2.2 Preparation process

Carbon fiber preform was put in closed vessel and infiltrated with PCS/Xylene(PCS/Xylene=1:1) solution under vacuum conditions for 3h, then pyrolysis at temperature 1200℃, time 1h, high purity flowing Ar gas was used as protective atmosphere in the whole pyrolysis course.

### 2.3 Characterization

Netzsch DIL 402C dilatometer was used for thermal expansion measurements. Several test specimens with the size of 4.0mm×4.0mm×25.0mm were cut in longitudinal and transversal directions from $C_f$/SiC composites. CTE measurement was conducted in Helium atmosphere from -150℃ to room temperature(25℃). Raise speed of Measurement temperature was 5℃/min. S4800 scanning electron microscopy (SEM) was employed to observe the micro-cracks of composites.

## 3. Results and Discussion

### 3.1 Thermal expansion properties of $C_f$/SiC composite at cryogenic temperature

The expansion of 3D5d $C_f$/SiC composite is shown in Fig.1. As can be seen, the expansion in longitudinal direction is lower than that in transversal direction over the entire temperature range. In Fig.1, the transversal thermal expansion is relatively higher at higher temperature. the longitudinal thermal expansion can be correlated by straight line equations in two temperature segments: (1) from -150℃ to -30℃ and (2) from -30℃ to 25℃. In segment (1), the expansion is negative for the expansion equation is $-1.56\times10^{-7}T-4.96\times10^{-5}$; in segment (2), the expansion equation is $1.78\times10^{-7}T-3.92\times10^{-5}$, it shows that thermal expansion of the composites in longitudinal direction is almost zero at cryogenic temperature range.
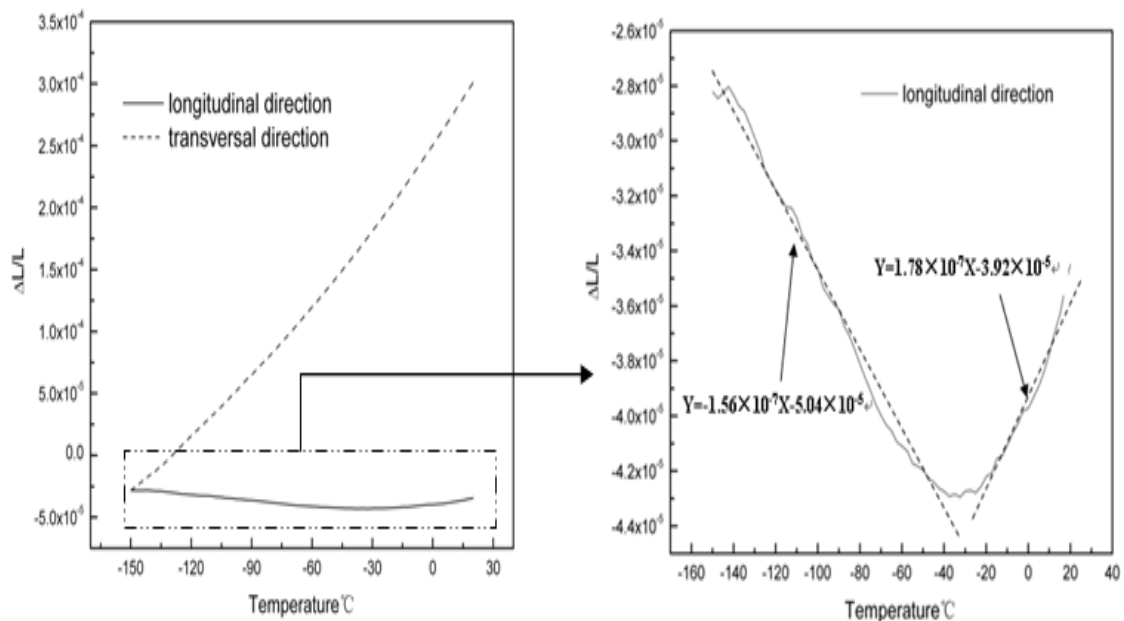


Fig.1 Relationship between expansion and temperature

Thermal expansion of $C_f$/SiC composites depend on the expansions of carbon fiber and SiC matrix mainly. T300 carbon fiber is an anisotropic material with CTEs of $-0.3\times10^{-6}$/℃ in axial and $3.1\times10^{-6}$/℃ in radial directions under room temperature.[8] However, SiC has the same CTEs in all directions for isotropic properties, PIP-SiC in this paper is amorphous structure and has lower CTE than CVD-SiC.[9] The available CTEs of T300 carbon fiber and SiC are shown in Table 1. The composites expansion in transversal direction was higher than that of longitudinal direction due to positive CTE of carbon

61

fiber in radial direction and high CTE of SiC matrix. For longitudinal direction of the composites, carbon fiber deeply restricts the expansion of SiC for negative CTE in axial direction, so it appears that the composites shrink at the beginning. With the temperature to about -30℃, CTE of SiC reach to about $0.6\times10^{-6}$/℃, carbon fiber have less restricting effect on expansion of SiC, thus composites expansion mainly depend on expansion of SiC, the curve of CTE in longitudinal direction decrease at the beginning and then increase from temperature -150℃ to 25℃. In a word, the change of thermal expansion is mainly due to competing between carbon fiber and SiC matrix.

Table 1 The CTE of carbon fiber and PIP-SiC

| Materials | CTE($\times10^{-6}$/℃) | |
| --- | --- | --- |
| | Axial directions | Radial direction |
| T300 carbon fiber | -0.3 | 3.1 |
| PIP-SiC | 2.7 | |

*3.2 Longitudinal thermal expansion*

Fig.2 shows the CTE of PIP-SiC and different braided structures $C_f$/SiC composites in longitudinal direction. In Fig.2, 3D5d $C_f$/SiC composites had the lowest CTE at the temperature range -150℃ to 25℃, the value is about $0.09\times10^{-6}$/℃. The CTE of 3D3d and 3D4d $C_f$/SiC composites is about $0.21\times10^{-6}$/℃ and $0.68\times10^{-6}$/℃, respectively. Longitudinal CTE of all the composites are lower than PIP-SiC, and their changed in a dissimilar increasing tendency with the raising of temperature, the curves slopes of the composites are smaller compare to PIP-SiC, it explain that carbon fiber can restricts the expansion of SiC, the composites shows lower expansion than SiC matrix. Furthermore, comparing to PIP-SiC, it would cause micro-cracks near interface in composites by residual stress due to CTE mismatch between carbon fiber and SiC during cooling process.[10] Although micro-cracks is just several tens nanometer to several micron in size, as shown in Fig.3 (a) and (b), there have micro-cracks in SiC matrix, these micro-cracks would exhibit positive effect to reduce CTE of the composites. During the temperature raise, the residual stress in composites was released and micro-cracks coalesced gradually, micro-cracks would provide space for thermal expansion of SiC matrix.
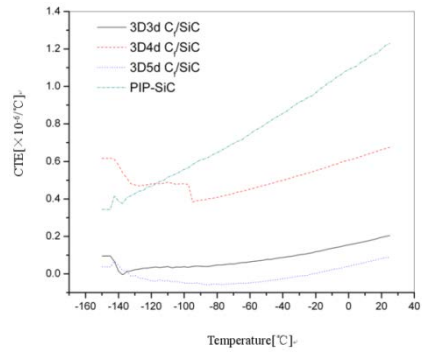
Fig.2 The longitudinal CTE of PIP-SiC and different braided $C_f$/SiC composites

For Fig.2, 3D3d, 3D4d, 3D5d $C_f$/SiC composites show different values of CTE due to their different braided structures of carbon fiber. In 3D4d $C_f$/SiC composites, four warp carbon fiber bundles are curving along longitudinal direction. But In 3D3d and 3D5d there have some warp bundles are straight line located in longitudinal direction of composites. Therefore, warp carbon fiber of 3D3d and 3D5d have stronger restrict to SiC than 3D4d due to negative axial CTE, so the longitudinal CTE of 3D3d and 3D5d is lower. Compare to 3D3d, Longitudinal CTE of 3D5d is lower for higher warp carbon fiber fraction in longitudinal direction.
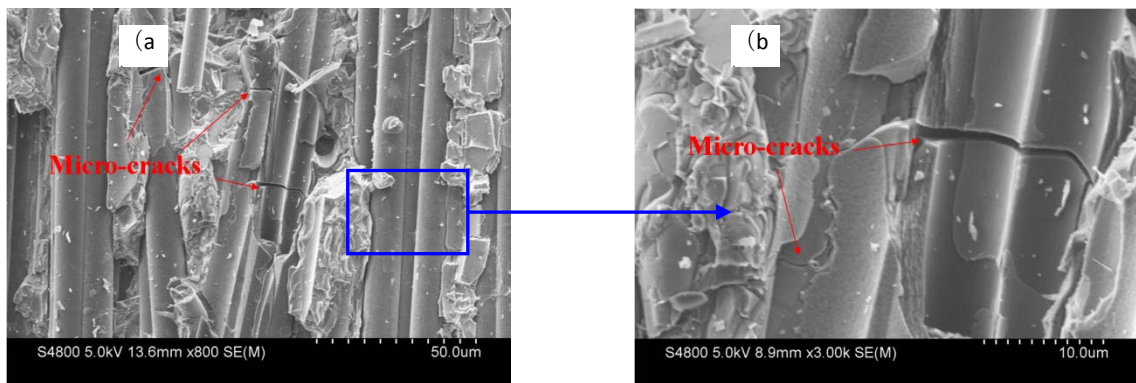


Fig.3 Micro-structures of $C_f$/SiC composites

## 3.3 Transversal thermal expansion

Transversal CTE of the $C_f$/SiC composites with different braided structures is shown in Fig.4. 3D3d $C_f$/SiC composites exhibit the lowest transversal expansion for the CTE values is $0.25 \times 10^{-6}$/℃. However, all the composites CTE of transversal direction are much higher than that of longitudinal direction. The observed rise of transversal CTE was mainly due to expansion in radial direction of carbon fiber in the temperature range.

63
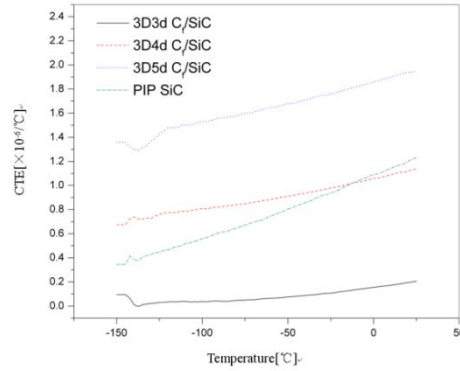
Fig.4 The transversal CTE of PIP-SiC and different braided $C_f$/SiC composites

For 3D3d braided structure, fraction of carbon fiber in transversal direction is the same as that in longitudinal direction. CTE is closed in two directions. The transversal CTE of 3D3d $C_f$/SiC composites was reduced due to the negative axial expansion of carbon fiber. But for 3D4d and 3D5d $C_f$/SiC composites, the transversal CTE is depend on radial expansion of carbon fiber. Higher longitudinal fraction of carbon fiber in 3D5d $C_f$/SiC composites which lead to high CTE in transversal direction compared to 3D4d $C_f$/SiC composites.

In transversal direction, the mismatch CTE would make de-bonded between carbon fiber and SiC matrix, but the de-bonded micro-space is much tiny and should be ignore compare to expansion of the composites.

## 4. Conclusion

This paper presents excellent thermal expansion of 3D braided $C_f$/SiC composites in the temperature range -150℃~25℃. 3D5d $C_f$/SiC have the lowest longitudinal CTE with the value of $0.09×10^{-6}$/℃, and 3D3d $C_f$/SiC have the lowest transversal CTE with the value of $0.25×10^{-6}$/℃via PIP process at 1200℃.

In the longitudinal direction thermal expansion of the composites was restricted by carbon fiber for its negative axial expansion in cryogenic, and micro-cracks can offset a part of thermal expansion of the composites, thus the CTE of the composites is lower than PIP-SiC. In transversal direction, composites CTE become higher for the high radial expansion of carbon fiber. Micro-space caused by De-bonding was negligible compare to composites expansion.

**References**

1.      Enya K, Yamada N, Imai T and et al. High-precision CTE measurement of hybrid C/SiC composite for cryogenic space telescopesCryogenics 2011;52:86-9.

2.      Odeshi AG, Mucha H,Wielage B. Manufacture and characterization of a low cost carbon fibre reinforced C/SiC dual matrix composite. Carbon, Vol. 44, No 10 (2006) 1994-2001.

3.      Zhou CC, Zhang CR, Hu HF and et al. Preparation process of $C_f$/SiC ceramic matrix composites. Rare metal materials and engineering. 2007; 36(1):659-662.

4.      Mentz J, Muller M, Kuntz M, et al. New Porous Silicon Carbide Composite Reinforced by Intact High-strength Carbon Fibres. J Eur Ceram Soc 2006;26:1715-1722.

5.      Michael D, Bauereisen S, Manufacturing and Performance of C/SiC Mirrors and Structures. *SPIE* 1997;3132: 171-82.

6.      Kaneda H, Nakagawa T, Onaka T, Enya K, Makeuti S, Takaki J, Haruna M, Kume M, Ozaki T. Cryogenic optical measurements of 12-segment-bonded carbon fiber-reinforced silicon carbide composite mirror with support mechanism. *Appl Opt* 2008;47(8):1122-8.

7.      Kumar S, Kumar A, Shukla A, et al. Investigation of expansion of 3D-stitched C-SiC composites. J Eur Ceram Soc 2009;29:2849-55.

8.      Liu XC, Cheng LF, Zhang LT, et al. Tensile properties and damage evolution in a 3D C/SiC composite at cryogenic temperatures. *Materials Science and Engineering A*. 2011;528: 7524-7528.

9.      Cheng LF, Xu YD, Zhang LT, Zhang Q. Effect of Heat Treatment on the Thermal Expansion of 2D and 3D C/SiC Composites from Room Temperature to 1400℃.Carbon 2002;411:1645-87.

10.     Wang JF, Chen ZH, Zheng WW and et.al. Thermal Stress Damage of Fiber in the Preparation of $C_f$/SiC. ACTA materiae compositae sinica. 2001;18(4):68-71.

# CONDUCTIVITY AND STRUCTURAL PROPERTIES OF HYBRID MATERIALS BASED POLYMER/INORGANIC COMPOSITES

**Uma Thanganathan[1], Fengxiang Yin[1], Gaur M. S. [2], Kumar sharma Amit [2]**

[1]*Research Core for Interdisciplinary Sciences (RCIS), Okayama University, Okayama, Japan*
[2]*Department of Physics, Hindustan College of Science and Technology, Farah, Mathura (U.P.)-281122, India*
*e-mail: umthan09@cc.okayama-u.ac.jp*

## Abstract

$SiO_2/P_2O_5/TiO_2/PVP$ hybrid composites membranes have been synthesized by the sol–gel method. The membrane was found to be homogeneous and transparent. The hybrid composites of different composition of $TiO_2$ were characterized by SEM, TGA, NMR, FTIR and conductivity measurement. The best inorganic-organic composition was chosen for chemical and electrical stability. NMR spectroscopy is used to investigate the properties of organic molecules present in hybride composites. SEM analysis of these hybride composites indicates no phase separation suggesting that PVP is well dispersed in the inorganic structure. The incorporation of PVP in sol–gel oxides provides an increase in conductivity with increase of molar % of $TiO_2$. The remarkable trends of conductivity have observed with respect to percentage humidity.

## 1.Introduction

The composite membrane fuel cell is potentially suitable for the power supply to all kinds of dynamoelectric vehicles, because it is eco-friendly and exhibits high efficiency. Proton exchange membrane (PEM), as proton conductive material, is a key component for transferring protons from the anode to cathode as well as providing a barrier to the fuel gas cross-leaks between the electrodes. The proton exchange membrane fuel cell (PEMFC) is an efficient energy conversion means for transportation application [1–2]. The membranes traditionally used in PEMFC are perfluorosulfonic polymers such as DuPont Nafion [3]. However, the high cost, high methanol permeability [4] and low conductivity at low humidity or high temperature [5] have limited its further application. Therefore, many researchers have been developing the high performance and low cost alternative conductive material [6].

The recent trend of researches is to develop the membrane of organic inorganic material. Several efforts have been made to develop proton-conducting membranes. Particularly, the membranes of inorganic material have been developed. For example, gels derived of $P_2O_5/ZrO_2$ and $SiO_2/P_2O_5/ZrO_2$ systems [7]. The sol–gel method is a simple low

cost method to produce proton conducting materials, because the gels contain a large number of micropores filled with liquid which can be used for fast proton transport.

In context of new composite conducting material, the polyvinylpyrrolidone (PVP) has good film-forming and adhesive behavior on many solid substrates. The amorphous structure of PVP also provides a low scattering loss, which makes it as an ideal polymer for composite materials for different applications. PVP is easily soluble in water, so it is preferred to avoid phase separation in the reactions [8-10]. In literature, alkali ions containing polymers are reported to be more promising possessing potential applications [11–12]. When low quantity of PVP doped with oxide material has also drawn more attention because of its possessing potential uses in electronics, optical filters, conducting adhesives, and in the development of composites membrane for fuel cell. There are several papers on sol-gel chemistry of phosphosilicates. These studied, showing that the choice of the phosphorus molecular precursors plays a fundamental role in the characteristics of the final product. The sol–gel chemistry of phosphosilicates has been extensively studied, showing that the choice of the phosphorus molecular precursors plays a fundamental role in the characteristics of the final product.

Because phosphate esters react more slowly with water at ambient conditions in comparison with silicon alkoxides [13], whereas, titanium oxide reacts too fast and it is necessary their complexation to decrease hydrolysis rate. The development of composite membranes had always been inspired by the fact that the selective transport through ordinary membranes is enabled by highly specialized macromolecular and supramolecular assemblies based on and involved in molecular recognition. The focus of this article will be onto improved or novel composite polymer membranes (i.e. the 'next generation' of membrane materials). The objective of present work is to prepare $SiO_2/P_2O_5/TiO_2/PVP$ hybrid composites and to study the structural, thermal and electrical conductivity.

## 2.Experimental Procedure

All chemicals were obtained from Japan and used as received. $Si(OC_2H_5)_4$ (TEOS, 99.9%, Colcote, Japan), trimethyl phosphate (Nacalai Tesque, Japan), poly(vinylpyrrolidone) with a molecular weight of 100,000 g/mol (Nacalai Tesque, Japan) and Titanium (IV) propoxide (Aldrich, 97 %) were used.

The hybrid composites were prepared in 2 stages: Initially, the starting material of TEOS was hydrolyzed in an acid mixture of ethanol and water ($C_2H_5OH:H_2O$, 1M HCl, 1:5 ratio) under magnetic stirring at room temperature. Then, trimethyl phosphate was added dropwise to the mixed solution. The total solution was stirred for 6 h under the slow speed of the reaction. In the second stage, PVP was dissolved in water at room temperature and then added to the above mixed solution. The organic part of composite (PVP) was mixed smoothly under stirring and a transparent solution was obtained. This solution was stirred for 24 h at room temperature, which led to the production of a homogenous transparent solution. The final solution was allowed to dry at room temperature to form a composite, after which the water and heat treatments at 150 and 120 ºC were applied for 24 and 12 h, respectively. Subsequently, the final composite membranes were ground to prepare a fine powder for the characterizations with SEM, TGA, FTIR, ^{1}H NMR, and conductivity examinations. The thickness of the membrane was in the range of 0.08–0.3 mm for the conductivity measurement.

Scanning electron microscopy (SEM) images were taken with a Hitachi S–3500N scanning electron microscope with an accelerating voltage of 20 kV. The thermal stabiliites of the hybrid composites were characterized using of thermogravimetric analysis (TGA) techniques. It was carried out on a DTG–50, Shimadzu instrument, performing simultaneous DTA–TG from room temperature to 600 ºC at a heating rate of 10 ºC/min under nitrogen. The chemical structure of the hybrid composite membranes was measured using FTIR spectroscopy (JASCO FTIR–460 spectrometer) in transmission mode (spectral range 4000–400 $cm^{-1}$). ^{1}H MAS NMR spectra were recorded on a Varian UNITYI NOVA300 FT–NMR (Fourier-transform NMR) spectrometer. Impedance spectroscopy studies were carried out on a Solartron, SI–1260 (impedance analyzer), where evaporated-platinum electrodes were used. The conductivity of the membranes was calculated from complex impedance plots in the frequency range from 1 Hz to 1 MHz. The samples were kept in open atmosphere at room temperature during the impedance measurements.

## 3.Results and discussion

Figures 1 shows the SEM images of $SiO_2/P_2O_5/TiO_2/PVP$ hybrid composite. It can be demonstrate from SEM images that the introduction of PVP in $SiO_2/P_2O_5/TiO_2$ composites

dramatically improves their dispersion and greatly enhance the interfacial adhesion between the inorganic and organic matrix.
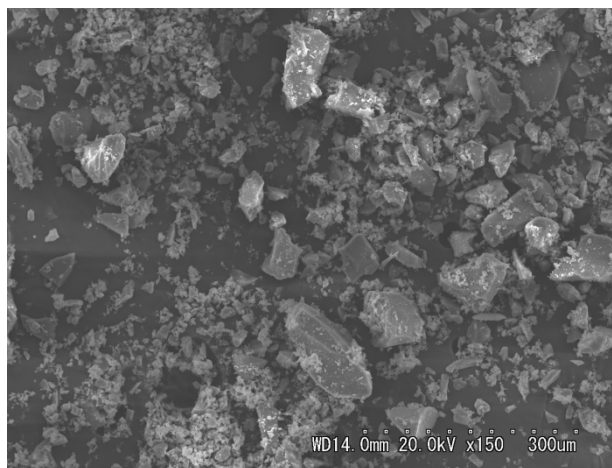


Fig.1. SEM image of $SiO_2/P_2O_5/TiO_2/PVP$ hybrid composite

The thermal behaviors of the different compositions in composites are observed to be similar. Figure 2 shows TGA curves (weight change curves) of samples of different composition. The general features of these characteristics are; TGA produces a decrease of maximum weight at low temperature due to the previous elimination of water and alcohol. However, weight loss decreases above 200 °C and finally almost saturated at higher temperature region. The TGA curves can be divided into four regions. The first, between room temperature and 200 °C with maximum rate of weight loss, this mainly attributed to desorption of physically adsorbed water and residual solvents from the sol preparation. Other region, between 200 and 450 °C, is assigned to the elimination of water and alcohol from condensation reactions. A third region, between 450 and 600 °C is associated with decomposition of organic residues from unhydrolyzed ligands bound to metal oxides and combustion of acetylacetone. Finally, above 600 °C no changes in weight are observed. The thermal stability of hybrid composite is better than the individual component, because the particle- matrix interfacial interaction and 'barrier effect', which limits volatilization of products and thermal transport during polymers decomposition, have been suggested as the two main reasons for the improved thermal stability in inorganic-organic composite material [14]. Therefore, it is reasonable to assume that the better dispersion and stronger interfacial interaction for $SiO_2/P_2O_5/TiO_2$ with PVP result in the enhanced thermal stability.
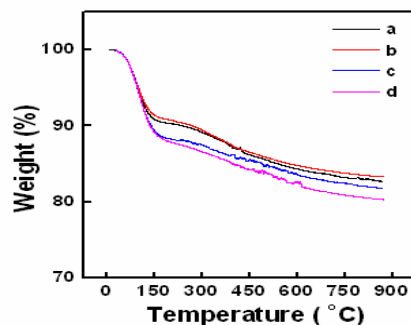
Figure 2. TGA of $SiO_2/P_2O_5/TiO_2/PVP$ hybrid composite (a) 97/2/1 (mol%)/1 g (b) 96/2/2 (mol%)/1 g (c) 95/2/3 (mol%)/1 g and (d) 94/2/4 (mol%)/1 g

Figure 3 shows the FTIR spectra in transmittance mode. The peaks at 457 cm$^{-1}$ are attributed mainly to bending modes of Si–O–Si and peak at 797 cm$^{-1}$ may be Si–O–Ti bending, 951 cm$^{-1}$ due to Ti–O–C characteristics vibration. The peak at 1087 is due to $PO_3^-$ and $PO_4$ symmetrical stretching. The peak at 1640 cm$^{-1}$ is due to C=C stretching. The peaks at 3381 cm$^{-1}$ shows that –OH group due to mutual interaction of oxidative material in PVP. In NMR spectrum, when percentage of PVP increases, the steric effect is produced due to the shifting of protons close to carbon atom (i.e. figure 4). It can be concluded that when molecular features cause a proton to be forced close to other protons, the proton will in general be deshielded and presents dispersion interactions with the oxidative material $(SiO_2/P_2O_5/TiO_2)$. It means that the lone pairs on nitrogen or oxygen (in PVP) are anti to a C–H band then the proton is shifted in upfield direction as decreasing the concentration of PVP in the membrane. It shows magnetic anisotropy effects on vinylic group (i.e. H–C=C at 4.5 ppm). The others peaks of protonation in the membrane structure is due to –C=O–N at 2.1 ppm, secondary proton –$CH_2$ at 5.8 ppm. Furthermore, the both spectra (IR and NMR) of PVP hybrid membrane concluded that as the concentration of oxidative material is increased with decreasing in the concentration of PVP, the protonation in the hybrid membrane is shifted in the direction of upfield and creates the gap between the atoms. It increases the transmittance of the hybrid membrane. The analysis of different functional group through IR and NMR are presented in Table 1.
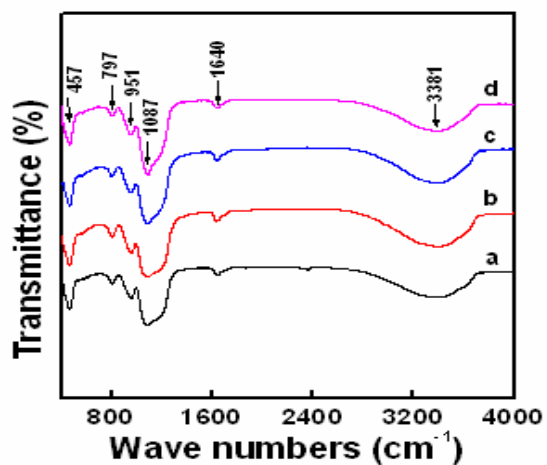
Fig. 3. FTIR characteristics of $SiO_2/P_2O_{5}$/$TiO_2$/PVP hybrid composite (a) 97/2/1 (mol%)/1 g (b) 96/2/2 (mol%)/1 g (c) 95/2/3 (mol%)/1 g and (d) 94/2/4 (mol%)/1 g.
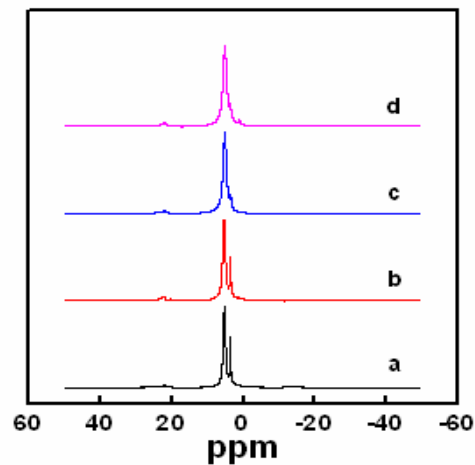
Figure 4. ^{1}H NMR characteristics of $SiO_2/P_2O_5/TiO_2$/PVP hybrid composite (a) 97/2/1 (mol%)/1 g (b) 96/2/2 (mol%)/1 g (c) 95/2/3 (mol%)/1 g and (d) 94/2/4 (mol%)/1 g

The effect of humidity on proton conductivity at room temperature was measured using AC impedance spectroscopy. Figure 5 shows the proton conductivity of $SiO_2/P_2O_5$/$TiO_2$/PVP hybrid composite at different humidity. Proton conductivity usually increases both with the hydrophobic chain length increasing and temperature increasing. In present case the proton conductivity was found to unaffected upto 60% humidity, but after this range conductivity decreases slowly in some cases when $TiO_2$ exhibits lower molar %. It has been observed that proton conductivity is unchanged under longer range of % humidity, if $TiO_2$ contents increases in composite matrix. The conductivity was found to have appreciable value because conducting behavior of $TiO_2$ and PVP. We have observed the two possible reason of proton conductivity first is due to the different reactivity between the sulfonated and nonsulfonated monomer [31], secondly, the morphology of hybrid composite. The morphology of hybrid composit is well understood by SEM, FTIR and NMR. The smooth change in conductivity shows the uniform and homogeneous dispersion of inorganic components in PVP.

Table 1. Analysis of functional groups in FTIR and NMR spectra.

| S. No. | IR analysis | | NMR analysis | |
|---|---|---|---|---|
| | Functional groups | Wave number $(cm^{-1})$ | Functional groups | Chemical shift (ppm) |
| 1 | bending modes of Si–O–Si | 457 | primary proton H–C=C | 4.5 ppm |
| 2 | Si–O–Ti bending | 797 | tertiary proton –C=O–N | 2.1 ppm |
| 3 | Ti–O–C characteristics vibration | 951 | secondary proton –CH$_2$ | 5.8 ppm |
| 4 | C=C stretching | 1640 | - | - |
| 5 | –OH group | 3381 | - | - |
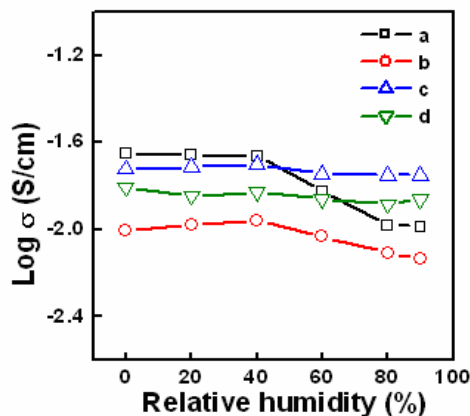
Fig. 5. Effect of humidity on conductivity of $SiO_2/P_2O_5/TiO_2/PVP$ hybrid composite (a) 97/2/1 (mol%)/1 g (b) 96/2/2 (mol%)/1 g (c) 95/2/3 (mol%)/1 g and (d) 94/2/4 (mol%)/1 g.

## 4.Conclusion

We have successfully prepared the crackles and transparent $SiO_2/P_2O_5/TiO_2/PVP$ hybrid composite membrane by sol–gel method. The proton mobility is accelerated by molecular water bound with the POH group causes the increase in conductivity. Remarkable result is that the conductivity is unaffected upto higher value of humidity. The adhesive behavior of $SiO_2/P_2O_5/TiO_2$ composite is strongly improved by PVP and make it fast protonic conductors, which are thermally and environmentally stable and have a great potential for practical applications.

## References

1. Marcenaro B. Fuel cell for public transportation, fuel cell seminar, 29 November-2 December 1992, Tucson, Arizona; 1992.
2. Mark J, Ohi J.M, Hudson Jr D.V. Fuel savings and emissions reductions from light duty fuel cell vehicles. NREL, 1994.
3. Alberti G, Casciola M. Composite membranes for medium-temperature PEM fuel cells. Ann Rev Mater Res 2003;33:129–154.
4. Kreuer K.D. On the development of proton conducting materials for technological applications. Solid State Ion 1997;97:1–15.

5.  Ciureanu M, Wang H. Electrochemical Impedance study of electrode membrane assemblies in PEM fuel cells. I. Electro-oxidation of $H_2$ and $H_2$/CO mixtures on Pt-based gas-diffusion electrodes. J Electrochem Soc 1999;146:4031–4040.

6.  Mathias U. Advanced functional polymer membranes. Polymer 2006;47:2217–2262

7.  Mosa J, Larramona G, Dur´an and et.al. Synthesis and characterization of $P_2O_5$/$ZrO_2$/$SiO_2$ membranes doped with tungstophosphoric acid (PWA) for applications in PEMFC. J Membr Sci 2008;307:21–27

8.  Rui Z.T, Ran L, Xin L.L and et.al. Photochromic Polyoxotungstoeuropate K12 [Eu $P_5W_{30}O_{110}$]/Polyvinylpyrrolidone Nanocomposite Films. J. Solid State Chemistry 2003;172:458–463.

9.  Ramya C.S, Selvasekarapandian S, Hirankumar G and et.al. Investigation Sonthe Effect of Complexation of NaFsalt with Polymerblend (PEO/PVP) Electroly Tesonionic Conductivity and Optical Energy-bandgaps. J Non-Crystal Solids 2008;354:1494–1502.

10. Zhang J, Liu H, Wang Z et.al. Low-Tempera- ture Growth of ZnO with Controllable Shapes and Band Gaps. J Crystal Growth 2008;310:2848–2853.

11. Fatima H, Sandrine T, Gilles M et.al. Photooxidation of Poly (N-vinylpyrrolidone) (PVP) in the Solid State and in Aqueous Solution," Polymer Deg-radation and Stability. 2009;94:2257–2266.

12. Kobayashi Y, Kosuge A, Konno M and et.al. Fabrication of High Concentration Barium Titanate/Polyvinylpyrroli- done Nano-Composite Thin Films and Their Dielectric Pro- perties. Applied Surface Science, 2008;255:2723–2729.

13. Uma T, Nakao A, Nogami M. Characterization and electrochemical properties of $P_2O_5$–$ZrO_2$–$SiO_2$ glasses as proton conducting electrolyte. Mater Res Bull 2006;41:817–824.

14. An L, Pan Y, Shen X and et.al. Rod-like attapulgite/ polyimide nanocomposites with simultaneously improved strength, toughness, thermal stability and related mechanisms. J Mater Chem 2008;18:928–4941

# MACRO-DEFECT-FREE (MDF)CEMENTS EXPOSED TO FLUIDS: EXPERIMENTAL STUDY

## Kosednar-Legenstein Barbara, Maier Günther

*Materials Center Leoben Forschung GmbH, Leoben, Austria*
*e-mail: barbara.legenstein@mcl.at*

## Abstract

Macro-defect-free cement (MDF) composites were immersed in water at room temperature and 60°C as well as in acid and alkaline solutions at 60°C. The flexural strength and the Young´s modulus were investigated on dry (after 7, 14 and 28 days) and wet samples after 28 days. The immersed samples showed a decrease of the flexural strength and the Young´s modulus of 60%. The mineralogical composition of the immersed samples was investigated and the results showed an interesting correlation between temperature, pH, mineralogical composition and the mechanical behaviour.

## 1.Introduction

Macro-defect-free (MDF)composites are a mixture of calcium aluminate cement (CAC), polyvinyl alcohol/acetate(PVA) and glycerine as plasticizer, characterised by a high flexural strength (> 140 MPa), a high Young´s Modulus (25-55GPa) and the absence of pores and defects greater than 200 µm. The material was developed and patented in the 1980`s by a research group at ICI led by Brichall [1] using a special processing method. Cement, PVA, glycerine and water are mixed in two steps: (1) mixing in a usual mixer and (2) high shear mixing in a twin roll mill.The following steps are pressing at low temperature (80°C) and low pressure (6 MPa) and a curing process at 80°C for 24 h.

The structure of MDF composites consists of unhydrated cement grain, a bulk polymer phase and a region which includes hydrated cement grains and polymer chains [2]. Because of its properties as a rheological aid the used PVA has a special role in this system andfills up the pores and reacts with the cement to form a network of cross-linked polymer chains (see Fig. 1) [2,3]. During the hydration of the cement the acetate group of the PVA reacts with $Ca^{2+}$ to calcium acetate and the and the hydroxyl groups of the PVA are cross-linked with aluminium ions and build a network.

One important limitation of the mechanical properties of MDF´s is the low moisture resistance of the material. After immersion in water a loss of the flexural strength is observed [2,7,8,9]. The PVA as well as unhydrated cement grains are associated with the problem of low moisture resistance, because moisture has the possibility to enter via the PVA-network into the samples and the PVA swells, and a hydration reaction of the unhydrated cement grains starts the irreversible process of

carbonation [2,10,11]. There are several studies about this subject with different approaches, like chancing the polymer phase or the cement (OPC), using sodium polyphosphate, heat treatment at 500°C, using a monomer and activation agent instead of a polymer [7,12,13,14,15,16]. In our study we investigated the influence of acid and alkaline solutions,in comparison with water at different temperatures, on the mechanical properties and the influence on the mineral composition.
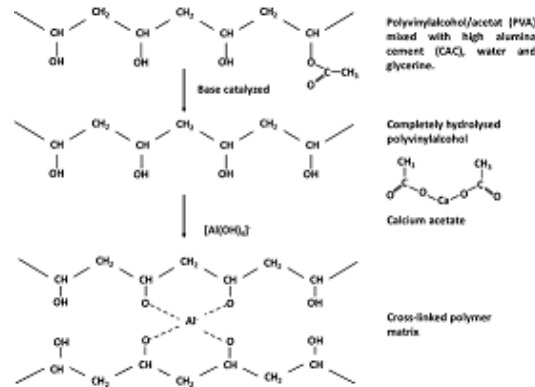


Fig. 1: Chemical reactions during the hydration of MDF cement [4,5,6].

## 2.Experimental

CAC (Secar 71, Kerneos) and two types of polyvinyl alcohol from Nippon Gohsei (KH-17 and GH-20)with different degree of hydrolysis (see Tab. 2) were mixed for 4-5 minutes in a Haake mixer (Polylab system) with glycerine and water in the ratio 1/0.07/0.007/0.12, respectively. The high shear mixing and calendering was done on a twin roll mill (Collin)and the prepared sheets (16 x 16 x 3 mm) were pressed at 80°C and 6 MPa for 10 minutes. The last steps of the sample preparation were the curing in an oven at 80°C for 24 hours and cutting of the samples (45 x 10 x 3 mm) afterwards. Tab. 1 shows the chemical composition of the cement (company product data sheet) measured by XRF, the properties of the PVAs KH-17 and GH-20 from Nippon Gohseiare given in Tab. 2.

The flexural strength of the dry samples, which were aged at room temperature in a closed vessel, was measured after 7, 14 and 28 days with a four point bending test (support span length 20 mm, loading span length 10 mm). The Young´s modulus was calculated. At an age of 14daysa part of dry aged samples were stored in different solutions (pH 2, pH 12, high salt concentration and distilled water) and 60°C for two weeks and the mechanical properties were determined.

Table. 1: Chemical Composition of Secar 71.

| Chemical composition | % |
|---|---|
| $Al_2O_3$ | $\geq 68,5$ |
| CaO | $\leq 31,0$ |
| $SiO_2$ | $\leq 0,8$ |
| $Fe_2O_3$ | $\leq 0,4$ |

Table. 2: Properties of the used PVA (product data sheet)

| Name | Hydrolysis mol % | Viscosity mPa s | pH |
|---|---|---|---|
| KH-17 | 79,6 | 36,0 | 5,8 |
| GH-20 | 87,8 | 43,4 | 5,5 |

Another part of samples were immersed in water at 20°C for 180 days. The mineralogical composition of these samples was investigated at 28 days, 70 days and 180 days. The density of all samples was investigated with the Archimedes Principle.

All characterisation experiments by X-ray diffraction methods (XRD) were conducted on a D8 Discover diffractometer (Bruker AXS, Germany) in parallel beam geometry (40 kV, 35 mA, Cu Kα radiation). The FT-IR analyses were made of the dried and powdered, mixed with KBr for tablets, samples with a spectrometer of Nicolet, Avatar 320.

## 3.Results and discussion

### 3.1.Mineralogical composition

The principal mineralogical phase of the high alumina cement (CAC) is CA (calcium aluminate, $CaO \cdot Al_2O_3$, ICDD 23-1036) the secondary phase is $CA_2$ (Calcium dialuminate, $CaO \cdot (Al_2O_3)_2$, ICDD 12-0408) as determined by XRD.

The mineralogical investigations of MDF samples showed that in dry samples (age 28d) the main phases, CA and CA2, of the cement were found, the assumed Ca-acetate (see Fig. 1) was not detected. In samples which were immersed in water for 28 days at 20°C the metastable phase CAH10 ($Ca_2Al_2O_5 \cdot 8H_2O$, ICDD 12-0408) approach, the main phases were aragonite ($CaCO_3$, ICDD 41-1475) and gibbsite ($Al(OH)_3$, ICDD 33-0018), whereas the amount of CA and CA2 slightly decreased (Fig. 2a) comparing with dry aged samples. After 70 days in contact with water the metastable phase CAH10 was disappeared, the amount of aragonite increased up to 50%, while gibbsite decreased to less than 2%. After 180 days water immersion gibbsite was built again, the amount of CA, CA2 and aragonite were decreasing, while calcite ($CaCO_3$, ICDD 05-0586) as new phase was established.

Compared to immersion in water and alkaline and acid solutions at 60°C for two weeks a different mineralogical composition was determined (Fig. 2b). Instead of the metastable phase CAH10 the calcium carboaluminate hydrate ($C_4AcH11$, $3CaO \cdot Al_2O_3 \cdot CaCO_3 \cdot 11H_2O$, ICDD 41-0219), the stable phase katoite C3AH6 ($Ca_3Al_2O_6 \cdot 6H_2O$, ICDD 24-0217), gibbsite and calcite were formed. Further small amounts of the cement phases CA and CA2 were still present.

The immersion in an acid solution (pH 2, 60°C) had almost no influence on the mineralogical composition compared to dry aged samples. CA and CA2 were still the main phases, and a third phase, Ca-acetate or Ca-Oxalate, which was not possible to identify clearly, appeared.

Using an alkaline solution (pH 12, 60°C), instead of water or acid only small amounts of katoite, gibbsite and a third phase were formed. We assume that this phase can be Ca-acetate or Ca-citrate. The main phases were again CA and CA2.

The XRD analyses showed that there are no stable phases like cement hydrates which are formed usually in concrete, these reactions are almost retarded by the PVA [5]. Due to the low amount of Ca-acetate it was not detectable by XRD, but it was possible to verify the formation of this phase via FT-IR. The formation of new phases in this systemin contact with water is continuing, with the type of reactions being a function of temperature. The metastable CAH10 is formed under 20°C [17].The formation of $CaCO_3$(calcite and/or aragonite) is explained by continuous diffusion of atmospheric $CO_2$ in the solutions and the reaction with $Ca^{2+}$of the cement phases.
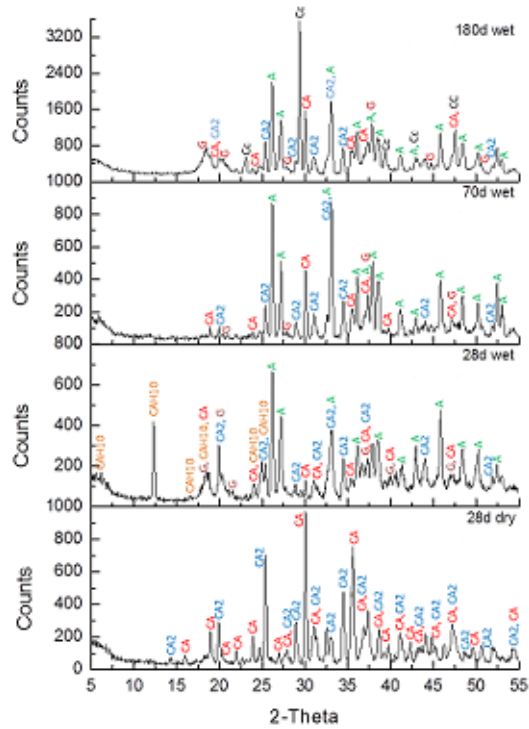
Fig. 2a: X-ray diffraction of immersed (water, 20°C) MDF samples. G: gibbsite, A: aragonite, Cc:calcite.
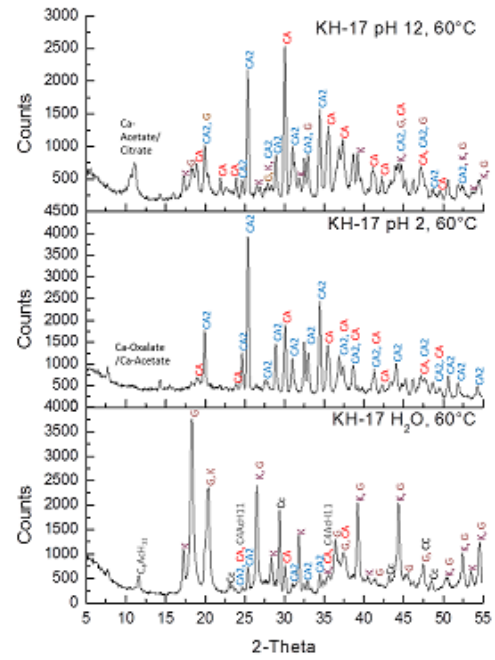
Fig. 2b: X-ray diffraction of immersed (water, acid and alkaline solutions, 60°C) MDF-samples. K: katoite, G: gibbsite, Cc: calcite.

The $Al^{3+}$ of the cement phases reacts with $H_2O$ to an aluminium hydrate phase (1) [17].

$$CAH10 + CO_2 + xH_2O \rightarrow CaCO_3 + Al_2O_3 \cdot yH_2O + (10 + x - y)H_2O \qquad (1)$$
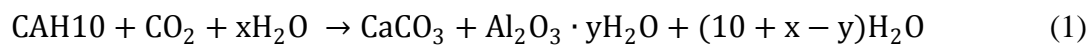
Immersion in water at higher temperatures (60°C) C3AH6, gibbsite (AH3) and C4AcH11 were formed after 28 days. In this case also carbonation and formation of aluminium hydrate following reaction 2 [17] took place:

$$C3AH6 + 3CO_2 + xH_2O \rightarrow 3CaCO_3 + Al_2O_3 \cdot yH_2O + (6 + x - y)H_2O \qquad (2)$$

The effect of carbonation and conversion from the metastable, hexagonal CAH10 to the stable and cubic C3AH6 [11] is an increase of porosity followed by a decrease of the mechanical properties, but it did not appear in samples immersed in alkaline or acid solutions.

Infrared analyses of a dry and immersed MDF samples at 20 and 60°C are shown in Fig 3. The founded bands are shown in Tab. 3.

Table. 3: Infrared bands for PVA and MDF samples stored under different conditions (sh: shoulder, b: broad, w: weak, s: strong).

| PVA | Assignment | MDF dry | MDF wet 20°C | MDF wet 60°C | Assignment |
|---|---|---|---|---|---|
| 3420 | O-H stretching | | 3671sh | 3646sh | |
| 2956 | | | 3504sh | 3511sh | O-H stretching |
| 2921 | C-H stretching, alkyl group | 3425b | 3440b | 3440b | |
| 2847 | | 2901b | 2915b | 2915b | C-H stretching, alkyl group |
| 1730 | C-O and C=Oacetate group | 2846w | 2848sh | 2846sh | |
| 1643 | water bond | 1619s | 1625s | 1629s | C-O-Al |
| 1630 | water bond | 1550w | 1558w | 1562w | Ca-acetate, stretching vibrations |
| 1452 | CH2 groups | 1454b | | 1452sh | $CO_3$ stretching |
| 1382 | | 1413b | 1411b | 1419b | Ca-acetate, stretching vibrations |
| 1260 | | 1382w | 1382w | | |
| 1121 | | 1243w | 1241sh | 1257s | |
| 1078 | C-O-C | | | 1078sh | C-O-C |
| | | 1016b | 1018s | 1016s | Al-O stretching |

The characteristic absorption bands for the PVA describe following vibration types [18]: O-H stretching bands at around 3400 cm$^{-1}$, 2970-2800 cm$^{-1}$ stretching C-H from the alkyl groups, C=O and C-O bands around 1750-1720 cm$^{-1}$ from the acetate groups of the PVA, around 1240 cm$^{-1}$ stretching of the C-C band and the band at 1140 cm$^{-1}$ provided information about the crystallinity of the PVA [19]. Infrared spectra of the MDFs shows a similar O-H stretching around 3400 cm$^{-1}$, whereas samples immersed at higher temperatures show broader peaks. Furthermore, there was no band found at 1750-1720 cm$^{-1}$, but two new peaks for Ca-acetate at around 1560 cm$^{-1}$ and 1410-1420 cm$^{-1}$ approached. Some peaks showed stronger intensity than the spectra of the PVA, e.g. at 1630 cm$^{-1}$ indicating that the cross-linked polymer matrix was with aluminium. [3,6]. The bands from 1410-1420 cm$^{-1}$ can be assigned to the stretching vibrations of $CO_3^{2-}$ [20].
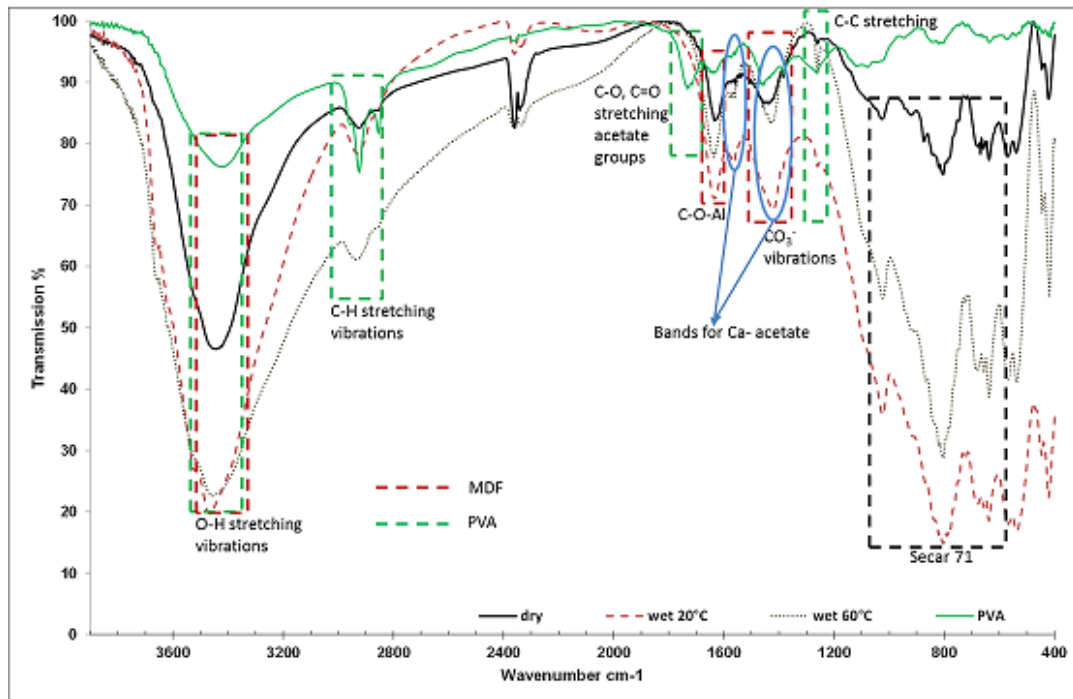
Fig. 3: Infrared analyses of the used PVA, dry MDF samples, and after immersion at 20°C and 60°C.

The infrared analyses showed changing of the structure during the hydration of the cement, e.g. the changing of the bands around 3500 cm$^{-1}$, and as well as the formation of the PVA-aluminium network. The formation of the network was indicated by the disappearing of the peak at 1720 cm$^{-1}$ and the development of the peaks at 1630 cm$^{-1}$. The method allows to identify small amounts of phases, like Ca-acetate, which was not possible by XRD.

*3.2.Results mechanical properties*

The results of the investigated mechanical properties, stored in water at 20°C, at pH 2, pH 12, salt solution and distilled water at 60°C,of the samples GH-20 and KH-17 at different ages are shown in Tab.4

Figure 4 shows the flexural strength (a) and the Young´s modulus (b) after 28 days. As expected, a flexural strength of dry samples around 120 MPa was observed, whereas the flexural strength of the immersed samples decreased for 60 to 70 %. The Young´s Modulus showed the same correlations (see Tab. 4 and Fig. 4b).
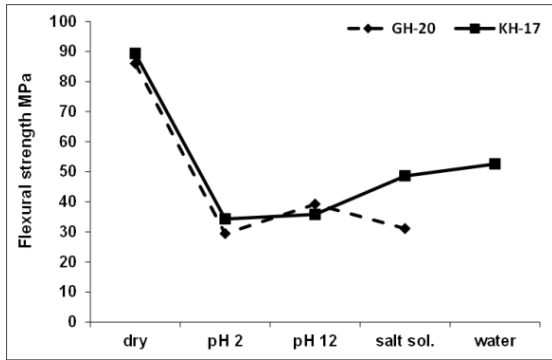
Fig. 4a: Flexural strength of MDF composites stored for 28 days under dry conditions and immersed in different solutions.
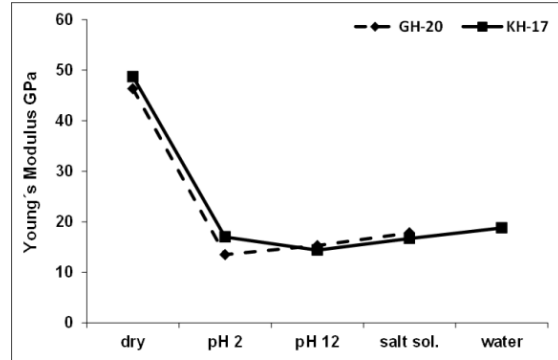
Fig. 4b: Young´s modulus of MDF composites stored for 28 days under dry conditions and immersed in different solutions

Table. 4: Mechanical properties of dry and immersed MDF composites (□ flexural strength, E: Young´s Modulus, □ density, STD: standard deviation).

| Sample | Age in Days | σ MPa | STD | E GPa | STD | ρ g/cm³ |
|---|---|---|---|---|---|---|
| GH-20 dry | 7 | 113.2 | 8 | 55.7 | 12 | 2.4 |
| | 14 | 120.1 | 16 | 56.4 | 6 | 2.5 |
| | 28 | 86 | 9 | 46.3 | 3 | 2.5 |
| GH-20 pH 2 | 28 | 29.4 | 7 | 13.5 | 2 | 2.4 |
| GH-20 pH 12 | 28 | 39.2 | 6 | 15.3 | 2 | 2.4 |
| GH-20 salt | 28 | 31.1 | 5 | 17.8 | 4 | 2.4 |
| KH-17 dry | 7 | 91.3 | 12 | 54.4 | 3 | 2.4 |
| | 14 | 104.5 | 16 | 50.9 | 6 | 2.4 |
| | 28 | 89.3 | 14 | 48.7 | 9 | 2.4 |
| KH-17 pH 2 | 28 | 34.3 | 6 | 17 | 3 | 2.5 |
| KH-17 pH 12 | 28 | 35.8 | 6 | 14.4 | 2 | 2.4 |
| KH-17 salt | 28 | 48.6 | 6 | 16.7 | 2 | 2.4 |
| KH-17 H$_2$O | 28 | 52.6 | 10 | 18.8 | 1 | 2.4 |

## 4.Conclusions

In the presented work a characterization of MDF cements, aged in different media was presented. It was found, that different aqueous media and the immersion at different temperatures have a high influence on the mineralogical composition of the materials.

The earlier reported loss of strengths due to water contact of this type of materials was proven. The main reasons for the loss of strengths seem to be the carbonation and conversion of the metastable CAH10 to C3AH6. Both phase formations are accompanied by volume changes in the composite. This leads most probably to a decrease of the mechanical properties. The network of cross-linked PVA chains is also influenced by the temperature, but seems to have no effect on the water sensitivity of the system.

**References**

1. Birchall J.D, Howard A.J, Kendall K. Flexural strength and porosity of cements. Nature 1981; 289: 388-389

2. Donatello S, Tyrer M, Cheeseman C.R Recent developments in macro-defec-free (MDF) cements. Constr Build Mater 2009; 23: 1761-1767.

3. Desai P.G, Lewis J.A, Bentz D.P. Unreacted cement content in macro-defect-free composites: impact on processing-structure-property relations. J Mater Sci 1994;29: 6445-6452.

4. Desai P.G.Cement polymer interactions in macro-defect-free composites. MSc thesis.Urbana-Champaign, Univercity of Illinois, 1992.

5. Rodger S.A, Brooks S.A, Sinclair W et. al. High strength cement pastes- Part 2 Reactions during setting. J Mater Sci 1985; 20: 2853-2860.

6. Ekincioglu O, Ozkul M.H, Struble L.J Optimization of material characteristics of macro-defect free cement. CemConc Com 2012; 34: 556-565.

7. Drabik M, Mojumdar S.C, Slade R.C.T. Prospects of novel macro-defect-free cements for the new milienium. Ceram-Silik 2001; 46(2): 68-73.

8. Lewis J.A, Boyer M. Effects of an organotitanatecross.linking assistive on the processing and properties of macro-defect free cement. AdvanCem-Bas Mater 1995; 2: 2-7.

9. Harsh S, Handoo S.K, Ahluwalia S.C Investigations on moisture absorption and its effect on the performance of HAC based MDF cement. Proceedings of the 10th international congress on the chemistry of cement, Gothenburg, Sweden 1997.

10. Lewis A, Boyer M, Bentz D.P Binder distribution in macro-defect-free cements: relation between percolative properties and moisture absorption. J Am CerSoc 1994; 77 (3): 711-716.

11. Popoola O.O, Kriven W.M, Young J.F Microstructural and microchemical characterisation of a calcium aluminate-polymer composite (MDF cement). J Am CerSoc 1991; 74 (8): 1928-1933.

12. Mojumdar S.C, Mazanec K, Drabik M. Macro-defect-free (MDF) cement – synthesis, thermal, chemical, SEM and magnetometric study and moisture resistance. J Therm Anal Cal 2006; 83: 135-139.

13. Santos R.S, Rodrigues F.A, Segre N et.al. Influence of poly(vinyl alcohol), cement type, and silica fume. CemConc Res1999; 19: 747-751.

14. Drabik M, Mojumdar S.C, Galikova L. Changes of thermal events of macro-defect-free (MDF) cements due to the deterioration in the moist atmosphere. CemConc Res 2001; 31: 743-747.

15. Chandrashekhar G.V, Shafer M.W. Polymerimpregnationof macro-defect-free cements. JMater Sci1989; 24: 3353-3355.

16. Titchell I. Environmental degradation of macrodefect-free cements – Part 1. Mechanical properties investigation.J MaterSci 1991;26: 1199-1204.

17. Pundienė I, Goberis S, Antonovič V et. al. Carbonation of Alumina Cement-bonded conventional refractory castable in fireplace. MaterSci (Medžiagotyra) 2006; 12(4): 333-337.

18. Patachia S, Moise G, Ozkul M.H et. al. Influence of the self crosslinkable polymers on the properties of the macro defect free (MDF) cements. Bull TransilvUnivBras2009; 2 (51): 181-186

19. Mansur H.S, Sadahira C.M, Souza A.N et. al. FTIR spectroscopy characterization of poly(vinyl alcohol) hydrogel with different hydrolysis degree and chemically crosslinked with glutaraldehyde. MaterSciEng 2007; 28: 539-548

20. Sugama T, Brothers L.E, Weber L. Calcium aluminate cements in fly ash/calcium carbonation and acid corrosion at low hydrothermal temperature of 90 °C. J Mater Sci 2002; 37: 3163-73.

# PREPARATION OF ɣ-AL$_2$O$_3$ NANOCRYSTALLITES VIA SOL-GEL AUTO COMBUSTION PROCESS AND PRODUCTION OF ALUMINUM MATRIX COMPOSITES REINFORCED WITH NANO AL$_2$O$_3$

**Baghchesara Mohammad Amin [a,] , Khorrami Saeid Abedini [b] and Lotfi Roshanak [b]**

[a]*Department of Metallurgy & Materials Engineering, Masjed Soleyman Branch, Islamic Azad University, Masjed Soleyman, Iran*
[b]*Chemistry Department, North Tehran Branch, Islamic Azad University, Tehran, Iran*
*e-mail: amsara2000@gmail.com*

## Abstract

In this research, γ-Al$_2$O$_3$ nanocrystallites were synthesized successfully by combination of sol-gel auto-combustion process and ultrasonic method. The overall process involves three steps: formation of homogeneous sol at 50˚C; formation of dried gel at 90˚C, and experiments revealed that Al$_2$O$_3$ dried gel derived from glycine (as fuel) and nitrates sol exhibits self propagating combustion at 400˚C that it is ignited in air. After auto-combustion process, the Al$_2$O$_3$ nanopowders were calcined at 1100˚C. Also, aluminum alloy matrix composites reinforced with 0.75 and 1.5 vol.% γ-Al$_2$O$_3$ nanoparticles were fabricated via stir casting method. Fabrication was performed at 850˚C temperatures. The resulting composites were tested for their nanostructure and present phases. Based on the obtained results, optimum amount of reinforcement were determined by evaluating the density, hardness and compression tests of the composites.

**Keywords:***γ-Al$_2$O$_3$, Auto-Combustion, Ultrasonic, Aluminum, Composite, Hardness, Density.*

## 1. Introduction

Alumina ceramic (Al$_2$O$_3$) is a hard refractory ceramic, which has been used in high temperature structural and substrate application because of its good strength and low thermal expansion coefficient. Nevertheless, like other monolithic ceramics, Al$_2$O$_3$ is apt to suffer from low ductility and low fracture toughness. Therefore, metals such as aluminum and cobalt or alloys are added to ceramics to improve their toughness [1-5].

However, nanoscale γ-alumina (γ-Al$_2$O$_3$) powder is difficult to obtain, because of two reason; First, γ-Al$_2$O$_3$ is an a stable phase after calcining at high temperature, which easily prompt the grain growth of powder, and make it difficult to get nanoscale particles, secondly, γ-Al$_2$O$_3$ particles tend to aggregate during dehydration process in wet chemistry method. Therefore, it is necessary to develop new methods to overcome this problem [6].

The sol-gel method, in particular, is one of the most useful and attractive method for the synthesis of nanosized materials because of its advantages such as; good stoichiometric control and production of ultrafine powder with narrow size distribution in

a relatively short processing time at a very low temperature [7]. Metal oxides powders with nanostructure particles have been synthesized by various methods [8-12].

There are many methods for fabrication of particulate reinforced metal matrix composites (MMCs) such as powder metallurgy [11], squeeze casting [13, 14], compocasting [15-18]. For the metal matrix composites, molten metal mixing is a cost effective method while powder metallurgy is costly, and squeeze casting provide good in filtration quality of chopped performs [19, 20].

In this research, the synthesis of $\gamma$-$Al_2O_3$ nanostructure was studied by combination of sol-gel auto-combustion and ultrasonic methods using aluminum nitrate and glycine as a precursors. Moreover, $\gamma$-$Al_2O_3$ nanopowders were incorporated into the molten A356 aluminum alloy via stir casting method at various conditions.

## 2. Experimental

Aluminum nitrate ($Al(NO_3)_3.9H_2O$), glycine, $NH_4OH$ and Al powder were obtained from Merck with analytical grade. All materials were used without further purification. Deionized water was used for all experiments. Aluminum (A356) was obtained from Kian Alloy Company (Kashan-Iran) as metal matrix of composites. The chemical analysis of Al alloy is given in Table 1.

Table 1. Chemical analysis of Al (A356)

| Element | Al | Si | Mg | Fe | Cu | Ni | Zn | Mn | Ti |
|---|---|---|---|---|---|---|---|---|---|
| Mass Percent | 91.73 | 7.23 | 0.38 | 0.32 | 0.18 | 0.05 | 0.05 | 0.02 | 0.01 |

Nanoparticles of $Al_2O_3$ were prepared by combination of sol-gel auto-combustion and ultrasonic methods. Appropriate amounts of analytical grade $Al(NO_3)_3.9H_2O$ and glycine were taken and a small amount of ammonium hydroxide was added carefully to the solution to change the pH value to 7. The mole ratio of nitrate to glycine is equal 1:3. During this procedure, the solution was continuously stirred for 8h and kept at 60°C. The resultant gel is poured in a platinum crucible and heated at about 400°C. Schematic flow chart of sol-gel processing that was applied in this study is shown in Fig. 1.

In this research, the reinforcement phases used to improve strength of A356 aluminum alloy matrix were nano $\gamma$-$Al_2O_3$ as ceramic reinforcing particles. Therefore, cast alloy (A356 Al) was selected. The $\gamma$-alumina powders were mixed homogeneously with 0.75 and 1.5 vol.% and Al powder at room temperature. Then, the mixture was

placed in stainless steel mold and 20 MPa of pressure was used to form the $Al_2O_3$ performs.
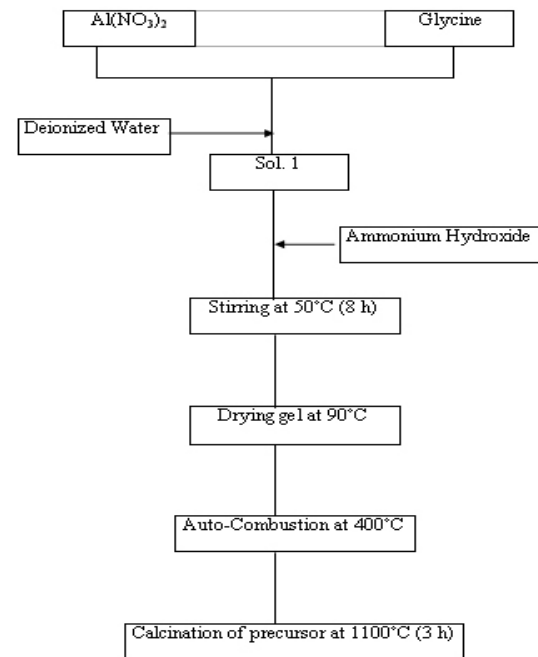


Fig. 1. Flow chart of sol-gel processing.

For casting Al-$Al_2O_3$ composite, a resistance furnace equipped with a stirring system was used. After smelting the aluminum ingots, an amount given of keryolite was added to the molten Al alloy and the stirring was established for a few minutes. $Al_2O_3$ nanopowders with 0.75 and 1.5 vol.% were wrapped into the aluminum foils and added to the melt Al alloy to produce Al-$Al_2O_3$ composite. The processing temperatures have been chosen at 850°C. Stirring was continued for another 10 minutes for homogenous dispersion and to prevent agglomeration of particulates. A metallic mold is used for casting. Finally, specimens fabricated in six various conditions were prepared for subsequent microstructural and mechanical analyses. The morphology of the γ-$Al_2O_3$ nanopowders and Al-$Al_2O_3$ composites were analyzed by scanning electron microscopy (SEM, Oxford CAMSCAN-MV2300), X-ray diffractometer (Model: XPERT-MPD, Phylips) using Cu $K_\alpha$ radiation (λ=1.05406Å) with operated at 40 kV and current of 40 mA and specimens were polished and etched using Keller solution.

The bulk density of samples was determined by the Archimedes method. Theoretical density was estimated by using mixture law. Hardness test were made with a load of 306.56 N and a punch diameter of 2.5 mm. Data of hardness were calculated using at

least ten indentations on two polished specimens. The compressive strength test was conducted in air at room temperature (Instron Universal Testing Machine-1195 machine) according to ASTM-B557.

## 3. Result and Discussion

### 3.1. XRD and Nanostructural Analyses

The XRD pattern of the $Al_2O_3$ nanoparticles is shown in Fig. 2.
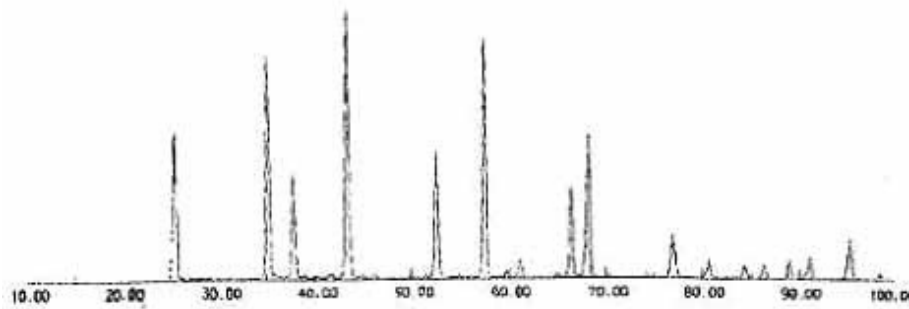


Fig. 2. The XRD pattern of the γ- $Al_2O_3$ nanoparticle.

The particle size of the samples has been determined from XRD peak, employing Scherrer's equation (1):

$$D = \frac{k\lambda}{\beta cos\theta} \quad (1)$$

Where $D$ is the crystallite size, $\theta$ is the Bragg angle, $\lambda$ is the wavelength of X-ray radiation (Cu $K_\alpha$) and $\beta$ is the full width at half maximum (FWHM) of the most intense diffraction peak. The results of XRD show the formation of single phase of γ-$Al_2O_3$ nanostructure. The grain size of the prepared γ-$Al_2O_3$ is found to be 31nm. The morphology of alumina was investigated with using SEM. The SEM image of γ-$Al_2O_3$ nanoparticles is shown in Fig. 3.

The morphology of the Al-γ-$Al_2O_3$ is shown in Fig. 4. The black matrix is aluminum; the white spots represent γ-$Al_2O_3$ nanoparticles and the grey area is silicon-rich interdendritic Al-Si eutectic. The phases are considered by arrow on SEM images. It should be noted that γ-$Al_2O_3$ nanoparticles were well dispersed in the aluminum matrix and just a partial agglomeration in composites with 0.75 and 1.5 vol.% of γ-$Al_2O_3$ can be considered in Fig. 4.

Fig. 3. SEM image of γ-Al$_2$O$_3$ nanoparticles.



Fig. 4. SEM images of Al-Al$_2$O$_3$ composite specimens with 1.5 vol.% Al$_2$O$_3$ at 850˚C and different magnifications: a) 500 x, b) 2.00 kx and c) 20.00 kx.

Similar nanostructure were observed for 0.75 vol.% Al$_2$O$_3$ composite. All results from XRD and SEM analyses confirm feasibility of stir casting method to produce this kind of composites with well distribution of reinforcement.

## 3.2. Density Measurements

The effects of volume percent of $\gamma$-Al$_2$O$_3$ nanoparticles on density of Al-Al$_2$O$_3$ composites produced by stir casting method is given in Table 2.

Table 2. The comparison experimental and theoretical densities of Al-Al$_2$O$_3$ composites containing 0.75 and 1.5 vol.% $\gamma$- Al$_2$O$_3$.

| Volume percent of $\gamma$-Al$_2$O$_3$ | Experimental Density (g.cm$^{-3}$) | Theoretical Density (g.cm$^{-3}$) |
|---|---|---|
| 0.75 | 2.65 | 2.66 |
| 1.5 | 2.65 | 2.68 |

According to the mixture law, by increasing the volume fraction of Al$_2$O$_3$ particle in aluminum, density of sampler should be increased, because the density of Al$_2$O$_3$ is more than aluminum. It should be noted that temperature plays an important effect to increase the wettability of particles.

## 3.3. Mechanical Properties

## 3.3.1. Hardness Test

The effects of the volume percent of $\gamma$-Al$_2$O$_3$ nanoparticles on hardness properties of the prepared composites with 0.75 and 1.5 vol.% is determined 58 and 64 BHN at 850˚C, respectively.

It is considered that hardness of Al$_2$O$_3$-reinforced composite is more than that of unreinforced alloy. It can be attributed to the higher hardness of ceramic particles compared to aluminum matrix alloy. Also, increasing the volume fraction of $\gamma$-Al$_2$O$_3$ nanoparticle at 850˚C is increased hardness values because of the number and total surface area of Al$_2$O$_3$ particles increase with increasing Al$_2$O$_3$ particle volume fraction [21, 22].

## 3.3.2. Compression Test

The effects of the volume percent of $\gamma$-Al$_2$O$_3$ nanopowder on the compression strength of Al-Al$_2$O$_3$ composites were determined with 0, 0.75 and 1.5 vol.% Al$_2$O$_3$ 700, 819 and 875 MPa at 850˚C, respectively. As demonstrated, with increasing the volume percent of reinforcing particles, the value of the compressive strength compared with unreinforced matrix alloy is increased at 850˚C.

The initial enhancement seems to be due to work-hardening behavior. This could be related to effects of elastic properties of ceramic particles and inhibition response of plastic deformation of matrix by them; ceramic particles can only deform elastically while aluminum matrix can deform plastically. So if the boundary is assumed to be strong, ceramic particles prevent plastic deformation of the matrix and this leads to higher work-hardening rate [22].

## 4. Conclusions

Nanocrystalline $\gamma$-$Al_2O_3$ powders were successfully synthesized by a combination of sol-gel auto combustion process and ultrasonic irradiation method. The well $\gamma$-$Al_2O_3$ nanopowder was prepared when pH=7. The particles have been calcined at 1100˚C for 3h. Then the product was placed in ultrasonic bath of n-propanol at room temperature for 15 minutes. The grain sizes of the nanopowder are found to be about 31 nm. The SEM results showed that grains were regular sphere-shaped nanoparticles. The XRD data shows $Al_2O_3$ nanoparticle have $\gamma$ structure.

A356 Aluminum reinforced with $\gamma$-$Al_2O_3$ nanocomposites was successfully fabricated via stir casting method. Reinforced particles were well distributed in the matrix of composites. However, partial agglomeration was observed in composites with increasing of $Al_2O_3$ content.

Mechanical properties such as hardness and compressive strength improved. Also, composite containing 1.5 vol.% $\gamma$-$Al_2O_3$ fabricated at 850˚C showed improved hardness and compressive strength of the alloy by 42 and 25%, respectively, in comparison with other specimens. Therefore, it can be concluded that composite with 1.5 vol.% $Al_2O_3$ content, cast at 850˚C, represent maximum mechanical properties and it can be considered at the optimum fabrication conditions.

## References

1.      Toy C., Scott W. D. J. Am. Ceram. Soc., 1990; 73: [1], 97-101.
2.      Flinn B. D., Ruhle M. et al. Acta Metall., 1989; 37: [11], 3001-3006.
3.      Halverson D. C., Pyzik A. J. et al. J. Am. Ceram. Soc., 1988; 72: [5], 775-780.
4.      Sigl L. S., Fischmeister H. F.. Acta Metall., 1988; 36: [4], 887-897.
5.      Shaw L., Abbaschian R. J. Mater. Sci., 1995; 30: 849-854.
6.      Jiang L., Yubai P. et al. Ceram. Inter., 2005; 32: 587-561.

7.      Srivastava M., Chaubey S. et al. Mater. Chem. Phy., 2009; 118: [1], 174-180.

8.      McCormick P. G., Tisuzuki T. et al. Advanced Mat., 2001; 13: 1008-1112.

9.      Gole J. L., Prokes S. M. et al. Advanced Mat., 2006; 18: 644-649.

10.     Kumari L., Du G. H. et al. Ceram. Inter., 2009; 35: 2401-2408.

11.     Pradeep A., Priyadharsini P. et al. J. Mat. Chem. Phy., 2008; 112: 572-576.

12.     Zamzam M., Ros D. et al. J. Key Eng. Mat., 1993; 79-80: 235-246.

13.     Mortensen A., Michaud V. J. et al.  J. Met., 1993; 45: [1], 36-43.

14.     Cooke P. S., Werner P. S. J. Mat. Sci. Eng., 1991; 44: [A], 189-193.

15.     Chong Y., Atkins H. V. et al. J. Mat. Sci. Eng., 1993; 173: [A], 232-237.

16.     Fukunaga H., Goda K. Bull. Jap. Soc. Mech. Eng., 1984; 27: [228], 1245-1250.

17.     Bardal A. J. Mat. Sci. Eng., 1992; 159: [A], 119-123.

18.     Lyod D. J. J. Inter. Mat. Rev., 1994; 39: [1], 1-23.

19.     Mansur L. J., Mortensen A. et al. J. Metal. Trans., 1998; 20: [A], 2547- 2553.

20.     Zhang Z., Long S.  et al. J. Comp. 1994; 25: [5], 380-392.

21.     Das S., Das S. et al. Comp. Sci. Technol., 2007; 67: 746-751.

22.     Zhang Q., Zhang H. et al. J. Mater. Letters, 2004; 58: 3545-3550.

# OPEN-CELL METAL-SIC COMPOSITE FOAMS MADE BY ELECTROLYTIC CO-DEPOSITION ON POLYURETHANE SUBSTRATES

**Mikutski V.[1], <u>Smorygo O.[1]</u>, Shchurevich D.[1], Marukovich A.[1], Ilyushchanka A.[1], Gokhale A.[2], Nadella R. [2], Sadykov V.[3], Usoltsev V.[3]**

[1] *Powder Metallurgy Institute, Minsk, Belarus*
[2] *Defense Metallurgical Research Laboratory, Hyderabad, India*
[3] *Boreskov Institute of Catalysis, Novosibirsk, Russia*
*e-mail: olegsmorygo@yahoo.com*

## Abstract

In this research, open cell Ni-SiC and Cu-SiC composite foams were manufactured by electrolytic co-deposition on the polyurethane foam substrates using conventional metal plating electrolytes with the suspended SiC nano-particles. The method ensured manufacturing the MMC open-cell foams; content of SiC inclusions in the metal matrix of up to 10 wt.% could be controlled by the SiC powder concentration in the electrolytes. Effects of the foam pore size (surface area) and the electrolyte composition on the content of SiC inclusions and the density gradient across the foam were studied.

**Keywords:** *open cell foam; electrolytic replication; MMC structure; co-deposition; silicon carbide*

## 1.Introduction

Open cell metal foams are permeable materials with a stiff 3D cellular structure that ensures extremely high porosity (80-98%), low density (up to 0.2 g/cm$^3$), high surface-to-volume ratio, high hydraulic permeability, etc. [1]. At present, open cell metal foams are used in many applications as the light-weight structural components, catalyst supports, battery electrodes, components of heat exchangers, mechanical energy absorbers and so on [2-4]. The most regular open-cell structure with the highest possible porosity of up to 97-98% can be attained via the replication of reticulated polyurethane foams (PUF) [2], and the electrolytic replication looks the most viable technology for practical implementation.

In general, the PUF electrolytic replication process comprises the following steps [5]: PUF substrate preparation (cutting to the required shape and etching); electrolysis deposition of a thin sub-layer to ensure electric conductivity; electrolytic metal deposition until the required foam density (electroplating); heat treatment in a protective atmosphere to burn away the PUF and sinter the metal. A limited range of metals can be deposited to the PUF substrate due to the electrolytic process limitations, and this is the significant drawback of this technology [6]. Cu and Ni foams are typical products manufactured by this method. In order to enhance the foam properties (e.g. corrosive or mechanical

properties), special treatments resulting in the foam alloying or formation of protective coatings are required [7, 8]. Modification of the metal foam microstructure by ceramic nano-inclusions looks an attractive approach to modify the material properties (structural stiffness, thermal expansion, surface morphology and so on). The approach could be advantageous since it does not require additional technological steps and could be realized via the simultaneous deposition of the matrix metal and ceramic inclusions.

Co-deposition is a well-known method to form the metal-matrix composite (MMC) coatings with the enhanced combinations of properties, such as hardness, wear resistance or corrosive resistance [9-11]. In such processes, ceramic particles are suspended in electrolytes and, during electrolytic deposition, can be incorporated into the growing metal matrix layer. The particulate mechanical entrapment, adsorption or electrophoresis can be the co-deposition driving forces [9]. The process is well studied and extensively applied to modify plain surfaces. In the case of porous volumetric substrates, the electrolytic process is attenuated towards the electrode depth due to the ohmic, polarization and concentration losses across the sample [6, 12], and introducing ceramic particles to the electrolytes can affect transversal gradients of the foam density and composition. Besides, since the open-cell foams are excellent materials for the particulate deep-bed filtration, delivery of the ceramic particles to the internal substrate surfaces can be hampered due to the screening effect, which can result in the more pronounced gradients.

In this research, we studied the electrolytic PUF replication processes to manufacture Ni-SiC and Cu-SiC composite open-cell foams using conventional electrolytes with the suspended nano-size silicon carbide particles.

## 2. Experimental procedures

### 2.1. Materials and procedures

PUFs of three pore size grades (10, 20 and 30 ppi) were used in this study. The PUFs were cut into thin slices with linear dimensions of 100x100x(4.5-5.0) mm, and experimental substrate samples with the thickness of about 24 mm were prepared by assembling the thin slices (five slices per one sample). This was done to study the density and composition gradients across final foams. The PUF substrates were etched in the 20% NaOH water solution prior the replication.

Electrolysis metal plating of the PUF substrates was performed using conventional processes applied in industry. Compositions of the solutions as well as the process regimes are extensively described in the reference literature, e.g. in Ref. [13-16]; water based solutions were used in all cases. Briefly, the following processes were performed. The PUF surface was sensitized in the tin chloride solution and then activated in the palladium chloride solution. Micron-scale electric conductive layers were deposited by the electrolysis deposition due to the metal ions chemical reduction on the activated PUF surface. For Cu-SiC foams, the layer was deposited using the solution based on tartaric acid with copper sulphate as the source of copper and formalin as the reducing agent. For Ni-SiC foams, the layer was deposited using the solution based on acetic acid with nickel chloride as the source of nickel and sodium hypophosphite as the reducing agent. Finally, electrolytic deposition of composite MMC coatings was performed. $CuSO_4$-$K_4P_2O_7$ based electrolyte was used for the Cu-SiC foam preparation (pH=5.5) and $NiSO_4$-$NiCl_2$ electrolyte was used for the Ni-SiC foam preparation (pH=8.5).

The electrolytic deposition was performed in a tank located in an ultrasonic bath with the operating frequency of 34 kHz. Additionally, mechanical stirrer with the rotation rate of 500–600 rpm was used to intensify the delivery of the ceramic particulate to the porous substrate internal surfaces. Conductive porous substrate (cathode) was located between two anodes (nickel or copper); the distance between anode and porous cathode was 100 mm. SiC nanopowder with the specific surface of 35 $m^2$/g was introduced to the electrolytes in the amount of 5, 10, 20 and 40 g/l. The SiC powder was received from NEOMAT Co, Latvia. In the as-received powder, loose agglomerates with dimensions of 1-10 µm consisted of nanoscale particles (30-100 nm). Co-deposition process was carried out at the overall current density of 1 A/$dm^2$ in all cases until the foam average density of 0.2–0.22 g/$cm^3$ had been attained

After the electrolytic deposition was completed, the samples were separated to original thin slices to study the density and composition gradients across the foams. Final heat treatment comprised the PUF thermal decomposition in air at 350$^o$C during 4 hours and sintering in the cracked ammonia atmosphere at 1000$^o$C during 1 hour.

## 2.2. Characterization of foams

The density was calculated by weighing the samples and measuring their linear dimensions. The elemental composition was studied by the energy dispersive X-ray

fluorescent analysis (EDXRF), Oxford ED2000. Ni, Cu and Si concentrations were detected and normalized to 100%. Then, SiC content was calculated (a mol of Si per a mol of C), and the detected composition of the metal-ceramic composite was corrected taking into account molar relationships. The analysis was performed in 6 areas of each experimental sample slice, and the results of the measurements were averaged. The images of the composite coatings were obtained with the scanning electron microscope Mira Tescan. Compressive strength of the foams was studied using Instron 1195 testing machine.

Density gradients across the foams were characterized by the density non-uniformity factor $k_\rho$ that was defined as the ratio of the minimum slice density $\rho_{min}$ within the sample to the average sample density $\overline{\rho}$:

$$k_\rho = \rho_{min} / \overline{\rho} \qquad (1)$$

The SiC content gradients across the metal foams were characterized by the SiC content non-uniformity factor $k_{SiC}$ that was defined as the ratio of the maximum silicon carbide concentration $[SiC_{max}]$ (wt.%) in a sample's slice to the average silicon carbide concentration within the sample $[\overline{SiC}]$:

$$k_{SiC} = [SiC_{max}] / [\overline{SiC}] \qquad (2)$$

The foam internal specific surface area $S_V$ was estimated using the inverted spherical model [17]:

$$S_V = \frac{1}{0,023 \cdot D_c \left( \dfrac{\varepsilon_o}{1-\varepsilon_o} + 7 \right)} \qquad (3)$$

where $\varepsilon_o$ is the foam open porosity and $D_c$ is its average cell diameter.

## 3.Experimental results

### 3.1.Ni-SiC foams

Ni-SiC foam strut surface is demonstrated in the SEM image inserted to the graph in Fig.1. SiC inclusions were distributed rather homogeneously within the nickel matrix and incorporated into the metal grains, which resulted in the spherical-shape formations on the surface. Such surface morphology was typical for all the studied SiC concentrations in the nickel plating electrolyte.
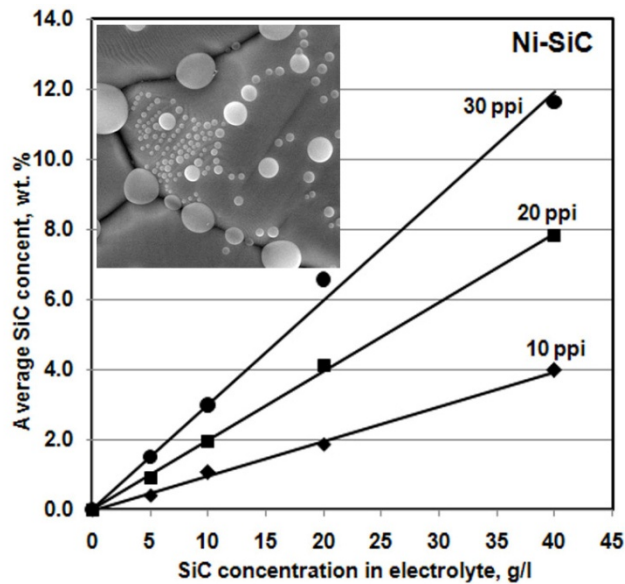


Fig. 1.Average SiC content in Ni-SiC foams vs. SiC nano-powder concentration in the electrolyte at different pore size grades.

Dependencies of the SiC content in the nickel-based MMC foams vs. SiC nano-powder concentration in the electrolyte at different pore size grades are presented in Fig.1. Average SiC content in the composite increased linearly with the increase of the SiC powder concentration in the electrolyte as well as with the increase of the cell density (i.e. with the increase of the foam specific surface). Linear interpolation of the experimental data resulted in the equation (4) with the reliability level of >0.99 for all the pore size grades studied:

$$[\overline{SiC}] = a \cdot S_V \cdot C_{SiC} \tag{4}$$

where $[\overline{SiC}]$ is the average SiC content in the MMC, wt.%; $S_V$ is the calculated specific surface of the foam-structure substrate [16], 1/m; $C_{SiC}$ is concentration of SiC powder in the electrolyte, kg/m$^3$; $a$ is an empiric coefficient equal to 2.2–2.6 for Ni-SiC foams.

Linear character of the $[\overline{SiC}] = f(S_V, C_{SiC})$ dependence means that the probability of collisions between the substrate surface and the suspended particles defines the final foam composition, and the adhesion/entrapment mechanism [9] is definitive in the MMC coating formation process. Maximum average SiC content in the nickel matrix attained in this study was more than 12 wt. % for foams with the cell size of 30 ppi.

Both density and composition transversal gradients were stated in all Ni-SiC foam samples. As it was expected [6], the foam density decreased towards the foam interior, and the more pronounced gradients corresponded to the foams with finer pores (Fig. 2). Content of SiC inclusions in the nickel matrix, on the contrary, increased towards the foam interior. Experimental curves demonstrating the SiC content change across the samples (Fig. 3) look as regular reflections of $\rho=f(z)$ curves (Fig. 2). Curves in Fig. 3 correspond to 10 ppi foams but are characteristic for all the cell size grades.
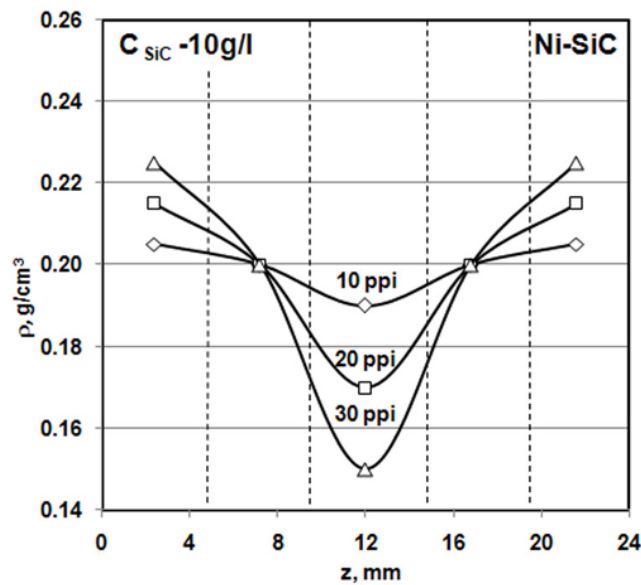


Fig. 2. Density distribution across Ni-SiC foams for different pore size grades. Concentration of SiC nano-powder in electrolyte – 10 g/l.

In general, the density gradient was stated to be strongly dependent on the foam cell size and not sensitive to the concentration of SiC nano-particles in the electrolytes within all the studied ranges. The density non-uniformity factor $k_\rho$ value (Eq. 2) for the

foam cell densities of 10, 20 and 30 ppi was stated to be equal to 0.95-0.97, 0.85-0.87 and 0.75-0.78,respectively.

As for the SiC content non-uniformity factor $k_{SiC}$ (Eq. 3), it was also dependent on the foam cell size: it's value for the foam cell densities of 10, 20 and 30 ppi was found to be equal to 1.15-1.20, 1.20-1.25 and 1.30-1.35, respectively. No reliable effect of the electrolyte composition was stated. Thus, a pronounced porous substrate screening effect that is evident for metal ion electrolytic deposition was not observed for the studied deposition regimes and sample thicknesses. The SiC content gradual increase towards the sample's interior was defined by the density gradual decrease, which, in its turn, was defined by the nickel ion penetration ability into the porous electrode.
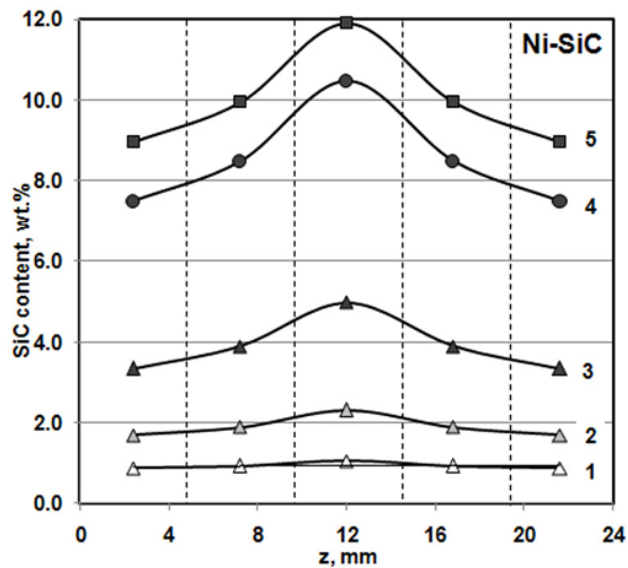


Fig. 3. SiC content distribution across Ni-SiC foams at different pore size grades and different concentrations of SiC nano-powders in electrolyte: 1 - 10 ppi, 10 g/l; 2 – 10 ppi, 20 g/l; 3 – 10 ppi, 40 g/l; 4 – 20 ppi; 40 g/l; 5 – 30 ppi, 40 g/l.

Mechanical strength of the foams was strongly dependent on the density gradients across the samples. Ni-SiC foams with the average density $\overline{\rho}$ =0.21 g/cm$^3$ and the density non-uniformity factor $k\rho$=0.95 had the compressive yield stress $\sigma_y$=0.65-0.70 MPa. For the foams with similar density and $k_\rho$ = 0.75-0.78, compressive yield stress was 0.30-0.35 MPa.

*3.2.Cu-SiC foams*

Cu-SiC foam strut surface is demonstrated in the SEM image inserted to the graph in Fig. 4. Nano-scale SiC inclusions were distributed rather homogeneously within the copper matrix and located predominately along the grain boundaries of the growing crystals, which was typical for all SiC concentrations in the electrolyte.

Dependencies of SiC content in the copper-based MMC foams vs. SiC nano-powder concentration in the electrolyte at different pore size grades are presented in Fig. 4. Similarly to the previous case, average SiC content in the composite was stated to increase linearly with the increase of the SiC powder concentration in the electrolyte and with the decrease of the foam cell diameter. Linear interpolation of the experimental data resulted in the equation (4) with the reliability level of 0.96-0.99. The empiric coefficient *a* value was stated to be equal to 1.5-1.7. Maximum average SiC content in the copper matrix attained in this study was ~ 7 wt. % for 30 ppi foam.
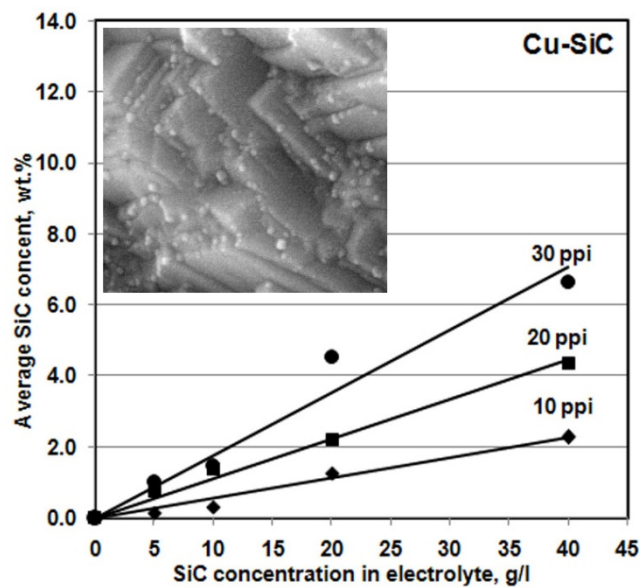


Fig. 4. Average SiC content in Cu-SiC foams vs. SiC nano-powder concentration in the electrolyte at different pore size grades.
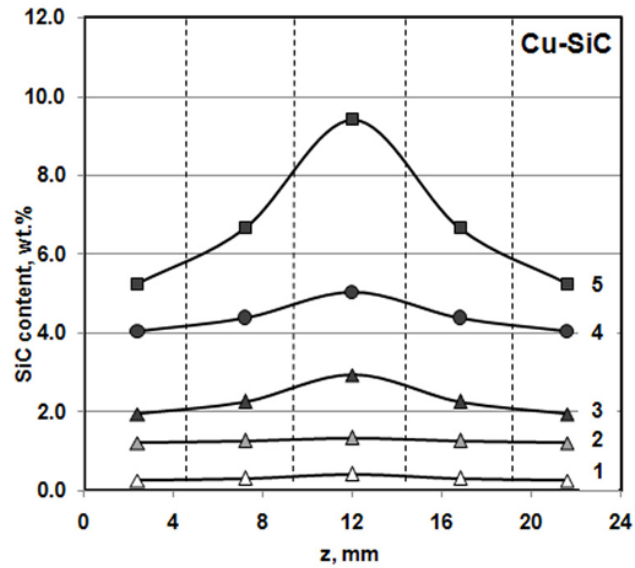
Fig. 5. SiC content distribution across Cu-SiC foams at different pore size grades and different concentrations of SiC nano-powders in electrolyte: 1 - 10 ppi, 10 g/l; 2 – 10 ppi, 20 g/l; 3 – 10 ppi, 40 g/l; 4 – 20 ppi; 40 g/l; 5 – 30 ppi, 40 g/l.

General character of $\rho=f(z)$ and $[SiC]=f(z)$ curves was similar to the previous case as well. Density of the Cu-SiC foams decreased towards the interior, and more pronounced gradients corresponded to the foams with finer pores; the density non-uniformity factor $k_\rho$ values were very close to the same in the Ni-SiC foams: 0.73-0.76, 0.85-0.88 and 0.95-0.96 for 10, 20 and 30 ppi cell size grades, respectively. SiC content in the copper matrix increased towards the porous substrate interior as given in experimental curves in Fig. 5; the curves were also the regular reflections of $\rho=f(z)$ curves (Fig. 2).

The SiC content non-uniformity factor $k_{SiC}$ value was sensitive to the foam cell size: it's value in this experiment was equal to 1.10-1.15, 1.30-1.35 and 1.40-1.50 for the foam cell densities of 10, 20 and 30 ppi, respectively. No reliable dependence of $k_{SiC}$ value on SiC concentration in the electrolyte was stated, which indicated the absence of a pronounced screening effect in the porous substrate.

The increase of the density non-uniformity across the Cu-SiC foam samples was accompanied by the remarkable decrease of their compressive yield stresses. The compressive yield stress decreased from 0.60-0.70 MPa to 0.28-0.33 MPa with the decrease of the density non-uniformity factor $k_\rho$ from 0.96 to 0.75-0.77.

## 4.Conclusions

Open-cell Cu-SiC and Ni-SiC foams with the MMC microstructure were produced by electrolytic co-deposition using conventional water-based electrolytes with the suspended SiC nano-particles. Linear increase of the SiC content in both nickel and copper matrixes with the foam-structure substrate specific surface and SiC powder concentration in the electrolytes was found. SiC content in the MMC structure was only dependent on the probability of collisions between the substrate surface and SiC particles suspended in the electrolytes. Experimental equation to control SiC content in the MMC foams was defined, and empirical coefficients were stated. Within the studied ranges and co-deposition regimes, SiC powder concentration in the electrolytes did not affect either density or composition gradients, but the pronounced effect of the foam cell size was stated. The process allowed manufacturing the MMC foams with the rather homogeneously distributed ceramic nano-inclusions incorporated into the metal matrix.

## References

1.      Ashby M.F. The properties of foams and lattices. Phil Transactions R Soc A 2006;364:15–30.

2.      Banhart J. Manufacture, characterisation and application of cellular metals and metal foams, Prog Mater Sci 2001;46:559–632.

3.      Giani L, Groppi G, Tronconi E. Mass-transfer characterization of metallic foams as supports for structured catalysts. Ind Eng Chem Res 2005;44:4993-5002.

4.      Lu T.J, Hess A, Ashby M.F. Sound absorption in metallic foams, J Appl Phys 1999;85:7528-7539.

5.      Leonov A.N, Smorygo O.L, Sheleg V.K.. Monolithic Catalyst Supports with Foam Structure. React Kinet Catal Lett 1997;60:259-267.

6. Leonov A, Romashko A. Quality control of foam metals produced electrochemically. In: Banhart J, Fleck N, editors. Cellular Metals: Manufacture, Properties, Applications. Berlin: Verlag MIT Publishing; 2003, p 158–161.

7. Smorygo O et al. Nickel foams with oxidation-resistant coatings formed by combustion synthesis. Scripta Mater 2008;58:910–913.

8. Smorygo O et al. Structured catalyst supports and catalysts for the methane indirect internal steam reforming in the intermediate temperature SOFC. Int J Hydrogen Energy 2009;4: 9505-9514.

9. Gomes A et al. Electrodeposition of metal matrix nanocomposites: improvement of the chemical characterization techniques. In: Reddy B, editor. Advances in Nanocomposites - Synthesis, Characterization and Industrial Applications. Rijeka: InTech; 2011. p 503–526.

10. Lee H.K, Lee H.Y, Jeon J.M. Codeposition of micro- and nano-sized SiC particles in the nickel matrix composite coatings obtained by electroplating. Surf Coat Technol 2007;201:4711–4717.

11. Zhu J et al. Study on composite electroforming of Cu/SiCp composites. Mater Lett 2004;58: 1634–1637.

12. Brown L.J, Sotiropoulos S. Electroplating and electroless plating of Ni through/onto porous a polymer in a flow cell, J Appl Electrochem 2001;31:1203-1212.

13. Galvanic coatings in Mechanical Engineering: Handbook. Shluger M.A, editor. Moscow: Mashinostrojenie; 1985 (in Russian).

14. Shalkauskas M, Vashkjalis A. Chemical metallization of plastics. Leningrad: Chemistry Publishing; 1985 (in Russian).

15. Electrodeposition of metallic coatings: Handbook. Belen'kij M.A, Ivanov A.F., editors. Moscow: Metallurgija; 1985 (in Russian).

16. Belen'kijj M. A., Ivanov A.F. Handbook of electrodeposition of metallic coatings (in Russian). — Moscow: Metallurgija, 1985 (in Russian).

17. Smorygo O et al. An inverted spherical model of open-cell foam structure. Acta Mater 2011;59:2669–2678.

# FABRICATION OF ALUMINA – COPPER COMPOSITE BY USING OF CERAMIC PREFORM

**Jach Katarzyna [1], Pietrzak Katarzyna [1,2], Wajler Anna [1], Strojny-Nedza Agata [1]**

[1] *Institute of Electronic Materials Technology, 133 Wolczynska Str., 01-919 Warsaw, Poland*
[2] *Institute of Fundamental Technological Research, Polish Academy of Science,*
*5B Pawinski Str., 02-106 Warsaw, Poland*

*e-mail: katarzyna.jach@itme.edu.pl*

## Abstract

In this work, alumina preforms with 85% and 90% open porosity were produced by the replication method. Obtained preforms were used for $Cu-Al_2O_3$ composites fabrication. The effect of pressure applied during hot-pressing process on the microstructure, mechanical and thermal properties of obtained materials were studied. As it was found, application of higher pressure (10 MPa) during sintering leads to the destruction of the ceramic preforms. It facilitated filling of remaining pores with copper which resulted in obtaining more homogeneous material with better mechanical and thermal properties.

## 1.Introduction

Porous ceramics is a promising material for use in medicine and power, electronic or automotive industry, for building elements such as implants, insulators for spark plugs in engines, brake pads and components for jet engines [1-6]. Addition of plastic metal conducts to obtaining materials with improved fracture toughness compared to a ceramic matrix. In particular, composites with interpenetrating phases have very attractive properties. Both the physical and mechanical properties of this kind of composites are strongly influenced by the properties of its individual components and production techniques [7-11]. Such materials, developed in recent years, are characterized by increased strength, hardness, wear resistance at room temperature and resistance to thermal shock. This paper, presents the results of obtaining this kind of alumina - copper composites. Copper is an excellent material for electrical applications whose efficiency can be enhanced by improving its mechanical properties. Pure copper don't have very well mechanical properties like tensile and yield strength. However, alumina ceramics due to its physical and mechanical properties is an attractive and functional construction material of great importance in the technique. This results from its high mechanical strength, high stability at high temperatures. On account of the future application of this developed material (necessity of high porosity), the ceramic preforms which were used in these investigation were produced following the replication method, which consists on depositing a ceramic slurry on a substrate made of polymeric sponge materials [12-14].

The method permits producing porous ceramic with the highest possible degree of porosity amounting to 99 vol.%. As the final product we obtain a ceramic material with a structure which is a precise copy of the adopted reference structure.

In this study, Cu-$Al_2O_3$ composites have been produced by hot pressing in the atmosphere of flowing argon. Ceramic preform with open porosity of 85% and 90% were used. The main aim of the presented investigation is to study the effect of sintering conditions on the microstructure and mechanical and thermal properties of copper – alumina composites.

## 2. Experimental

The solid phase used for the preparation of the slurry was α-$Al_2O_3$ (A16SG, Almatis) with the following parameters: average grain size – about 0.5μm, specific surface area (measured by BET technique) – 8.9$m^2$/g, and the density (measured by the pycnometric method) – 3.89g/$cm^3$. Duramax D-3005 (Rohm&Haas) in an amount of 0.8wt% with respect to the mass of the solid phase was used as a dispersant of the ceramic slurry. The binders was a dispersion of a polymer based on acrylic acid ester and styrene (50% aqueous solution), Mowilith DM765, Celanese Emulsions GmbH. Ceramic preforms were prepared as described in an earlier publication [15].The $Al_2O_3$ content in the slurry was chosen to be 80.0wt%. In a nutshell, in order to prepare the slurry, appropriate amounts of the ceramic powder, solvent and dispersant were mixed in a Pulverisette planetary mill using a corundum container and corundum balls.  In the next step, the binder was added to the slurry which was mixed again. The studied level of the acrylic-styrene dispersion addition was in the range of 1.0 - 10.0 wt% of the mass of the ceramic powder. The sintering process was divided into two stages: $1^{st}$ included burning the organic substrate, $2^{nd}$ sintering the ceramic material. The burning was conducted at a heating rate of 0.8$^o$C/min to a temperature of 600$^o$C, and then at a rate of 2$^o$C/min to 1100$^o$C. Sintering was realized at a temperature of 1700$^o$C for 60min.

### 2.1. Characterization

The rheological behavior of the slurries was examined using a stress-controlled rheometer (R/S Plus, Brookfield). The microstructure of the ceramic preforms was characterized using a scanning electron microscopy (AURIGA, Zeiss).The relative density and open porosity were determined by measuring the dimensions and mass of the

sintered samples. The bending strength was examined in a ZWICK 1446 strength machine. Laser flash method was applied for thermal properties measurement of obtained $Al_2O_3$-Cu composite materials. The thermal diffusivity was measured within temperature range of 50-600°C by laser flash method (Netzsch LFA 457) in the argon atmosphere.

## 3.Results and discussion

The quality of the ceramic layer deposited on a polymeric substrate strongly depends on the viscosity of the suspension. It is also important to maintain as high solid content as possible. In this work, optimization of the slurries composition made it possible to prepare suspensions with 80 wt.% solid content. Fig. 1 presents the influence binder level (1 to 10 wt.%) on suspensions rheology.
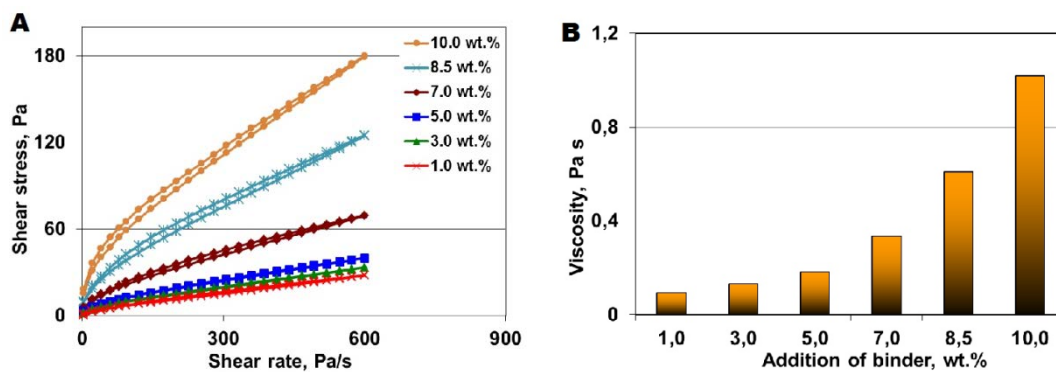


Fig.1. Effect of the binder's content in the ceramic slurries with 80.0wt.% of solid phase on: (A) the flow curves, (B) the dynamic viscosity.

The greatest stability can be observed in the case of suspensions with 1-5 wt.% binder addition (Fig.1A). Obviously, the larger the addition of binder, the greater the viscosity, as shown in Fig. 1b. On this basis, it was determined that the optimum addition of the binder is 5 wt.%.

As can be seen in Fig. 2, porous material with homogeneous microstructure was obtained. The presence of triangular pores (shown in Fig. 2A) is a result of the used preform manufacturing technique. The pores are remains of the decomposed polymeric substrate.

The next step of the technology process was placing of the ceramic preform into a graphite form (Fig. 3) and the addition of copper powder (NewMet Koch, purity 99.5%).

The sintering process ran at 1050 °C for 30 min, at 3 and 10 MPa in a hot-press (ASTRO, Thermal Technology, USA) in the atmosphere of flowing argon.
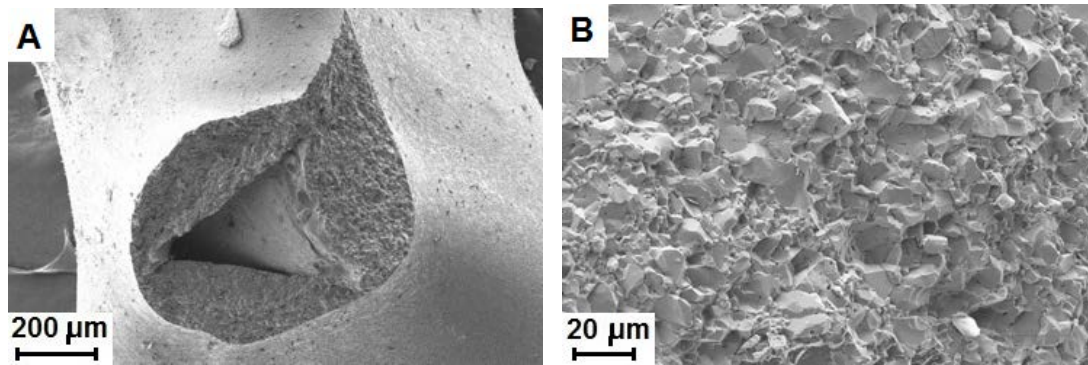


Fig.2. Microstructure of a ceramic preform.
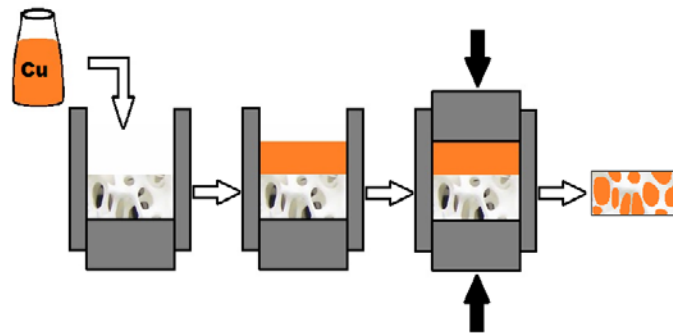


**Fig.3.** Copper-alumina composite manufacturing technology.

As a result of the sintering processes under applied pressure of 3 MPa, alumina-copper composites with 90Cu-10Al$_2$O$_3$ and 85Cu-15Al$_2$O$_3$ compositions by volume have been received. They were subjected to observation under an optical and a scanning electron microscope (Fig. 4). Also the elemental analysis was performed on the samples (Fig. 5). As presented in the Fig. 4, after sintering under 3 MPa pressure, there are pores remained in the ceramic phase after burning of organic substances. However, good connection between ceramics and copper has been created.

The next step, in order to avoid the presence of above mentioned triangular pores in ceramic phase which were not filled with copper, higher pressure (10 MPa) was applied during hot-pressing. The structure and microstructure of the resulting composite are shown in Fig. 6.
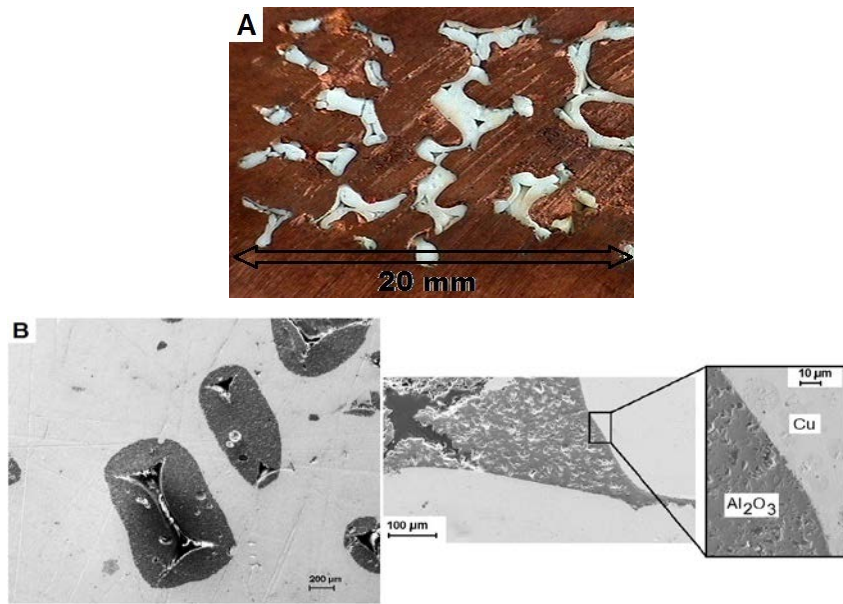
Fig.4. Structure (A) and microstructure (B) of 85Cu – 15Al$_2$O$_3$ composite (3 MPa).
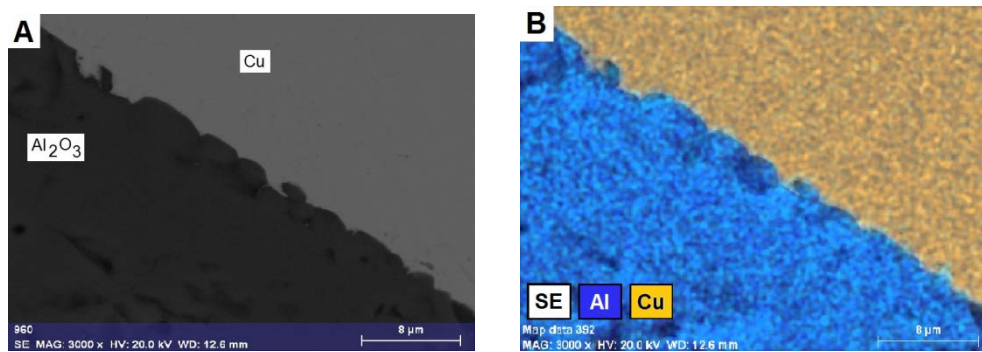


Fig.5. The microstructure (A) and surface distribution of elements (B) on the boundary

85Cu – 15Al$_2$O$_3$ composite (3 MPa).
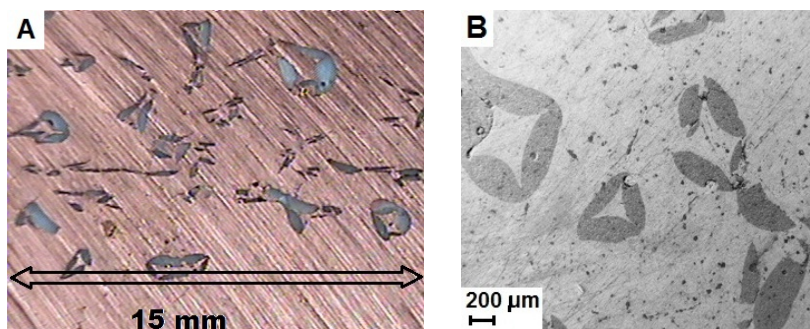


Fig.6. Structure (A) and microstructure (B) of 90Cu – 10Al$_2$O$_3$ composite (10 MPa).

An increase of pressure caused destruction of the ceramic preform, but it still remained suspend in a metallic phase. Consequently, the pores present in the ceramic to a large extent are being filled by the copper, as expected.

Table 1. The physical, mechanical and thermal properties of obtained composites.

| Materials composition (vol.%) | Pressure of sintering, MPa | Density $d$, g·cm$^{-3}$ | Bending strength $\sigma$, MPa | Thermal conductivity (50 $^o$C) $\lambda$, W·m$^{-1}$·K$^{-1}$ | Thermal diffusivity (50 $^o$C) $D$ $(T)$, m$^2$·s$^{-1}$ |
|---|---|---|---|---|---|
| 90Cu -10Al$_2$O$_3$ | 3 | 7.1 ± 1.4 | 47.5 ± 6.0 | 242.3 | 6.8 x 10$^{-5}$ |
| | 10 | 7.3 ± 0.6 | 60.2 ± 11.3 | 288.1 | 8.4 x 10$^{-5}$ |
| 85Cu-15Al$_2$O$_3$ | 3 | 5.6 ± 0.9 | 50.4 ± 5.5 | 188.5 | 5.6 x 10$^{-5}$ |
| | 10 | 6.1 ± 0.4 | 82.5 ± 9.8 | 224.7 | 5.9 x 10$^{-5}$ |

Physical, mechanical and thermal characterization of obtained composites was performed. As shown in Table 1, the composites which contain a higher volume fraction of alumina, irrespective to the pressure applied, have a lower density. of course This is due the fact, that the density of pure alumina(3.89 g·cm$^{-3}$) is significantly lower than the density of copper (8,96 g·cm$^{-3}$). The opposite situation occurs in the case of mechanical strength. Here, increasing the share of ceramic phase causes an increase in strength of composites. This applies to the both of the materials, obtained at 3 MPa and 10 MPa. Furthermore, the composites sintered at a pressure of 10 MPa, are characterized by the greater mechanical strength than the composites sintered at 3 MPa. As a reason of this phenomenon, better compaction of higher pressured hot pressed materials can be assumed. Theoretically, thermal diffusivity and thermal conductivity values should be lower in the material, which contains more of the ceramic phase. If one compared separately composites prepared at a pressure of 3 MPa and 10 MP, this trend can be observed (decrease from 242.3 to 188.5 W·m$^{-1}$·K$^{-1}$ and from 288.1 to 224.7 W·m$^{-1}$·K$^{-1}$, respectively). However, this cannot be told by comparing them with each other. For example, thermal conductivity of 90Cu - 10Al$_2$O$_3$ composite prepared at 3MPa pressure is 242.3 W·m$^{-1}$·K$^{-1}$ and at 10 MPa - 288.1 W·m$^{-1}$·K$^{-1}$. This can be explained by the fact

that in the first case, besides the metal phase and a ceramic phase there are empty spaces in material (Fig. 4), which strongly influence measured diffusivity. In the latter case, the destruction of the ceramic structure resulted in substantial elimination of pores by supplementing them with metal (Fig. 6), which in turn resulted in an increase of the measured thermal conductivity values. Our current work is underway to optimize sintering process for an even better filling the ceramic preform by metal in order to obtain a more homogeneous and porosity free materials.

## 4.Conclusions

In this study, Cu-Al$_2$O$_3$ composites have been successfully produced by hot pressing at 3 MPa and 10 MPa of 85% and 90% porosity alumina preforms filled with copper powder. The main aim of the presented investigation was to study the effect of sintering conditions on the microstructure, mechanical and thermal properties of copper – alumina composites. As it was found, application of higher pressure (10 MPa) during sintering leads to the destruction of the ceramic preform. It facilitated filling of remaining pores with copper. As a result, destruction of the composite preform structure resulted in obtaining more homogeneous material with better mechanical and thermal properties.

## Acknowledgments

## References

1. Young-Wook Moon, Kwan-Ha Shin, Young-Hag Koh, Novel Ceramic/Camphene-Based Co-Extrusion for Highly Aligned Porous Alumina Ceramic Tubes, J. Am. Ceram. Soc. 2012; 95[6]: 1803-1806.
2. M. Montero, T. Molina, M. Szafran, R. Moreno, M.I. Nieto, Alumina porous nanomaterials obtained by colloidal processing using d-fructose as dispersant and porosity promoter, Ceramics International 2012; 38: 2779-2784.

3. C. B. Yoon, S. H. Jun, S. M. Lee, et.al, "Piezoelectric Fibers with Uniform Internal Electrode by Co-Extrusion Process," J. Am. Ceram. Soc. 2006; 89[4]: 1333-6.

4. L. Liu, S. Liu, and X. Tan, Zirconia Microbial Hollow Fibre Bioreactor for Escherichia Coli Culture, Ceram. Int. 2010; 36[7]: 2087-93.

5. Jong-Jin Choi, Sung-Hoon Oh , Ho-Sung Noh, et.al, Low temperature fabrication of nano-structured porous LSM–YSZ composite cathode film by aerosol deposition, Journal of Alloys and Compounds 2011; 509: 2627-2630.

6. Duanyang Li, Meishuan Li, Preparation of porous alumina ceramic with ultra-high porosity and long straight pores by freeze casting, J Porous Mater 2012; 19: 345-349.

7. F. Scherm, R. Völkl, A. Neubrand, F. Bosbach, U. Glatzel, Mechanical characterisation of interpenetrating network metal–ceramic composites, Materials Science and Engineering A 2010; 527: 1260-1265.

8. K. Konopka, M. Szafran, Fabrication of Al2O3–Al composites by infiltration method and their characteristic, Journal of Materials Processing Technology 2006; 175: 266-270.

9. Katarzyna Pietrzak, Katarzyna Jach, Dariusz Kalinski, Marcin Chmielewski, J. Morgiel, Processing and Microstructure of $Al_2O_3$-Cu Composite Material Interpenetrating Network Type, Proceedings of the Euro PM 2011 Congress and Exhibition vol. 2

10. Osayande L. Ighodaro,  Okenwa I. Okoli, Mei Zhang, et.al, Fabrication of Metal/Ceramic-Reinforced Composites, Int. J. Appl. Ceram. Technol. 2012; 9[2]: 421-430.

11. Katarzyna Pietrzak, Katarzyna Jach, Dariusz Kalinski, Marcin Chmielewski, Improving alumina wettability by modification of copper alloys chemical composition,  Proceedings of PM2010 World Congress and Exhibitions, 2010; 2: 361-367.

12. Tae Young Yang, Won Young Kim, Seog Young Yoon, Hong Chae Park, Macroporous silicate ceramics prepared by freeze casting combined with polymer sponge method , Journal of Physics and Chemistry of Solids 2010; 71: 436-439.

13. Fei Chen, Ying Yang, Qiang Shen, Lianmeng Zhang, Macro/micro structure dependence of mechanical strength of low temperature sintered silicon carbide ceramic foams, Ceramics International 2012; 38: 5223-5229.

14. Angela B. Sifontes, Marianis Urbina, Frank Fajardo, Preparation of c-alumina ceramic foams employing hydrophilated polyester polyurethane sponges, J. Mater. Sci. 2009; 44: 4507-4509.

15. Katarzyna Jach, Katarzyna Pietrzak, Dariusz Kalinski, Marcin Chmielewski, Influence of Binder on Porous Ceramic Properties Prepared by Polymeric Sponge Method, Advances in Science and Technology 2010; 65: 164-169.

# PREPARATION OF AL$_2$O$_3$/NI CERMETS COMPOSITES BY AQUEOUS GELCASTING

**Miazga Aleksandra** [1]**, Konopka Katarzyna** [1]**, Gizowska Magdalena** [2]**, Szafran Mikołaj** [2]

*[1]Warsaw University of Technology, Faculty of Materials Engineering, Warsaw, Poland*
*[2]Warsaw University of Technology, Faculty of Chemistry, Warsaw, Poland*
*e-mail: aleksandramiazga86@gmail.com*

## Abstract

The main objective of producing ceramic- metal composites is an improvement of the fracture toughness of the brittle ceramic matrix. Classical methods of powder metallurgy (such as isostatic or uniaxial pressing) are not capable of fabrication complex-shape elements. For this reason colloidal processes are recently willingly applied in manufacturing of ceramic matrix composites.

In the present work Al$_2$O$_3$/3 vol. % Ni composites were prepared by aqueous gelcasting process and sintering in reducing atmosphere. The commercially available monomers 2-hydroxyethyl acrylate and N,N`-methylenebisacrylamide as a cross-linking were used. The activator was N,N,N`,N`,-tetramethylenediamine (TEMED) and the ammonium persulfate was added as an initiator of polymerization process. Composite slurries were obtained from alumina powders (grain size 0.21 µm) and 3 vol% (in respect to total solid volume) of two nickel powders of different grain size (~10 µm and ~0.4 µm). The paper describes the rheological properties of the obtained composite slurries. The properties of green and sintered elements have been also presented. It was found that the presence of nickel particles had a significant influence on slurries polymerization process. The green body and sintered body relative density was in every case higher than 57% and 97% respectively.

## 1.Introduction

Application of alumina ceramics as engineering elements is handicapped by its low fracture toughness. One way to improve this property is addition of metallic phase to a ceramic matrix [1]. The toughness enhancement by the incorporation of ductile phase such as nickel, aluminum or iron has been investigated extensively [2-6]. Widely applied powder metallurgy methods used to manufacture ceramic-metal composites (such as uniaxial, isostatic or hot pressing) has some disadvantages. One of them is difficulty in obtaining complex-shaped parts without expensive machining. Such possibility gives colloidal methods including gelcasting method. Gelcasting combines the conventional moulding method from slips with polymerization reaction. At first it was applied to the preparation of ceramic materials. At present gelcasting is increasingly used to obtain a ceramic-ceramic composites and ceramic metal composites [7]. The biggest problem in complex systems is the selection of ingredients of a suspension to produce flowable, stable slurry and provide, inter alia, deagglomeration of powders. The goal of the present paper is to determine the influence of size of nickel powder on preparation of Al$_2$O$_3$/Ni cermets by gelcasting process.

## 2.Experimental procedure

### 2.1.Materials and process

The materials used for making the $Al_2O_3/Ni$ composites were $\alpha$-$Al_2O_3$ powder (TM-DAR, Taimei Chemicals Co., Ltd, Japan) of density d = 3.8 $g/cm^3$ and particle size $D_{50}$ = 0.21 $\mu$m, and two nickel powders (Sigma Aldrich). First (further marked M)- with an average particle size $D_{50}$ = 10.45 $\mu$m (Figure 1A), second (further marked S)- with $D_{50}$ = 0.42 $\mu$m (Figure 1B). The density of both powders was 8.9 $g/cm^3$.
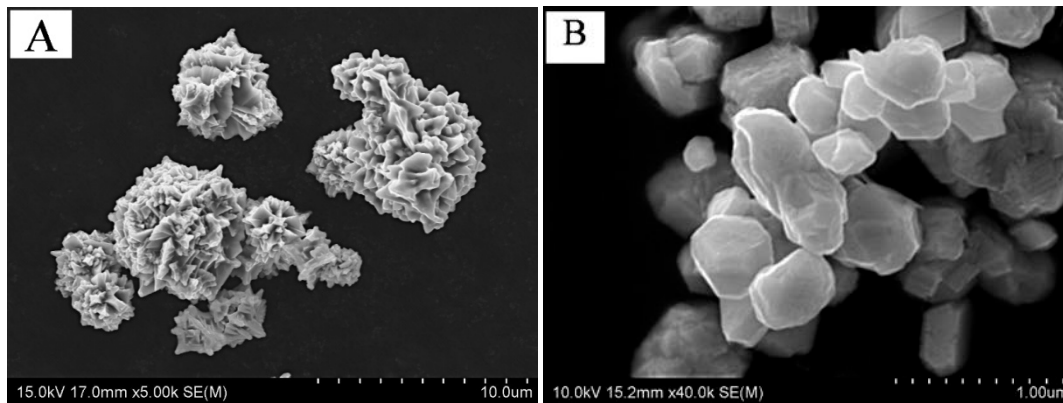


Fig.1. SEM results for two kinds of nickel powders:
1A -  Nickel powder (M) with $D_{50}$ = 10.45 $\mu$m,1B - Nickel powder (S) with $D_{50}$ = 0.42 $\mu$m

The schematic of gelcasting process is described on Figure 2. Water-based slurries (with50 vol%, 52 vol%, 54 vol% solid content) were prepared with 3 vol% of two different nickel powder with respect to total solid volume. The mixture of deflocculants such as diammonium citrate and citrate acid were added. As a monomer 2-hydroxyethyl acrylate, as well as a cross-linking agent N,N'- methylene bisacrylamide were used. The activator was N,N,N,`N`,-tetramethylenediamine, and ammonium persulfate was added as the initiator of polymerization. The ingredients were homogenized in a planetary mill with a rotating speed of 250 r.p.m. for 80 minuts. Afterwards slurry was degassed for 10 min under low pressure in a vacuum desiccator with magnetic stirrer. After addition of initiator and activator of polymerization process, slurry was casted into molds. The specimens were dried for 96 hours at room temperature and then sintered in reducing atmosphere at temperature of 1350°C for 2 hours.
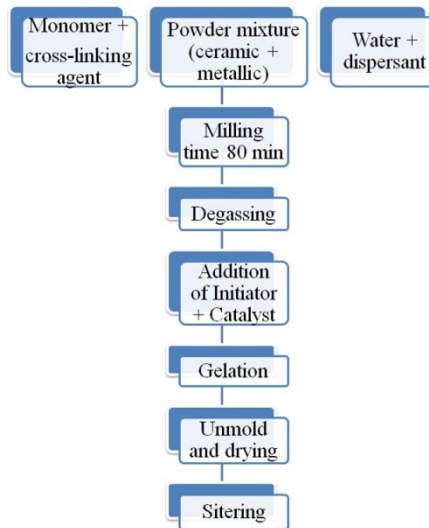
Fig. 2 Schematic of gelcasting process

## 2.2. Characterization techniques

Rheological properties of the alumina and composite slurries were measured by Brookfield DV II Pro. The tests were carried out by increasing and decreasing shear rate. Gelation time, which is the time after which polymerization process in the slurry begins and abrupt increase in viscosity is observed, of the slurry with initiator was measured as a function of time at a constant share rate. The main aim was to select the appropriate amount of the initiator, so that gelation time of the specimen was about 15-60 minutes. In order to investigate the shrinkage of composite green body after drying, the shrinkage rate is defined by:

$$S = \frac{[D_0 - D]}{D} * 100\% \quad (1)$$

where $D_0$ is the diameter of green body before drying; D is the diameter of green body after drying.

The tensile strength of the green body samples was determined by the Brazilian test [8] using Testing Machine TITNUS OLSEN TOROPOL H10KS. The tensile strength was calculated based on the following equation:

$$\sigma_t = \frac{2P}{\pi h D} \quad (2)$$

where $P$ is force, $h$ is height and D is diameter of the obtained sample.

The densities of sintered samples were measured by the Archimedes' method in distilled water.

Morphology of nickel powder and fracture surface of green and sintered bodies was observed by using SEM (Hitachi SU-70).

## 3.Results And discussion

### 3.1.Rheological properties of slurry

The micrometer nickel particles (M) was about 50 times bigger than alumina particles. In case of submicrometer nickel the difference in size was not so big than for micrometer one: metal particles were two times larger than ceramic particles. The larger the particles, the fewer the possible number of particle-particle contact points. The difference in the size of the metal powder particles caused the differences of the composite slurries. Fig. 3A shows that the presence of nickel particles cause a significant increase of viscosity. Nevertheless the viscosity is low enough to fill precisely the mould in all cases. Furthermore, no sedimentation of nickel particles was observed.
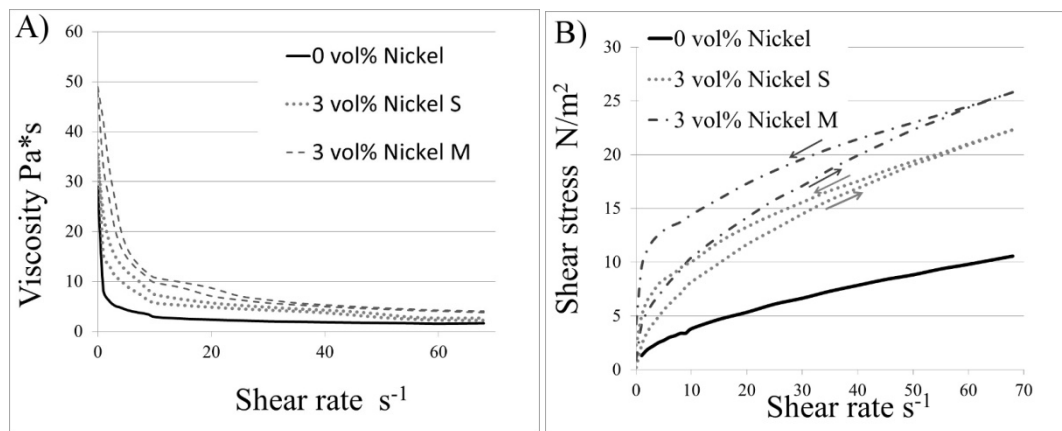


Fig.3.Viscosity and shear stress as a function increasing and decreasing shear rate :
A) - Viscosity as a function increasing and decreasing shear rate of $Al_2O_3$ and $Al_2O_3+$ 3vol% Ni slurries (54 vol% solid loading); B) - Shear stress as a function increasing ($\rightarrow$) and decreasing ($\leftarrow$) shear rate of $Al_2O_3$ and $Al_2O_3+$ 3vol% Ni slurries (54 vol% solid loading)

With the increase in average particle size of nickel powder slip showed a higher viscosity and had a stronger character antithixotropic, demonstrated by increasing the area under the curve of the hysteresis loop flow (Fig. 3B). Antithixotropic effect indicates the

presence of slip structures in the slurry, which are stable at very rapid shear. This properties might result from the occurrence of the interaction between particles of different kinds.

*3.2.Effect of initiator amount*

The advantage of gelcasting method is the ability to control the idle time (time after which the gelation process starts), by selecting appropriate amount of activator and initiator of polymerization. The amount of activator in slurry was constant and fixed at 1.0 wt% based on monomer content. Experiments were carried out for slurries with 54 vol% solid loadings. Fig. 4 shows the results obtain for powder: A) M, B) S. Comparing the idle time the difference between nickel powder M and S were observed. In the case of powder M (with the same amount of initiator) the gelation process occurred twice faster. This could be due to a greater amount of contaminants in the powder M, which resulted in acceleration of the polymerization process.

Table 1 lists the values of solid loading, linear shrinkage, density, tensile strength of green bodies obtained and relative density of sintered body. It can be noticed, that samples containing nickel powder S have slightly higher green and sintered density than those containing nickel M. With the increase in solid loading decreases shrinkage (after 96 h of drying). The tensile strength is higher for samples obtained with nickel S. The specimens containing nickel powder S exhibit a higher homogeneity and a smaller number of places, where cracks can be initiated.

The SEM micrographs of typical composite green sample is shown in Fig. 5A. It indicates that the nickel particle in green bodies is thoroughly covered with alumina particles and well embedded in the composite matrix. No clusters of polymeric chains are visible, what can means that used monomer wets alumina and nickel grain well enough. Fig. 5B shows fracture surface of sintered body. The nickel particles were distributed uniformly in whole volume of the material. Single metal particles were tightly surrounded by alumina grains without visible transition area and major pores.

## 4.Conclusions

The gelcasting technique in aqueous system was successfully employed to manufacture $Al_2O_3$-Ni composites. The influence of metal particle size were investigated.

Table 3. Properties of green and sintered composites bodies

| Sample | Solid loading [vol%] | Linear shrinkage after 96 hours of drying [%] | Green density [%] | Tensile strength of green body [MPa] | Relative density of sintered body [%] |
|---|---|---|---|---|---|
| $Al_2O_3$+3 vol% Nickel M | 50 | 5.2 ± 0.9 | 57. 3± 0.7 | 0.63 ± 0.05 | 96.6 ± 0.3 |
| $Al_2O_3$+3 vol% Nickel M | 52 | 4.3 ± 0,2 | 58.9 ± 0.5 | 0.72 ± 0.03 | 97.2 ± 0.5 |
| $Al_2O_3$+3 vol% Nickel M | 54 | 3.8 ± 0.5 | 59.3 ± 0.3 | 0.79±0,11 | 97.6 ± 0.4 |
| $Al_2O_3$+3 vol% Nickel S | 50 | 6.1 ± 1.1 | 57.8 ± 0.4 | 0.73 ± 0.09 | 97.2 ± 0.4 |
| $Al_2O_3$+3 vol% Nickel S | 52 | 4.6 ± 0.7 | 59.5 ± 0.5 | 0.89±0.13 | 97.9 ± 0.4 |
| $Al_2O_3$+3 vol% Nickel S | 54 | 3.1 ± 0.6 | 60.1 ± 0.4 | 0.88±0.09 | 98.3 ± 0.3 |

± confidence interval with probability 0.99
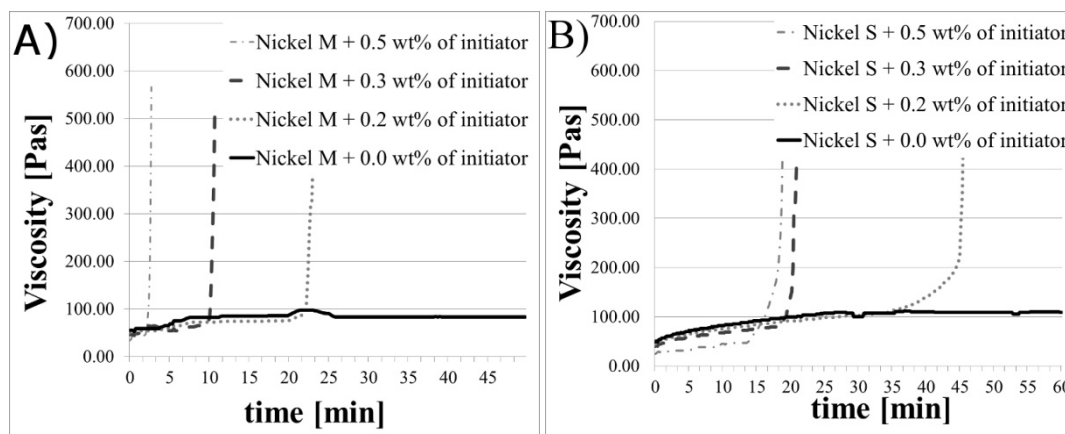


Fig 4 Influence of quantity of initiator on viscosity of slurries with A) 3 vol% of nickel powder S (54 vol% solid loading) and B) 3 vol% of nickel powder M
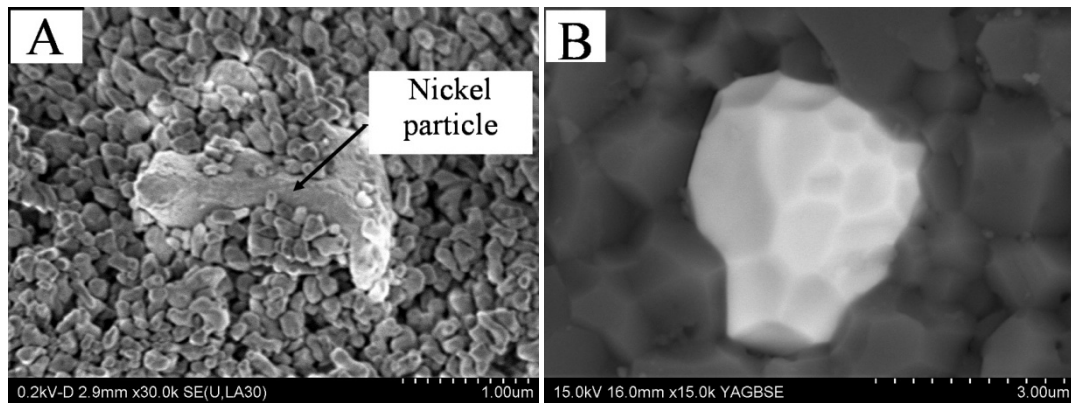
Fig. 5. SEM of fracture surface green body of $Al_2O_3$+3 vol% of nickel M(A),and sintered body of $Al_2O_3$+3 vol% of nickel M(B

Significant influence of presence of different nickel particles on the rheological stability of the slurries was observed. These results may suggest that interaction between alumina and nickel particles occurs.

The properties of composite slurries, green bodies as well as idle time are different for each nickel powder what indicate that the size of second metallic phase have important influence on the shaping process of composite material.

## Acknowledgements

## References

1.      Konopka K., Maj M., Kurzydłowski K.J. Studies of the effect of metal particles on the fracture toughness of ceramic matrix composites. Materials Characterization 2003;51:335-340.

2.      Moya J.S., Lopez-Esteban S., Pecharroman C. The challenge of ceramic/metal microcomposites and nanocomposites. Progress in Materials Science 2007;52:1017-1090.

3.      Konopka K., Oziębło A. Microstructure and the fracture toughness of the $Al_2O_3$–Fe composites. Materials Characterization 2001;46:125-129.

4.      Ellerby D.T., Loehman R.E. $Al_2O_3$-Ni Composites with High Strength and Fracture Toughness J.Am. Ceram. Soc. 2000;83:1279-1280.

5.      Omatete O.O, Janney MA, Nunn S.D. Gelcasting: From Laboratory Development Toward Industrial Production. J Eur Ceram Soc 1997;17:407–413.

6.      Bednarek P. et al, J.Eur. Ceram. Soc., 2010;30:1795-1801.

7.      Haij M. et al. Gelcasting of $Al_2O_3$/Ag nanocomposite using water-soluble solid-salt precursor. Ceram. Int. 2012;38:867-870.

8.      Stampfl J. et al. Rapid prototyping and manufacturing by gelcasting of metallic and ceramic slurries. Materials Science and Engineering 2002;A334:187-192.

9.      Yang J., Yu J., Huang Y. Recent developments in gelcasting of ceramics. J Eur Ceram Soc 2011;31:2569-2591.

10.     Capua Proveti J.R, Michot G. The Brazilian test: a tool for measuring the toughness of a material and its brittle to ductile transition, Int J Fract 2006;139:455–60.

# WETTING OF SOME NONSTOICHIOMETRIC OXIDE CERAMIC MATERIALS BY LIQUID METALS

## Durov O.V., <u>Sydorenko T.V.</u>

*Frantsevich Institute for Problem of Materials Science, National Academy of Science of Ukraine*
*e-mail: tvsid@ukr.net*

## Abstract

The contact interaction of ceramic nonstoichiometric materials ($TiO_2$, $ZrO_2$, $HfO_2$, $BaTiO_3$) some with metal alloys has been researched. Wetting of $TiO_2$ and $HfO_2$ oxides by a number of metals were studied. For Fe, Co, Ti and Pt the formation of second liquid phase in fact was revealed, these liquids wets the ceramic much better than metals. In experiments with Fe containing alloys was established, that temperature of second liquid formation is near 1380 ºC. So for Fe, Co and Ti temperatures of second liquid formation are in good agreement to temperatures of corresponding oxides melting. Microscopy and elements distribution research have shown the interaction in system and the presence of Hf in platinum drop. Like for platinum to zirconia interaction.

## 1.Introduction

Investigations of wetting and contact interaction in solid non-metal material — metal melts systems are important both on fundamental and practical view — for brazing, metallization, refractory technologies elaboration ets. Materials based on light elements oxides such as $Al_2O_3$ were mainly studied [1-7].

Wetting of zirconia by was also studied enough [8-11]. At the same time transition metals oxides has some features, in particular they can to lose oxygen (at annealing in vacuum or reduction annealing, at contact to active metals ets.) with non-stoichiometrric phases formation. It may influence the oxide to metal interaction. Tide contact of oxide to metal electrode is needed in these cases, so study of metals to $HfO_2$, $TiO_2$ is important.

$BaTiO_3$ materials are also interesting and important object — barium titanate can lose oxygen too, and transforms to semiconductor from ferroceramic due to it. So we have compared the wetting date for $HfO_2$, $TiO_2$ and $BaTiO_3$.

## 2.Materials and procedures

Dense (melted) rutile of technical purity, 3,5 % $Y_2O_3$ stabilized $HfO_2$-ceramic, metals of high purity (0,9999) were used in experiments. Substrates were machined to 3 mm thickness plates and polished by 0,5 µm diamond powder. Wetting experiments were carried out in vacuum by sessile drop method.

Initially $TiO_2$ was of stoichiometric composition but at vacuum annealing it lose the oxygen and becomes nonstoichiometric. Temperature of intensive

destoichiometrisation for these materials are near 600 ºC, when reach 1000 ºC oxygen evolution almost finished. As experimental temperatures were higher then 1000 ºC so wetting of non-stiochiometric $TiO_2$ were studied.

## 3.Results and discussion

Wetting experiments were performed firstly. Results are represented in table 1.

Table 1. Results of wetting experiments

| Metal | Temperature, ºC | Contact angle, degree | | | $\Delta H^\circ {}_{oxide}$, on 0,5 mole $O_2$ kJ/mol |
| --- | --- | --- | --- | --- | --- |
| | | $TiO_2$ | $HfO_2$ | $BaTiO_3$ | |
| Sn | 1000 | 100 | 136 | 115 | -290 |
| Al | 1000 | 73 | 73 | 129 | -558 |
| | 1100 | 70 | 71 | 91 | -516 |
| Cu | 1100 | 153 | 120 | 122 | -166 |
| Ag | 1000 | 112 | 138 | 132 | -30,6 |
| Au | 1100 | 127 | 130 | 127 | -3,35 |
| Si | 1460 | 99 | 93 | 84 | -428,5 |
| Ge | 1000 | 126 | 142 | 113 | -269,9 |
| Pd | 1560 | 105 | 113 | 116 | -115,6 |
| Pt | 1800 | — | 108 | — | -41 |
| Ni | 1500 | 108 | 110 | 113 | -244,6 |
| Co | 1500 | 107 | 116 | 108 | -239,5 |
| | 1830 | 39 | 101 | — | -90 |
| Fe | 1580 | 16 | 92 | 96 | -266 |
| Ti | 1800 | 70 | 74 | — | -522 |
| Zr | 1860 | — | 75 | — | -540 |

For cobalt similar picture was observed: although after melting and during heating to 1830 ºC contact angle was near 105º (fig. 2 b), at 1830 ºC second liquid appears (fig. 2 c). It need to remark that cobalt oxide CoO melts also at temperature 1830 ºC [12], so for cobalt case second liquid appearance may be explained by formation and melting of cobalt oxide.
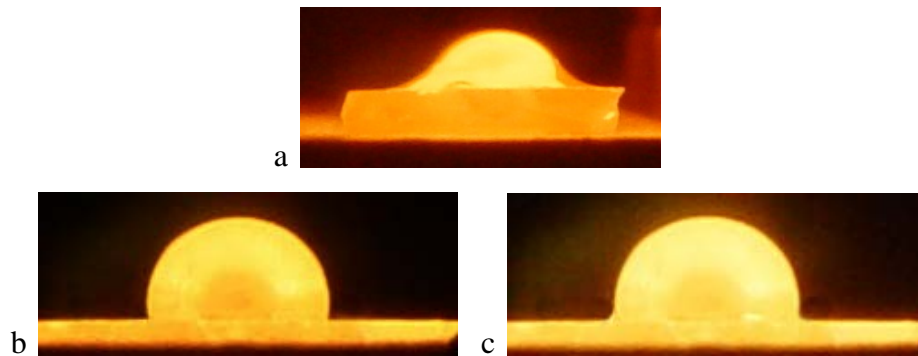
Fig.1. Wetting of the rutile surface by iron at 1580 ℃ (a), cobalt at 1600 ℃ (b) and cobalt at 1830 ℃ (c)

It is notable in cooled samples and cross-sections that the interaction was intensive and with liquid phase formation (fig. 2). Suggests that two liquid phases differently wet the oxide were presented on the rutile surface.



Fig.2. Sample after wetting experiment of rutile by iron: solidified drop (a) and its cross-section (b)

To verify the assumption that second liquid appearance in Fe-TiO$_2$ system is explained by FeO formation end melting, wetting of rutile by Fe-Au was studied. Gold was selected as a solvent because its melt can solve large quantity of iron at relative low temperature and alloy with 28 at. % Fe was selected because lowest liquidus temperature [13].

In wetting experiment only one liquid was observed firstly (fig. 3, a), but when heating to 1380 ℃ second liquid appeared (fig. 3, b). In iron-titanium system eutectics with relatively low temperature of liquid phase formation are also exists [14]. So wetting of rutile by iron-titanium alloy of second eutectic composition (16 at. % Ti) was studied (fig. 3 b, c). Second liquid appearance was also observed at 1380 ℃. This temperature is really close to iron oxide FeO melting point (1371 ℃ [15]).

a                                    b



c                                    d
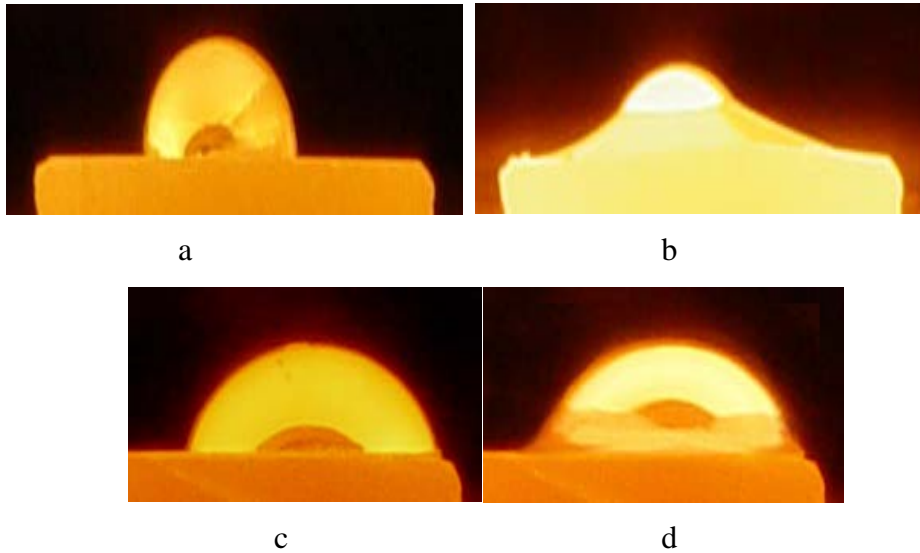
Fig.3. Wetting of rutile by Au-28Fe alloy (a – 1100 ℃, b – 1380 ℃) and

by Fe-16Ti alloy (c – 1300 ℃, d – 1380 ℃)

Special sample for X-ray research was prepared: rutile was grinded to sift through 063 sieve, obtained and iron powders were mixed to 30 at % Fe proportion. Mix was pressed at 400 MPa pressure, sample was annealed in vacuum at 1580 ℃ during 5 min. Sintered sample was studied by X-ray diffraction method.

The next structures presents in sample after annealing: iron, rutile and pseudobrookite $Fe_3Ti_3O_{10}$ ($Fe_2TiO_5$ – $FeTi_2O_5$ range). So, iron was oxidized. As the titania can lose oxygen and forms non-stoichiometric phases, reaction in system may be described by equation:

$$3xFe + (10+3x)\times TiO_2 = xFe_3Ti_3O_{10} + 10TiO_{2-x}$$
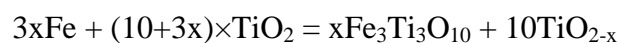
Pseudobrookite melts is 1570 ℃ [16], it is higher than iron melting point. But eutectic between pseudobrookite and rutile forms at 1515 ℃ [16], so second liquid forms just melted the iron.

So at interaction of iron melt and rutile the oxidization of ion by oxygen from substrate takes place, then fusible oxide FeO melt and intensive interact to $TiO_2$ substrate with relatively low melting eutectic formation.

Second liquid formation was also observed in experiments when titanium and platinum melts on $TiO_2$ surface (fig. 4).

a                  b
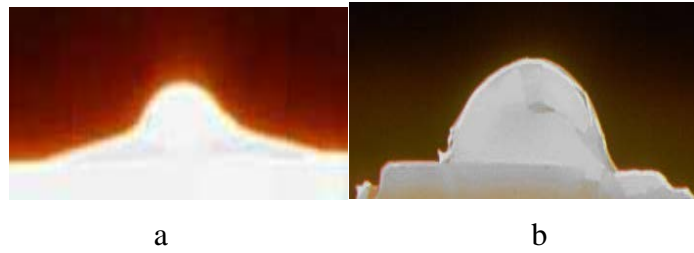
Fig.4. Wetting of $TiO_2$ by titanium (a) and platinum (b)

For Ti – $TiO_2$ contact couple the eutectic exist between $TiO_2$ and $Ti_2O_3$ [17], and its formation explain the second liquid appearing. $Ti_2O_3$ may form both by titanium oxidization and by $TiO_2$ reduction. Process may by schematically described by reaction:

$$Ti + 3TiO_2 = 2Ti_2O_3$$
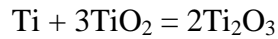
Formation of second liquid when platinum to $TiO_2$ interaction needs the special investigation.

For $HfO_2$ to iron melt interaction besides relatively low contact angle it is notable that some dark area forms under the drop. To explain this effect $HfO_2$-ceramic was grinded to sift the 063 sieve then mix of $HfO_2$ and iron powder was prepared, pressed, annealed in vacuum at 1600 ℃ and studied by X-ray method. Only $HfO_2$ and iron were detected. But the iron quantity decreased significantly (from 10 to 5 mass. %) and $HfO_2$ was in monoclinic modification although init powder was $Y_2O_3$ stabilized in tetragonal phase. Obviously the process described in [17] occurred, were $Fe_2O_3$ in $HfO_2$-ceramic introduction destabilized it and lead to monocline phase appearing. Interconnection of this process and wetting needs additional researches.

For platinum and palladium contact angles on $HfO_2$ substrate are also relatively low (table 1). Beside that, although $HfO_2$-ceramic turned dark after vacuum heating it save white color under and around platinum drops. Analogous phenomenon was observed for zirconia in [8] although substrate lightened fully but not only near the drops. These phenomena may be explained by noble metals to hafnium of substrate interaction: hafnium deficit may be considered as the hafnium surplus, so some of hafnium interact to noble metal and dissolve as in scheme:

$$HfO_{2-x} = HfO_2 + xHf_{(Pt)}$$

Thus hafnia stoichiometry regained. Microphotogtafy of $HfO_2$ – Pt contact zone obtained on the cross-section of solidified on $HfO_2$-substrate platinum drop is represented on fig. 5.
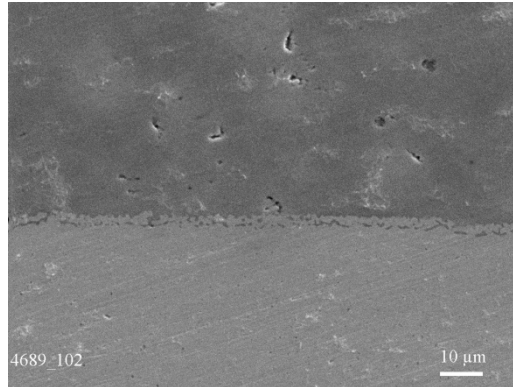


Fig.5. Microstructure of $HfO_2$ – Pt interface ($HfO_2$ - up, Pt - down)

As one can see, transition layer is developed enough so the platinum really interacted to the $HfO_2$.

**4.Conclusion**

Wetting of $TiO_2$, $HfO_2$ by a number of pure metals was studied. Common correlation of contact angle and affinity of metal to oxygen was notified. Appearance of second liquid was revealed for iron, cobalt, titanium and platinum to $TiO_2$ interaction, for iron, cobalt and titanium this phenomenon was explained by formation of fusible oxides and its interaction to $TiO_2$. Diffusion of iron in the $HfO_2$-ceramic was observed. For Pt-$HfO_2$ system interaction of platinum to hafnium was observed.

**References**

1. Naidich Y.V. Contact phenomena in metal melts. Kiev: Naukova dumka; 1972. 196 p. (in Russian).
2. Saiz E, Cannon R.M, Tomsia A.P. High-Temperature Wetting and the Work of Adhesion in Metal/Oxide Systems. Annual Review of Materials Research 2008;38: 197-226.
3. Peden C, Kidd K.B, Shinn N.D. Metal/Metal-Oxide Interfaces: A surface science approach to the study of adhesion. The Journal of Vacuum and Science Technology 1991;9:1518–1524.

4. Finnis M.W. The theory of metal-ceramic interfaces. Journal of Physics, Condensed Matter 1996;8:5811–5836.

5. Pint, B.A. Progress in Understanding the Reactive Element Effect Since the Whittle and Stringer Literature Review. Metals and Ceramics Division 2010;18(18):2159–2168.

6. Santella M. L, Horton J. A, Pak J. J. Microstructure of Alumina Brazed with a Silver-Copper-Titanium Alloy. Journal of the American Ceramic Society 1990;73:1785-1787.

7. Seiichi S, Miho K, Shinji A, Masako N. Solid-state reactions of the Ag–Cu–Ti thin film–$Al_2O_3$ substrate system. Journal of materials research 1993;8(8):1805.

8. Durov A, Naidich Y, Kostyuk B. Investigation of interaction of metal melts and zirconia. Journal of Materials Science 2005;40(9-10):2173-2178.

9. Humenik M, Kingery W. Interaction of zirconia and liquid metals. J. Amer. Cer. Soc 1954;37:18.

10. Ueki M, Naka M, Okamoto I. Wettability of some metals against zirconia ceramics. J. Mater. Sci. Lett. 1986;5:1261-1262.

11. Ueki M, Naka M, Okamoto I. Wettability of some metals against zirconia ceramics. J. Mater. Sci. Lett. 1986;5:1261-1262.

12. http://www.crct.polymtl.ca/findcmpd.php?formule=CoO#

13. http://steelcast.ru/equilibrium_diagram_fe_au

14. http://www.crct.polymtl.ca/fact/phase_diagram.php?file=Fe-Ti.jpg&dir=SGTE

15. http://www.crct.polymtl.ca/findcmpd.php?formule=FeO#

16. http://www.docstoc.com /docs/21873254/TiO-phase-diagram

17. http://www.crct.polymtl.ca/fact/phase_diagram.php?file=Ti-O_Ti2O3-TiO2.jpg&dir=FToxid

# ULTIMATE THIN LAYER JOINING BY GAS ADSORPTION

## Taga Yasunori  and Majima Takashi

*Thin Film Research Center, Chubu University Kasugai, Aichi 487-8501, Japan*
*e-mail: y-taga@isc.chubu.ac.jp*

## Abstract

Attempt has been made to join borosilicate glass and cycloolefin(COP) polymer film by using gas adsorption method. Prior to joining, corona plasma treatment in air atmosphere by changing plasma energy was carried out to control surface functional group on both surfaces. An (3-glycidoxypropyl)trimethoxysilane, GPS was adsorbed on glass and an (3-aminopropyl)triethoxysilane, APS on COP both in air atmosphere, resulting in
coadsorption of water vapor and organosilane gases.

Surface characterization of plasma treated and gas adsorbed surfaces was carried out by X-ray photoelectron spectroscopy (XPS) using Mg kαX-ray source. Joining was carried out by a roll laminator after contact of both surfaces at room temperature, followed by annealing at 130˚C for 10 min. Adhesion strength was evaluated by 180 degree peel test based on ASTM D-903 and durability was examined under the conditions of 60°C and 95 % RH.

Surface functional group of OH can be seen on glass surface after plasma treatment. On the other hand, XPS spectra of C1s revealed the existence of complex functional groups of O-H, C-O, C=O, O-C=O and CO3. In addition, plasma treatment energy gives an influence on the concentration of those functional groups on COP surface. At low energy plasma treatment, dominant functional group of COP surface was C-O and O-H and the surface concentration was estimated to be more than 70%. With increase in applied plasma energy, surface concentration C-O and O-H decreased slightly and C=O increased instead, and then O-C=O emerged on the surface as a result of further increase in energy. CO3 carbonate functional group appeared clearly on COP surface after plasma energy over 10 KJ/m2. Thickness of APS gas adsorption layer on COP was evaluated by the intensity of XPS Si2p peak. It was found that thickness rapidly increased to reach constant value after several minutes, where saturation thickness was estimated to be 1.1 nm by taking inelastic mean free path of Si2p photoelectron into consideration. Adhesion force by pulling test revealed strong adhesion and was found to be more than 5N/25 mm corresponding to almost equal to COP bulk tensile strength. In addition, durability of this adhesion strength remained unchanged over 2000 hrs even after exposure to the durability test conditions of 60°C and 95 % RH. The results can be explained in terms of formation of H-H hydrogen bonding and Si-O covalent bonding via silanols will be made at the interface as a result of lamination and annealing processes.

In conclusion, direct joining method using gas adsorption was carried out in the system of glass and cycloolefin polymer film at low temperature. Joining thickness was estimated to be 1-5 nm and joining force more than 5N/5mm and long term durability were also confirmed. The results of ultrathin joining can be explained in terms of formation of hydrogen and covalent bondings at the interface by low temperature reaction process.

## 1. Introduction

Manufacturing process of advanced information devices such as flat panel display, cellular phone, electronic paper and mobile display such as smart phone has made a great progress in the past decade. The leading concept of this process innovation is to manufacture the devices in more light in weight, more thin in thickness and more small in size using  nergy-saving method. For example, information devices mentioned above have been formed on inorganic substrates such as Si wafer and glass by high temperature process. The devices thus manufactured are mechanically rigid and chemically stable but heavy in weight and consumptive in energy for production. In response to strong requests

from industry, thin glass sheet less than 50 μm in thickness has become available commercially by advanced manufacturing process. Adopting plastic substrate instead of inorganic glass is so effective to reduce the device weight but difficulties in handling of thin glass sheet substrates during production process has become prominent because of their fragile properties. Backing thin glass sheet with transparent polymer film is effective for protection of thin glass sheet from destruction. In fact, joining of plastic film to inorganic glass at low temperature is carried out by using chemical adhesives to form strong joined stacks of combination with a ckness about 1-10μm. For example, liquid crystal display panels are actually made by 10 to 20 joined stacks such as film on film and film on glass systems, which resulted in forming useless thickness contrary to the leading concept of more thin devices. Low temperature process is of course indispensable for polymer incorporated panel manufacturing. Moreover, adhesive agent at the interface was sometimes attacked by ultraviolet light to deteriorate in coloration as a result of practical application.

In practical joining process, plasma treatment of both surfaces was primarily applied to control surface wettability, and then chemical adhesives of 5-10μm in thickness such as an acrylic resin or a silane oupling agent were coated in solution for adhesion (1-2). Strong adhesion was actually achieved by using a silane coupling agent.

On the other hand, challenge for a direct bonding of poly(methyl methacrylate) for polymer microchips has been made after plasma treatment without coating chemical adhesives (3). However, this type of joining is fundamentally considered to be hydrogen bonding at the interface, resulting in insufficient durability under exposure to the conditions of 60°C and of 95 % relative humidity(RH).

In this study, adhesive-free direct joining method was examined in the system of glass and cycloolefin polymer film at low temperature by the aid of gas coadsorption of water and silane coupling agent after sophisticated plasma treatment of both surfaces.

## 2. Experimental procedure

Borosilicate glass sheet of 0.7 mm thick and cycloolefin polymer(COP) film with 100μm in thickness were directly joined at low temperature by gas adsorption. A necessary condition for joining of COP and glass is at first to make the contact surfaces clean, where surface cleanliness is evaluated by contact angle of distilled water droplet of 3μL according to a standard method(4).

Prior to joining, corona plasma treatment in air atmosphere by changing plasma energy was carried out to control surface functional group on both glass and COP surfaces.

Surfaces COP and glass thus plasma treated were placed separately into 600 cm3 metallic container with a glass cup with 5 cm3 different organosilane liquid. The container was then sealed with a cap and kept at room temperature for coadsorption of evaporated silane gas and water vapor gas in the atmosphere. In this study, Organosilanes used in this study was an epoxysilane compound of (3-glycidoxypropyl)trimethoxysilane GPS, adsorbed on glass and an aminosilane compound, (3-aminopropyl)triethoxysilane APS, on COP. As a result, coadsorption of water vapor and organosilane gas will occur on COP and glass surfaces, where chemical vapor pressures of GPS and APS were 0.02 Pa and 3 Pa at 50°C. The organosilane molecule in the container vaporized and reacted with the OH groups on each sample surface. Surface characterization of plasma treated and gas adsorbed surfaces was carried out by X-ray photoelectron spectroscopy (XPS) using Mg kαX-ray source.

Joining was carried out by a roll laminator after contact of both surfaces at room temperature, followed by annealing at 130°C for 10 min. Adhesion strength was evaluated by 180 degree peel test based on ASTM D-903 and durability was examined under the conditions of 60°C and 95 % RH.

## 3. Results and discussion

Figure1 shows changes in contact angle of water droplet with time of plasma treatment. As shown, contact angle on glass surface changed drastically to less than 5 degree after treatment for only 3 sec. On the contrary, contact angle on COP surface gradually decreased to 40 degree after 10 sec treatment. Surface chemical conditions after plasma treatment was examined by XPS with a special attention on C1s binding energy. Surface functional group of OH can be seen on glass surface after plasma treatment. On the other hand, XPS spectra of C1s from COP surface after plasma treatment revealed the existence of complex functional groups of O-H, C-O, C=O, O-C=O and CO3 as shown in figure 2.
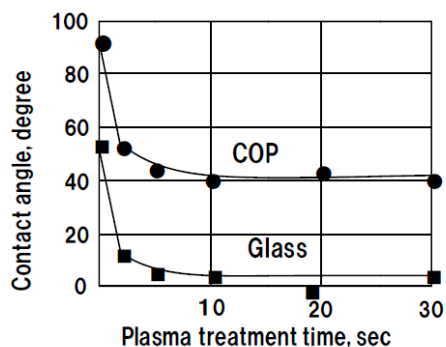
Fig. 1   Changes in contact angle of COP and glass with Corona plasma treatment time
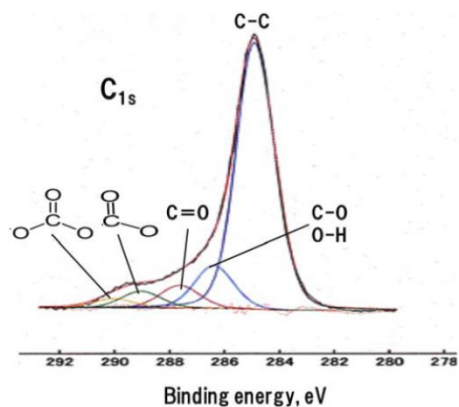


Fig. 2   High resolution XPC C1s on COP after O2 plasma treatment.

In addition, plasma treatment energy gives an influence on the concentration of those functional groups on COP surface and the result was depicted in figure 3. At low energy plasma treatment, dominant functional group of COP surface was C-O and O-H and the surface concentration was estimated to be more than 70%. With increase in applied plasma energy, surface concentration C-O and O-H decreased slightly and C=O increased instead, and then O-C=O emerged on the surface as a result of further increase in energy. Finally, CO3 carbonate functional group appeared clearly on COP surface after plasma energy over 10 KJ/m2. Results in figure 3 can be explained in terms of changes in oxidation states of COP surface with applied plasma energy. It may be possible to speculate that the concentration of functional group on COP surface may give an influence on the joining strength. On the contrary, functional group of glass surface was dominantly O-H and remained unchanged after further high energy plasma treatment. Adsorption of GPS on glass and APS on COP was separately carried out at room temperature for several minutes.

Figure 4 shows typical example of changes in APS concentration on COP as a function of exposure time, where the concentration was measured by the intensity of XPS $Si_{2p}$ peak arising from constituent element. Surprisingly, Si2p intensity corresponding to the thickness of adsorbed GPS increased steeply with time to saturate after 30 min exposure but few amount of adsorption can be seen on the surface without plasma treatment. Inelastic mean free path (IMFP) (5-7) of $Si_{2p}$ was estimated to be 1.1 nm from photoelectron kinetic energy of 1153.8 eV, which corresponds to $Si_{2p}$ binding energy of 99.8 eV. As a result, the saturated thickness of adsorbed APS on COP is at least thicker than 1.1 nm.

Figure 3. Changes in concentration of functional group of COP surface with plasma energy.

Figure 4. Changes in $Si_{2p}$ intensity with exposure time of GPS on COP.
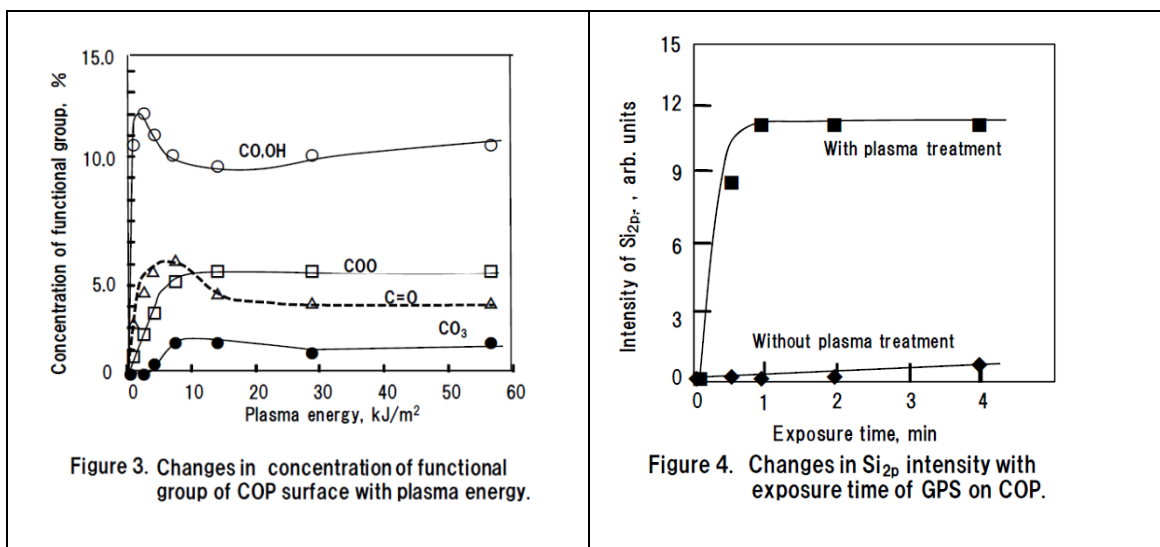
In order to obtain more information of concentration profile in-depth, a take-off angle measurement was carried out by inclining the sample to the photoelectron detector. Figure 5 showed the results of concentration changes in C, O and Si of GPS on COP as a function of take-off angle $\Theta$, where Si was not included in the substrate but a constituent element of GPS. As shown in the figure, surface concentration of Si remain unchanged until $\Theta=45$ degree and then began to increase gradually.

Concentration profile in depth by changing take-off angle can only be obtained below 45 degree. Similar result was actually obtained for APS on glass. Thickness of adsorbed organosilane layer was reported previously to be at about a few nm (8-11).
For example, Sugimura and Nakagiri(8) estimated the thickness of organosilane monolayer formed by chemical vapor depositon based on ellipsometric data to be 0.4-2.0 nm.

By taking the above discussion into consideration, thickness of the adsorption layer of GPS was evaluated to be at least thicker than 0.78 nm, corresponding to the same order of 1.1 nm by IMFP consideration. Similar result was obtained for APS adsorption on glass where the concentration of APS was evaluated by the intensity of XPS N1s peak of constituent element.

During the course of a long history of SCA application in practical joining, reaction mechanism was proposed on the basis of speculation (12-13) but no direct evidence of reaction unit process is not yet presented.

132

In this paper, the thickness of gas adsorption layer was directly determined by taking the escape depth of $Si_{2p}$ photoelectrons into consideration, thickness of the coadsorption layer of water and APS can be estimated to be 2-10 nm. Considering from the reaction mechanism of silane coupling agent with organic and inorganic substrates, it can be explained that the concentration of adsorbed APS molecules may saturate in accordance with that of functional group on COP surface. Similar result was obtained for GPS adsorption on glass where the concentration of GPS was evaluated by the intensity of XPS $N_{1s}$ peak of constituent element of GPS. In this case, a saturated concentration of GPS may be dependent on the concentration of OH functional group. Based on both adsorption experiments of APS on COP and GPS on glass, it can be concluded that concentration of adsorbed organosilane gas can be controlled in accordance with the conditions of corona plasma treatment of both surfaces.

It can be understood from XPS analyses in figure 1 that oxidation states of COP surface change with plasma energy applied on the surface. Formation of H-H hydrogen bonding and Si-O covalent bonding via silanols will be made at the interface as a result of lamination and annealing processes.
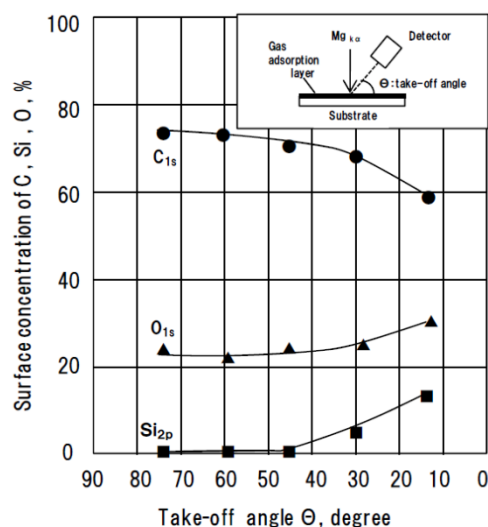


Figure 5. Changes in surface concentration with take-off angle.

Reaction process at the interfaces will be schematically shown in Fig. 5. Adhesion force may be proportional to the concentration of surface functional group. Adhesion force by pulling test revealed strong adhesion and was found to be more than 5N/25 mm corresponding to almost equal to COP bulk tensile strength. In addition, durability of this adhesion strength remained unchanged over 2000 hrs even after exposure to the durability test conditions of 60°C and 95 % RH.

## 4. Summary

Adhesive-free direct joining method was confirmed in the system of glass and cycloolefin polymer film at low temperature. The results can be explained in terms of formation of hydrogen and covalent bondings at the interface as a result of low temperature joining process. Bonding layer was considered to be less than several nanometer in thickness.

## References

1.      A.Namkanisorn, A.Ghatak, M.K.Chaudhury and D. Berry, J. Adhesion Sci. Technol. 15, 1725(2001).

2.      Won-Seck Kim and Jung-Ju Lee, J. Adhesion Sci. Technol. 21, 125(2007).

3.      H. Shinohara, J. Mizuno and S. Shoji, IEEJ Trans. 2, 301(2007).

4.      A. Adamson, Physical Chemistry of Surfaces, John Wiley & Sons, Academic Press Inc., London,1985. A. Ulman, Introduction to Ultrathin Organic Films ( Academic Press, San Diego, 1991).

5.      S. Tanuma, C. J. Powell, D. R. Penn, Surf. Interface Anal. 21, 165(1994).

6.      M. P. Seah and W. A. Derch, Surf. Interface Analysis 1, 2(1979).

7.      D. R. Penn, Phys. Rev. B 35, 482(1978).

8.      H. Sugimura and N. Nakagiri, J. Photopolymer Science and Technology 10, 661(1997).

9.      H. Shinohara, T. Kasahara S. Shoji and J. Mizuno, J. Micromech. Microeng. 21, 085028(2011).

10.     U. Srinivasan, M. R. Houston and R. J. Maboundian, Microelectromech. Syst., 7 252(1998).

11.     I. Luzinov, D. Julthongpiput, A. Liebmann-Vinson, T. Cregger, M. D. Foster and V. V. Tsukruk, Langmuir 16, 504(2000).

12.     B. Arkles, Chemtech 7, 766(1977).

13.     F. D. Osterholtz and E. Pohl, J. Adhesion Sci. Technol. 6, 127(1992).

# JOINING SIC/SIC COMPOSITE PLATES BY A DISILICIDE COMPOUND

**Jacques E.[1], Le Petitcorps Y.[1], Maillé L.[1], Lorrette C.[1,2] and Chaffron L.[2]**

[1] *University of Bordeaux, Laboratoire des Composites Thermostructuraux, Pessac-France*
[2] *CEA-Nuclear Energy Division, Nuclear Material Department, Section for Applied Metallurgy Research, Technology for Extreme Materials Laboratory*
*e-mail: maille@lcts.u-bordeaux1.fr*

## 1.Introduction

Joining ceramic/ceramic composites (CMC's) is of interest for numerous applications in the aeronautic or nuclear fields. This joining may concern the assembly of two CMCs parts or the assembly of one CMC part against a metallic alloy. This study deals with the assembly of two silicon carbide/silicon carbide composite plates designed for a fuel cell component within the framework of the Fourth Generation Reactor Program [1]. In order to achieve this goal, many requirements have to be followed: (i) the joint must be tight enough to avoid the gas leaks in service and, (ii) has to withstand temperatures such as 1000°C for very long durations (service conditions) and 1500°C for short durations (accidental conditions) without damaging the CMC properties, (iii) the process has to be compatible with the nuclear constraints and must not damage the composite properties which are very sensible to fibre degradations. The composite material for this application is made of a woven silicon carbide fibre perform (Hi-Nicalon Type S$^{TM}$ or Tyranno SA3$^{TM}$ fibre) infiltrated by a silicon and carbon based precursor (CVI process). Both the matrix and the fibre are nearly pure silicon carbide which gives to the composite a good thermal stability up to 1600°C. The CMCs assembly research is not a new but this requirement in temperature stability (1500°C) makes the answer not trivial [2-5]. Conventional silicon based compositions cannot be used since the melting point of Si is too low. Thus a material selection study has been done in order to select compounds able to withstand these requirements. The selection of the right composition for the joint has been done from the physical properties, the thermodynamic data of the different candidates in order to avoid a too important mechanical and chemical mismatch with the silicon carbide. Various assembly processes have been evaluated (solid state

bonding, liquid state bonding) and several ways of short heating have been tested (microwave, High Frequency heating). The quality of the assembly has been evaluated through metallographic observations on polished sections or with tomography images on the whole assembly.

## 2.Materials and methods

### 2.1.Material selections

The silicon carbide material is a covalent crystal characterized by a low coefficient of thermal expansion CTE, a high modulus, a high melting point and a intermediate toughness which makes the ceramic sensible to flaws (Table 1). Unfortunately the silicon carbide reacts at medium temperature (above 800°C) with most of the refractory metals. Thus these metals cannot be chosen which purpose. However the analysis of the ternary phase diagram involving Si, C and Metallic atoms indicates that some compositions can be in a thermodynamical equilibrium with SiC (Figure 1). The carbide (here $TiC_X$) and the disilicide (here $TiSi_2$) are thermodynamically stable with SiC in the solid state whereas the other silicides react with SiC. In addition to a poor thermal expansion mismatch with SiC, TiC has not been chosen due its too high melting point which could be a problem if the joint has to be melted for the assembly. The remaining choice is the metallic disilicide. This disilicide is related to a ionic-covalent crystals which exhibits an intermediate Young's modulus and a higher CTE than SiC. Due to this CTE mismatch, the joint will be in tension and the silicon carbide in compression on cooling. One way to reduce the CTE of the joint is to incorporate SiC particles within the silicide. By controlling the volume fraction of SiC added, the CTE and the Young's modulus can be tailored. Due to the relatively high thermal stability of $TiSi_2$, this disilicide has been selected. The $TiSi_2$ compound will be reinforced by SiC particles (less than 1☐m in size) and with different volume fraction (from 0 to 30%).

### 2.2.Material heating

Since the disilicide do not react with the silicon carbide substrate in the solid state, the bonding between the joint and the SiC substrate should not be strong enough.

Table 1: Physical Properties of the potential candidates for joining SiC [6]

|  | Si | SiC | TiSi2 | TiC |
|---|---|---|---|---|
| Melting (°C) | 1414 | 2700 | 1540 | 3140 |
| CTE ($10^{-6}$/K) | 5.7 | 4.5 | 10.4 | 7.6 |
| Young's Modulus (GPa) | 130 | 400 | 260 | 450 |
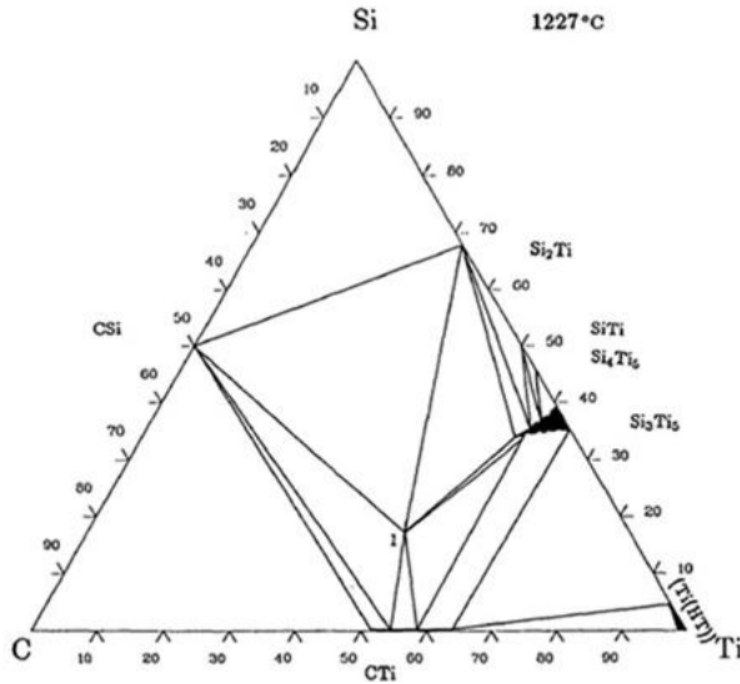


Fig. 1: Ternary phase diagram of Ti, Si,C plotted at 1500K [7]

In order to get this bonding, the melting of the joint should be done very rapidly in order to promote and to limit the chemical reaction with the silicon carbide substrate. A microwave furnace (2450MHz) can be used for melting ceramics which have an effective electrical conductivity between 1 and 10 $Sm^{-1}$ such as semiconductors. It is supposed to be a more economical process than the other conventional processes like the high frequency induction furnace. The principle was to selectively heat the joint and not the silicon carbide substrate. Thus the joint could be melted without heating the composite itself. Unfortunately the silicon carbide absorbs at the same wave than the titanium disilicide. Finally, a more conventional high frequency furnace has been chosen (60% of power – Five Celes HF MP3, 12kW). With that equipment, the joint between two silicon carbide plates is melted in less than 1

minute and cooled down for few seconds later after the melting. The assembly is maintained by a graphite susceptor inside a chamber under a purified argon atmosphere. The wettability is of great importance in the brazing technology and has been studied for the different compositions by recording the value of the contact angle during the spreading of the drop.

*2.3.Material characterizations*

In order to characterize the physical properties of the joint (CTE and Young's modulus) model materials of $TiSi_2$ + x% of $SiC_p$ were prepared by spark plasma sintering. After sintering, the materials were nearly fully dense (95% of the theoretical density). The CTE has been measured by a TMA device (dilatometer Netzsch DIL402C) and the Young's modulus measured from the room temperature to 1000°C was determined by a Grindosonic apparatus (LEMMENS Inc.).

The quality of joining has been studied on polished cross sections by SEM and WDS analysis (Hitachi S4500). A particular attention has been paid to the ocurrence of cracks in the joint, the thickness of the reaction zone between the melted joint and the SiC substrate, as well as its chemical composition. The macroscopic characterization of the joint has been done by X ray tomography (Phoenix X Ray nanotom S).

**3.Results and discussions**

*3.1.Decreasing the residual stresses in $TiSi_2$ by addition of submicronic SiC particles ($SiC_p$)*

Although the values are below the data expected from a rule of mixture (ROM), the $SiC_p$ have a positive effect on the Young's modulus from room temperature to 1000°C (Figure 2). This difference from the ROM can be explained by the submicronic size of the particles, the aspect ratio of them which is closed to one and the presence of 5% of porosities. A 10% decrease in the CTE is also measured on $TiSi_2$ reinforced with 20% in Vo. of $SiC_p$.

The consequences on the network of cracks in the joint can also be seen on figure 3. In order to avoid a chemical reaction between the $TiSi_2$ and the SiC from both the particles and the substrate, the material was also prepared by spark plasma sintering at 1200°C. The presence of the SiC particles induce a decrease in the residual

stresses within the joint which exhibits also a clear interface with the silicon carbide substrate.
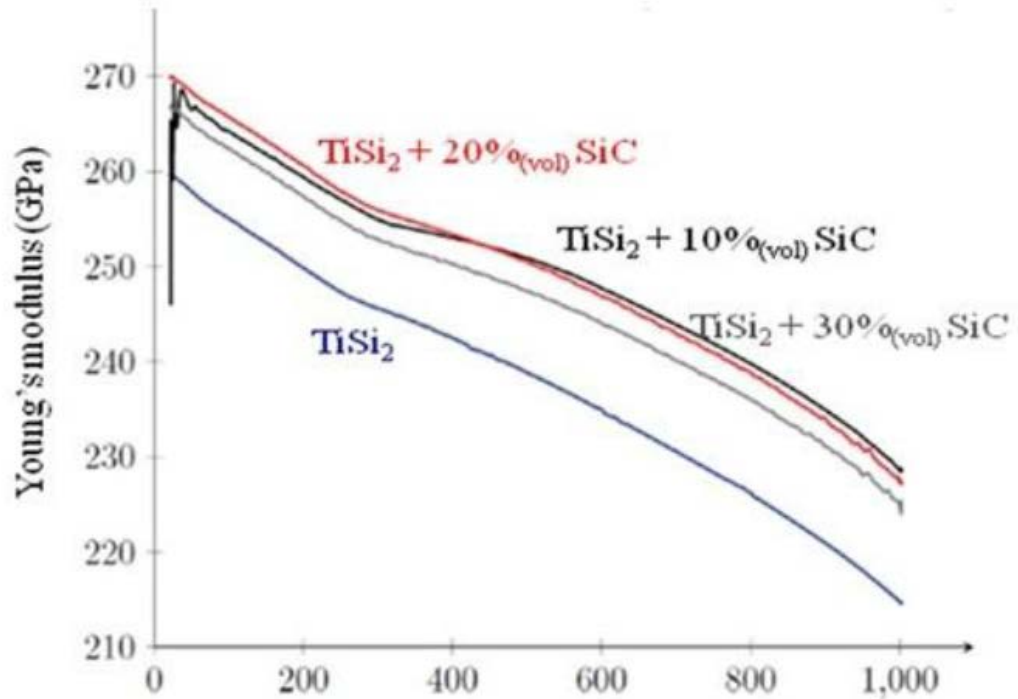


Figure 2: Young's modulus versus the temperature for TiSi$_2$/SiC systems with different content of additions
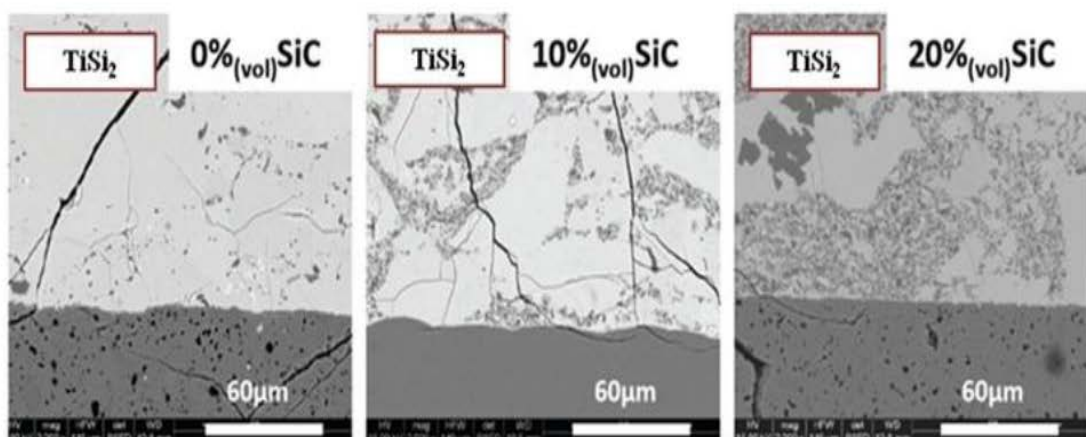


Figure 3: Crack pattern in the TiSi$_2$ joint reinforced with 10 and 20%Vo. of SiC$_p$

## 3.2.Wettability of $TiSi_2+SiC_p$

For pure $TiSi_2$, the contact angle decreases from 80° to 12°, 4 seconds after the melting (Figure 4). $TiSi_2$ has a very low contact angle which is very useful for its infiltration in small cavities of the materials to join. The reason of this kinetic of wettability can be explained by the reactivity of the liquid Ti-Si alloy with the SiC substrate [8]. When SiC particles are added, the contact angle is increased to 30° for 30%Vo. of $SiC_p$ after 4 seconds in the liquid state. The particles induce an increase in the viscosity as well as they react with the titanium disilicide matrix. However, the contact angle measured with 30% of SiC is very closed to the contact angle measured with pure silicon. The contact angle and the kinetic of spreading can be tailored by the amount of $SiC_p$. It is important to control the time during the melting step in order to limit the reaction zone thickness between the joint and the SiC substrate.
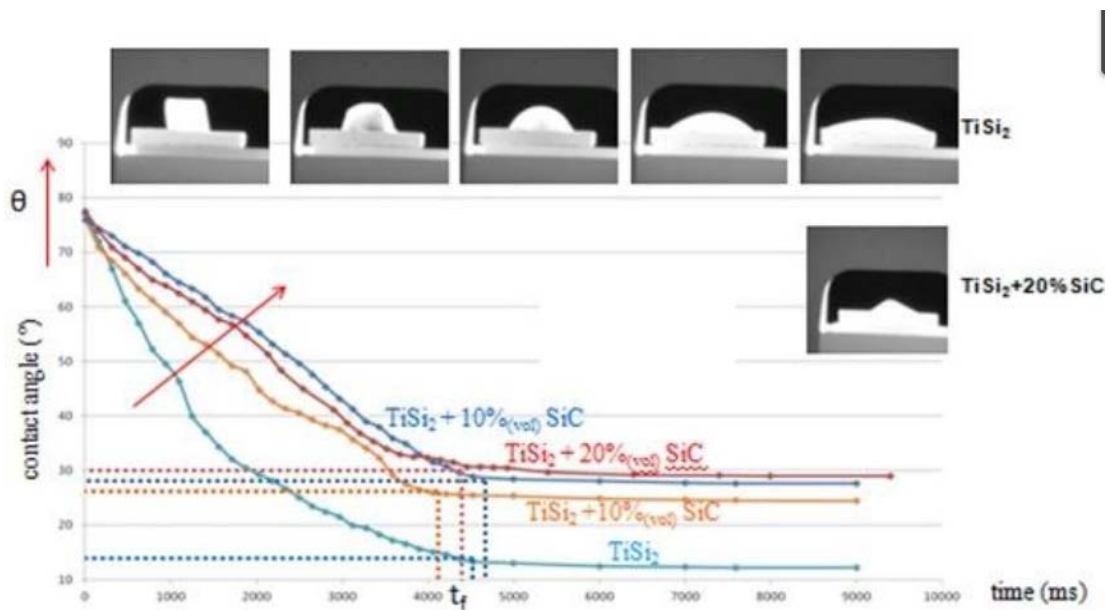


Figure 4: Wettability studies for different compositions of $TiSi_2$ and $SiC_p$

## 3.3.Reactivity of liquid (Ti,Si) + $SiC_p$ with the SiC substrate

In the liquid state, the liquid containing Ti and Si atoms should react with SiC. From the SiC to the $TiSi_2$, the interface is composed of $Ti_3SiC_2$ and TiC (Figure 5). If

the joint contains $SiC_p$ they also should react with the liquid and the liquid should be less aggressive against the SiC substrate. Consequently, the reaction zone thickness at the Joint/SiC interface decreases with an increase in $SiC_p$ amount (Table 2).

Table 2: Influence of the amount of $SiC_p$ on the Reaction Zone thickness at the $TiSi_2$/SiC interface

| | Pure TiSi2 | TiSi2+ | TiSi2+ | TiSi2+ |
|---|---|---|---|---|
| Reaction zone | 20 | 6-7 | 4-5 | 4-5 |
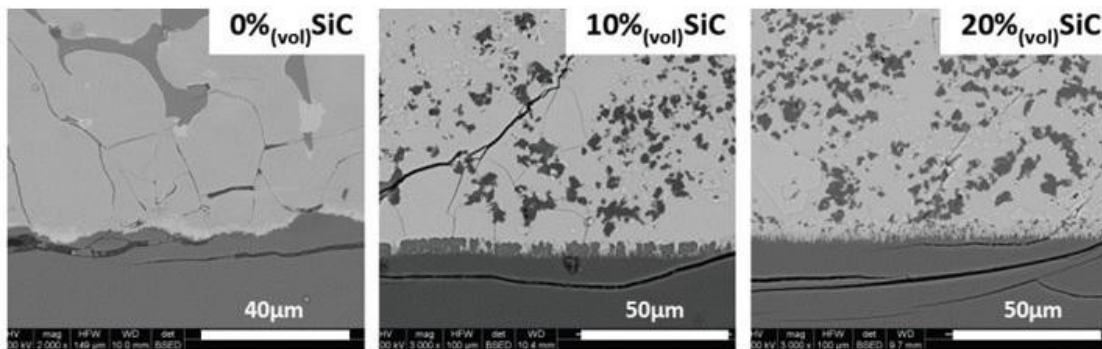


Figure 5: Reaction Zone thickness and morphologies at the SiC/$TiSi_2$ interface

*3.4. Characterization of a real assembly between two plates of SiC*

Two plates of SiC have been joined by melting the $TiSi_2$ mixture and followed by a rapid cooling. It can be seen that the brazing is nearly uniformly present even though some depletion of matter can be seen. No pressure was applied on the surface of the sample, a possible explanation of this lack of matter could be the presence of gas confined during the melting. However these first results are encouraging.

**4. Conclusions**

The aim of this work was to find an adequate brazing composition which is stable with SiC between 1000°C to 1500°C for long durations. Titanium disilicide can reach such a goal but due to the mismatch in the physical properties between SiC and $TiSi_2$, the joint is drastically cracked. The addition of submicronic particles of SiC

inside the joint reduces the tensile residual stresses. The $SiC_p$ have also an other beneficial effect on the chemical stability of the joint when the disilicide is melted during the brazing step. The interest of this type of brazing has now to be confirmed by the mechanical testing of the assembly.
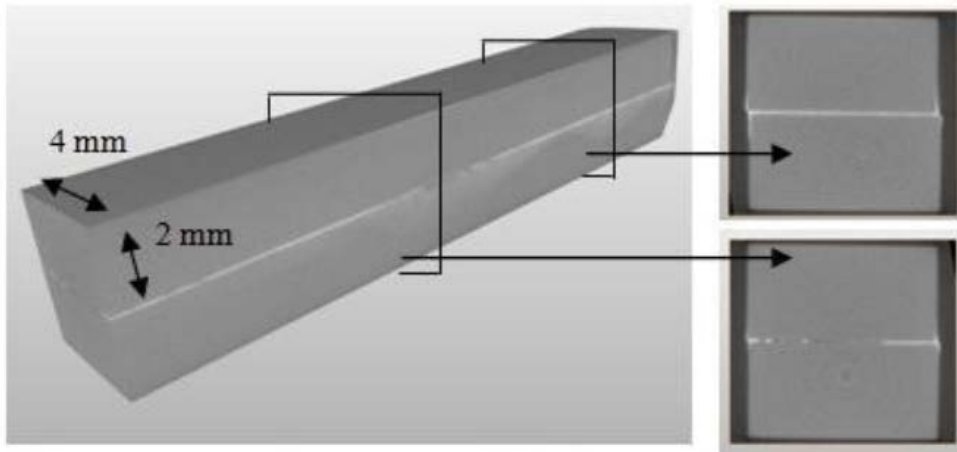


Figure 6: X-Ray tomography images of the brazing between two plates of SiC

## Acknowledgments

## References

1.      L. Chaffron *et al.* Innovative $SiC_f$/SiC composite Materials for Fast Reactor Application, , Transactions of the American Nuclear Society, ANS annuel meeting, San Diego 2010.

2.      B. Riccardi, C.A. Nannetti, T. Petrisor, J. Woltersdorf. High temperatures brazing for SiC and $SiC_f$/SiC ceramic matrix composites, International Symposium on $SiC_f$/SiC composites materials research and development 2002.

3.      B. Riccardi, C.A. Nannetti, T. Petrisor, J. Woltersdorf. Issues of low activation brazing of SiCf/SiC composites by using alloys without free silicon. Journal of Nuclear Materials 2004; 329:p.562–566.

4.       B. Riccardi, C.A. Nannetti, T. Petrisor, M. Sacchetti. Low activation brazing materials and techniques for SiCf/SiC composites, Journal of Nuclear Materials 2002; 307: p.1237–1241.

5.      E. Jacques, L. Maillé, Y. Le Peticors, C. Lorrette, C. Sauder. Preliminar results on joining of thin SiC/SiC composites by silicides coumpounds and local heating, Ceramic Engineering and Science Proceedings 2011; 32: p.73-83

6.      Materials Handbook, A concise Desktop Reference, F. Cardarelli, Springer, ISBN 1-85233-043-0.

7.      Handbook of ternary alloy phase diagrams 1995.

8.       A. Gasse, Thesis, Université de Grenoble, France 1996.

# THE PREPARATION OF DIAMOND PARTICLE REINFORCED SILICON CARBIDE COMPOSITES BY LOW PRESSURE GASEOUS SILICON INFILTRATION

**Rongjun Liu, Yingbin Cao, Changrui Zhang, Pengbo He**

*Science and Technology on Advanced Ceramic Fibers and Composites Laboratory, National University of Defense Technology, Changsha 410073, China*
*e-mail: rongjunliu@163.com*

## Abstract

The characteristic of high thermal conductivity of diamond/SiC composites lead to their industrial application as heat spreaders. In this paper, a new technology without high pressure for fabrication of Diamond/SiC composites is proposed, namely low pressure gaseous silicon infiltration. The microstructures of the composites prepared under different conditions were analyzed using X-ray diffraction, Scanning electron microscopy, it's found that diamond particles was distributed homogeneously in the composites. The grain size and content of diamond on the properties of diamond/SiC composites were analyzed, the results show that the thermal conductivity of the composites increase with the increasing grain size and content of diamond powder. When the grain size and content of diamond are 300μm and 80 wt% respectively, the thermal conductivity of the composites approach the maximum value of 280W/mk.

**Keywords:** *Diamond; Silicon carbide; Composites; Gaseous silicon infiltration.*

## 1.Introduction

Diamond/SiC composites possess many key physical properties such as high thermal conductivity, exceptional hardness, wear resistance. The characteristic of high thermal conductivity of diamond/SiC composites lead to their industrial application as heat spreaders, as more demanding thermal management issues arise in the microelectronics industry [1-3] . The diamond/SiC composites are typically produced by the liquid silicon infiltration method under high pressure and high temperature (HPHT)[4-8], which is usually done at pressure 6–10 GPa and temperature 1700–2100 K. SiC matrix phase is formed as a result of the reaction between diamond and silicon. However, there exit several drawbacks in HPHT liquid silicon infiltration method. Firstly, HPHT method can only produce samples with simple shape, and show a high preparation cost. Secondly, Liquid silicon infiltration cannot adequately penetrate diamond compact, This restriction is caused by the closure of pores in the diamond compact due to the formation of silicon carbide, This effect becomes increasingly more pronounced with decreasing size of diamond crystals.  The purpose of the present work is to propose a new method to prepare Diamond/SiC composite, we called this method low pressure gaseous silicon infiltration[9-11]. This process needn't high pressure so avoid high preparation cost, at the same time, gaseous silicon infiltration is a gentle reaction, it can avoid self-stop phenomenon in liquid silicon infiltration method because of rapid reaction between liquid

Si and C. In this paper, the microstructures of the composites prepared under different conditions were analyzed using X-ray diffraction, Scanning electron microscopy; the grain size and content of diamond on the properties of diamond/SiC composites were studied.

## 2. Experimental

Diamond preforms were produced using commercial diamond powders with four different particle sizes 37.5, 75, 150 and 300μm. The composition of the diamond preforms was modified by the content of diamond powder and phenolic resin, the weight percent of diamond particles range in 40wt%~80wt%.
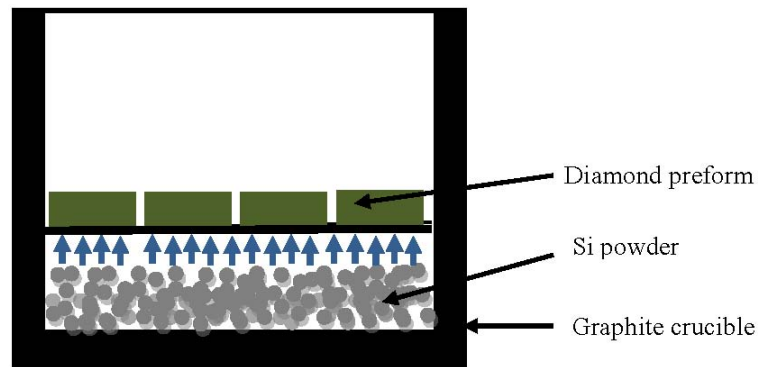


Fig.1. Set-up for the gaseous silicon infiltration experiments

The functions of phenolic resin include two sides: at first, it acts as a binder during the hot mould forming of diamond compact; secondly, phenolic resin provide carbon source for silicon infiltration and prevent the diamond from reacting with silicon. For the preparation of diamond preforms, diamond powder was mixed with phenolic resin solution (alcohol was used as the resolvent) to form slurry, then the slurry was dried in drying oven, the resulting powder was compacted to 35mm length, 30mm width and 5mm height under pressure of 40 MPa and temperature 200℃, the compact obtained using this methods were then pyrolysed in argon up to a temperature of 1000℃, at last, the obtained diamond preforms (green body) and silicon powder were loaded in a graphite crucible (Fig.1.), the green body located on the top of silicon powder, there exist certain distance between silicon powder and green body to avoid liquid silicon infiltration at high temperature, the crucible were placed in a vacuum furnace and heated to the gaseous silicon infiltration temperature of 1600℃. The resultant materials were characterized by

X-ray diffractometry (XRD) at a wavelength of 1.5418 A (Cu $K\alpha$ radiation) and scanning electron microscopy (SEM).

## 3. Results and discussion

Fig.2 shows the effects of mean particle size of diamond on the bend strength and thermal conductivity of diamond/SiC composites, all the samples have the same diamond content of 40wt%, the particle size of diamond range from 37.5~300μm. The thermal conductivity of the composites increases with the increasing of diamond particle size, it approaches a maximum value of 138.1 w/m·K at the diamond particle size of 300μm.
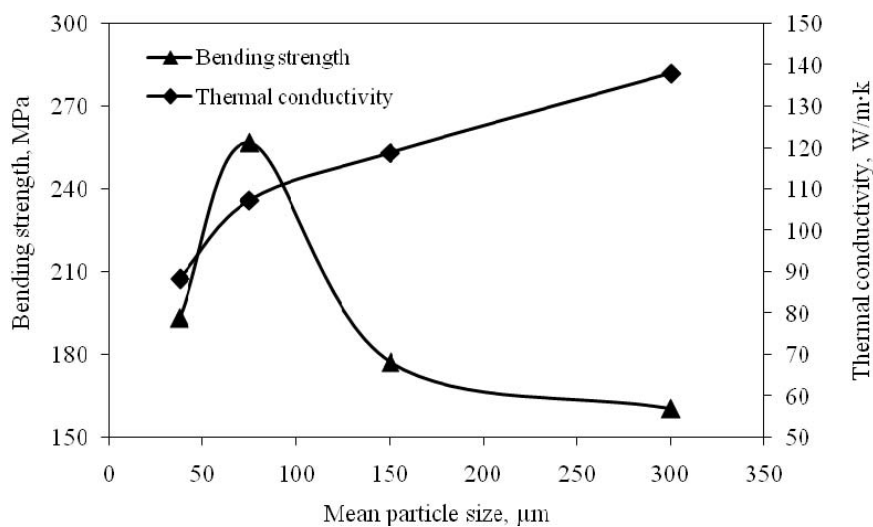


Fig.2. Effects of mean particle size of diamond on the bend strength and thermal conductivity of diamond/SiC composites

The increase of the composite's thermal conductivity with the increase of diamond grain size from 37.5μm to 300μm, can be explained on the base of a "two-zones" microstructure model 1,12of diamond grain in the composite（Fig.3).

According to this model, the diamond particles in the composites are comprised of two zones: a sintering-induced eroded surface layer of a fixed thickness with low thermal conductivity and a core of pristine diamond with undisturbed thermal conductivity. The grain size of diamond particles will become smaller after silicon infiltration. Because the eroded layer thickness is considered to be in dependent of diamond grain sizes, therefore, the composites will remain more volume percent pristine diamond and show good thermal conductivity as the grain size of diamond increase. The bending strength of the composites increase with the increasing of diamond particle's size at first, however, the

146

composites' strength decrease with the further increasing of diamond particle size. In the experiment, diamond/SiC composites reach the maximum value of 256.8 MPa at the diamond particle size of 75 µm. For the particle reinforced ceramic matrix composites, the reinforced particle with too big size is likely to break, which will lead to the prepared composites possess poor mechanical properties. The reinforced particle with too small size is likely to be eroded in the silicon infiltration, the strengthening effect of the particles become weak and the composites show poor mechanical properties too.



| (a) Green body | (b) Diamond/SiC composites |
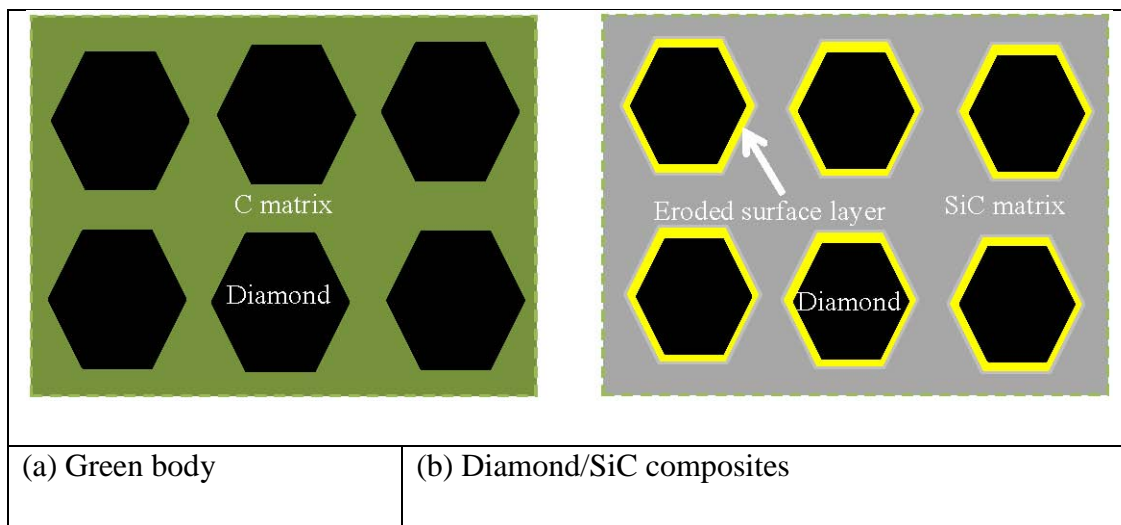
Fig.3.Schematic representation of the green body before Si infiltration (a) and the composites after Si infiltration (b)
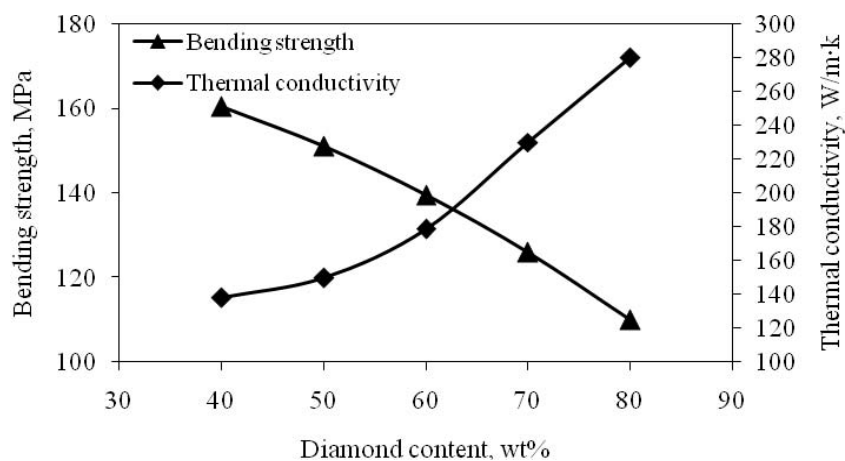


Fig.4. Effects of diamond content on the bending strength and thermal conductivity of Diamond/SiC composites

Fig.4 shows the effects of diamond content on the bend strength and thermal conductivity of diamond/SiC composites, all the samples have the same diamond particle size of 300µm. The result shows that the thermal conductivity of the composites increases with the increasing of diamond content, in our experiment, the maximum content of diamond is 80wt% and the composite approaches a maximum thermal conductivity value of 280 w/m·K. On the contrary, the bending strength decreases with the increasing of diamond content. With the increasing content of diamond, the content of formed SiC matrix will reduce, which result the decrease of Diamond/SiC composites' bending strength.
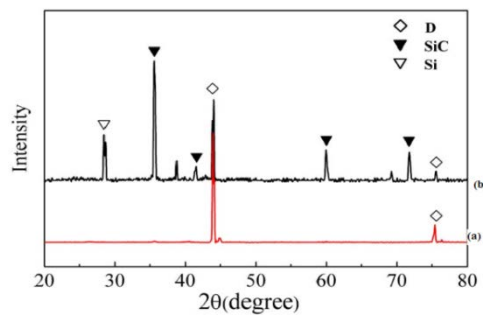


Fig.5. X-ray diffraction patterns: (a) Diamond compact, (b) Diamond/SiC composite; D=diamond

Fig.5 shows the XRD patterns of the diamond compact and Diamond/SiC composite. The diamond compact composes of diamond particles and phenolic resin, only diamond peaks show in the XRD patterns. It can be seen that after gaseous silicon infiltration, the formed Diamond/SiC composite are constituted by diamond, SiC and Si (Fig.5b). These can be explained by that carbon reacted with Si and β-SiC was formed [13]. As both peaks of diamond and Si were existed and strong, it can be inferred that pyrolytic carbon from phenolic resin completely transformed into SiC, little diamond reacted with Si. The products contain some free silicon due to their large pores in the preform, after infiltration and as the furnace temperature decrease, gaseous Si will agglomerate and fill in the pores of the preform to form a dense composite.

Figure 6 shows a SEM microstructure of green body and diamond/SiC composite with 300µm diamond particle sizes. It can be seen that pyrolytic carbon coated the diamond homogeneously (Fig.6a), Diamond grain was not eroded (Fig.6a), which is due to the protection of pyrolytic carbon [10]. Diamond was surrounded with phenolic resin by wet mixing, then phenolic resin transformed into pyrolytic carbon after pyrolysis.

Pyrolytic carbon has higher reactive activity than diamond particles, as a result, gaseous Si will firstly react with pyrolytic carbon except diamond, form a compact SiC coating around diamond which can prevent the erosion of Si. However, it is also observed that the surface of a few diamond is corroded slightly, because of the coating of diamond powders were not thorough enough.
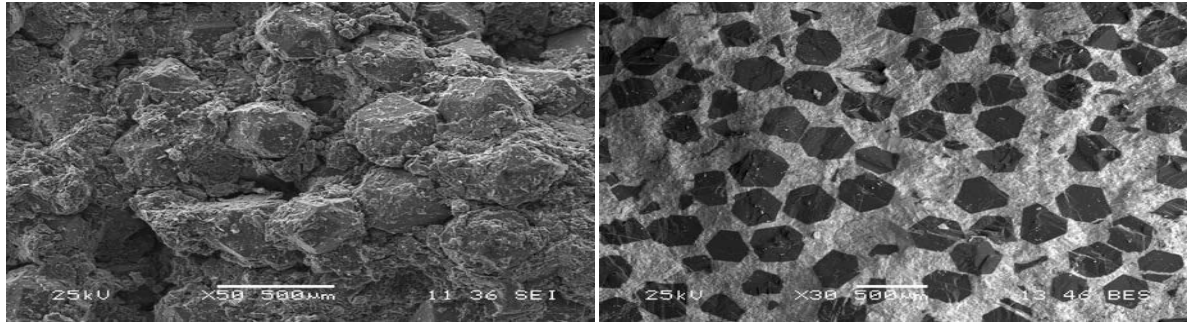


(a) green body                              (b) Diamond/SiC composite

Fig.6. Typical cross-sectional SEM micrographs of green body (a) and Diamond/SiC composite (b)

## 4.Conclusions

Diamond/SiC composites with high thermal conductivity were prepared by low pressure gaseous silicon infiltration. XRD result shows that Diamond/SiC composites compose of β-SiC, diamond and Si. It's found in the SEM results that Diamond particles distribute homogeneously in the composites and were not eroded, which is due to the protection of pyrolytic carbon. The grain sizes and content of diamond have strong effects on the properties of diamond/SiC composites, the thermal conductivity of the composites increase with the increasing grain size and content of diamond powder. When the grain size and content of diamond are 300µm and 80 wt% respectively, the thermal conductivity of the composites approach the maximum value of 280W/mk.

**References**

1.      E.A. Ekimov, N.V. Suetin, A.F. Popovich, et al, Thermal conductivity of diamond composites sintered under high pressures, Diamond Relat. Mater. 17 (2008)

838–843.

2.	Q. M. Zhang, Research on Ceramic Matrix Composites (CMC) for Aerospace Applications, Advanced Materials Research. 284(2011) 324-329.

3.	M. Herrmann, B. Matthey, S. Hohna, et al., Diamond-ceramics composites—New materials for a wide range of challenging applications, J. Eur. Ceram. Soc. 32 (2012) 1925-1923.

4.	Ko YS, Tsurumi T, Fukunaga O, Yano T. High pressure sintering of diamond-SiC composite. J Mater Sci 2001;36:469–75.

5.	G. Voronin, T. Zerda, J. Qian, Y. Zhao, D. He and S. Dub, Diamond-SiC nanocomposites sintered from a mixture of diamond and silicon nanopowders, Diamond Relat. Mater. 12(9) (2003) 1477-1481.

6.	G. Voronin, T. Zerda, J. Gubicza, T. Ungar and S. Dub, Properties of nanostructured diamond-silicon carbide composites sintered by high pressure infiltration technique, J. Mater. Res. 19(9) (2004) 2703-2707.

7.	K. Mlungwane, M. Herrmann and I. Sigalas, The low-pressure infiltration of diamond by silicon to form diamond-silicon carbide composites, J. Eur. Ceram. Soc. 28(1) (2008) 321-326.

8.	S. Nauyoks, M. Wieligor, T. W. Zerda, et al., Stress and dislocations in diamond-SiC composites sintered at high pressure, high temperature conditions, Composites Part A. 40(5) (2009) 566-572.

9.	H.L. Wang, X.G. Zhou, J.S.Yu, et al., Microstructure, mechanical properties and reaction mechanism of KD-1 SiC(f)/SiC composites fabricated by chemical vapor infiltration and vapor silicon infiltration, Mater. Sci. Eng. A 528 (2011) 2441–2445.

10.	Z.L. Yang, X.B. He, M.Wu, et al., Microstructural characterization of Diamond/SiC composites fabricated by RVI, Key. Eng. Mater. 512-515 (2012) 1105-1110.

11.	H.L. Wang, X.G. Zhou, J.S.Yu, et al., Fabrication of SiCf/SiC composites by chemical vapor infiltration and vapor silicon infiltration, Mater. Lett.64 (2010) 1691–1693.

12.	V.B. Kvaskov, Diamond in Electronics, Energoatomizdat, Moscow, 1990, p. 153, (in Russian).

13.	J. Gubicza, T. Ungar, Y. Wang, et al., Microstructure of diamond-SiC nanocomposites determined by X-ray line profile analysis, Diamond Relat. Mater. 15(9) (2006) 1452-1456

# ADVANCED TECHNOLOGIES FOR NANOSIZED $(Mo_{0.9}Cr_{0.1})Si_2$ SOLID SOLUTION PREPARATION

**Uvarova I., Kud I., Yeremenko L., Lykhodid L., and Ziatkevich D.**

*Frantsevich Institute for problems of Materials Sciences of NASU, Kyiv, Ukraine*
*e-mail:uvarova@ipms.kiev.ua*

## Abstract

The work was devoted to investigation of the regularities of the solid solution $(Mo_{0.9}Cr_{0.1})Si_2$ formation through a solid state synthesis in vacuum depending on the energy acquired by the system under milling in comparison with the behavior of the same initial mixture in the absence of preliminary mechanical activation. The reaction products at all of the stages of the synthesis were examined using XRD, TEM and chemical analyses. The energy acquired by the reaction mixture in the course of milling in planetary mills has been evaluated for mechanical activation of the initial mixture to be used in the further synthesis of molybdenum silicide powder. The calculations were performed in order to select an efficient mechanical activator and to optimize its action. The specific energy transferred under milling from the milling bodies to the mass unit of the mixture per a collision and second was calculated for various milling conditions in planetary mills LAIR 0.015 and Pulverizette 6. The research has demonstrated that the regularities of solid solution formation are affected by the dispersity and reactivity of the initial mixture, that is, by the acquired energy.

**Keywords**: *$(Mo_{0.9}Cr_{0.1})Si_2$ solid solution, mechanosynthesis, mechanical activation.*

## 1.Introduction

Advanced technologies require systematic control over the phase composition, properties and structure of materials at all of the synthesis stages in order to guarantee successful use of them in definite areas. It is especially important to control all the stages of processing materials under non-equilibrium (or far-from-equilibrium) conditions, which include processes of mechanochemistry and mechanical activation followed by low temperature synthesis [1].

As noticed [2], the principal reasons for change in the reactivity of solids upon milling are not only refinement of reagents and increase in their specific surface area, but also formation of additional crystalline defects and inclusions. Most of the energy acquired by the system is accumulated in different defects and only about 10 % of it is spent on particle refinement and increase in the specific surface area [3].

The increase in the reactivity with refinement of particles makes it possible to conduct those mechanochemical reactions that under conventional conditions require high temperatures. The higher force acts on the powder under milling and shorter its action, the more significant mechanochemical effect [4].

Hence, the ability of different processing techniques to synthesize metastable structures can be evaluated by measuring or estimating the deviation from equilibrium, i.e., the maximum energy that can be stored as an excess compared to that of the equilibrium structure. On the other hand, under certain conditions of mechanical alloying or mechanochemical reactions, a mechanically activated self-propagating synthesis (MASPS) may take place [1].

Silicides of transition metals refer to the most promising compounds for creation of heat-resistant materials. Among them there is molybdenum disilicide, which is widely used in manufacture of heaters that operate in air to $1700^{\circ}C$. A shortcoming of the heaters is the low resistance to heat cycling as a result of fracture of the oxide film and evaporation of the protective molybdenum oxide at relatively low temperatures (700-$900^{\circ}C$) [5].

One of the ways to overcome this shortcoming is selection of optimal combination of molybdenum disilicide with other refractory compounds, which provides higher physicochemical properties compared to the individual compounds and production of novel composite refractory materials. One of such combinations is the $MoSi_2$-$CrSi_2$ system, which refers to the eutectic type with limited dissolution and has a broad enough region of solid solutions on both the side of molybdenum disilicide (up to 46 mol% $CrSi_2$) and chromium disilicide (up to 36 mol% $MoSi_2$). Herein intermediate solutions are $Mo_3Si$-$Cr_3Si$, $Mo_5Si_3$-$Cr_5Si_3$, and $MoSi_2$-$CrSi_2$ [6].

## 2.Materials and methods

In the investigation of solid phase interaction in the Mo-Cr-Si system, powders of silicon (99.998 % Si, Ssp = 2.2 $m^2$/g produced by the Svitlovodsk Plant of Hard Alloys, Ukraine); molybdenum PM 99.95 (99.95 % Mo, Ssp = 0.5 $m^2$/g, Firm "Polema", Russia), and electrolytic chromium PERCr-1/280 (98.7 % Cr, Ssp = 0.2 $m^2$/g, "Polema", Russia) were used. The initial mixtures were calculated for the expected products: $MoSi_2$, $CrSi_2$, $Mo(Cr)$, $Mo_xCr_ySi_2$. They were homogenized by mixing in a planetary mill Pulverizette–6 in a steel drum at a rotation speed of 100 rev/min for 2 h in a reverse regime. The particle size did not exceed 10 µm.

Both mechanical activation and mechanosynthesis of powder mixtures were performed in an argon medium in a planetary mill AIR-0,015 at a drum rotation speed of 1350 rev/min with the acceleration 25 g and in a planetary mill Pulverizette–6 at a drum

rotation speed of 200 rev/min. The steel drums and milling 10 mm diameter balls were prior charged with silicon to avoid contamination of the products with the reactor material.

Mechanosynthesis process was studied depending on the energetic state of the system which was regulated by varying the milling time (60 and 90 min) and the balls-to-powder mass ratio (BPR) (10:1, 20:1, and 30:1). The drum surface temperature was controlled in a discrete way.

The effect of the process duration on the kinetics and mechanism of formation of refractory compounds during heat treatment was studied in vacuum at the same BPR. Mechanical activation of initial mixtures was performed at softer energetic state: BPR 10:1, process duration 30, 60, and 90 min (AIR) and 10,30,50 h (Pulverizette), which resulted in refining the powder and accumulation of structural defects, but such a degree of activation did not provide the occurrence of the chemical reaction that yields silicide, boride, and carbide phases under milling.

Solid-phase interaction in briquetted powdered reaction mixtures took place in an electric vacuum furnace SNV-–1.3, 1/20–I1 in a vacuum of $\approx 1 \cdot 10^{-3}$ Pa in the temperature range 400–1200$^{\text{o}}$C at an isothermal holding of 2 h.

The synthesis products were examined by an XRD analysis using a diffractometer DRON-3 under filtered Co radiation. The angles were determined with an error of $\pm 0.05$ grad. The size of crystallites was calculated using the Sherrer formula. The phases were identified following the powder diffraction database file ICDD-JCPDS PDF-2. The particle size and elemental composition of the powders produced by a low temperature synthesis were determined with help of a transmission electron microscope JEM 2100 S (Japan). Standard techniques of chemical analysis were used for determination of the elemental composition of the final product and estimation of the amount of iron milled into it.

## 3.Results and discussion

As known, solid solutions of refractory materials are traditionally synthesized via solid phase reactions between the elements or between the individual silicides at high temperatures. . Therefore the process of solid state interaction of Mo, Cr and Si at high temperature synthesis was studied and phase composition of the products in this system is presented in Fig. 1.
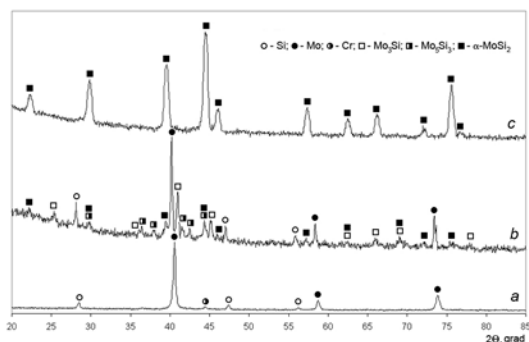
(a) 600; (b) 1000; (c) 1200°C

Fig.1. The XRD patterns from the products of solid-phase interaction of microsized initial components Cr, Mo and Si in vacuum
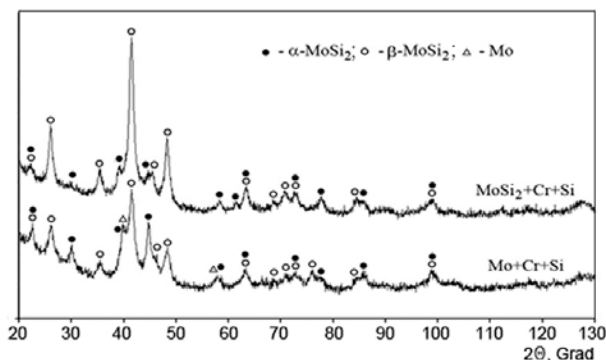
Fig.2. The XRD patterns from mechanosynthesis products

The XRD data for the products of solid-phase interaction in vacuum of microsized powders of chromium and molybdenum disilicides (Table 1) evidence the fact that processes of formation of substitution solid solutions in the temperature region 900-1200°C proceed due to the mutual diffusion of molybdenum into chromium disilicide and chromium into molybdenum disilicide, which is confirmed by the changes in the lattice parameters of the initial compounds.

Table 1. The XRD data for solid-phase interaction in vacuum of molybdenum and chromium disilicides powders

| Conditions of interaction | | XRD data | | | | |
|---|---|---|---|---|---|---|
| | | | Lattice parameters, nm | | | |
| | | Phase composition | $MoSi_2$ | | $CrSi_2$ | |
| Temperature, °C | Time, h | | a | c | a | c |
| Initial mixture | | $MoSi_2$, $CrSi_2$ | 0.321 | 0.786 | 0.443 | 0.636 |
| 900 | 2 | $MoSi_2$, $CrSi_2$ | 0.320 | 0.787 | 0.445 | 0.638 |
| 1000 | 2 | $MoSi_2$, $CrSi_2$ | 0.318 | 0.788 | 0.442 | 0.637 |
| 1100 | 2 | $MoSi_2$, $CrSi_2$ | 0.319 | 0.788 | 0.442 | 0.638 |
| 1200 | 2 | $MoSi_2$, $CrSi_2$ | 0.318 | 0.787 | 0.444 | 0.635 |
| | 4 | $MoSi_2$, $CrSi_2$ (traces) | 0.319 | 0.788 | – | – |
| | 5 | $MoSi_2$, $(Mo_{0.9}Cr_{0.1}Si_2)$ | 0.319 | 0.789 | – | – |

In molybdenum disilicide $a$ reduces and $c$ increases over the whole temperature range, which reflects the fact of the lattice distortion. As for chromium disilicide, the parameters change chaotically. Beginning from the solid state interaction temperature, the reflection intensities of chromium disilicide decreases, whereas those for molybdenum disilicide monotonously rise and reach a maximum at $1200^{o}C$ and an isothermal holding of 5 h. First of all, this may be attributed to the difference in the diffusivities of molybdenum and chromium by three orders of magnitude ($D_{Mo}$=2.7 $10^{-3}$ cm$^2$/sec, $D_{Cr}$=4.8 cm$^2$/sec) [7].

Synthesis of nanosized powders of refractory compounds and their solid solutions under intense milling may proceed in two directions: mechanosynthesis and mechanical activation with following thermal treatment.

Process of mechanosynthesis was researched depending on the intensity of milling which varied by changing BPR (10:1 and 20:1) and duration of milling (60 and 90 min) using a pulse regime with a discrete control of temperature on the drum surface with taking into account the temperature gradient through the drum volume equal to $\approx 60^{o}C$.

Refractory compounds can be produced via mechanosynthesis using some versions: (i) synthesis from powders of individual elements; (ii) synthesis from compounds (precursors) containing necessary elements, and (iii) synthesis from both elements and compounds [8-10]. It has been noticed that mechanosynthesis may proceed more intensely when one of the reagents is taken in the form of a compound with the others being elements. Therefore, a comparative investigation has was carried out for obtaining a nanosized $Mo_{0,9}Cr_{0,1}Si_2$ powder via the following versions of mechanosynthesis:

- mechanosynthesis  from powders of initial elements;
- mechanosynthesis  of reaction  mixture composed of prior prepared nanosized $MoSi_2$ (as a precursor) and chromium and silicon powders.

Nanosized molybdenum disilicide powder was obtained by mechanosynthesis of initial components under before established conditions: BPR 20 : 1, process duration 90 min, impulse regime. Mechanosynthesis of the solid solution $Mo_{0,9}Cr_{0,1}Si_2$ was conducted under the same conditions from all of the above initial mixtures. The interaction products were examined by chemical, XRD and TEM analyses. The phase composition of the mechanosynthesis products is given in Table 2

Table 2. The data of XRD analysis for mechanosynthesis products

| Initial mixtures | Phase composition of synthesis products (lattice parameters, nm) |
|---|---|
| Mo, Cr, Si, | Mo (a=0,315); $\alpha$-MoSi$_2$ (a=0,319; c=0,788); $\beta$-MoSi$_2$ (a=0,458; c=0,657) |
| MoSi$_2$, Cr, Si | Mo (a=0,316); $\alpha$-MoSi$_2$ (traces); $\beta$-MoSi$_2$ (a=0,461; c=0,665) |

By the XRD data, mechanosynthesis provides formation of the $Mo_{0,9}Cr_{0,1}Si_2$ solid solution: the $MoSi_2$ lattice parameters change for all mixtures used, but each mixture demonstrates its own peculiarities. For the first version of mechanosynthesis, the initial mixture is composed of Cr, Mo and Si powders and the product is a solid solution on the basis of molybdenum disilicide of two modifications, tetragonal $\alpha$-MoSi$_2$ and hexagonal $\beta$-MoSi$_2$, with their practically equal amounts. For the second version, the basic phase is $\beta$-MoSi$_2$ added with $\alpha$-MoSi$_2$ traces. This feature may be prescribed to some difference in the mechanisms of solid solution formation for either version. In the first case, a chemical reaction prevails which is accompanied by formation of molybdenum disilicide formation of two modifications. In the second case (when the reaction mixture contains prior prepared nanosized powder of precursor mainly composed of $\beta$-MoSi$_2$ and traces of $\alpha$-MoSi$_2$), a solid solution is formed by a diffusion mechanism.

In addition, there is free molybdenum in the mechanosynthesis products. No chromium silicide phase was detected by XRD. The diffraction maxima from machanosynthesis products indicate a nonequilibrium and high energetic state of the system at the expense of its high imperfectness, formation of new surfaces, and high dispersity (Fig. 2).

The chemical analysis of mechanosynthesis powders obtained via the both versions manifests an elevated oxygen (2.3 and 3.7 mass%) and iron (4.2 and 6.7 mass%) contents, respectively. The great difference in contamination of the powders depending on the reaction mixture composition may be connected, first of all, to the fact that in the

second version, nanosized molybdenum disilicide (precursor) powder was used as an initial mixture component with an iron content of 2.6 mass%.

Hence the investigation performed has shown that it is impossible to produce a homogeneous nanosized powder of the solid solution $Mo_{0.9}Cr_{0.1}Si_2$: the products contain molybdenum. A solid phase synthesis takes place thanks to high-energy refining the initial powder and proceeds by the mechanism of reaction diffusion in the initial component contact areas. The phase and chemical compositions of mechanosynthesis depend on the state of the initial reaction mixtures.

The effect of the process parameters of high-energy processing of powders (mechanically activation) under different milling conditions on the state of reaction mixture of initial component (molybdenum, chromium, and silicon) was studied at the same BPR(10:1) and at different milling times in the planetary mills AIR and Pulverizette.

According to the XRD data, the type of a mill, that is, milling conditions are of great importance. The patterns from mixtures that underwent high-energy treatment in the Pulverizette-6 mill are characterized by sharp decrease in the intensities and broadening of diffraction maxima for all of the initial components caused by refinement, which is also confirmed by monotonous increase in the specific surface area from 3.58 (5 h) to 5.35 $m^2$/g (50 h).

The mixtures produced in the AIR mill (Fig. 3) are characterized, in addition to changes in the intensities and broadening of diffraction peaks after 30 min milling (Fig. 3 a), by the absence of silicon and formation of the higher silicide molybdenum nuclei after 60 min milling (Fig. 3 b). The XRD data from the reaction mixture milled for 90 min indicate marked changes in the phase composition (Fig. 3 c): silicon and chromium disappear, and formation of a solid solution based on the high temperature molybdenum disilicide modification β-$MoSi_2$ begins, which is exhibited by the difference in the lattice parameters (a=0.457, c=0.678 nm against the reference values a=0.464, c=0.653 nm).

Mechanical alloying is a high-energy milling process, in the course of which internal strains arise in a solid body, which deform interatomic bonds, initiate defects of crystalline structure and excite the electronic subsystem of the crystal. In the formation of a new surface, energetic expenses on structure reconstruction are minimal and the near-surface atoms have a great extra energy resource, which creates favorable conditions for diffusion and chemical processes in contact areas, like the action of the temperature factor. In this case, therefore, a continuous row of solid solutions may be expected.
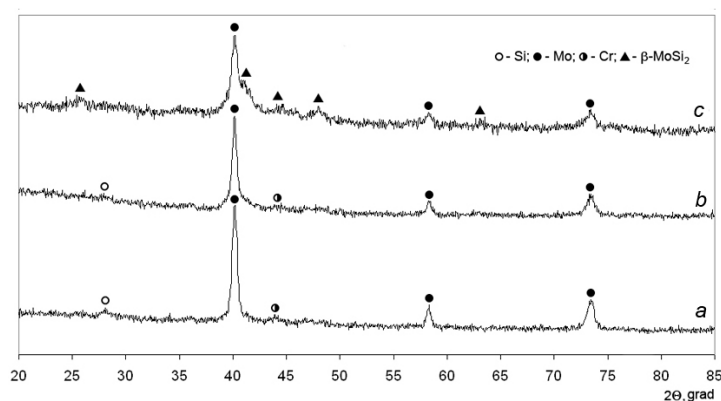
(a) 30; (b) 60; (c) 90 min

Fig.3. The XRD patterns from reaction mixture milled in the planetary mill AIR.

The morphology of the powders obtained (Fig. 4) differs as well. The powder prepared in the planetary mill Pulverizette is composed of separated rolled particles whereas the use of AIR yields more agglomerates.



a                                    b                                    c
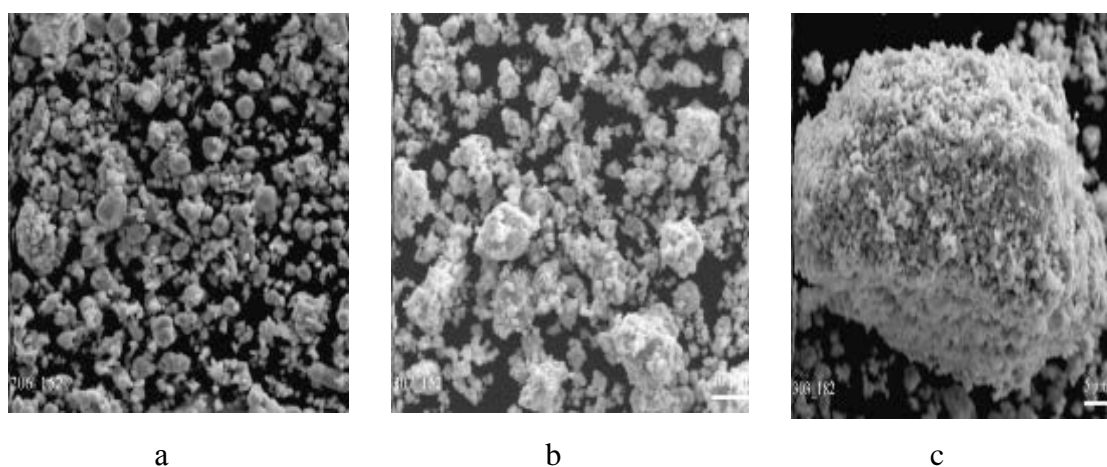
(a) Pulverizette (1800 min); (b) AIR (60 min); (c) AIR (90)min

Fig.4 The morphology of powder particles obtained in planetary mills of different type at a BPR of 10:1

The regularities of the solid solution $Mo_{0.9}Cr_{0.1}Si_2$ formation in the process of solid-phase interaction of mechanically activated reaction mixtures were investigated in the temperature range 400–1000$^{o}$C. The data of XRD analysis of the products (phase composition) are presented in Tab.3.

Table 3. XRD Data for the Products of Two-hour Solid State Interaction of Mechanically Activated

Reaction Mixtures in Vacuum

| Temperature of interation, °C | Phase composition | | | | |
|---|---|---|---|---|---|
| | Time of mechanical activation in "Pulverizette-6", min | | Time of mechanical activation in "AIR-0.015", min | | |
| | 1800 (mixture 2) | 3000 (mixture 3) | 30 (mixture 4) | 60 (mixture 6) | 90 (mixture 7) |
| Reaction mixture | Mo, Si, Cr | Mo, Si, Cr | Mo, Si, Cr | Mo, $\alpha$-MoSi$_2$ | Mo, $\alpha$-MoSi$_2$ |
| 400 | Mo, Si, Cr | Mo, Si, Cr | Mo, Si, Cr | Mo, $\alpha$-MoSi$_2$ | Mo, $\alpha$-MoSi$_2$ |
| 500 | Mo, Si, Cr | Mo, Si, Cr | Mo, Si, Cr | Mo, $\alpha$-MoSi$_2$ | Mo, $\alpha$-MoSi$_2$ |
| 600 | Mo, Si, Cr, Mo$_3$Si, Mo$_5$Si$_3$ | Mo, Si, Cr, Mo$_3$Si, Mo$_5$Si$_3$ | Mo, Si, Cr, $\beta$-MoSi$_2$[*] | Mo, $\alpha$-MoSi$_2$, $\beta$-MoSi$_2$ | $\alpha$-MoSi$_2$, $\beta$-MoSi$_2$, Mo[*] |
| 700 | Mo, Si, Cr, Mo$_3$Si, Mo$_5$Si$_3$ | Mo, Si, Cr, Mo$_3$Si, Mo$_5$Si$_3$ | Mo, Si, $\alpha$-MoSi$_2$, $\beta$-MoSi$_2$ | Mo, $\alpha$-MoSi$_2$, $\beta$-MoSi$_2$ | $\alpha$-MoSi$_2$, $\beta$-MoSi$_2$ |
| 800 | Mo, Si, Cr, Mo$_3$Si, Mo$_5$Si$_3$ | Mo, Si, Cr, Mo$_3$Si, Mo$_5$Si$_3$ | Mo, Si, $\alpha$-MoSi$_2$, $\beta$-MoSi$_2$ | $\alpha$-MoSi$_2$, $\beta$-MoSi$_2$ | $\alpha$-MoSi$_2$ |
| 900 | Mo, Si, Mo$_3$Si, Mo$_5$Si$_3$, $\alpha$-MoSi$_2$ | Mo, Si, Mo$_3$Si, Mo$_5$Si$_3$, $\alpha$-MoSi$_2$ | $\alpha$-MoSi$_2$, $\beta$-MoSi$_2$[*] | $\alpha$-MoSi$_2$ | - |
| 1000 | Mo$_3$Si, Mo$_5$Si$_3$, $\alpha$-MoSi$_2$, Mo[*], Si, | Mo$_3$Si, Mo$_5$Si$_3$, $\alpha$-MoSi$_2$, Mo[*], Si, | $\alpha$-MoSi$_2$ | - | - |
| 1100 | $\alpha$-MoSi$_2$, Mo$_5$Si$_3$[*], Si[*] | $\alpha$-MoSi$_2$, Mo$_5$Si$_3$[*], Si[*] | - | - | - |
| 1200 | $\alpha$-MoSi$_2$ | $\alpha$-MoSi$_2$ | - | - | - |

When reaction mixtures were subjected to mechanical processing in the Pulverizette mill for 1800 and 3000 min, the beginning of solid-phase interaction was fixed as early as at $500^{\circ}$C (for comparison, $700^{\circ}$C for microsized powders) and went on through successive formation of solid solutions on the basis of silicide phases of molybdenum, namely $Mo_3Si$ and $Mo_5Si_3$. At $900^{\circ}$C, the higher molybdenum silicide $\alpha$-$MoSi_2$ appeared, and at $1000^{\circ}$C the interaction products were a mixture of the initial components and all of the above phases.

According to the XRD patterns from the reaction mixture mechanically activated for 30 min, at $600^{\circ}$C. the interaction product contains all the initial components, that is Mo, Si, and Cr, plus $\beta$-$MoSi_2$ nuclei. In the temperature range $700$-$800^{\circ}$C, chromium peaks disappear and an $\alpha$-$MoSi_2$ based phase is formed, the amount of which gradually increases. At $900^{\circ}$C the interaction yields the solid solution $(Mo_x,Cr_y)Si_2$ on the basis of the both ($\alpha$ and $\beta$) modifications of molybdenum disilicide, and at $1000^{\circ}$C the $\beta \rightarrow \alpha$ polymorphic transition occurs.
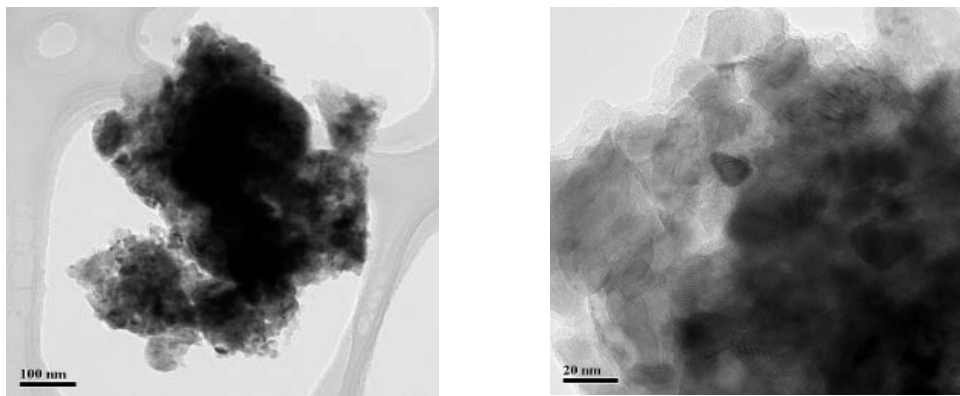


Fig.5. The microstructure of nanosized powders of the solid solution
$Mo_{0.9}Cr_{0.1}Si_2$ obtained at $600^{\circ}$C

The solid state interaction of reaction mixtures activated in the planetary mill AIR for 60 and 90 min is different from that for 30 min, which is due to a higher acquired energy and different composition of mechanically activated reaction mixtures containing $\alpha$-$MoSi_2$ nuclei, molybdenum and XRD-amorphous silicon. As formation of silicides through a solid state synthesis is determined by silicon-in-metal diffusion, the availability of much silicon in an XRD-amorphous state ensures its higher reactivity compared to crystalline silicon and leads to the formation of solid solution on the basis of molybdenum

disilicide of both modifications at 700 and 800 $^{o}$C depending on the milling duration. The size of polycrystals calculated using the Sherrer formula is 20 nm for $\alpha$-MoSi$_2$ and 15 nm for $\beta$-MoSi$_2$. The rise in synthesis temperature by 100 $^{o}$C stimulates the polymorphic $\beta \rightarrow \alpha$ transition.

Figure 5 shows the structure of nanosized powders of the solid solution Mo$_{0.9}$Cr$_{0.1}$Si$_2$ obtained at 600$^{o}$C from both the initial elements and the precursor with silicon.

Nanosized powder of the solid solution Mo$_{0.9}$Cr$_{0.1}$Si$_2$ synthesized from initial elements is composed of polycrystalline agglomerates sizing to 100 nm, whose grains do not exceed 10 nm.

To sum up, the work done has shown that the dominant factor affecting the kinetics of solid solution formation is the reactivity of initial mixture, and the size factor practically does not influence the kinetics of solid solution formation.

## 4.Conclusions

The performed researches have revealed the peculiarities of solid solution formation depending on the state of initial components and solid-phase synthesis conditions.

The formation of solid solution from microsized powders proceeds by a reaction-diffusion mechanism via successive formation of solid solutions based on both lower and higher silicide phases of molybdenum followed by their interaction (homogenization) 1200 $^{o}$C. Herein diffusion processes prevail.

Mechanical activation of the initial components mixture for 90 min is characterized by marked increase in the process rate accompanied by significant decrease in the temperatures of the end (by 400$^{o}$C) of interaction. The formation of the solid solution Mo$_{0,9}$Cr$_{0,1}$Si$_2$ is characterized by the absence of intermediate lower molybdenum silicide phases.

Formation of refractory metal disilicides occurs by a reaction diffusion mechanism, characterized by prevailing the chemical reaction rate over that of diffusion processes. Therefore, it is impossible to yield a homogeneous nanosized powder of the solid solution Mo$_{0,9}$Cr$_{0,1}$Si$_2$ by mechanosynthesis: the products contain molybdenum.

## References

1.      Suryanarayana C, Mechanical alloying and milling Progress in Materials Science 46 (2001) 1±184.

2.      Болдырев В.В., Ляхов Н.З., Чухахин А.П. Химия твердого тела.- Москва Знание, 1982.- 63 с.

3.      Скороход В.В., Уварова І.В., Рагуля А.В. Фізико-хімічна кінетика в наноструктурних системах.- Київ Академперіодика, 2001, 177 с.

4.      H. Gleiter.      Nanoctructural      Materials:      Basic      Concepts      and Microstructure, Acta. Mater., *2000, 48* (1) P.1-29

5.      Самсонов Г.В., Дворина Л.А., Рудь Б.М. Силициды. – М.: Металлургия, 1979. – 271с.

6.      H.J.Goldschmidt "Interstitial alloys", Butterworths, London, 632 p.,1967.

7.      Свойства элементов. Ч.1 Физические свойства. Справочник. М., Металлургия, 1976, 384 с.

8.      Grigorieva T.F., Barinova A.V., Lyakhov N.Z. Mechanosynthesis of Nanocomposites //J. of Nanoparticle Research. – 2003. – 5. – P. 439–453.

9.      Болдырев В.В. Механохимия и механическая активация твердых веществ //Успехи химии. – 2006. – Т. 75, №3. – С. 203–216.

10.     Le Caer G., Bau E., Er–g Rosse, Pianelli A., Bouzy. Mechanically Driven Syntheses of Carbides and Silicides //J. Mater. Sci. – 1990. – 25. – P. 4726–4731.

# MICROSTRUCTURE AND MECHANICAL PROPERTIES OF AL$_2$O$_3$-20 WT%AL$_2$TIO$_5$ COMPOSITE PREPARED FROM ALUMINA AND TITANIA NANOPOWDERS

**Ebadzadeh T., Barzegar-Bafroei H.**

*Materials & Energy Research Centre, POBox: 31787/316, Karaj, Alborz, Iran*
*e-mail: ebadzadehtouradj@yahoo.co.uk*

## Abstract

Al$_2$O$_3$-20wt%Al$_2$TiO$_5$ composite was prepared from reaction sintering of alumina and titania nanopowders. After mixing, the nanostructured powders were pressed and pressureless-sintered into bulk ceramics at different temperatures. SEM observations showed a proper interface between Al$_2$TiO$_5$ and Al$_2$O$_3$ grains and preferential distribution of aluminiumtitanate particles in the grain boundaries. XRD analysis indicated the absence of rutile and titania in the sintered composite ensuring complete formation of aluminiumtitanate. Hardness of samples sintered at 1300°, 1400°, 1500 °C were 4.8, 6.2 and 8.5 GPa, respectively.

**Keywords:** *Alumina; Aluminiumtitanate; Nanopowders; Microstrucrure.*

## 1. Introduction

Aluminumtitanate (AT), Al$_2$TiO$_5$, is known to be a promising candidate material for the application fields of refractory and engine components because of its low thermal expansion, excellent thermal shock resistance, and low thermal conductivity [1]. AT exhibits two allotropic forms: α and β, where β-AT is the stable phase [2]. In general, AT can be formed by the solid-state reaction between Al$_2$O$_3$ and TiO$_2$ above the eutectoid temperature 1280°C [3]. AT exhibits microcracking during cooling from the sintering temperature especially above critical sintered grain size of 1.5µm bringing out the necessity for obtaining fine-grained microstructure [4]. Alumina is widely employed in various applications because of its high temperature stability, chemical inertness and wear resistance. However, alumina has poor thermal shock resistance [5]. In alumina based composites, much attention has been focused on the improvement of fracture toughness and thermal shock resistant of alumina matrix either by the addition of second phase. Earlier reports suggest that the addition of AT particles to alumina improves thermo-mechanical response of alumina–AT composite through control of grain size [6,7]. Improved flaw tolerance has been observed as a result of addition of AT due to induced residual stresses by virtue of thermal expansion mismatch between alumina and AT [8]. The alumina–AT composites exhibit functional as well as structural properties for applications as thermal barrier coating, insulating components for diesel engines and high temperature substrates [9]. Further improvement in mechanical properties of alumina–AT

composite is attributed to the combined effect of internal stresses developed due to AT and large particle size of alumina [10]. In the present work, we report the preparation of $Al_2O_3$-20wt%$Al_2TiO_5$ composite from alumina and titania nanopowders using reaction sintering method.

## 2. Experimental procedures

$Al_2O_3$ (α phase, 99% grade, PL-A-AlO, Plasmachem, Germany) and $TiO_2$ (mixture of anatase and rutile, 99% grade, P25, Degussa Co., Frankfurt, Germany) nanopowders were used as the received powders. The nanosized powders were blended in a ball-mill uniformly to produce a powder mixture containing 80 wt.% $Al_2O_3$ and 20 wt.% $TiO_2$. Powder mixtures were uniaxially compacted under different loads in a rigid die (10 mm diameter) using PVA as the binder. The green density was obtained by measuring the ratios of weight to volume of the green compacts. These compacts were sintered at temperatures of 1300°, 1400° and 1500°C for 2h in air. In order to suppression of aluminiumtitanate decomposition, the cooling rate of 30°C/min in temperature range 1200° -800°C was applied. X-ray diffraction instrument with CuKα radiation (Philips, X'Pert) was used to determine the phase composition. Microstructural observations were performed using a scanning electron microscope (Philips XL30, Netherlands) equipped with energy dispersive X-ray spectrometer (EDS). The determination of size and shape of nanoparticles was performed using a transmission electron microscope (TEM, CM200FEG, Philips, Netherlands). Mechanical properties were assessed by Vickers microindentation using loads from 9.8 to 98 N (from 1 to 10kg). Ten indents were made for each measurement. The density of the sintered specimens was measured by the Archimedes method using distilled water as the liquid.

## 3. Results and discussion

Fig. 1a and b show the morphology and XRD of the reconstituted powders, respectively. It can be observed that the nanostructured reconstituted powders consist of agglomerates which are composed of fine crystallites (fig. 1a). Fig. 1b shows XRD patterns of the nanostructured reconstituted powders. The mixture shows mainly three major crystalline phases: α-Alumina, rutile and anatase that similar to nanosized raw materials powders. One of the most crucial features for producing dense ceramics is the

powder compressibility by which the compact green density and therefore the density of sintered samples are directly contributed.
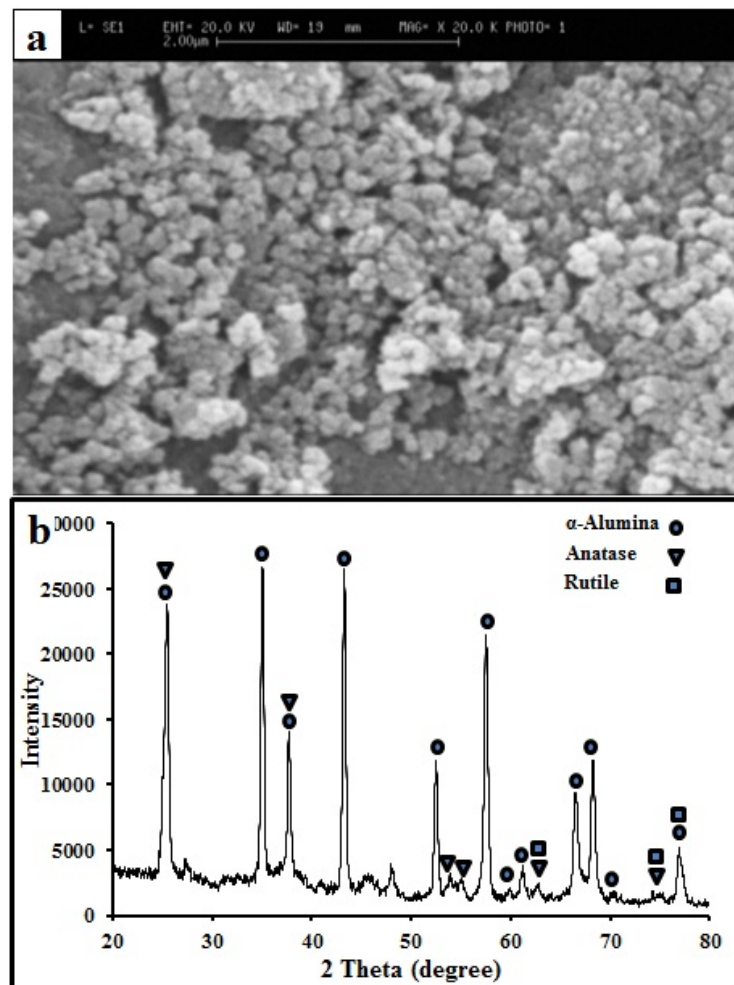


Fig 1. (a) SEM micrograph and (b) XRD patternof $Al_2O_3$-$TiO_2$ nanocomposite powder.

Groot Zevertetal. [11] showed that in the case of the agglomerated powders, there was a turning point ($P_y$) in the plot of the relative density versus logarithm of the applied pressure, like that shown in Fig. 2. The curve was divided into two sharply separated linear parts with an interception at point $P_y$.

The interception was called "strength of the agglomerates". After compaction at a pressure of around $P_y$, these agglomerates were gradually fragmented and then rearranged at lower pressures [11]. As can be seen the agglomeration strength of the powder is about 156 MPa. The value of $P_y$ depends heavily on the method of synthesis and calcinations temperature [12]. Fig.3a and b illustrate the X-ray diffraction patterns recorded from the $Al_2O_3$-20wt.%
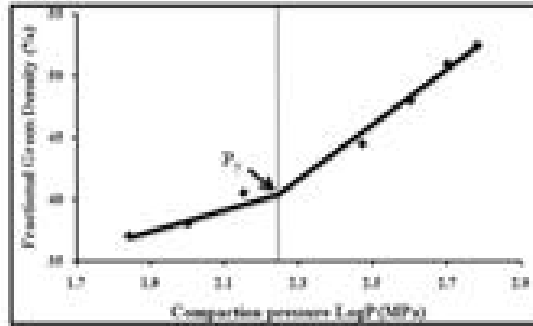
Fig 2. Fractional green densities of composite nanopowder as function of log compaction pressure (P).
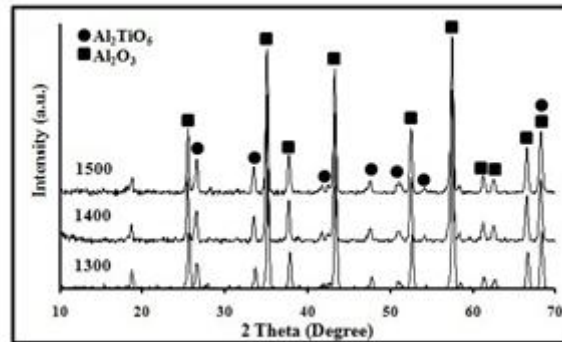


Fig. 3. (a) and (b) XRD patterns of the composites obtained from the nanostructured $Al_2O_3$-$TiO_2$ powders sintered at different sintering temperature.

AT composites treated at different temperatures for 2h. From XRD results it is clear that the composites sintered at different temperatures are composed of the same phases, i.e. $\alpha$-$Al_2O_3$ and AT. It can also be noted from XRD patterns the absence of the diffraction peaks of $TiO_2$, which means all of $TiO_2$ reacted with $Al_2O_3$ to form AT. In order to get a better compare the relative intensities of alumina and aluminiumtitanate phases, XRD patterns of sintered samples were applied in the $2\theta$ range between 25 and 28 (fig. 3b). The density and mechanical properties of $Al_2O_3$-20 wt.% AT bulk composites sintered at different temperatures are listed in Table 1. The apparent and relative densities increased from 3.41 to 3.67 g/cm$^3$ and 87.3 to 94.1%, respectively, as the sintering temperature increased from 1300° to 1500°C.

This can be attributed to a large number of contact points because of nanostructure composite powders and the higher fractions of fine particles resulting in the shorter diffusion paths. This in turn increases the average coordination number of particles,

166

leading to enhanced sintering [13]. The mechanical properties of the reaction sintered $Al_2O_3$-20wt.% AT ceramics are also shown in Table 1.

Table 1. Properties of $Al_2O_3$- 20% wt $Al_2TiO_5$ ceramic composites obtained at different sintering temperatures.

| Sintering temperature (°C) | Relative density (%) | Apparent density (g/Cm$^3$) | Fracture toughness (Mpam$^{1/2}$) | Vickers hardness (Gpa) |
|---|---|---|---|---|
| 1300 | 87.3 | 3.41 | - | 4.8±0.3 |
| 1400 | 91.05 | 3.55 | 3.4±0.1 | 6.2±0.5 |
| 1500 | 94.1 | 3.67 | 4.16±.27 | 8.5±0.7 |

From this table, the relationship between the fracture toughness and Vickers hardness showed the same trend as the between relative density and sintering temperature. As known, ceramics prepared by the nanostructured powders obtain highly homogeneous microstructure as the result of their beneficial sintering behavior than those prepared by micron size powders. Therefore, the nanostructured composites have more excellent mechanical properties compared with microstructured ones reported in literatures.

High magnification SEM (Fig. 4) proved a proper interface between AT and $Al_2O_3$ grains and also preferential distribution of aluminiumtitanate particles in the grain boundaries. The distribution of aluminiumtitanate grains in the alumina matrix was confirmed by SEM-EDX analysis as shown in Fig. 4. The microstructure analysis of the composite sintered at 1500 °C showed that the grain size of aluminiumtitanate is lower than that of alumina.

## 4. Conclusion

$Al_2O_3$-20% wt AT composites were prepared by the reaction sintering of alumina and titania nanopowders at different temperatures. The relative density of composite after sintering at 1500°C was 94.1%. Fracture toughness and hardness increased with increasing sintering temperature, reached to 4.16 MPam$^{1/2}$ and 8.5 GPa, respectively.
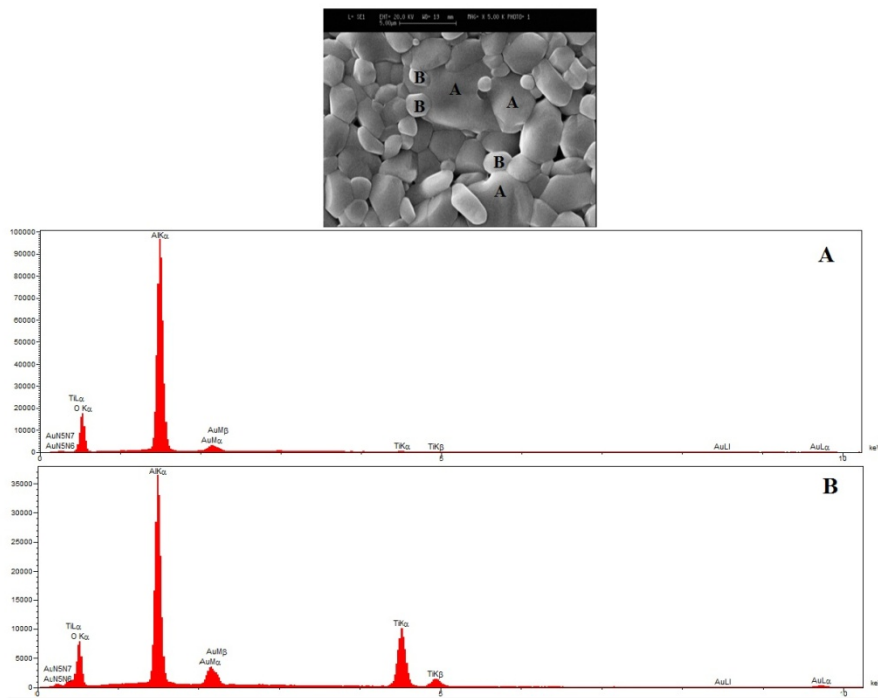
Fig. 4. Nanostructured $Al_2O_3$-20% wt $TiO_2$ powders sintered at1500°C (marked area is the spot where the EDX analysis was performed).

## References

1.      Thomas H.A.J. and Stevens R. Aluminum titanate a literature review, Part 1: microcracking phenomena. Br. Ceram. Trans. J. 1989; 88 : 144-151.

2.      Prasadarao A.V., Selvaraj U., Komarneni S., Bhalla A.S. and Roy R. Enhanced densification by seeding of sol–gel-derived aluminum titanate. J. Am. Ceram. Soc. 1992; 75: 1529-151533.

3.      Kato E., Daimon K. and Takahashi J. Decomposition temperature of B-$Al_2TiO_5$. J. Am. Ceram. Soc. 1980; 63 : 355-356.

4.      Padture N.P., Runyan J.L., Bennison S.J., Braun L.M. and Lawn B.R.: Model for toughness curves in two-phase ceramics, II: microstructural variables. J. Am. Ceram. Soc. 1993; 76 : 2241-2247.

5.      Runyan J.L. and Bennison S.J. Fabrication of flaw-tolerant aluminum titanate-reinforced alumina. J. Eur. Ceram. Soc. 1991; 7 : 93-99.

6.      Jayasankar M., Hima K.P., Ananthakumar S., Mukundan P., KrishnaPillai P. and Warrier K.G.K. Role of particle size of alumina on the formation of aluminum titanate as

well as on sintering and microstructure development in sol–gel alumina–aluminum titanate composites Mater.Chem.Phys. 2010; 124 : 92-96.

7.      Uribe R. and Baudin C. Influence of a dispersion of aluminum titanate particles of controlled size on the thermal shock resistance of alumina. J. Am. Ceram. Soc. 2003; 86 : 846-850.

8.      Padture N.P., Bennison S.J. and Chan H.M. Flaw-tolerance and crack-resistance properties of alumina–aluminum titanate composites with tailored microstructures. J. Am. Ceram. Soc. 1993; 76 : 2312-2320.

9.      Nieto M.I., Baudı́n C. and Santacruz I. Reaction sintering of colloidal processed mixtures of sub-micrometric alumina and nano-titania. Ceram.Int. 2011; 37 : 1085–1092.

10.     Bueno S., Hernández M.G., Sánchez T., Anaya J.J.  and Baudín C. Non-destructive characterisation of alumina/aluminum titanate composites using a micromechanical model and ultrasonic determinations, Part I: evaluation of the effective elastic constants of aluminum titanate. Ceram.Int. 2008; 34 : 181-188.

11.     Groot Zevert W.F.M., Winnubst A.J.A., Theunissen G.S.A.M. and Burggraaf A.J. Powder preparation and compaction behavior of fine-grained YTZP. J. Mater. Sci. 1990; 25 : 3449-3455.

12.     Bukaemskiy A.A., Barrier D. and Modolo G. Compressibility and sinterability of $CeO_2$-8YSZ by a wet chemical method. J. Eur. Ceram. Soc. 2009; 29 : 1947-1954.

13.     Mazaheri M., Zahedi A.M., Haghighatzadeh M. and Sadrnezhaad S.K. Sintering of titania nanoceramic: densification and grain growth. Ceram.Int. 2009; 35 : 685-691.

# SPARK PLASMA SINTERING OF ZRC-ZRO$_2$ COMPOSITES

**Hussainova Irina [1], Voltšihhin Nikolai [1], Cura Erkin [2], Hannula Simo-Pekka [2], Rainer Traksmaa [3]**

[1]*Department of Materials Engineering, Tallinn University of Technology, Ehitajate 5, 19086 Tallinn, Estonia*
[2]*Department of Materials Science and Engineering, Aalto University School of Chemical Technology, POB 16200, Aalto 00076, Finland*
[3]*Centre for Materials Research, Tallinn University of Technology, Ehitajate 5, 19086 Tallinn, Estonia*
*e-mail: irina.hussainova@ttu.ee*

## Abstract

ZrC matrix composites added by nanosized partially stabilized zirconia were sintered by spark plasma sintering technique to >99% of theoretical density at 1600 °C and pressure of 50 MPa. The volume fraction of additives varied from 25 to 40 % in the precursor powder blend. Microstructural analysis shows quite uniform phase distribution, while phases are in the micron size range. The presence of the retained tetragonal zirconia in ZrC-ZrO$_2$ composite increased the fracture toughness due to stress induced by transformation toughening.

**Keywords:** *ceramic composite; spark plasma sintering; microstructure; mechanical properties*

## 1.Introduction

Zirconium carbide (ZrC) belongs to a class of ultra-high temperature ceramics, which can be used in environments that exhibit extreme temperature, chemical reactivity, erosive attack, etc. [1]. Its fracture toughness is relatively low regarding its high hardness. Addition of zirconia (ZrO$_2$) with relatively high fracture toughness could be a solution for this problem. Zirconia is another representative of high melting point (about 2700°C) materials and it is used in refractory applications, such as crucibles [2], parts of jet engines and others. Its unique phase transformation from cubic to tetragonal and then to monoclinic modification made it one of the most studied ceramic materials. There were a lot of attempts to use zirconia as a toughening component for other ceramic materials, including TiB$_2$, TiC, WC, ZrC and others [3,4,5]. Only few of those, however, were consolidated with spark plasma sintering technique (SPS).

Tetragonal to monoclinic phase transformation and the associated volume change of ZrO$_2$ is one of the challenges when it is used to modify other ceramics. Transformability of stabilized zirconia can be affected by the variety of factors, such as stabilizer type, stabilizer amount [6], grains size and grain size distribution [7] and residual stresses [8]. Thermal residual stresses during sintering process and during high temperature loads are the most critical parameters influencing transformability of

tetragonal $ZrO_2$ particles located in the carbide material matrix. However zirconia can undergo polymorphic transition at room temperature if the suficcient stress is applied [9].

In this study different ZrC based and $ZrO_2$ doped composites were processed with SPS technique at different parameters. Phase changes of zirconia was investigated before and after sintering by XRD analyses. Influence of $ZrO_2$ content and sintering parameters on the hardness, modulus of elasticity and fracture toughness of the composites had been investigated.

## 2. Materials and methods

Designed composites were produced from micronsize ZrC powders (Strategic Metal Investments Ltd) with a mean particle size of about 3.5µm and 99% purity and from partially stablized (3 mol% $Y_2O_3$) $ZrO_2$ (Tosoh) nanopowders with a mean particle size of about 30nm. From these powders ZrC - 40 vol% $ZrO_2$ and ZrC - 25 vol% $ZrO_2$ compositions were prepared and designated $40ZrO_2$ and $25ZrO_2$ respectively

The composite powders were milled in a planetary ball mill device (Fritsch, Pulverisette 6 classic) during 6 hours and regime 300 rpm. The milling media was $ZrO_2$ balls (Ø10mm) with a ball to powder ratio of 4:1. The milling was performed either dry or in ethanol in order to find whether phase transformation of zirconia can be initiated at different milling energies.

Sintering was done by SPS (FCT GmbH) with a vertically located pyrometer temperature control. Parameters for the sintering process were chosen following the high melting points of the compounds. The first experiment was done at 1900°C, then the temperature of sintering was reduced to 1600°C. Parameters of the sintering processes are given in Table1. Influence of the heating rate on the densification and grain growth is material dependent, therefore the heating rate was kept the same during all our experiments [10,11]. Mechanical pressure of 50 MPa was applied to the powder at room temperature and kept constant during the experiment. The Ø20mm graphite mould was used to produce cylindrical shape samples.

Densities of the specimens were measured using Archimedes method with distilled water as an immersing media. The bulk Vickers hardness was measured using Indentec 5030 SKV at the load of 10 kg according to ISO 6507. Modulus of elasticity was measured using indentation technique [12] according to EN ISO 14577 (ZHU zwicki-

Line Z2.5). Fracture toughness of the materials was measured by the indentation fracture toughness (IFT) technique with both Palmqvist and Median crack systems [13].

Table1. Sintering parameters for the SPS cycle

| Material | Heating rate °C/min | Dwell T°C | Dwell time | Cooling rate °C/min | Pressure MPa | Atmosphere |
|---|---|---|---|---|---|---|
| 40ZrO$_2$_1 | 100 | 1900 | 10 | 300 | 50 | Vacuum |
| 40ZrO$_2$_2 | 100 | 1600 | 10 | 300 | 50 | Vacuum |
| 25ZrO$_2$_1 | 100 | 1600 | 10 | 300 | 50 | Vacuum |
| 25ZrO$_2$_2 | 100 | 1600 | 6 | 300 | 50 | Vacuum |

Chemical compositions of the powder mixtures and bulk samples were analyzed with the help of XRD (Philips PW3830 X-ray Generator, 4 kW, Cu-Anode) using CuKa radiation at 40 kV and 30 mA, with a step size of 0.02° and a count time of 0.4 s. Microstructures of the polished bulk surfaces were studied by Scanning Electron Microscopy (SEM, Hitachi S-4700) .

## 3.Results and Discussion

### 3.1. XRD of the blended ZrC-ZrO$_2$ composition powders

Milling of the 40ZrO$_2$ and 25ZrO$_2$ mixtures in dry environment has revealed spontaneous transformation of ZrO$_2$ particles from tetragonal into monoclinic phase. It is important to retain the tetragonal state of zirconia particles and to induce this phase transformation in a controlled manner and not as an unexpected result discovered after some of the fabrication stages. The powder milled in ethanol showed the desired phase transformation partially whereas dry milled powder was fully transformed into monoclinic phase (Fig.1). Presence of new peaks can be observed in comparison with powders mixed in ethanol. Dry environment at high rotating speeds creates conditions for severe plastic deformation on microscale level and thus the stress level is sufficient for transformation of tetragonal phase into monoclinic.

### 3.2. Sintering behavior

Previously ZrC-ZrO$_2$ compositions were fully densified by the means of pressureless sintering in different conditions at temperatures higher than 2000°C [5]. In SPS technique the current is applied directly to the material therefore local current densities are very high and as the result the measured sintering temperatures are lower in

comparison with conventional methods [14]. For this reason the composites were firstly sintered at 1900°C. However, observation of the sintering process and analysis of the densification curves after the experiment has revealed much lower dwell temperature needed for densification to occur. In sintering experiments movement of the upper electrode during the process is recorded and it can give a rough idea about the densification. Dependence of displacement rate of the upper electrode from sintering time is presented at Fig. 2. When the pressure is applied at room temperature the densification displacement is positive and the powder is compressed to its green density (stage 1). In the heating stage due to the expansion of the graphite moulds the displacement is in the opposite direction (stage 2). In the next step densification occurs and piston speed increases rapidly between 1000 and 1640 °C (stage 3).
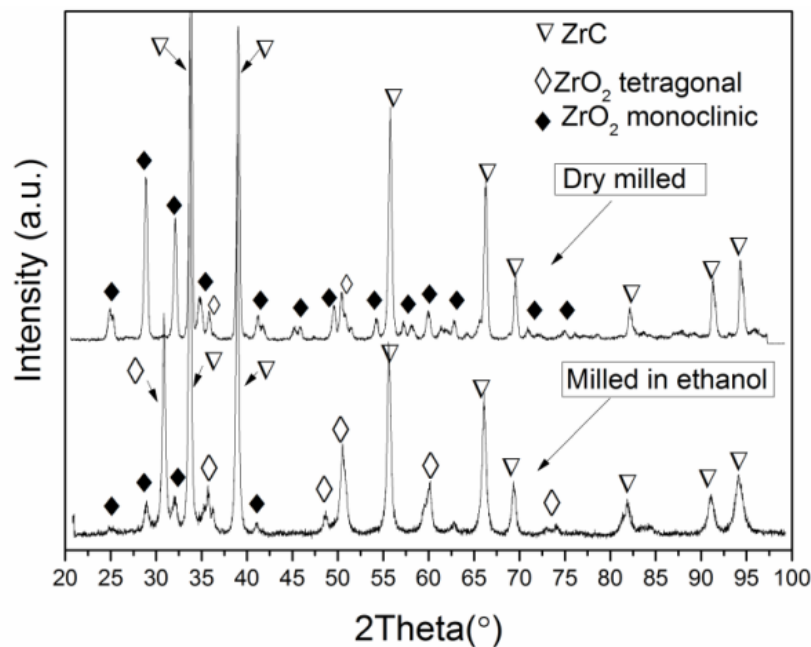


Fig.1. XRD patterns of $40ZrO_2$ composites milled in dry conditions and in ethanol

During the first step densification is determined by rearrangement of particles and their plastic deformation under the applied pressure of the pistons. The densification step has a large rise because of the nanosize of the zirconia particles which tend to decrease their surface area and rearrange as soon as distance between them is decreased. In the second step the maximum pressure is reached and pistons movement is completed. Also some negative movement can be observed because of the thermal expansion of the powder and graphite material. In the third step densification is induced by increase in temperature. Densification starts between 1000 and 1100°C. $ZrO_2$ and ZrC particles

located very close to each other after the first step now start to interact threw high heating and pressure energies. Densification now occurs by mass transfer mechanism and necks between $ZrO_2$ particles start to form. ZrC micronsize particles covered by zirconia particles from all sides also get involved in neck formation with each other and zirconia. Neck formation leads to initiation of grain boundaries. Nanosize of zirconia particles and its lower melting point (2700°C) helps ZrC with very high melting point (3500°C) to densify and makes densification to start and finish early. There is some negative slope after major densification is finished indicating thermal expansion of the material.
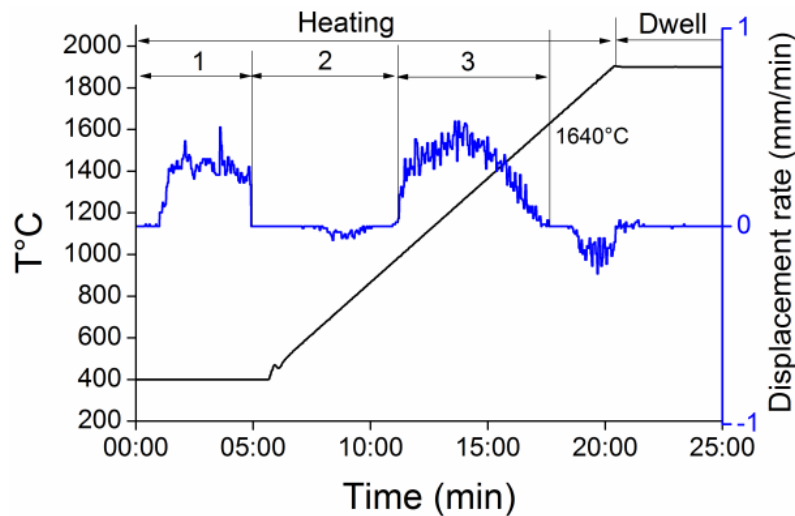


Fig.2. Change of piston speed during sintering of $40ZrO_2$.

According to the graph the major densification of the powder is between 1600°C and 1700°C. Hence next sintering was made at 1600°C temperature which is 300˚C lower than previous sintering. For $40ZrO_2$ composition this temperature still seemed high because the densification is ending during first minutes of dwell period. Though there is still some pistons movement during whole dwell period indicating that some insignificant densification processes are taking place, while those processes can play important role in final densification and homogeneity of the produced specimen. $25ZrO_2$ composition was sintered at the same dwell temperature. For this composition the densification is started at 1100˚C and is finished during first minute of dwell time. There is no big difference between sintering behavior of $25ZrO_2$ and $40ZrO_2$. To optimize the process it was decided to sinter the $25ZrO_2$ composition at 1600˚C for 6 minutes and to study the effect of dwell time on the final properties of the composite. The sintering showed that powder

densification is over at first minute of dwell temperature, however there were still some small pistons movements during next 5 minutes.

## 3.3. Properties of the obtained specimens

Produced specimens have demonstrated moderate properties in comparison with calculated values according to the rule of mixtures on the basis of the starting nominal compositions assuming no impurities, no porosity and no reactions and transformations during processing. Calculated theoretical density is equal $6.43 g/cm^3$ for $25ZrO_2$ and $6.36$ $g/cm^3$ for $40ZrO_2$. Investigated powders could be consolidated up to the value equal 99% from theoretical density by SPS. It is too high taking into account refractory nature of the carbide. The hardness of the composites was between 12 and 15 GPa. Following rule of mixtures, the  hardness of the $25ZrO_2$ specimen should be at least 17GPa. The graph shows reverse dependence and it can be seen that hardness of the lower ZrC containing specimen is higher than $25ZrO_2$ specimen.
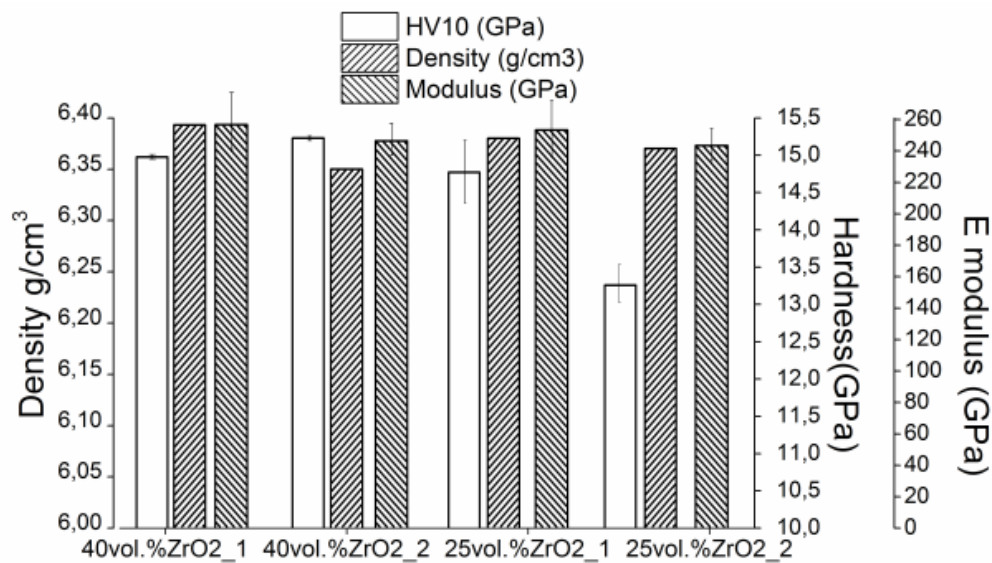


Fig.3. Properties of the sintered composites.

The reason for such behavior can be explained by poor sinterability of the high ZrC containing material and short dwell time. It can be also concluded from the error bars that materials were not densified homogeneously because of wide distribution of hardness values for $25ZrO_2$. Especially low hardness can be observed for the specimen sintered at 1600°C for 6 minutes. Even though the density of the specimen is high the hardness is lower in comparison with other specimens.

Elastic moduli of all samples are between 245 and 260 GPa while again the maximum value is exhibited by lower ZrC containing specimen. Still the modulus is far from theoretical, which should be 320 GPa for $40ZrO_2$ and 350GPa for another composition. The lowest modulus is again for 6 min sintered $25ZrO_2$ specimen indicating not sufficient sintering time.

From analysis of the properties it can be concluded that increasing of zirconia content improves their sinterability and homogeneity, while samples with higher ZrC content do not demonstrate any advantages in hardness for example. ZrC is difficult to sinter alone therefore an additional phase such as nano sized zirconia enhances sinterability noticeably and lowers the sintering temperature of ZrC.

*3.4. Fracture toughness and XRD*

In the Fig. 4 the XRD patterns of the sintered compositions can be observed. Tetragonal zirconia phases are detected on both of the patterns meaning the possibility of stress induced transformation during impact or loading in future experiments. Tetragonal zirconia was found on the surface of the specimens sintered at both high 1900°C and lower 1600°C temperatures, which shows the possibility of sintering zirconia doped composites at high temperatures without unexpected transformations.
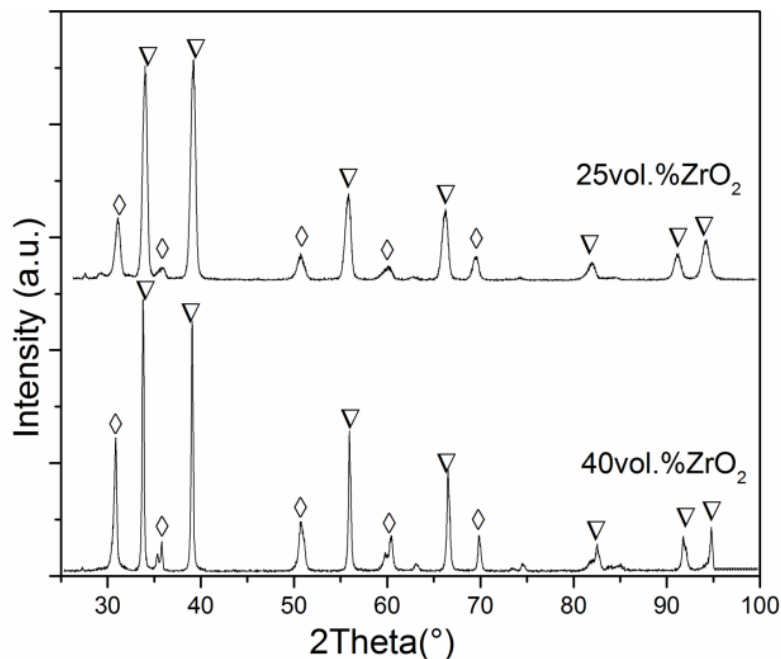


Fig.4. XRD patterns of the bulk samples

Fracture toughness of the produced specimens was measured and compared with values measured with notched beam technique according to [13] (Table 2). Very high standard error is indicative of the inhomogeneity in the microstructure of the sintered material and presence of porosity. Presence of porosity could also influence the IFT positively because pores can serve as crack barriers. Another possibility of high IFT is an influence of zirconia on the crack stopping processes. From Fig. 5 cracks propagating from Vickers indent can be seen. The fracture is mainly transgranular and goes through all grains on its path with crack branching and deflections.

Table 2. Fracture toughness

| Specimen | IFT Palmqvist crack MPa·m$^{1/2}$ | IFT Median crack MPa·m$^{1/2}$ | Notched beam Ref [5] MPa·m$^{1/2}$ |
|---|---|---|---|
| 40ZrO$_2$_1 | 6.53±1.2 | 7.5±1.2 | 5.8 |
| 40ZrO$_2$_2 | 5.83±3 | 7.1±4 | 5.8 |
| 25ZrO$_2$_1 | 7.24±2.2 | 8.9±3.2 | 4.5 |
| 25ZrO$_2$_2 | 7.8±2 | 9.3±3 | 4.5 |
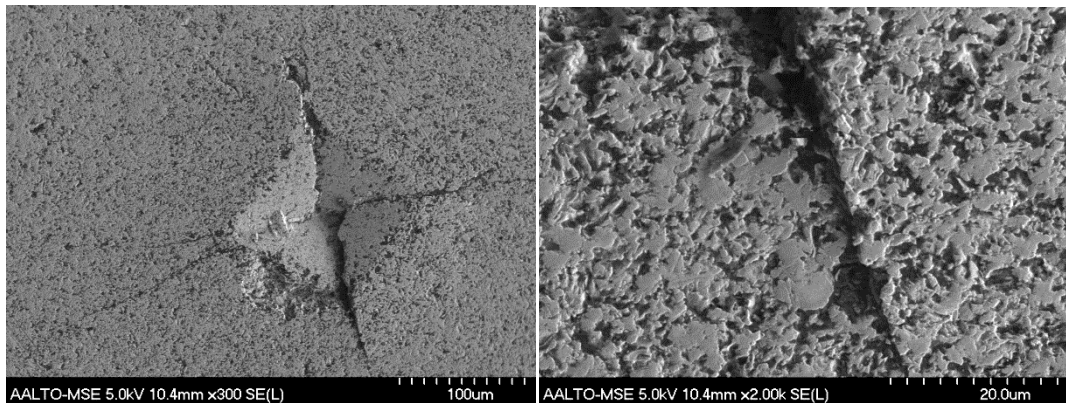


Fig.5. Indentation imprint and crack propagation taken from the surface of the 40ZrO$_2$ composite.

## 3.5. Microstructure

Microstructures of the sintered composites are shown in Fig. 6. Two phases can be distinguished on every micrograph. The light areas are ZrC and dark areas are ZrO$_2$. Comparing Fig. 6a with Fig.6b the reduction of dark regions and increase of light areas can be noticed. It is indicating the composition difference between two of the materials,

having 40% of $ZrO_2$ in Fig.6a and 25% of $ZrO_2$ for Fig.6b. However, this difference in $ZrO_2$ content and distribution did not influence upon mechanical properties noticeably. The different phases seemed more like agglomerates instead of grains in the microstructure. On the other hand the size of the agglomerates is from 1 to 4 micrometers which is about the size of the starting ZrC particles before sintering. Assuming that these are ZrC whole grains the sintering mechanism can be determined as consolidation of $ZrO_2$ nanoparticles around microsized ZrC grains. Starting to densify at temperatures between 1000 and 1100 ˚C (Fig. 2) $ZrO_2$ particles enclose ZrC particles and form the final microstructure. From dark areas it can be concluded that zirconia has completely lost particulate appearance and takes shape of a long thick agglomerated sleeve between ZrC islands. Such large agglomerates of ZrC and $ZrO_2$ could be the reason for relatively low hardness of this composition.



a)                              b)
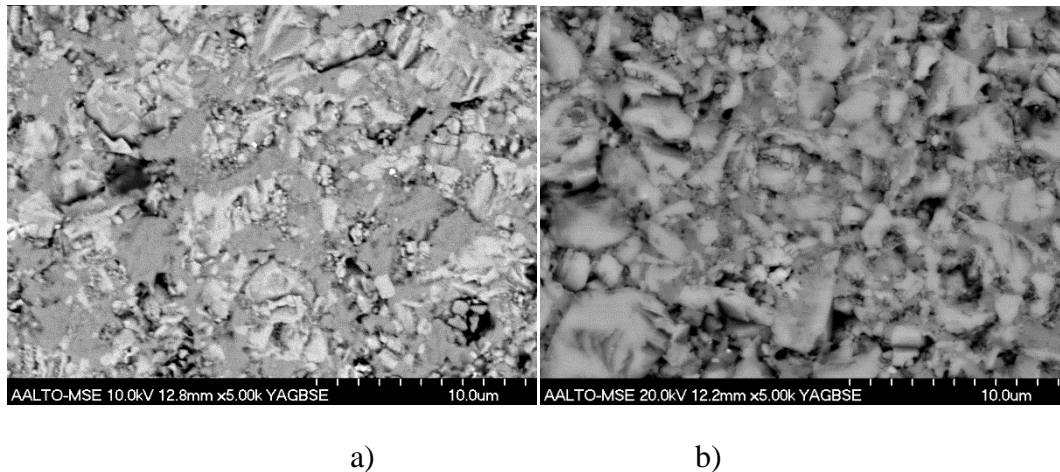
Fig.6. Microstructures of  a) $40ZrO_2$ sintered at 1600°C for 10m; b) $25ZrO_2$ sintered at 1600°C for 10m

## 4.Conclusions

In this study ZrC powders were mixed in dry state and in ethanol with 25 vol% and 40 vol% of $ZrO_2$ powders and then were sintered using SPS technique at different temperatures and dwell times. Mixing in dry environment has resulted transformation of tetragonal zirconia particles into monoclinic polymorphs, while no transformation was observed for mixing in ethanol. Study of the densification behavior had shown that it is possible to sinter these composites at 1600°C during 10 minutes. The density and mechanical properties of the composites were deteriorate when the dwell time was decreased to 6 minutes. The composites had hardness ranging from 13 to 15GPa while

relative density was about 99% compared with theoretical density of 6.4 g/cm$^3$. Elastic modulus was ranging from 245 GPa to 260 GPa. Hardness and elasticity modulus were the lowest for specimen sintered for 6 minutes, indicating insufficient time for formation of homogeneous bulk body. Materials with 40 vol% $ZrO_2$ showed very similar mechanical properties in comparison with samples containing 25 % $ZrO_2$ but had better densification behavior. IFT of the materials was relatively high while the reason for it can be porosity as well as contribution of zirconia as toughening agent.

## Acknowledgments

## References

1. Wuchina E. et al. UHTCs: Ultra-high temperature ceramic materials for extreme environment applications. Electrochem Soc Interface 2007;16(4):30-36.

2. Garvie C. et al. Partially stabilized zirconia refractory. New York;1971.

3. Vleugels J, and Van der Biest O. Development and characterization of $Y_2O_3$-stabilized $ZrO_2$ (Y-TZP) composites with $TiB_2$, TiN, TiC, and $TiC_{0.5}$N. J Am Ceram Soc 1999;82:2717–20.

4. Hussainova I, Antonov M, Voltsihhin N. Assessment of zirconia doped hardmetals as tribomaterials. Wear 2011;271:1909–1915.

5. Eungi Min H, William D.S. Sintering and mechanical properties of $ZrC$-$ZrO_2$ composites. J Mater Sci 1988;23:2865-2870.

6. Hannink R. H. J, Swain M.V. Progress in transformation toughening of ceramics. Annu Rev Maler Sci 1994;24:359-408.

7. Hussainova, I.; Smirnov, A.; Antonov, M. (2011) Mechanical characterization and wear performance of WC-ZrO2-Ni cermets produced by hot isostatic pressing. Advanced Materials Research. Book series: Advances in Key Engineering Materials, 2011, vol. 214, 344 – 348

8.    Krell A, Teresiak A, Schläfer D. Grain size dependent residual microstresses in submicron $Al_2O_3$ and $ZrO_2$. J  Eur Ceram Soc 1996;16:803–811.

9.    Hannink R.H.J,  Kelly P.M, Muddle B.C, Transformation toughening in zirconia-containing Ceramics. J Am. Ceram Soc 2000;83:461–487.

10.   Shen Z, Johnsson M, Zhao Z et.al. Spark plasma sintering of alumina. J Am Ceram Soc 2002;85:1921–1927.

11.   Anselmi-Tamburinia U, Garaya J.E, et.al. Spark plasma sintering and characterization of bulk nanostructured fully stabilized zirconia: Part II.Characterization studies. J Mat Res 2004;9:3263-3269.

12.   Oliver W.C, Pharr G.M. Improved technique for determining hardness and elastic modulus using load and displacement sensing indentation experiments. J M Res 1992.

13.   Niihara K. A fracture mechanics analysis of indentation-induced Palmqvist crack in ceramics J Mater Sci Lett 1983;2:221–223.

14.   Voltsihhin N, Cura M.E, Hussainova I, Hannula S.-P. Sintering routes for zirconia doped hardmetals. In: Proceedings of the 8th International DAAAM Baltic Conference, editor:Otto T, Tallinn, Estonia, 2012. p 765-770.

# FABRICATION OF NANOSIZED HIGH-MELTING POINT COMPOSITES BY SPARK PLASMA AND RATE CONTROLLED SINTERING (BRIEF REVIEW)

## Zgalat-Lozynskyy Ostap

*Frantsevich Institute for Problems of Materials Sciences of NAS of Ukraine, Kyiv,Ukraine*
*e-mail:ostap@materials.kiev.ua*

## Abstract

Nano-structured materials, including nanocrystalline monolithic aggregates and nanocomposites, became the object of increasing interest. To consolidate the nanocomposites and achieve desired properties the new technological processes have been applied. Rate Controlled Sintering (RCS) and Spark Plasma Sintering (SPS) are successfully used to obtain near fully dense high melting nanocomposites with grain size within nanometric scale and make sintering process faster and cheaper.

**Keywords:** *RCS, SPS, TiN, TiCN, Si₃N₄, nanocomposites.* 

*(Keywords:* $RCS, SPS, TiN, TiCN, Si_3N_4,$ *nanocomposites.)*

## 1. Introduction

It is well accepted that the sinterability, hardness and fracture toughness for metals and ceramics can be substantially increased if the materials have nanograined microstructure (<100 nm). As predicted from Hall-Petch relationship hardness (strength) of materials increase continually with decreasing of grain size. Improvement of mechanical properties is possible by decreasing grain size in the compositions to the nanometer scale (less than 100nm), exploring so called "size effect" - rise of hardness and bending strength with decreasing of grain size. It is looks optimistically to start work with nanomaterials. But some experiments showed non adequate hardness data as predicted by conventional Hall-Petch relationship. To estimate influence of grain size on hardness of bulk materials, the modified relationship of Hall-Petch (1) was used [1]

$$H = H_g \cdot (1 - f) + H_{gb} \cdot f \qquad (1),$$

where $H_g$, $H_{gb}$ – hardness of grains and grain boundaries, f – volume of grain boundaries.

The modified relation take into account not only grain size of material but the volume of grain boundaries, what is the critical value for nanomaterials. Dependence of hardness *vs.* grain size has been calculated for titanium nitride [6]. Experimental data [2-5] were compared with simulation. Revealed that maximal hardness (around 32 GPa) achieved for material with grain size 10 nm, what is the critical size of pile-up dislocations existence in titanium nitride (fig. 1). This is a good evidence to start the work with TiN based materials and fabricate bulk nanocomposites with maximum of hardness.

## 2. Rate-Controlled Sintering

We selected RCS because of its structurally oriented strategy [7, 8]. The advantage of the RCS over the linear heating rate regime and isothermal hold of standard sintering is the possibility to achieve a material's density of approximately 99.9 % while keeping the grain size bellow 100 nm. Additionally, we use the sintering technology with rapid decreasing of sintering temperature for fine ceramic compounds presented in the paper [9] to suppress grain growth more. Common schedule, how to sinter the nanostructured powders presented on the fig 2. On the 1 stage we apply the calculated RCS regime to achieve 0,9 – 0,95 theoretical density of the pellet. On the second stage we instantly decrease process temperature down to 100-200 $^{0}$C with isothermal hold [4, 6, 10].
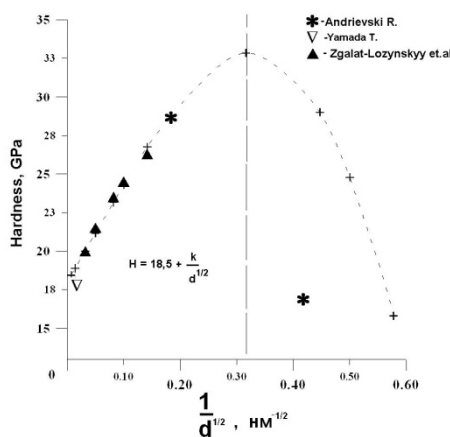


Fig.1. Hardness *vs.* grain size for TiN [6].
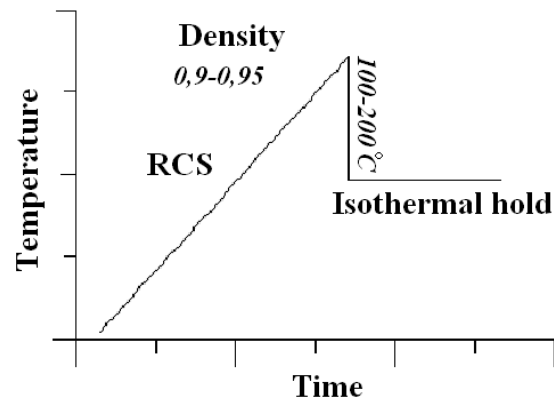
Fig 2. Modified RCS schedule for nanopowders consolidation

*2.1 RCS of TiN*

To estimate optimal parameters of sintering for TiN non-isothermal runs with constant heating rates were performed. After analysis of obtained data porosity - grain size - temperature was found that at the 1250-1300 $^{0}$C volume of pores with average sizes 20-30 nm negligibly low but volume of pores (defect structure of particles surface) with size 2-3 nm stable [10]. Temperatures ~1300 $^{0}$C are critical for TiN, above this temperature non controlled grain growth observed. The compromise: to obtain the nanoceramic we have to finalize sintering process for TiN in temperature rage below

1300 $^{0}$C, but residual porosity for this ceramics could exceed 5 %. To optimize relationship grain size – porosity the modified RCS regime for sintering of TiN-based powders has been developed (fig. 3). Applying RCS modified regime the final temperature of consolidation was decreased down to 1150-1250 $^{0}$C, and residual porosity in sintered bodies was estimated as 1,5 - 2% [10].

Specimens sintered under modified rate-controlled regimes in vacuum ($10^{-5}$ torr) demonstrated fine grained structure (around 100 nm), "clean" grain boundaries and possessed nanohardness up to 26 GPa (fig. 4).
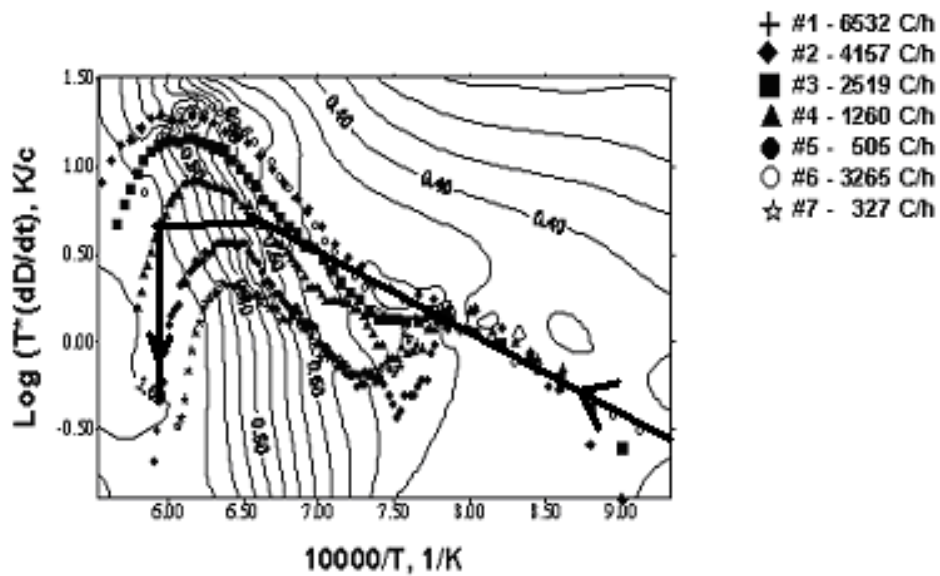


Fig 3. Calculated RCS regime to sinter TiN nanopowders [10]



a                                                    b
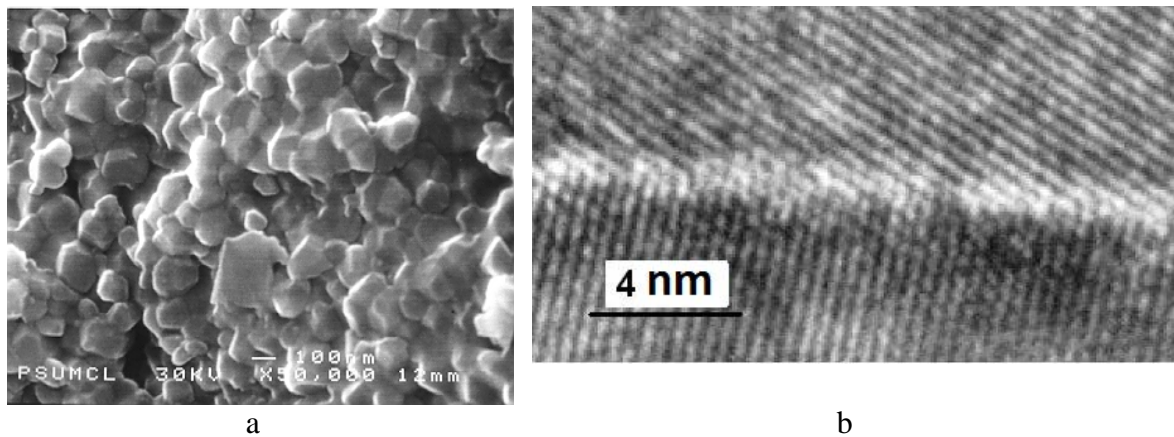
Fig.4. TEM image of RCS densified nano-TiN: a – grain structure; b- grain boundary

*2.2 RCS of high melting point nitrides*

Nanocrystalline powders of TiN produced by H C Starck GmbH (PVD), aluminum and silicon nitrides prepared by plasmachemical synthesis (PCT ltd. Latvia) were used in the present investigation, see table 1.

Table 1. Properties of nanosized powders

| Powder | Crystallite size, [nm] | Specific surface, [m$^2$/g] | [O], wt.% | [N], wt.% |
|--------|------------------------|-----------------------------|-----------|-----------|
| TiN | 15 | 33 | 1,8 | 19,8 |
| β-Si$_3$N$_4$ | 30-50 | 70 | 2,1 | - |
| AlN | 20 – 50 | 27 | 2,8 | - |

The same optimal RCS regimes were calculated for TiN- based ceramic composites [6]. For investigated compositions, the RCS-regime applied until the residual porosity achieved 10-15%, then temperature drop of 100 - 50 °C and the final sintering stage of isothermal hold until full densification. Final stage was completely isothermal for 10-30 min. to allow the uniform porous structure to relax self similarly to zero. The TiN – Si$_3$N$_4$ composites were doped with 6 wt.% Y$_2$O$_3$ and 4 wt.% Al$_2$O$_3$ to form liquid phase with silica on grain boundaries at T$_{evt}$~1550 °C. Sintering of TiN – Si$_3$N$_4$ composites in hydrogen resulted in almost dense nanograined ceramics with the residual porosity less than 1 % already at 1550 $^0$C, whereas sintering in nitrogen demands much higher temperatures for completion the densification. This fact can be explained by activation of powder surface in hydrogen, and *vise versa* passivation in nitrogen [4].

Composition TiN-5wt% AlN could be successfully densified applying RCS technology to near fully dense nanocomposite at 1600 $^0$C without specific additives (tab. 2)..

To highlight advantages of RCS technology a number of specimens from the same nanopowder compositions were consolidated by conventional presureless sintering (CS) with isothermal hold 10 min to achieve relative density 98-99 % of theoretical. As a result, this CS regime needs in much higher temperatures to achieve residual porosity ~1%, what subsequently brings to abnormal grain growth (table 2).

Table 2. Regimes of consolidation and characterization of TiN – based composites

| Composition | Regime | Regime | | Grain size, nm | Porosity,% |
| | | Medium | $T_{final}$, $^0$C | | (±0.2%) |
| --- | --- | --- | --- | --- | --- |
| TiN -50wt% $Si_3N_4$ | RCS | hydrogen | 1550 | <100 | 0.6 |
| TiN -50wt% $Si_3N_4$ | RCS | nitrogen | 1630 | >100 | 0.8 |
| TiN -50wt% $Si_3N_4$ | CS | hydrogen | 1700 | 500-1000 | 0.6 |
| TiN -5wt% $Si_3N_4$ | RCS | hydrogen | 1650 | <100 | 0.9 |
| TiN -5wt% $Si_3N_4$ | CS | hydrogen | 1720 | 500-1000 | 0.7 |
| TiN-5wt% AlN | RCS | vacuum | 1600 | <100 | 1 |
| TiN-5wt% AlN | CS | vacuum | 1700 | ~500 | 1 |

Structures of RCS consolidated composites presented on the fig. 5. Grain size of sintered composites estimated in the range 50-150 nm. Moreover, distribution of grain size and porosity for RCS consolidated nanomaterials remains unchanged across the sample, and this fact is the best evidence of successful implementation for the sintering technique with shrinkage rate control.
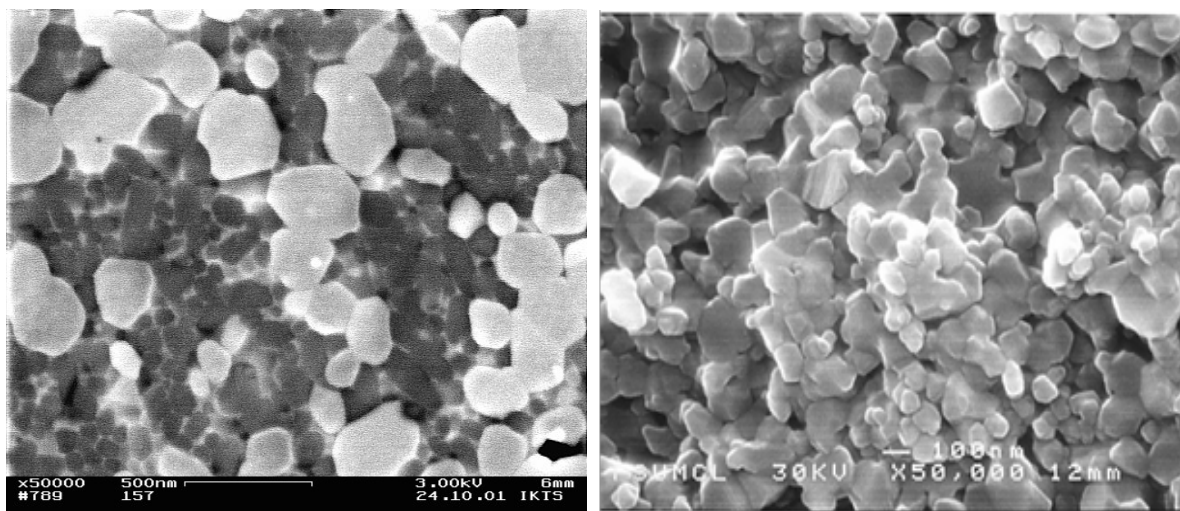


a)                                          b)

Fig. 5. SEM images of sintered composition: a) 50 wt.% TiN – 50 wt.% $Si_3N_4$, b) TiN-5wt% AlN.

## 3. Spark Plasma Sintering

Novel sintering technique which promotes densification process and attractive to consolidate nanopowders of various metals and ceramics is Spark Plasma Sintering (SPS) or Field Assisted Sintering Technique (FAST).

Conventionally, SPS regime organized as rapid heating 100-200 $^0$C/min under pressure of 100-200 MPa and soaking at the high temperatures. This SPS regime caused to materials densities 95-97% at the temperatures 150-300 $^0$C lower than conventional sintering. But the structure of nanopowders sintered in this FAST schedules is around 250-400 nm [11- 13]. The other approach to consolidate high melting point nanopowders by SPS technique has been proposed by authors [14]. Appling the rate-controlled technology [8, 10] to the SPS consolidation the few step (or non-linear) regime of SPS has been developed (fig. 6) and tested on nanopowders of high melting point compounds [14,15].



| Fig.6 Scheme of non-linear SPS regime [15] | Fig.7 SPS regimes for consolidation TiCN nanopowders [14] |
|---|---|
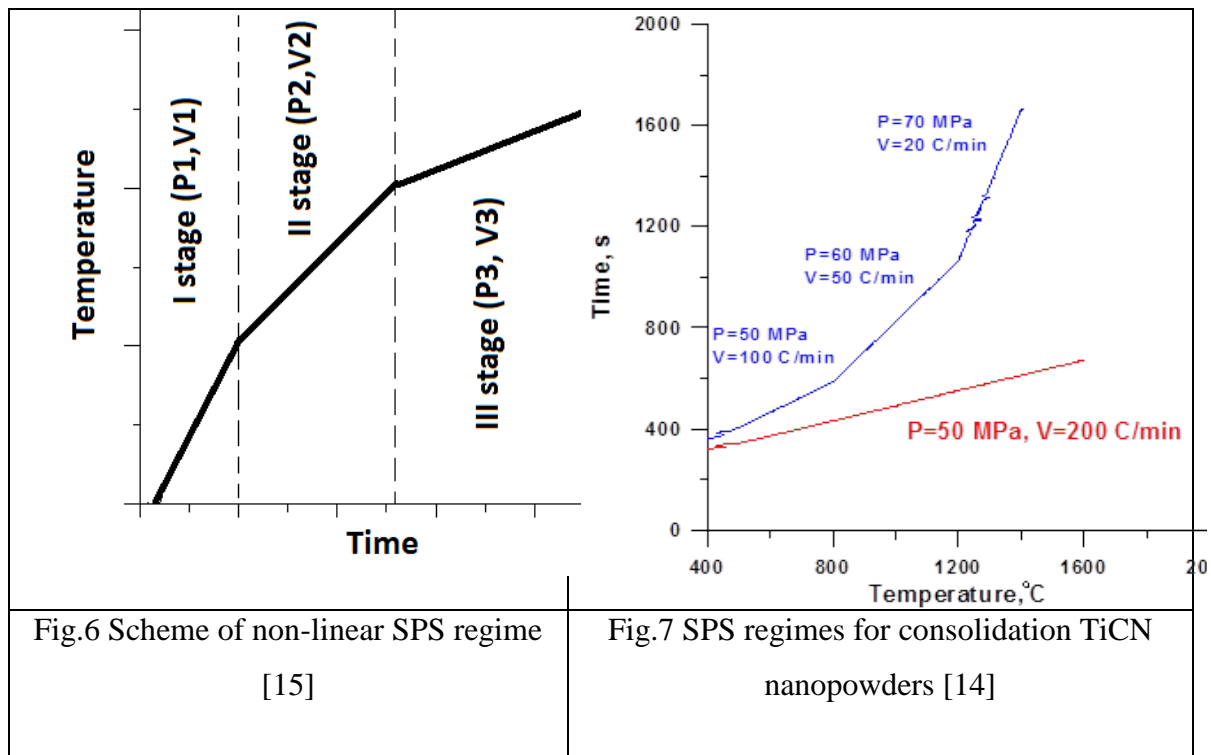
The non-linear SPS regime could include a few stages when process pressure (P) and heating rate (V) varied. Preliminary developed and tested non-linear SPS regime consists of the next stages: i)initial stage with high heating rate($V_1$), when about 75% of the

material's density is achieved; ii) intermediate stage when the heating rate is partially decreased ($V_2 < V_1$), and iii) final stage with slowest heating rate($V_3 < V_2 < V_1$) [15].

On the first stage densification is preferably stimulated by the particle rearrangement and on the next stages controlled by diffusion. Increasing of pressure and decreasing the heating rate during the consolidation process take place prolongation the particle rearrangement period when the grain growth is minimal. On the other hand, regulation of heating rate value could help us densify materials to 95 – 97 % of theoretical density and "fabricate" strong grain boundaries –parameter which together with grain size is critical for nanomaterials properties.

For example, densification of TiCN nanopowder (70 nm, PCT Ltd., Latvia) by SPS with parameters P= 50 MPa and heating rate 200 $^0$C /min carried out up to the temperature 1600 $^0$C to achieve density 96-98% of theoretical. At the same time utilizing few step SPS TiCN nanopowders has densified more intensively and reach 99% density at 1400 $^o$C (fig.7) [14]. Moreover, this regime helps to control grain growth during consolidation of materials and fabricate nanoceramic with strong grain boundaries.

*3.1 SPS consolidation of high melting point nanocomposites*

The high melting point nitrides, borides and titanium carbonitride nanopowders and nanowhiskers from HC Stark GmbH (Germany), Plasma Ceramics Technologies (Latvia) and Nanostructure and Amorphous Materials Inc. (Nanoamor, USA) were used for the SPS consolidation experiments. Characterization of the nanopowders and compositions utilized in the work are presented in the table 3.

The SPS experiments have been carried out using an SPS- apparatus HPD 25 FCT Systems GmbH (Tmax = 2400 $^0$C , Pmax = 250 kN, I max = 8000 A, U max = 10 V, mediums: vacuum - $5 \cdot 10^{-2}$ mbar, nitrogen) in a graphite die 30 and 70 mm diameter with punch unit. All parameters were monitored during the experiment. The sintering experiments were organized by the next schedule: nanopowders have been consolidated in few stage regimes with sequential increasing of pressure from 50 to 70 MPa and decreasing of heating rate from 100 $^0$C /min to 20 $^0$C /min (fig. 7). The electric current was pulsed periodically pulse rate 20 ms and 1 ms pause between pulses. The temperature was measured by means of a pyrometer on the inner surface of the upper graphite piston. No isothermal hold at the high temperatures used to exclude uncontrolled grain growth.

All the sintered specimens in few step schedules possessed by fine structure with average grain size 100-150 nm and residual porosity below 2 %. (fig. 8) [15].

Table 3 Nanopowders and nanocompositions characterization

| Nanopowder/ Nanocomposition | Producer | $d_{aver.,}$ nm | Specific surface, $m^2/g$ | [O], wt.% |
|---|---|---|---|---|
| TiN | HC Stark GmbH. | 17 | 33 | <1.5 |
| TiN-20 wt%TiB$_2$ | PCT ltd. Latvia | 54 | 26 | 0.8 |
| TiC$_{0.5}$N$_{0.5}$ | PCT ltd. Latvia | 58 | 56 | 1.2 |
| Si$_3$N$_4$ (nanowhiskers) | Nanoamor, USA | L=300-1000 D=30-100 | - | 0.9 |

$d_{aver.}$ – average particle size estimated by laser granulometry and TEM.

Moreover, composites like TiCN-Si$_3$N$_4$ (with high quantity of conductive phase) consolidated by SPS didn't needed in special additives (like Y$_2$O$_3$, Al$_2$O$_3$, etc.) which promote densification process to achieve high density. Decreasing of sintering temperature and avoidance of additives for these composites is the important factors for the further refining grain size of investigated composites down to 10 nm and subsequently enhance of materials mechanical properties.

**4 Application and properties of nanocomposites**

Nanocomposites based on high melting point compounds are the good candidates for application as cutting tools and wearproof parts [6, 16]. The main advantages of the non-linear SPS and RCS techniques is easy adaptation of sintering schedule for industrial equipment with achievable of high degree reliability. For example, on the fig. 9 presented small parties of tools based on high melting point nitrides produced by RCS technology in IPMS (Ukraine).

To prove advantages of developed SPS and RCS regimes we compare properties of nanocomposites consolidated under different regimes and methods for the same nanopowders.
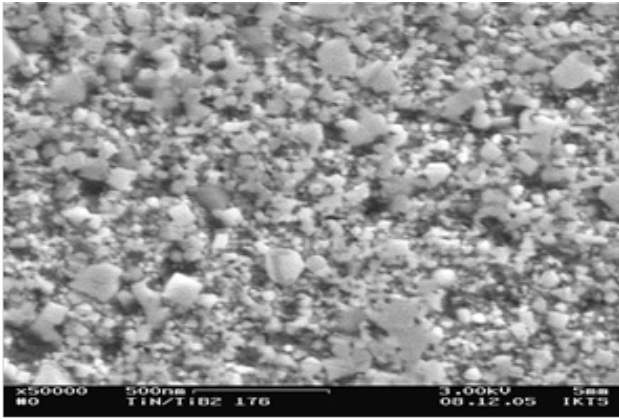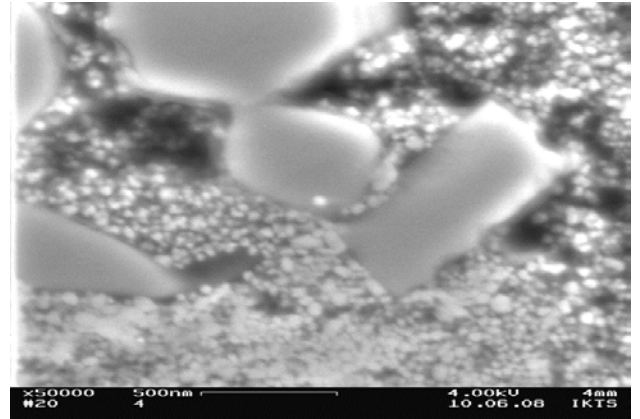
a                                        b
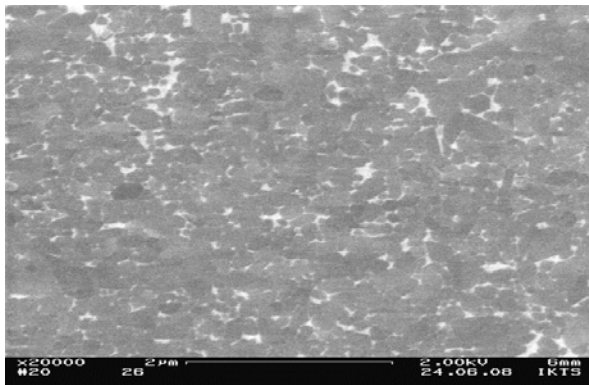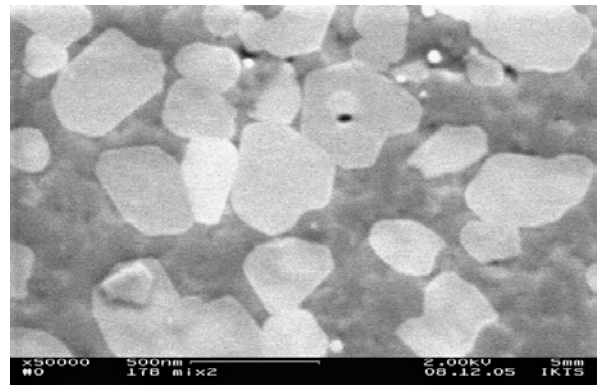




c                                        d

Fig. 8. Scanning electron microscope micrographs: a - TiN-TiB$_2$; b - TiN enhanced by Si$_3$N$_4$ nanowhiskers; c - Si$_3$N$_4$ nanoparticles-nanowhiskers (additives Y$_2$O$_3$, Al$_2$O$_3$), d - TiCN-50wt.%Si$_3$N$_4$.
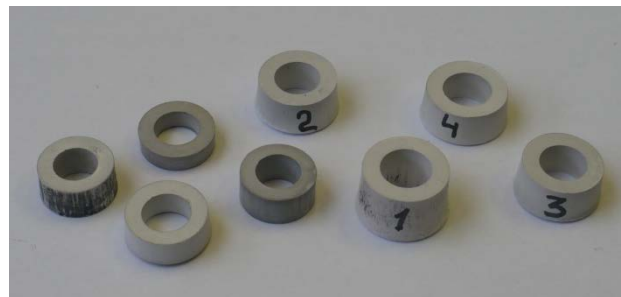




a                                        b

Fig.9. Parts produced by RCS technology: a – batch of cutting tools from TiN-Si$_3$N$_4$ nanocomposite; b - rollers from nano Si$_3$N$_4$ enhanced by whiskers

Results of mechanical and tribological tests summarized in Table 4. Vickers hardness and fracture toughness of sintered composites were measured at 50g and 2 kg load conditions by MMT-3 (Buehler) hardness tester. Sliding tests were conducted in a block-on-ring type tester under non-lubricated conditions in a constant climatic atmosphere (20°C, 50-60% relative humidity) under load 10 kg. Counterbodies for tested materials have been selected 100cr6 steel and hard alloy VK6 (tungsten-carbide base alloy with 6 percent Co).

Table 4. Properties of consolidated composites

| Composition | Regime of consolidation | Process parameters | Porosity,% | Grain size, nm | HV, GPa | K1c, MPa·m$^{1/2}$ | f |
|---|---|---|---|---|---|---|---|
| $Si_3N_4$- TiN (additives $Y_2O_3$,$Al_2O_3$) | Modified RCS | $T_f$=1450 $^0$C | 0,5 | 50-70 | 20,5±0,9 | 6,3 | 0.38 |
| TiN - 20 wt%$TiB_2$ | Non-linear SPS | $T_f$=1470 $^0$C, P=50-70 MPa V=100-20 K/min | 1.3 | <100 | 22.5±2.1 | 4.1 | - |
| TiN-20 wt%$Si_3N_4$ | Non-linear SPS | $T_f$=1300 $^0$C, P=50-70 MPa V=100-20 K/min | 1.9 | <100 | 20.3±1.8 | 5.3 | 0.42 |
| $Si_3N_4$- TiCN | Non-linear SPS | $T_f$=1450 $^0$C, P=50-70 MPa V=100-20 K/min | 1,2 | <100 | 19,6±1,6 | 5 | 0.45 |
| $Si_3N_4$- TiCN | Conventional SPS | $T_f$=1600 $^0$C, P=80 MPa V=200 K/min | 4 | 300-500 | 16±0,6 | 4,8 | 0.67 |
| $Si_3N_4$- TiCN з добавками $Y_2O_3$,$Al_2O_3$ | Conventional pressureless sintering | $T_f$=1700 $^0$C | 1,8 | >500 | 17,5±0,6 | 6 | - |

$T_f$- final temperature of consolidation; f – friction coefficient

Tested composites consolidated by non-linear SPS and RCS exhibited moderate growth of mechanical properties compared with traditional methods. For example, non linear SPS regime for TiCN-Si$_3$N$_4$ composition is most perspective because processed at much lower temperatures and results in much finer structure and enhanced mechanical properties. Magnitudes comparison for composites consolidated in conventional method and under densification rate controlled regimes are ~15% growth for hardness and ~5% for fracture toughness.

Most promising for utilizing of nanocomposites produced by SPS and RCS techniques are wearproof parts. Obviously, that tribological property of nanosized ceramic demonstrates much better values of friction coefficient compared with the same coarse ceramics consolidated in conventional way.

## 4.Conclusions

Presented results proved the advantages of rate-controlled approach to sintering techniques of nanopowders compared with conventional sintering modes. Implementation of non-linear temperature (pressure) -time regimes results in fabrication of dense, fine-grained, hard and wearproof nanocomposites. This total effect became possible due decreasing of process temperature and formation of uniform and nanograined structure for non-oxide high melting point composites.

To predict properties of investigated nanocomposites supplemented investigations of the grain boundaries are necessary. This investigation helps to clarify the mechanisms of hardening for the ceramics under different modes of SPS and RCS and modify consolidation schedule more precisely.

## References

1.  D.A. Konstantinidis, E.C. Aifantis// Nanostructured materials.-  vol. 7, №10. (1998) 1111-1118.

2.  D.T. Castro, J.Y. Ying, // Nanostruct. Mater. 9 (199767-70)

3. T.Rabe, R. Wasche Nanostructured materials 6, (1995) 357-360

4. O.B. Zgalat-Lozynskyy , A.V. Ragulya, M. Herrmann // Series II:Mathematics, physics and chemistry .- vol. 16 : functional gradient materials and surface layers prepared by fine particles tachnology, eds. M.-I. Baraton and i. Uvarova. (2000) 161 – 167.

5. R.A. Andrievsky, G.V. Kalinnikov, A.F. Potafeev and V.S.Urbanovich, // Nanostructured materials 6, 1-4 (1995) 353

6. O.B.Zgalat-Lozynskyy, A.V.Ragulya, M. Herrmann //Silicates Industries.- Vol. 69, No.7-8 . - July-August (2004) 147-152

7. H.Palmour III, M.L.Huckabee and T.M. Hare //Material Science Monographs. - Elsevier. - Amsterdam. Vol. 4. (1979) 46-56.

8. A.V. Ragulya, V.V. Skorokhod //Nanostructured Materials, 5 (1995) 835-843.

9. I.-Wei Chen, X.-H. Wang //NATURE.- Vol 404 (2000) 168 – 171

10. O.B Zgalat-Lozinskii, V.V.Skorokhod, A.V.Ragulya, I.I.Timofeeva, V.N. Bulanov //Powder metallurgy and Metal Ceramics. Plenum publishing corporation. –. - Vol. 40 . - No.11-12 (2001) 537 - 581

11. P. Angerer, L.G. Yu, K.A Khor, G. Korb,. I. Zalite// J. Europ. Ceram. Soc., Vol. 25, No. 11 (2005) 1919-1927

12. M. Nygren, Z. Shen, //Solid State Sciences 5 (2003) 125–131

13. J.R. Groza, A. Zavaliangos,// Mater. Sci. Eng. A 287 (2000) 171.

14. O. Zgalat-Lozynskyy, A.V.Ragulya, M. Herrmann,// Journal of the European Ceramic Society 31 (2011) 809–813

15. O.B.Zgalat-Lozynskyy, A.V.Ragulya, M. Herrmann, M. Andrzejczuk , A. Polotai//Archives of Metallurgy and Materials, Vol. 57, Issue 3 (2012) 853-858

16. I. Schulz, M. Herrmann, I. Endler et al.//Lubrication Science 2009; 21: 69–81

# CHARACTERIZATION OF MAGNETIC AND MAGNETOELECTRIC PROPERTIES IN SOFT FERRITE – PFT-PT BULK COMPOSITE

## Piotr Guzdek

*Institute of Electron Technology, Cracow Division, Zabłocie 39, 30-701 Cracow, Poland*
*e-mail:pguzdek@ite.waw.pl*

## Abstract

Magnetoelectric effect in multiferroic materials is widely studied for its fundamental interest and practical applications. The magnetoelectric effect observed for single phase materials like $Cr_2O_3$, $BiFeO_3$, $Pb(Fe_{0.5}Nb_{0.5})O_3$ is usually small. A much larger effect can be obtained in composites consisting of magnetostrictive and piezoelectric phases. This paper investigates the magnetoelectric properties of nickel ferrite $Ni_{0.3}Zn_{0.62}Cu_{0.08}Fe_2O_4$ - relaxor $Pb(Fe_{0.5}Ta_{0.5})O_3$ - $PbTiO_3$ bulk composite. The magnetic properties of composite shows a dependence typical of such composite materials, i.e. it consists of a dominating signal from ferrimagnetic phase (ferrite) and a weak signal from paramagnetic (antiferromagnetic) phase (relaxor). Magnetoelectric effect at room temperature was investigated as a function of static magnetic field (300-6500 Oe) and frequency (10 Hz-10 kHz) of sinusoidal modulation magnetic field. The magnetoelectric effect increase slightly before reaching a maximum at $H_{DC} = 750$ Oe and then decrease.

**Keywords:** *Multiferroic materials, Magnetoelectric composite, Dielectric properties, Magnetic hysteresis, Magnetoelectric effect.*

## 1.Introduction

Magnetoelectric effect (ME) in multiferroic materials has been studied at great length for its fundamental usefulness and practical applications [1 - 10]. In the past decade, multiferroic materials have attracted increasing interesting because of their practical applications in sensors, actuators, memory devices, transducers, filters, waveguides, switches, phase invertors [1,10].

A few single phase materials ($Cr_2O_3$, $BiFeO_3$, $Pb(Fe_{0.5}Nb_{0.5})O_3$) are magnetoelectric, but the effect is usually weak. A much stronger magnetoelectric effect could be realized in a composite of magnetic and ferroelectric phase in which the ME coupling is mediated by mechanical stress. Multiferroic composites have been fabricated as bulk ceramics, bilayers, multilayers, thin films, core-shell nanostructures [6-9].

The magnetoelectric response is the appearance of an electric polarization P upon application of a magnetic field H [1,2]. The induced polarization is $\delta P = \alpha \cdot \delta H$, where $\alpha$ is the magnetoelectric coefficient. The magnitude of magnetoelectric effect in multiferroics is determined by magnetostrictive deformation and piezoelectric effect in the material. The magnetoelectricity is directly proportional to the piezomagnetic coefficient $d\lambda \backslash dH$, where $\lambda$ is magnetostriction of the material. The stress generated in the piezoelectric subsystem directly corresponds to the stiffness in the subsystem, which results in

effective mechanical coupling [1,2]. The stress causes an increase in the polarization of the domains oriented in the direction of tension and a decrease in the polarization of those oriented in the direction of compression. The change in polarization causes a bound electric charge to appear at the domain wall. These bound charges induce an electric field in the grains [1,2].

It is very important to select a suitable combination of magnetic and ferroelectric material to get ME effect. From a practical point of view Ni-Zn ferrite is frequently used in strong magnetostrictive materials, because it possesses good dielectric and magnetic properties and high magnetostriction [9,10]. As a piezoelectric phase, the ferroelectric relaxor $Pb(Fe_{0.5}Ta_{0.5})O_3$ (PFT) has often been employed in several applications because it has good dielectric and ferroelectric properties [11]. Earlier examinations have revealed that PFT is a biferroic with ferroelectric (ferroelectric Curie temperature, $T_C=250K$) and antiferromagnetic (Neel temperature, $T_N=180K$) properties in the same phase [11,12].

Ferroelectric PbTiO3 is one of the most studied ferroelectric materials. Because of its simple perovskite structure, it has been widely used as a model system to understand various phenomena related to cubic-tetragonal phase transition which takes place at about 760K.

In the present work we report on our investigation of new magnetoelectric composite based on $Ni_{0.3}Zn_{0.62}Cu_{0.08}Fe_2O_4$ ferrite as a magnetostrictive phase and $0.85Pb(Fe_{1/2}Ta_{1/2})O_3–0.15PbTiO_3$ relaxor as a ferroelectric phase. The composite was prepared as bulk ceramic sample. The magnetic and magnetoelectric properties of the composite are presented.

## 2.Experimental

The syntheses of composite components were carried out by a conventional mixed oxides method. The fabricating process of the $Ni_{0.3}Zn_{0.62}Cu_{0.08}Fe_2O_4$ ferrite has been previously described in detail elsewhere [13].

The synthesis of PFT was carried out by the "wolframite" method. The wolframite $FeTaO_4$ was prepared by ball-milling $Fe_2O_3$ and $Ta_2O_5$ in stoichiometric proportions in isopropyl alcohol for 8h. After drying, the powder was pressed into pellets and calcined at 1000°C for 5h. The reaction product was then mixed by ball milling with PbO, dried, pelletized and calcined at 850°C for 5h.

The PT was synthesized by solid state reaction method. The mixed powders (PbO, $TiO_2$) were calcined at 900 °C for 8h in air then pressed into cylindrical pellets and finally sintered at 1000 °C for 10 h in air.

Crystal structures of the synthesized materials were tested by standard X-ray powder diffraction using $CuK_\lambda$ radiation (TUR - M61 diffractometer). X-ray diffraction analysis of the synthesized powders confirmed their single phase compositions.

Bulk composite were prepared by ball - milling ceramic constituents for 8h in a stoichiometric proportions corresponding to $0.5Ni_{0.3}Zn_{0.62}Cu_{0.08}Fe_2O_4$ – $0.425Pb(Fe_{1/2}Ta_{1/2})O_3$-$0.075PbTiO_3$, followed by pressing into pellets and sintering at $950^oC$ for 4h. $PbTiO_3$ was introduced to shift upwards the ferroelectric transition temperature.

Magnetization measurements performed using a vibrating sample magnetometer from a Quantum Design PPMS6000 system were taken in the external magnetic field up to 85 kOe in the temperature range 10 – 400 K. A magnetic field of H=50 Oe was applied for the zero-field (ZFC) and field-cooled (FC) magnetization profiles, both of which were acquired at increasing temperature. The same field value was to cool the sample prior to FC measurements. Magnetic hysteresis curves were measured at temperature range from 10K to 393K. The direction of the applied magnetic field was parallel to the layers. The magnetoelectric effect was evaluated at room temperature by dynamic lock-in method, which has been described previously in the literature [14]. The induced voltage between sample surfaces was measured with a lock-in amplifier (Stanford Research System, model SR 830) with input resistance of 100 MΩ and a capacitance of 25 pF. The lock-in amplifier was used in differential mode. To measure the DC and AC magnetic field, a Hall probe SM 102 was employed.

## 3.Results and discussion

In Fig. 1 the real part of dielectric permittivity of a bulkcomposite is depicted as a function of temperature for various frequencies. Two peaks are observed in the plots. The first peak is observed near the Curie temperature of PFT-PT ferroelectric phase and second one near the Curie temperature of magnetic phase. These maxima decrease and shifted to higher temperature with rising frequency. The position and shape of the maxima imply rather overlapping of peaks related to dielectric relaxation of the relaxor and the ferrite phases.
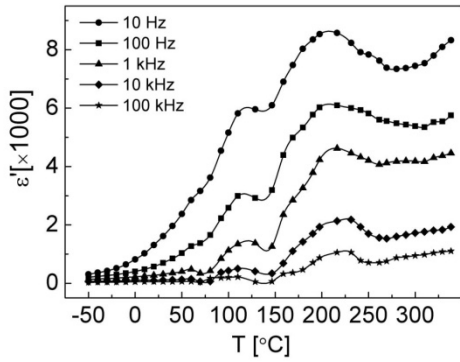
Fig.1 Temperature dependence of dielectric permittivity for bulk $Ni_{0.3}Zn_{0.62}Cu_{0.08}Fe_2O_4/Pb(Fe_{0.5}Ta_{0.5})O_3$ - $PbTiO_3$ composite in the frequency range 10 Hz- 100 kHz.
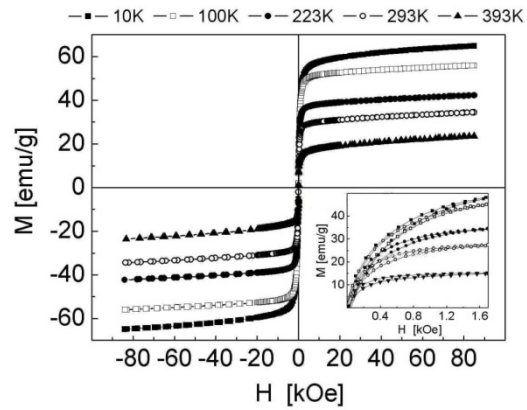
Fig.2 Magnetic hysteresis loops measured up to 85 kOe in the temperature range 10-393 K for composite (closer inspection of the low field parts are presented in the inset).

The hysteresis loops for composite (Fig. 2) are typical of a mixture of soft, ferrimagnetic material (ferrite) with a significant amount of paramagnetic(PFT) /ferromagnetic(PT) material; there is an abrupt increase up to the saturation field of ferrite and a further linear increase.

Fig. 3 shows a comparison of the ZFC-FC profiles measured at low magnetic field (50 Oe) and FC profile measured at high magnetic field (85 kOe). The ZFC and FC magnetizations for bulk composite diverge at the relatively high temperatures of 385 K, indicating that coercivity varies considerably with temperature. Going to the low temperatures, ZFC and FC curves increase and reach their flat maxima between 75 K and 155 K. At the lowest temperatures - below $\sim$ 75 K - the ZFC and FC magnetizations of composite are meaningly reduced due to a significant increase of the coercive field at low temperatures, which reaches the value of the order of the applied field, i.e. 50 Oe. The irreversibility observed in the ZFC and FC curves (Fig. 3b) increasing with decreasing temperature, suggests the existence of a spin-glass phase in the ferrite at low temperatures [15].

In Fig. 4 the magnetoelectric coefficient $\alpha_{ME}$ [1,2] determined for ferrite – PFT-PT composite is plotted versus the bias magnetic field $H_{DC}$. The AC and DC magnetic fields were applied perpendicular to the sample surfaces. At lower magnetic field, the $\alpha_{ME}$ coefficient increases before reaching a maximum at $H_{DC}$ = 800 Oe and then decreases.

The increase in $\alpha_{ME}$ coefficient can be attributed to the improvement of the magnetostrictive properties and piezomagnetic coefficient of the composite. It was found that for a higher applied $H_{AC}$ magnetic. Thus, the magnetoelectric coefficient nonlinearly increases with amplitude of $H_{AC}$ magnetic field.
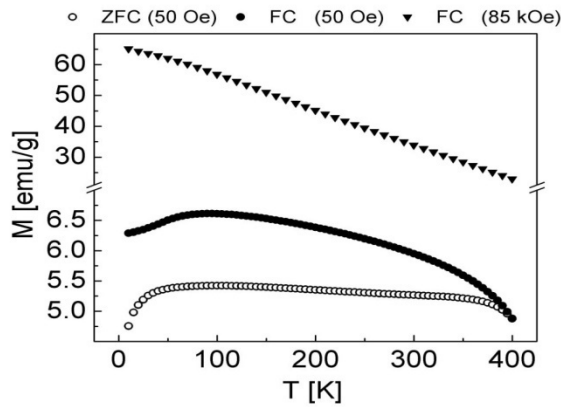


Fig.3 Zero-field (ZFC) and field-cooled (FC) profiles of magnetizations measured at 50 Oe (85 kOe) for composite.
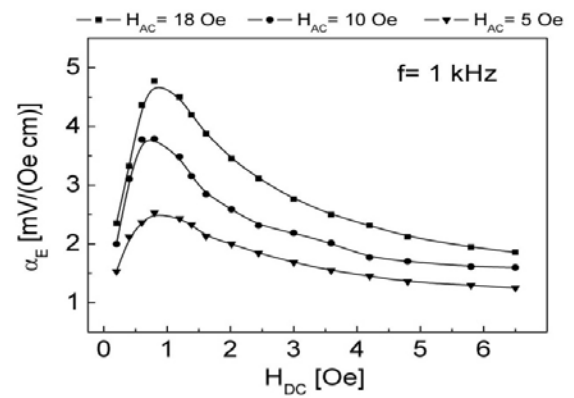
Fig.4 Magnetoelectric coefficients determined at room temperature as a function of bias magnetic field $H_{DC}$ for ceramic (at frequency of the $H_{AC}$ magnetic field 1 kHz). Values of amplitude $H_{AC}$ magnetic field are presented
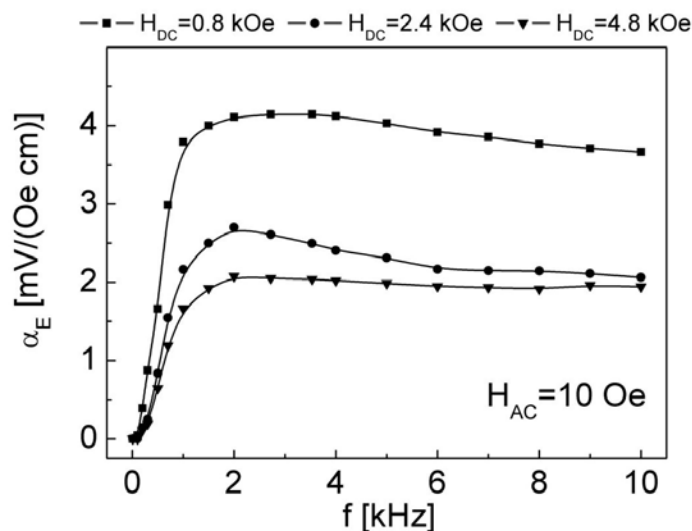


Fig.5 Magnetoelectric coefficients determined at room temperature versus frequency of $H_{AC}$ magnetic field for magnetoelectric composite (at amplitude of the $H_{AC}$ magnetic field 10 Oe). Values of bias magnetic field $H_{DC}$ are presented.

Fig. 5 shows the dependence of magnetoelectric coefficient versus frequency. The magnetoelectric coefficient $\alpha_{ME}$ strongly increases at frequencies 0.1- 2.5 kHz . At higher frequencies $\alpha_{ME}$ coefficient slight decreases. In general, magnetoelectric coupling between magnetostrictive phase and relaxor phase increases with the frequency of the AC magnetic field rising up to a value corresponding to the resonance magnetoelectric effect, and then decreases [16]. However, the resonance effect is observed at frequencies much higher than those applied in this work (several dozen to a few hundred kHz) [16]. However, at higher frequencies magnetoelectric coupling is often suppressed due to leakage current in the ferrite phase.

## 4.Conclusions

A magnetoelectric composite consisting of a solid solution containing ferrimagnetic ferrite $Ni_{0.3}Zn_{0.62}Cu_{0.08}Fe_2O_4$ and mixture of ferroelectric perovskites $Pb(Fe_{0.5}Ta_{0.5})O_3$ and $PbTiO_3$ was prepared as bulk ceramic.

The sample shows high and broad maxima of dielectric permittivity, which decreasing and shifting to higher temperatures with increasing frequency. At moderate and high magnetic fields the sample reveals properties typical of a mixture of ferrimagnetic and of paramagnetic(PFT)/ferromagnetic(PT) material. Here the properties are affected by a small amount of additional phase of the higher magnetocrystalline anisotropy observed in the sample. The bifurcation of field and zero-field cooled magnetizations observed for bulk composite implies spin-glass behavior.

At lower magnetic field, the magnetoelectric coefficient increases slightly before reaching a maximum at $H_{DC}$ = 800 Oe and then decreases. The magnetoelectric coefficient nonlinearly increases with amplitude of sinusoidal magnetic field. The magnetoelectric coefficient $\alpha_{ME}$ increases at frequencies 0.1- 2.5 kHz and then slight decreases.

## Acknowledgments

# References

1. Fiebig M. Revival of the magnetoelectric effect. J Phys D Appl Phys 2005;38:R123-R152.

2. Grossinger R, Duong G.V, Sato-Turtelli R. The physics of magnetoelectric composites. J Magn Magn Mat 2008;320:1972-1977.

3. Fetisov Y.K, Kamentsev K.E, Ostashchenko A.Y. Magnetoelectric effect in multilayer ferrite - piesoelectric structures. J Magn Magn Mater 2004;272-276:2064-2066.

4. Kanamadi C.M, Kim J.S, Yang H.K and et. al. Magnetoelectric effect and complex impedance analysis of $(x)CoFe_2O_4 + (1-x)Ba_{0.8}Sr_{0.2}TiO_3$ multiferroics. J Alloys Compd 2009;481:781-785.

5. Li Y.J, Chen X.M, Lin Y.Q and et. al. Magnetoelectric effect of $Ni_{0.8}Zn_{0.2}Fe_2O_4/Sr_{0.5}Ba_{0.5}Nb_2O_6$ composites. J Eur Ceram Soc 2006;26:2839-2844.

6. Bochenek D, Guzdek P. Ferroelectric and magnetic properties of ferroelectro-magnetic $PbFe_{1/2}Nb_{1/2}O_3$ type ceramics. J Magn Magn Mater 2011;323:369-374.

7. Kulawik J, Guzdek P, Szwagierczak D and et. al. Dielectric and magnetic properties of bulk and layered tape cast $CoFe_2O_4$ - $Pb(Fe_{1/2}Ta_{1/2})O_3$ composites. Compos Struct 2010;92:2153-2158.

8. Venkata Ramanaa M, Ramamanohar Reddy N, Sreenivasulu G and et. al. Enhanced magnetoelectric voltage in multiferroic particulate $Ni_{0.83}Co_{0.15}Cu_{0.02}Fe_{1.9}O_{4-\delta}/PbZr_{0.52}Ti_{0.48}O_3$ composites – dielectric, piezoelectric and magnetic properties. Cur Appl Phys 2009;9:1134-1139.

9. Solopan S.A, V'yunow O.I, Belous A.G and et. al. Magnetoelectric effect in composite structures based on ferroelectric / ferromagnetic perovskites. J Eur Ceram Soc 2010;30:259-263.

10. Corral-Flores V, Bueno-Baqués D, Ziolo R.F. Synthesis and characterization of novel $CoFe_2O_4$–$BaTiO_3$ multiferroic core–shell-type nanostructures. Acta Mater 2010;58:764-769.

11. Choudhury R.N.P, Rodriquez C, Bhattacharya P and et. al. Low-frequency dielectric dispersion and magnetic properties of La, Gd modified $Pb(Fe_{1/2}Ta_{1/2})O_3$ multiferroics. J Magn Magn Mater 2009;105:253-260.

12. Nguyen Van Minh, Le Mai Oanh, Pham Van Doan. Investigation of structural, optical and magnetic properties in $PbTi_{1-x}Fe_xO_3$ ceramics. Ceram Int 2011;37:3785-3788.

13. Guzdek P, Kulawik J, Zaraska K and et. al.  NiZnCuFe ferrite applied for LTCC microinductor. J Magn Magn Mater 2010;322:2897-2901.

14. Duong GV, Grossinger R, Schoenhart M and et. al. The lock-in technique for studying magnetoelectric effect. J Magn Magn Mater 2007;316:390-393.

15. Sato-Turtelli R, Duong G.V, Nunes W and et.al. Magnetic properties of nanocrystalline $CoFe_2O_4$ synthesized by modified citrate-gel method. J Magn Magn Mater 2008;320:e339-e342.

16. U. Laletsin, N. Padubnaya, G. Srinivasan and et. al. Frequency dependence of magnetoelectric interactions in layered structures of ferromagnetic alloys and piezoelectric oxides. Appl Phys A 2004;78:33-36.

# CO DOPING EFFECTS ON STRUCTURAL AND TRANSPORT PROPERTIES OF $BI_{1.6}PB_{0.4}SR_{2-X}M_XCACU_2O_{8+D}$ (M= LA, CE) SUPERCONDUCTING CERAMICS

**Benmaamar F., <u>Mosbah M.-F</u>, Hamel M., Kalkoul N. and Mahdjoub S.**

*Material Sciences and Applications Research Unit, Physics Department, Mentouri University, B.P. 325 Route d'Ain El Bey, 25017 Constantine. Algeria.*
*e-mail: faycalmos@yahoo.fr*

## Abstract

The structural and transport properties of $Bi_2Sr_2CaCu_2O_{8+d}$ (Bi2212) family of superconducting ceramic compounds are greatly influenced by the disorder occurring between the planes at the Ca site or out of the planes at the Sr site. This disorder affects in the $CuO_2$ planes the density of charge carriers which plays a key role in the superconductivity of high critical temperature superconductors. Reducing this kind of disorder may improve significantly the structural quality of the samples and their temperature of superconductive transition (Tc). This work presents the situation when Bi2212 is co doped by lead (Pb) on bismuth (Bi) site and cerium (Ce) or lanthanum (La) on strontium (Sr) site. Used at low content, both Ce and La have the same valence (+3) in their ionic state but the first one has a magnetic moment of spin and the second is without. The doping by Pb on Bi site reduces the modulation of structure usually observed in this family of compounds. The effect of the co doping on the structural and transport properties is expected to give an idea on how the order in the planes is changed. The $Bi_{1.6}Pb_{0.4}Sr_{2-x}M_xCaCu_2O_{8+d}$ (M = Ce, La and $0 \leq x \leq 0.025$) superconductive ceramic samples were prepared by a solid-state reaction method. The samples were characterized by X-ray diffraction, scanning electron microscopy and resistivity versus temperature measurements. Results show how the structure, the normal state resistivity and the Tc are influenced by the co doping.

## 1. Introduction

Disorder is the main parameter to control and enhance superconducting properties of high Tc superconductors (SHTC). In the Bi2212 ($Bi_2Sr_2CaCu_2O_{8+d}$) phase the disorder occurs at the blocks surrounding or staying between the two $CuO_2$ planes belonging to the crystallographic unit cell of the phase: the $Bi_2O_2$ block, the SrO block and the Ca block. Disorder in the SrO block gives major effects on Tc [1-2]. Reducing the Sr site disorder through substitutions at the Bi and Ca sites is a possible way to obtain higher Tc [2]. The substitution of $Bi^{3+}$ by $Pb^{2+}$ by increasing the density of holes in the $CuO_2$ planes and reducing the structural modulation of the $Bi_2O_2$ block enhances Tc and the critical current density Jc [3-6]. This effect is improved with co doping by Pb at Bi site and a rare earth (RE) at Sr site. The substitution of $Sr^{2+}$ ion by a $RE^{3+}$ ion reduces the density of holes in the $CuO_2$ planes and compensates the effect of the substitution by Pb. Using ytterbium, terbium, holmium, lutetium, europium, gadolinium, dysprosium and yttrium [7-14] gives higher Jc and irreversibility line at higher fields. Doping by La the free lead Bi2212 phase results in a contraction of *c* axis cell parameter when the substituted ion, as for $Sr^{3+}$ [15], has a higher radius than $La^{3+}$, but also when, as for $Ca^{2+}$ [15, 16], the radius is lower. The

contraction of the *c* axis is mainly the effect of the reduction of the distance between two adjacent BiO planes caused by an increase of oxygen [17, 18]. $La_2O_3$ contributes to the increase of oxygen when it substitutes in the CaO or Sr block. The contraction of the *c* axis is always present when there is co doping with lead [19,20] which is supposed to lower the oxygen content. As for other rare earth substitution (except holmium), La improves Tc. This improvement is generally obtained by optimum oxygenation and occurs also when La is added to the (Bi,Pb)2212 phase [21]. Doping by cerium gives, in the free lead Bi2212 phase, results different from those obtained with the other rare earth [22-26]. Substitution by Ce on the Ca site presents a threshold rate between 15 and 20% where below it the Tc is improved and over it the Tc is strongly decreased. As for the substitution on the Ca site by other rare earths, the ionic radius of $Ce^{3+}$ or $Ce^{4+}$ is higher than the $Ca^{2+}$ one and there is a contraction of the *c* axis parameter. The result is nearly the same when Ce is added to the (Bi,Pb)2212 phase [27,28]. This fact has been explained by the tetravalent state of Ce corresponding to a spinless state of the ion. The work presented here compares the effects of co doping with lead andLa or Ce in the Bi2212 phase. La or Ce substitute in the Sr site at a very low rate not exceeding 1.25%.

## 2. Experiment

Bi(Pb,M)2212 (M = La, Ce) samples were prepared with nominal composition of $Bi_{1.6}Pb_{0.4}Sr_{2-x}M_xCaCu_2O_{8+\delta}$ (x varying from 0 to 0.025) using solid state reaction method. High-purity (more than 99.99%) $Bi_2O_3$, PbO, $SrCO_3$, $CaCO_3$, $La_2O_3$, $Ce_2O_3$ and CuO powders were weighed, mixed and ground in an agate mortar, then put in a cylindrical crucible and calcined at 800°C during 30h. The calcined powders were ground, pressed in pellet shape and sintered at 840°C during 50h. Structural properties and phase purity were characterized by X-ray diffraction using $Cu_{K\alpha}$ radiation. Diffraction spectra peaks were identified using ICDD data base. The lattice parameters of the Bi(Pb,M)2212 phases were obtained using Dicvol software [29]. Microphotographs were taken using a Scanning Electron Microscope (SEM). The electrical resistivity $\rho(T)$ was measured by a classical four-lead probe technique using an AC current with constant amplitude of 1mA and a Janis ST100 cryostat working from room temperature to liquid nitrogen temperature.

## 3. Results and discussions

The XRD patterns of Bi(Pb,La)2212 and Bi(Pb,Ce)2212 samples are shown in figures 1 and 2, respectively, with the Miller indices of the diffracting planes. The lattice parameters, obtained with Dicvol [29], show that the obtained phases are tetragonal. The angular position of the peaks changes significantly with the introduction of La or Ce. The displacement is toward higher angles for both doping. The insert in the left top of the figure shows the relative angular positions of (008) peaks for the different rates of doping.
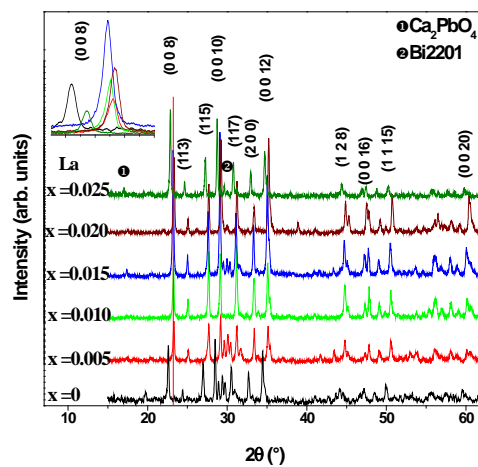


Fig. 1.

XRD patterns of samples doped with Pb and La with the Miller indices of the diffracting planes on the corresponding peaks. The insert in the left top shows the relative positions of the (008) peaks.
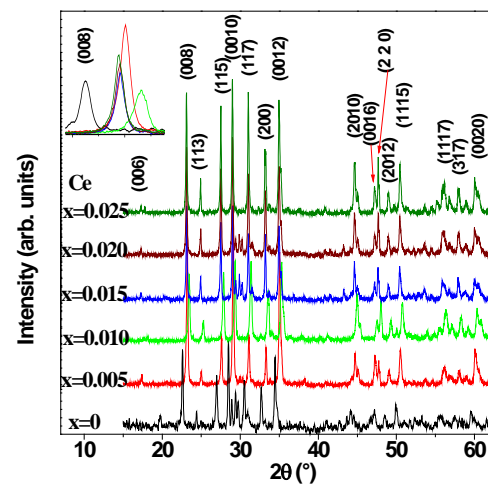
Fig. 2.

XRD patterns of samples doped with Pb and Ce with the Miller indices of the diffracting planes on the corresponding peaks. The insert in the left top shows the relative positions of the (008) peaks.

For La doped samples (figure 1), the displacement is maximum for rates $x \leq 0.02$ and decreases slowly with x, except for $x = 0.02$ which the maximum displacement. The intensities of main peaks are maximum for $x = 0.015$. For Ce doped samples (figure 2), the displacement of the peaks increases until $x = 0.01$ then decreases slowly for higher rates with a nearly constant angular position indicating a kind of saturation of substitution by Ce. For these samples the intensities of main peaks are maximum for the lower rate (x

= 0.005). All the samples doped and undoped, show a preferential orientation of their grains along the (00*l*) direction suggested by the higher intensities of the corresponding peaks. The parasitic phases (Bi2201 and $Ca_2PbO_4$) are more present in the La doped samples with x = 0.005 and x = 0.015. In the Ce doped samples the $Ca_2PbO_4$ parasitic phase is absent in all the spectra when the Bi2201 parasitic phase (not indicated in the figure and staying at about $2\theta = 29.9°$) is present for rates x = 0.015 and x = 0.02. For x = 0.005, the intensities of the peaks of the (00l) planes are more important than the other ones indicating a preferential orientation of the sample along these directions.
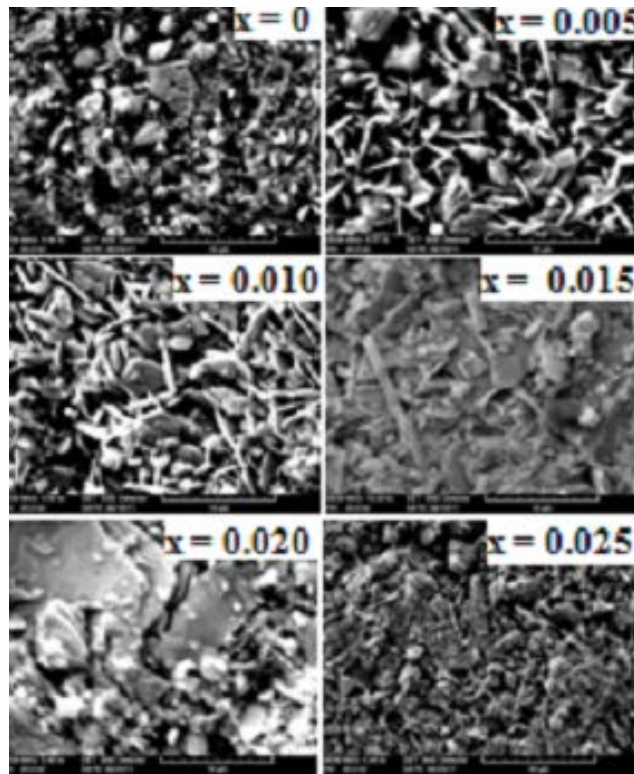


**Fig.3.** SEM photos of the samples doped with Pb and La with the content x of La indicated on each photo.
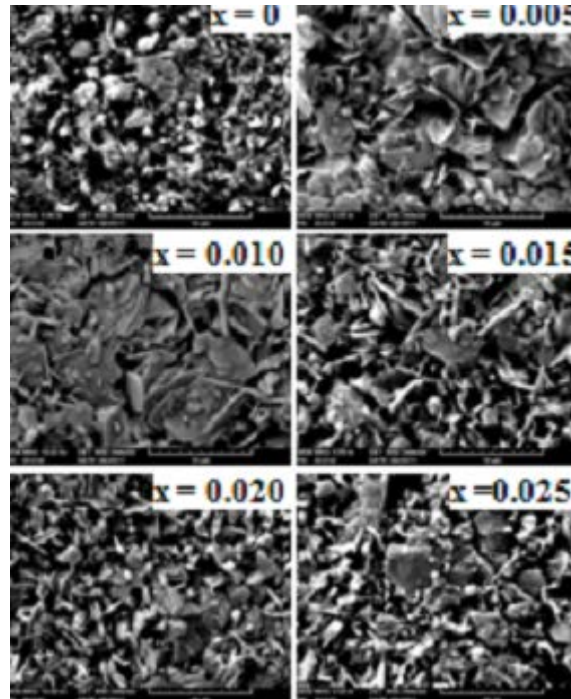
**Fig. 4.** SEM photos of the samples doped with Pb and Ce with the content x of Ce indicated on each photo.

The SEM photos of the La doped in figure 3 show the evolution of the morphology of the grains with the rate of doping. The apparent grain radius increases with x until x = 0.02. For the lower rates of La, more grain with whisker's shape may be noticed indicating a better crystal quality. The sample with x = 0.02 shows the highest grain radius (over 10 µm) and the presence of white nodules indicating the possibility of undissolved $La_2O_3$. For the highest rate, the grain radius decreases remarkably and their morphology is comparable to the undoped sample one. The samples doped with Ce (figure 4) present a different evolution of their morphology with the content of Ce. The maximum (more than 10 µm) of the grain radius is observed for x = 0.01 and for higher rate the grain radius decreases. Fewer grains with whisker's shape are observed and the white nodules are rare.
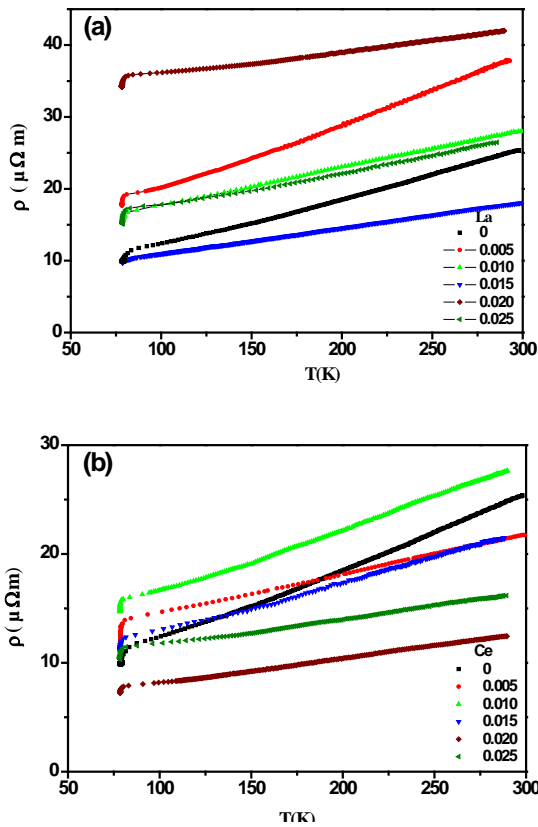
Fig. 5 Resistivity ρ(T) of the samples doped with Pb and La (a) or with Pb and Ce (b).
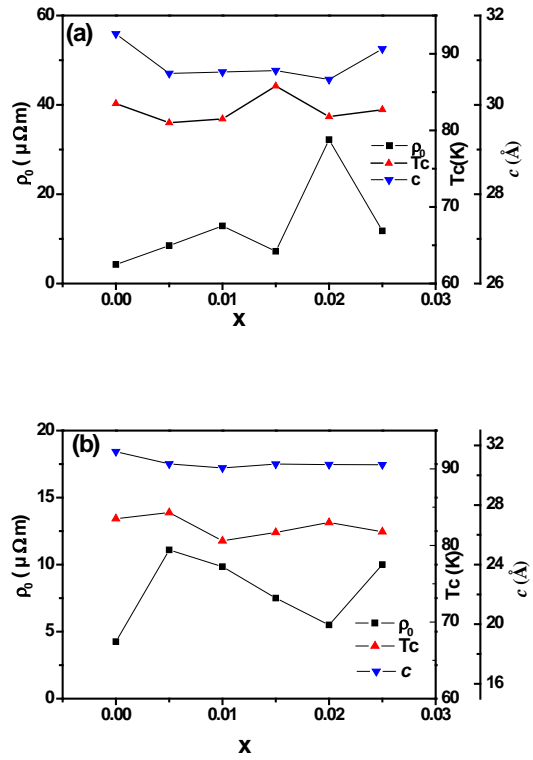
Fig. 6 Residual resistivity $\rho_0$, critical temperature of transition $T_c$ and *c* axis cell parameter versus the content x of La (a) or Ce (b).

Figure 5 shows the resistivity ρ(T) of all the samples. Doping with La (Figure 5(a)) increases the normal state resistivity except for the case x = 0.015. The normal state resistivity goes through a minimum when x increases from 0.005 to 0.02. The result is different for doping with Ce (Figure 5(b)) where the normal state resistivity is lowered except for the case x = 0.01. Extrapolating to O K the normal state part near 300 K of ρ(T) gives for all the sample the residual resistivity $\rho_0$ which is shown in figure 6 ((a) La doped samples; (b) Ce doped samples) together with the Tc and the *c* axis cell parameter. The temperature of critical transition Tc is measured for each ρ(T) at its deviation from its normal part and analysis of its derivative. For the La doped samples (Figure 6(a)), the improvement of Tc is obtained only for x = 0.015. The values of $\rho_0$ of these samples show that La doping decreases the density of charge carriers. This decrease is very important

for x = 0.02. The contraction of the c axis parameter correlates with the decrease of Tc except for x = 0.015 where there is an increase. These results, obtained for low rates of La, are different from those obtained for higher rates [19-21]. On the other hand, doping with La or Ce improves the obtaining of the (Bi,Pb)2212 phase, the different samples having been prepared in the same conditions. For the Ce doped samples (figure 6(b)), the improvement of Tc is obtained only for the lowest rate. The residual resistivity $\rho_0$ of these samples is increased by Ce and, until x = 0.02, decreases with x. On the other hand, the c axis cell parameter of these samples decreases and show a saturation effect for x greater or equal 0.015. The results obtained for Ce doping are qualitatively different from those obtained for La doping. Since $La^{3+}$ is spinless, the main process intervening in the doping is based on the charge transfer. If only the charge transfer is considered for Ce, similar results must be obtained. Ce has two ionic states $Ce^{3+}$ and $Ce^{4+}$ with energies very close to each other. Ce has also phase transition upon cooling or heating. The results presented here suggest strongly that not only the charge transfer effect is to be considered but also the spin effect connected with the $Ce^{3+}$ ionic state, the substitution of the spinless $Sr^{2+}$ supposed to give more disturb than in the spinless $Ce^{4+}$. This effect of the spin on the structural properties needs more study and is to be compared to the results obtained with holmium doping [9].

**4. Conclusion.**

The effects of co doping by La or Ce and Pb on the Bi2212 phase have been studied in this work. The obtaining of the (Bi,Pb)2212 is improved by both kind of doping until a rate which is much lower with Ce. Improvement of Tc is obtained at the lowest rate for Ce and at x = 0.02 for La. Comparison of residual resistivity and contraction o c axis cell parameter indicates a saturation effect in Ce doping and suggests that Ce is its spin state corresponding to a $Ce^{3+}$ ionic state.

**References**

1.      Eisaki H, Kaneko N, Feng D. L and et.al. Effect of chemical inhomogeneity in bismuth-based copper oxide superconductors. Phys. Rev. B 2004;69:064512-1-064512-8.

2.      Hobou H, Ishida S, Fujita K and et.al. Enhancement of the superconducting critical temperature in $Bi_2Sr_2CaCu_2O_{8+\delta}$ by controlling disorder outside $CuO_2$ planes. Phys. Rev. B 2009;79:064507-1-064507-6.

3.     Shimoyama J, Nakayama Y, Kitazawa K and et.al. Strong flux pinning up to liquid nitrogen temperature discovered in heavily Pb-doped and oxygen controlled Bi2212 single crystals. Physica C 1997;281:69-75.

4.     Shi L, Dong Q, Zhang Y. Effect of Pb-doping and annealing on the structure and Tc of Bi-2212 phase superconductor. Physica C 2000;341–348:649-650.

5.     Nishiyama M, Ogawa K, Chong I and et.al. Scanning tunneling microscope studies on the atomic structures in $Bi_2Sr_2CaCu_2O_{8+\delta}$ highly doped with Pb. Physica C 1999;314:299-307.

6.     Horvat J, Wang X.L, Dou S.X. Vortex pinning in heavily Pb-doped Bi2212 crystals. Physica C 1999;324:211-219.

7.     Sarun P.M, Vinu S, Shabna R and et.al. Microstructural and superconducting properties of Yb-substituted (Bi,Pb)-2212 superconductor sintered at different temperatures. J. Alloys Compd. 2009;472:13-17.

8.     Vinu S, Sarun P.M, Shabna R and et.al. Enhancement of flux pinning and Anderson–Dew-Hughes pinning analysis in $Bi_{1.6}Pb_{0.5}Sr_{2-x}Tb_xCa_{1.1}Cu_{2.1}O_{8+\delta}$ superconductor. J. Alloys Compd. 2009;477:L13-L17.

9.     Shabna R, Sarun P.M, Vinu S and et.al. Structural and electrical properties of $Bi_{1.7}Pb_{0.4}Sr_{2-x}Ho_xCa_{1.1}Cu_{2.1}O_{8+\delta}$ system across the metal to insulator transition. J. Alloys Compd. 2009;481:797-801.

10.    Vinu S, Sarun P.M, Shabna R and et.al. Microstructure and transport properties of $Bi_{1.6}Pb_{0.5}Sr_{2-x}Lu_xCa_{1.1}Cu_{2.1}O_{8+\delta}$ superconductor. Mater. Chem. Phys. 2010;119:135-139.

11.    Sarun P.M, Vinu S, Shabna R and et.al. Highly enhanced superconducting properties of Eu-doped (Bi,Pb)-2212. Mater. Lett. 2008;62:2725-2728.

12.    Vinu S, Sarun P.M, Shabna R and et.al.. Improved microstructure and flux pinning properties of Gd-substituted (Bi,Pb)-2212 superconductor sintered between 846 and 860 °C. Mater. Lett. 2008;62:4421-4424.

13.    Sarun P.M, Vinu S, Shabna R and et.al. Properties of superconducting, polycrystalline dysprosium-doped $Bi_{1.6}Pb_{0.5}Sr_{2-x}Dy_xCa_{1.1}Cu_{2.1}O_{8+\delta}$ ($0 \leq x \leq 0.5$). Mater. Res. Bull. 2009;44:1017-1021.

14.    Amira A, Boudjadja Y, Saoudel A and et.al. Effect of doping by low content of yttrium at Ca and Sr sites of Bi(Pb)-2212 superconducting ceramics., Physica B 2011;406:1022-1027.

15.    Uemoto H, Maki, Kishida S. Growth of La-doped $Bi_2Sr_2CaCu_2O_z$ single crystals by a self-flux method. J. Cryst. Gr. 2002;237-239:753-755.

16.     Jin H, Kötzler J. Effect of La-doping on growth and superconductivity of Bi-2212 crystals. Physica C 1999;325:153-158.

17.     Zhao X, Sun X, Fan X and et.al. Correlation between $T_c$ and $n_s/m^*$ in $Bi_2Sr_2CaCu_2O_{8+\delta}$ single crystals. Physica C 1998;307:265-270.

18.     Miura S, Yoshitake T, Manako T and et.al. Low temperature annealing effect of as grown BiSrCaCuO thin films on superconducting property and the c axis lattice constant. Appl. Phys. Lett. 1989;55:1360-1362.

19.     Biju A, Kumar R.G.A, Aloysius R.P and et.al. Flux pinning properties of rare earth modified (Bi, Pb)-2212 superconductors. Supercond. Sci. Technol. 2006;19:854-859.

20.     Ait Kaki A, Benmaamar F, Mosbah M.-F and et.al. Effect of co-doping by Pb and La on structural and magnetic properties of Bi2212 superconducting ceramics. Int. J. Mat. Res. 2009;9:1226-1229.

21.     Biju A, Vinod K, Aloysius R.P and et.al. Improved superconducting properties by La addition in (Bi,Pb)-2212 bulk superconductor. J. Alloys Compd. 2007;431:49-55.

22.     Jordan F, Peña O. Texturation and critical currents in cerium-substituted cuprates $Bi_2Sr_2Ca_{l-x}Ce_xCu_2O_{8+\delta}$. J. Magn. Magn. Mater. 1995;140-144:1315-1316.

23.     Wang R.P, Jinz H, Sekine H and et.al. Thermoelectric power of $Bi_2Sr_2Ca_{1-x}Ce_xCu_2O_{8+y}$ single crystals. J. Phys. Condens. Matter 1997;9:9615-9620.

24.     Thamizhavel A, Prabhakaran D, Jayavel R and et.al. Growth and characterization of superconducting $Bi_2Sr_2Ca_{(l-x)}Ce_xCu_2O_{8+\delta}$ single crystals. Physica C 1997;275:279-283.

25.     Wang R.P, Jin H, Sekine H. Thermoelectric power in $Bi_2Sr_2Ca_{l-x}Ce_xCu_2O_{8+y}$ single crystals and polycrystals based on NL model. Physica C 1997;282-287:1259-1260.

26.     Rama Sita D, Singh R. Structural and superconducting properties of $Bi_2Sr_2Ca_{l-x}Ce_xCu_2O_y$. Sol. St. Comm. 1995; 94:969-972.

27.     Biju A, Sarun P.M, Aloysius R.P and et.al. Comparison of superconducting properties of Ce added (Bi, Pb)-2212 with other rare earth additions. J. Alloys Compd 2007;433:68-72.

28.     Shabna R, Sarun P.M, Vinu S and et.al. Charge carrier localization and metal to insulator transition in cerium substituted (Bi,Pb)-2212 superconductor. J. Alloys Compd 2010;493:11-16.

29.     Boultif A, Louer D. Indexing of powder diffraction patterns for low-symmetry lattices by the successive dichotomy method. J. Appl. Crystallography 1991;24:987-993.

# PECULIARITIES OF ZNCDSE NANOLAYERS BY CHEMICAL DEPOSITION

## Jafarov M.A., Nasirov E.F.

*Baku State University, Baku 1045, Z.Khalilov st.23, Azerbaijan*
*e-mail: maarif.jafarov@mail.ru*

## Abstract

In this work the results on the investigation of the pecularity near the solar spectrum region, of $Zn_{1-x}Cd_xSe$ nanofilms, nanoscale heterojunction prepared on silikon and alumminium substrates by precipitation from aqueous solutions are presented. The temperature dependence of dark and light conductivity, spectrum and optical quenching of primary and impurity photoconductivity are investigated. The obtained results show that when controlling ionic composition and heat-treatment (HT) conditions, one can purposely control the properties of $Zn_{1-x}Cd_xSe$ ($0 \leq x \leq 0.6$) films, achieve the appropriate degree of compensation of different recombination levels and traps attributed to intrinsic defects or impurities, which result in high level of photoelectrical parameters near the IR region. Just after deposition the photoconductivity spectrum maximum of $Zn_{1-x}Cd_xSe$ ($0 \leq x \leq 0.6$) films is observed at $\lambda_1 = 0.545 \div 0.495 \mu m$ versus the film composition.

**Keywords:** *chemical bath deposition, nanoparticle, nanofilms, nanoscale junction, micro emulsion system, photoconductivity, solar cells*

## 1.Introduction

Among the many different methods available to deposit films of semiconductors, chemical bath deposition (CBD) must rank as conceptually the simplest. CBD refers to depositions from solution (usually aqueous) where the required deposit is both chemically generated and deposited in the same bath. Thus, deposition from a supersaturated solution or spin coating from a colloidal sol are not included under the aegis of CBD: in both cases, the layer material must be pre-prepared. Neither is sol–gel layer formation, although it could be reasonably argued that the cross-linking which occurs during the process constitutes a chemical reaction. Successive ion layer adsorption and reaction (SILAR) is a related technique, where a substrate is first dipped in an ionic solution of one component, rinsed, then dipped in a solution of the second component and rinsed; this ideally results in a single monolayer of the desired compound. Liquid phase deposition (LPD) is a specific subset of CBD often used for acidic oxides. In spite of it being so simple, it is one of the least known [1-5]. If scientists or engineers in general would be asked to name some semiconductor film deposition methods, evaporation, chemical vapour deposition, sputtering, may be even electrodeposition, would be the most obvious techniques that would spring to mind: CBD would probably be well down the list (with the obvious exception of those who work with the method). A part of the reason

(probably not the main part, which remains non-obvious) is the many different terms used to denote CBD: chemical solution deposition (used to be more popular, but a consensus is beginning to appear favoring CBD), chemical deposition (when it is clear that chemical vapour deposition—a very different technique—is not meant) and liquid phase deposition (used for certain oxide depositions).[7-11]

The last decade sharply increased, the interest to nano-objects with the most distinguishes features. It related with the unique properties of particles with this sizes which differ them from according macro phase. The investigation of the properties of nanoparticles is one of the main aims of the novel directions of physical chemistry. Developing of this direction is closely connected with the simple and accessible methods of synthesis, which allow preparing of nanoparticles with the simulated size and rather narrow separation on sizes. The reverse micro emulsion systems are thermodynamically sustainable double phase systems, that consist of polar phase micro drops, separated in nonpolar ambient. Surface-active materials (SAM) are used for stabilization of the systems like this. It makes possible caring out chemical reactions among materials in polar phase and forming hard-solved compounds. The advantage of this preparing method of nanoparticles is relatively simplicity and also possibilities of simultaneous synthesis and stabilization of prepared particles [12-14].

The obtained results show that when controlling ionic composition and HT conditions, one can control properties of the $Zn_{1-x}Cd_xSe$ films. Furthermore, the above films are nearly similar in their main photoelectric properties and parameters to such model crystals as CdSe and ZnSe, to allow for the effect of sticking centers, conditioned polycrystalline structure. Since the $Zn_{1-x}Cd_xSe$ films can be used as photodetectors of the near IR region. To determine the general regularities and characteristic of recombination and electron-molecular processes, determinant high sensitivity in IR region, versus the composition and heat-treatment (HT) conditions, the photoelectrical properties of $Zn_{1-x}Cd_xSe$ ($0 \leq x \leq 0.6$) films deposited from the solution is the purpose of present investigations [15-18].

## 2.Experiment

In this paper, it was investigated preparing of nanoparticles of ZnCdS in micro emulsion system stabilized with nonionic surface active materials and impact of volume of the drops and supersaturation to size of forming ZnSe particles. Hexamethylene was

used as a non polar phase. We used water, water solution of $Cd(Ac)_2$, $ZnCl_2$ and precrystallized $Na_2Se_2O_3$ as a polar phase. All solutions have been prepared in bidistilled water. Reverse micro emulsion systems were prepared by solubilization of water, water solutions according to salts in reverse micelles system, which Tx-100 concentration was 0.3 M and SAM/n-SAM ratio was 4:1. The water or water solutions of corresponding salts were added to the defined volume of this solution with drops in such amount that W=[$H_2O$] /[SAM] ratio have been varied in the range of 5-15. Equal volume of micro emulsion with similar content, containing ions of reacting substances in aqueous phase was mixed for preparing cadmium sulfide.

Particle size of cadmium sulfide prepared during reaction process has been defined by spectrophotometrical method. Dependence of optical density on wavelength was measured by spectrophotometer in cuvette in the range of wavelength 320-500 nm.

The $Zn_{1-x}Cd_xSe$ (0≤x≤0.6) films of 0,8-2μm thickness were deposited on Si substrates from aqueous solution by the method described in[3]. This was prepared by adding into the beaker containing the stirred deionized water at 85°C, $Cd(CH_3COO)_2$, $Zn(CH_3COO)_2$, $NH_4OH$, and $Na_2Se_2O_3$, from 0.05, 0.05, 12 and 0,2M stock solutions, respectively, in that order. The nanofilms composition (0≤x≤0.6) was changed by partial substitution of the thiourea and was controlled by chemical, spectral and X-ray phase analyses.

The spectral dependence of optical transmittance of $Zn_{1-x}Cd_xSe$ films were using in fig.1. A part of films was subjected to heat-treatment in the air at temperatures of 400-500$^0$C for 0-30 min. The temperature dependence of dark ($\sigma_{dk}$) and light conductivity ($\sigma_{ph}$), the spectrum and optical quenching of photoconductivity ($\sigma_{oq}$), the current-illumination characteristics, thermostimulated conductivity in the range of 80-400 K has investigated. According to thermopower measurements, the films were n-type. The dark conductivity of $Zn_{1-x}Cd_xSe$ films was found to vary with x, from $10^{-4}$ to $10^{-5}$ S/cm.

The ratio of photocurrent to the dark current reached $10^2$ to $10^3$. The carrier concentration determined from Hall measurements was 3-5x$10^{14}$ cm$^{-3}$ and $10^{16}$cm$^{-3}$ for the films with x=0 and x=0.3, respectively.

Photoconductivity spectrum maximum of $Zn_{1-x}Cd_xSe$ (0≤x≤0.6) films is observed at 0.545-0.495μm versus the composition. Just after deposition the above films are characterized by long-term relaxation photoeffects. Subsequent to heat-treatment, the considerable changes in photoelectric (PE) properties versus the composition, temperature

and annealing time ($\tau_a$) are observed. The dependence of conductivity as a function of time ($\tau_0$) has nonmonotonically character, i.e. with low $\tau_a$, the conductivity of films increases and achieves a maximum value exceeding the initial one by more than four orders of magnitude. The further increase of annealing time up to 15min leads to a sharp decrease of conductivity. The $\sigma_c(\tau_a)$ dependence has an extremum character, i.e. primarily it increases at annealing times to 15min, then (t≥15 min) a slow decay is observed. With increasing annealing temperature and x, a shift of the above dependence extremums toward the lower times takes place. Subsequent to heat treatment, the photoconductivity spectrum considerable widens and the peaks at (0.58-0.70) μm and (0.90-1.13) μm appear. With increasing time, to 4≤$\tau_a$≤15min, the intensities of additional maximum increases and intensity of principal maximum decreases. The $Zn_{1-x}Cd_xSe$ (0≤x≤0.6) films after the heat treatment at $500^0C$ for 5-10min exhibit high sensitivity ($\sigma_{ph}/\sigma_{dk}= 10^7$ to $10^8$) over a wide spectral range.

The photosensitivity in near IR region is comparable with proper photoconductivity. But with increasing temperature from nitrogen to room, the photosensitivity stays constant. At low temperatures the $Zn_{1-x}Cd_xSe$ (x=0.2) films have a complex spectrum of the impurity photoeffects, i.e. a superpositio The energy positions of the photoactive levels (impurity and defects levels) were determined from the impurity photoconductivity spectra when comparing them with the calculated data for deep compensated centres with a spectral dependence of photoionisation section in the c-band $S_n(h\nu)$ and the v-band $S_p(h\nu)$ [6-8].
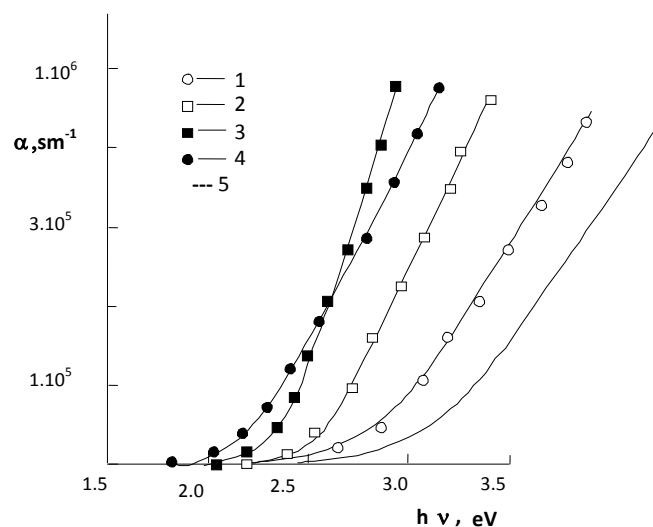


Fig. 1. The spectral dependence of optical transmittance of $Zn_{1-x}Cd_xSe$ films, versus x; 1-(0,9), 2- (0.7), 3- (0.4), 4- (0.3), 5- (0.1).

In the solar cell of CdTe, the lattice mismatch between n-CdSe and p-CdTe and the low bandgap of CdSe window layer are known to have some drawback on cell performance. Using higher bandgap materials like ZnSe or $Zn_{1-x}Cd_xSe$ as a heterojunction partner to CdTe can improve the window bandgap, but the lattice mismatch of these materials is worse than that of CdSe. Trading off the latter mismatch for the higher bandgap may not be the solution, for the loss in cell performance due to lattice mismatch outweighs the gain due to the increase in window bandgap.
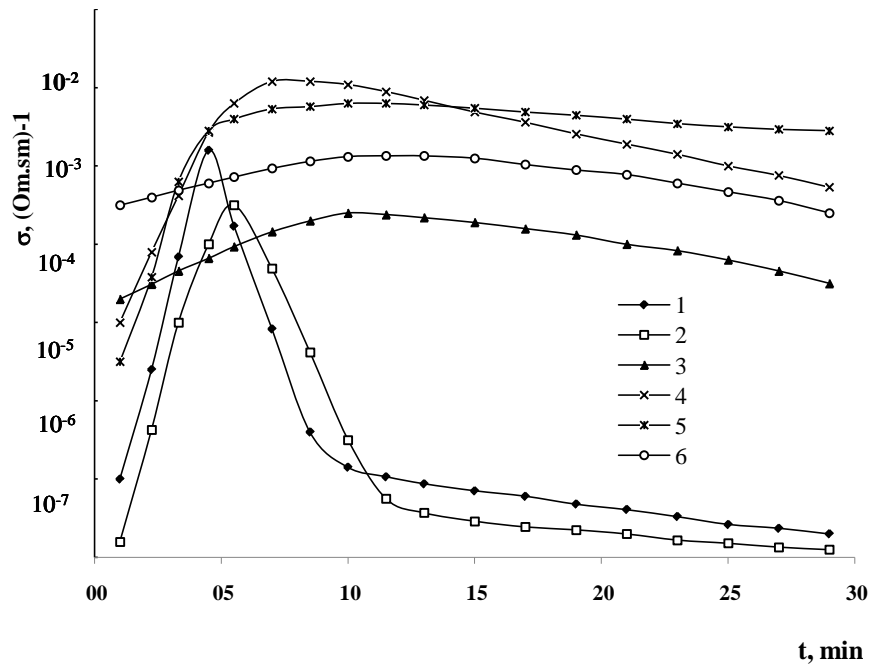


Fig.2. Semilog plot of (1,2,3) dark conductivity and (4,5,6) photoconductivity in $Zn_{1-x}Cd_xSe$ ($0 \leq x \leq 0.6$) films vs. annealing time; x=(1,4) 0.1, (2,5) 0.2, (3,6) 0.4.

Therefore, to retain the compatibility of CdSe and CdTe and still improve the short wavelength spectral response of CdTe solar cell, its traditional CdSe/CdTe structure should be changed to $Zn_{1-x}Cd_xSe$/CdTe. In other words, a $Zn_{1-x}Cd_xSe$/CdSe layer should replace the CdSe-only window layer. Since the CBD-grown CdSe layer has produced some of the best performing cells, the growth of the new $Zn_{1-x}Cd_xSe$/CdSe window layer by CBD should therefore be explored. Each experimental solution contained 300 ml of deionized water.

We have demonstrated using chemical and thermal activated diffusion that $Zn_{1-x}Cd_xSe$ thin films can be synthesized from electrochemical deposited ZnS/CdS multilayers. A more homogeneous $Zn_{1-x}Cd_xSe$ film is obtained at low processing temperature if the stacked layers are thin. Of great importance is that the grown structure

is almost homogenized in the chemical bath at the temperature below $90^0$C. The homogenization of our structure is achieved by annealing at $400^0$C, the temperature generally used for processing solar cells. The low processing temperature developed here in the fabrication of $Zn_{1-x}Cd_xSe$ means that the proposed $Zn_{1-x}Cd_xSe/CdSe$ solar cell window could be grown at temperatures that will not damage the glass or the underlying transparent conducting oxide generally used as substrate in solar cells. To achieve the new $Zn_{1-x}Cd_xSe/CdSe$ structure proposed for the CdTe window layer, what is required is simply an additional growth of CdSe on top of the $Cd_{1-x}Zn_xSe$ layer obtained from a chemical deposition ZnSe/CdSe multilayer. The structures are n-Si/CdSe/$Zn_{1-x}Cd_xSe$/contact, type 1 (a) and p-Si/CdSe/$Zn_{1-x}Cd_xSe$ type 2 (b) (Fig.3.). In type 1 $Cd_{1-x}Zn_xSe$/CdSe window, a 0.15µm-thick ZnCdSe film was first deposited on Si substrate. This was then dipped in $CdCl_2$ methanol solution for about 30 s to improve the conductivity, then dried with an infrared lamp, and then rinsed in the deionized water. This was followed by an additional deposition of 0.05µm CdSe thin film to complete the window fabrication. In type 2 CdSe/$Zn_{1-x}Cd_xSe$ window, a 0.15µm thick CdSe film, sandwiched between two 0.04 µm-thick ZnSe films, was first deposited by CBD on Al substrate. The sample was then annealed in $CdCl_2$/Ar ambient at $400^0$C for 15 min.

## 3. Discussion of results

The interpretation of experimental results becomes complicated due to a simultaneous occurrence of several processes (evaporation, generation and transformation of intrinsic defects) in films at the heat treatment. The kinetics of every process has a complicated character[9]. The dependence observed in photoelectric properties of films point out the changes of concentration of defects of donor and (or) acceptor character due to film annealing. The decreases of film photosensitivity at low annealing times ($\tau_a$) indicate the increase in concentration of fast-recombination centres (s-centres), i.e. the increase of the recombination flux ($g_s$), and hence the decrease in the life of electrons takes place. The measurements of the current- illumination characteristics of samples show that at low annealing times the decrease in hole concentration on the slow recombination centres (r - centers) is observed. This fact can be attributed either to increase of compensating shallow donor concentration or decrease of the r-centre concentration. A simultaneous increase in concentration of shallow donor centres responsibly for increase of dark conductivity and the fact recombination centres causing

the decrease of photosensitivity allows to assume that the s-centres are the complexes consisting of shallow donors [19].
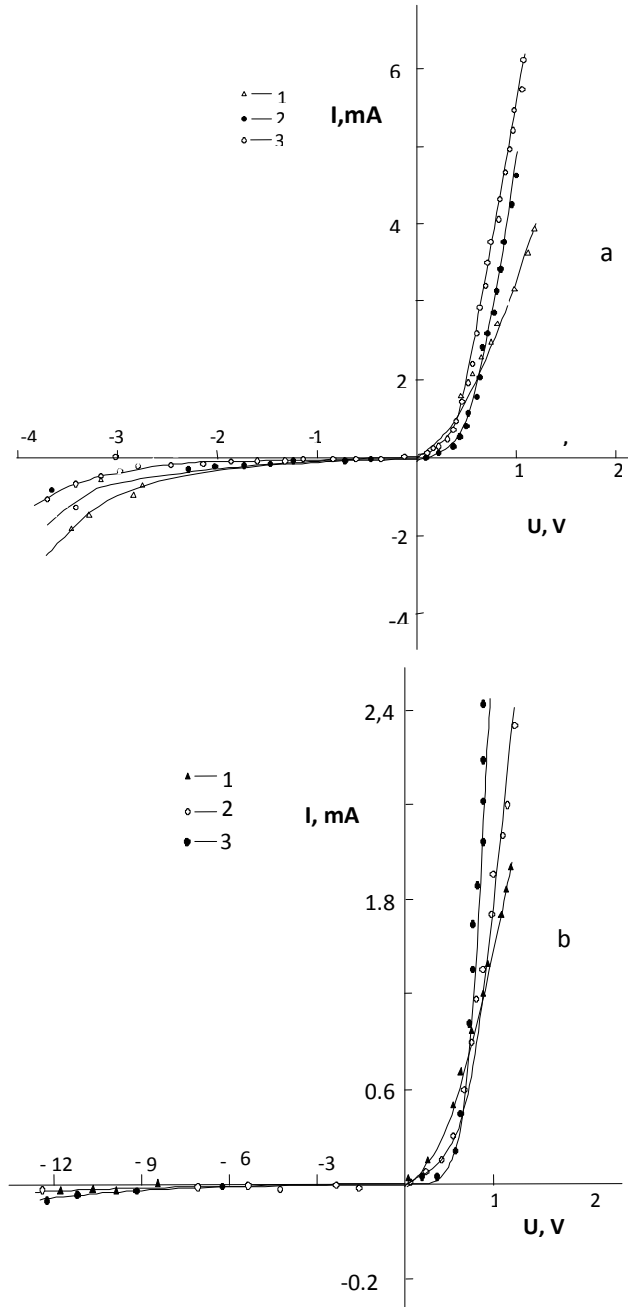


Fig. 3. VAX of the structures n-Si/CdSe/Zn$_{1-x}$Cd$_x$Se/contact, type 1 (a) and p-Si/CdSe/Zn$_{1-x}$Cd$_x$Se type 2 (b)

The change observed at $\tau_a \geq 5$min can be explained when the anion and the cation vacancies diffusing into the volume are formed on their surfaces. Due to heavy evaporation of metal at initial stages of annealing, the near-surface region is mainly

enriched by cadmium and sulfur vacancies playing the role of slow recombination centres. Their diffusion to the volume leads to increase of photosensitivity and to decrease of dark conductivity. In this case, the complexes of cadmium, sulfur and selenium vacancies, i.e. the recombination r-centres, are formed.

The decrease of photoconductivity of annealing times $\tau_a > 15-20$min is attributed to a single electron-molecular mechanism considering the initial state of film surface as were as local and collective phenomena at chemisorption. At initial state of annealing the increase of surface potential barrier due to chemisorption leads to increase of film sensitivity due to slow recombination. When the recombination controlled by the r-centres, the increase in their occupancy by holes due to chemisorption results in decrease of the lifetime of photoholes, i.e. the photoconductivity decreases. In this case, with increasing sulfur concentration in films the effect of oxygen becomes lower.

The main peculiarities of the POQ process are determined by the energy structure of r-centres with the excited state of holes: the hole transfer from the ground state to the excited one followed by thermal preexcitation of holes to the v-band at phonon absorption beads to the occurrence of the long-wavelength POQ maximum. The short-wavelength POQ maximum is attributed to optical transition of the hole directly to the v-band [20].

The experiments carried out shown that there are no difference in kinetics of photocurrent reduction under illumination with the wavelengths corresponding to the both quenching maximum and this testifying their relations to one type of recombination centres.

The curve of photocurrent reduction is characterized only by the time of that recombination centre where the electrons from v-band are transferred by impurity light.

The obtained results show that when controlling ionic composition and heat treatment conditions, one can control the properties of $Zn_{1-x}Cd_xSe$ ($0 \leq x \leq 0.6$) films, achieve the appropriate degree of compensation of recombination levels and traps attributed to intrinsic defects or impurities. In this way model crystals, as CdSe and ZnSe, can explain the main photoelectrical properties and parameters of $Zn_{1-x}Cd_xSe$ ($0 \leq x \leq 0.6$) films.

## 4.Conclusion

The $Zn_{1-x}Cd_xSe$ ($0 \leq x \leq 1$) films deposited from solution the sensitivity condition of these films have been determined. The obtained results show that when controlling ionic

composition and HT conditions, one can control the properties of $Zn_{1-x}Cd_xSe$ ($0 \leq x \leq 1$) films.

Furthermore, the above films are nearly electron similar on their main photoelectric properties and parameters to such model crystals as CdSe and ZnSe. The recombination schemes and electron transitions in $Zn_{1-x}Cd_xSe$ ($0 \leq x \leq 1$) films and $A^2B^6$ crystals are identical. Not only a chemical composition but also a degree of crystallization are not determining, and the difference in photoelectric properties is attributed to the nature and the concentration distribution of recombination centres and trapping levels.

## References

1. M.A Jafarov., Inorganic materials, v.35, N.11, p.1307-1312, (19990.

2. M.A Jafarov., Inorganic materials, v.35, N 3, p.300-302, (1999).

3. A.Sh. Abdinov, M.A. Jafarov, *Proc.of SPIE*, 6636, (2007) ,68-71.

4. R. I S. Yang, T. Zhang, L. Zhang, S. Wang, Z. Yang, B. Ding, *Colloids Surf. A: Physicochem. Eng. Aspects*, **296**, 1-3, (2007), 37.

5. A.S. Khomane, P.P. Hankare, *J. Alloys Comp.* 489, (2010), 605.

6. A.V. Kokate, U.B. Suryavanshi, C.H. Bhosale, *Sol. Energy* 80, (2006),156.

7. M. Izaki, T. Shinagawa, K. Mizuno, Y. Ida, M. Inaba, A. Tasaka, *J. Phys. D* 40, (2007), 3326.

8. A. Ates, M. Saglam, B. Güzeldir, M.A. Yıldırım, A. Astam, *J. Opt. Adv. Mater.* 12, (2010), 1466.

9. A. Cortes et al. *Solar Energy Materials and Solar Cells*, **2**, № 1-2, (2004), 21.

10. P. Kumar et al. *Optical Materials*, №27, (2004), 261.

11. A. Dumbrava, *Chalcogenide Letters*, **6**, 9, (2009), 437.

12. A.Sh.Abdinov, M.A.Jafarov, E.F. Nasirov, *Proc.SPIE*, 4467, (2003), 186-194.

13. S.V. Bagul, S.D. Chavhan, R. Sharma, *J. Phys. Chem. Solids* 68, (2007), 1623.

14. J. Liu, D. Xue, *J. Cryst. Growth* 311, (2009), 500.

15. C. Yan, D. Xue, *J. Phys. Chem. B* 110, (2006), 25850.

16. Hao Lin, Wei Xia, Hsiang N. Wu, and Ching W. Tang, CdS/CdTe solar cells with MoOx as back contact buffers, Appl. Phys. Lett. 97, 123504 (2010).

17. Zhou Fang, Xiao Chen Wang, Hong Cai Wu, and Ce Zhou Zhao, Achievements and Challenges of CdS/CdTe Solar Cells, International Journal of Photoenergy. Vol.2011, Article ID 297350 (2011).

18. Abdinov A.S., Jafarov M.A., Nasirov.E.F., Proc. of SPIE, v.4340, p.107-111, (2000)

19. V.E.Lashkarev, A.V.Lubchenko, M.K.Sheinkman, Nonequilibrium processes in photoconductors, Kiev, 1981, pp.264.

20. A.V.Burlak, A.V.Ignatov, V.V.Serdyuk, Phys. and Techniques of Semiconductors, v.20, n. 9, pp. 1713-1716, (1986)

# AUTHOR'S INDEX

Organized by

**Frantsevich Institute for Problems of Materials Science**

**of National Academy of Sciences of Ukraine**

**03142, 3 Krzhyzhanovsky Str., Kyiv, Ukraine**

**www.ipms.kiev.ua**



**Ukrainian Materials Research Society**

**03142, 3 Krzhyzhanovsky Str., Kyiv, Ukraine**

**www.umrs.kiev.ua**